A Ten-Fold Improvement to the Limit of the Electron Electric Dipole Moment

A thesis presented
by

Benjamin Norman Spaun

to
The Department of Physics
in partial fulfillment of the requirements
for the degree of
Doctor of Philosophy
in the subject of

Physics

Harvard University
Cambridge, Massachusetts
May 2014

Thesis advisor Author

Gerald Gabrielse **Benjamin Norman Spaun**

A Ten-Fold Improvement to the Limit of the Electron Electric Dipole Moment

Abstract

The wonderfully successful Standard Model is incomplete in that it fails to explain how a matter universe survived annihilation with antimatter following the big bang. Extensions to the Standard Model, such as weak-scale Supersymmetry, explain this phenomena by asserting the existence of new particles and interactions that break time-reversal symmetry. These theories predict a small, yet potentially measurable electron electric dipole moment (EDM), d_e. Our new measurement of the electron EDM with thorium monoxide (ThO) gives $d_e = (-2.1 \pm 3.7_{\mathrm{stat}} \pm 2.5_{\mathrm{syst}}) \times 10^{-29}$ e cm, which corresponds to an upper limit of $|d_e| < 8.7 \times 10^{-29}$ e cm with 90 % confidence. This order of magnitude improvement in EDM sensitivity sets strong constraints on new physics at an energy scale (TeV) at least as high as that directly probed by the Large Hadron Collider. The unprecedented precision of this EDM measurement was achieved by using the extremely high effective electric field within ThO to greatly magnify the EDM signal. The reported measurement is a combination of about 200,000 separate EDM measurements performed with about 20 billion ThO molecules in a cold, slow buffer gas beam. Unique features of ThO, such as a near-zero magnetic moment and high electric polarizability, drastically suppress potential systematic errors.

Contents

List of Figures

List of Tables

Papers and Publications

1. "Search for the electric dipole moment of the electron with thorium monoxide," A.C. Vutha, W.C. Campbell, Y.V. Gurevich, N.R. Hutzler, M. Parsons, D. Patterson, E. Petrik, B. Spaun, J.M. Doyle, G. Gabrielse and D. DeMille, *Journal of Physics B* **43**, 074007 (2010).

2. "A cryogenic beam of refractory, chemically reactive molecules with expansion cooling," N. R. Hutzler, M. F. Parsons, Y. V. Gurevich, P. W. Hess, E. Petrik, B. Spaun, A. C. Vutha, D. DeMille, G. Gabrielse, J. M. Doyle, *Phys. Chem. Chem. Phys.* **13**, 18976-18985 (2011).

3. "Magnetic and electric dipole moments of the $^3\Delta_1$ state in ThO," A. C. Vutha, B. Spaun, Y. V. Gurevich, N. R. Hutzler, E. Kirilov, J. M. Doyle, G. Gabrielse, D. DeMille, *Phys. Rev. A*,**84**, 034502 (2011).

4. "Advanced Cold Molecule Electron EDM.," ACME Collaboration: W. C. Campbell, C. Chan, D. DeMille, J. M. Doyle, G. Gabrielse, Y. V. Gurevich, P. W. Hess, N. R. Hutzler, E. Kirilov, B. OLeary, E. S. Petrik, B. Spaun, and A. C. Vutha., *EPJ Web of Conferences*, **57**, 02004 (2013).

5. "Shot-noise-limited spin measurements in a pulsed molecular beam," E. Kirilov, W.C. Campbell, J.M. Doyle, G. Gabrielse, Y.V. Gurevich, P.W. Hess, N.R. Hutzler, B.R. O'Leary, E. Petrik, B. Spaun, A.C. Vutha, D. DeMille, *Phys. Rev. A* **88**, 013844 (2013).

6. "Order of Magnitude Smaller Limit on the Electric Dipole Moment of the Electron," ACME Collaboration: J. Baron, W. C. Campbell, D. DeMille, J. M. Doyle, G. Gabrielse, Y. V. Gurevich, P. W. Hess, N. R. Hutzler, E. Kirilov, I. Kozyryev, B. R. O'Leary, C. D. Panda, E. S. Petrik, B. Spaun, A. C. Vutha, A. D. West., *Science*,**343**, p. 269-272 (2014).

7. "Zeeman interaction in ThO H $^3\Delta_1$ for the electron EDM search," A.N. Petrov, L.V. Skripnikov, A.V. Titov, N.R. Hutzler, P.W. Hess, B.R. O'Leary, B. Spaun, D. DeMille, G. Gabrielse, and J.M. Doyle, *Submitted to Phys. Rev. A*, (2014).

Acknowledgments

The work described in this thesis would not have been possible without the hard work and leadership of the professors, postdocs, and students I have been privileged to work with and under for the past six years. I would first like to thank my thesis adviser, Gerald Gabrielse for guiding and supporting my work on the ACME experiment, and for convincing me on my first day at Harvard that electric dipole moments were exciting. I have also greatly benefitted from the guidance and support of the other ACME PIs, John Doyle and David DeMille.

The contributions of the graduates, undergraduates, and postdocs of ACME are too many to number. However, I would like to specifically thank the other four graduate students who, over the past six years, have taken this project from its development stage to its first EDM result. It has been a true pleasure working with Nick, Paul, Elizabeth, and Brendon. I can think of no other group of students with whom I would rather brain storm and problem solve. I would also like to thank Yulia and Amar, the two original graduate students of ACME, for helping me get me feet wet in lab and teaching me about lasers, cryogenics, and physics beyond the standard model. I thank Emil for showing up at just the right time and pushing this project forward with his remarkably fast work. The future of ACME is in good hands with Adam, Elizabeth, Brendon, Cris, and Jacob pushing for another factor of ten in EDM precision.

Outside of ACME, I am lucky to have worked in a department with such wonderful and helpful staff and students. I would like to thank Jan Ragusa for helping with many administrative tasks and for taking care of the entire Gabrielse group. Thanks to Stan Cotreau and Jim MacArthur for making fun of me, giving me something to

laugh about, and making lots of parts for ACME. Thanks to the Doyle group for letting me steal their food and coffee, and for always being so fun and cheerful to be around. I consider myself extremely fortunately to have been a part of the very supportive Gabrielse group. I thank Josh, Shannon, Paul, Jack, Elise, Rita, Phil, Yulia, Steve, Rob, Kathryn, Mason, Nathan, and the other Josh for lots of enjoyable conversations and for helping me keep life in perspective.

I am very thankful for the many friends and family members who have made it possible for me to pursue and complete my doctorate. I thank my parents, Frank and Joy, for being my very first science teachers and for encouraging me to pursue a subject that I found truly fascinating. I thank my undergraduate mentors Donna and Kamesh for their encouragement and guidance over the years. Thanks to my four siblings and many in-laws who have helped keep me grounded. Finally, I thank my wife Bridgette for her steadfast love and support, and for sacrificing much time and sleep to take care of our son while I completed my PhD research.

Chapter 1

Motivation and Background

Despite the many successes of the Standard Model (SM) of particle physics and cosmology, there are important facts of the universe that the Standard Model simply cannot explain. Perhaps the most fundamental mystery is how our universe made of matter survived after the Big Bang produced equal amounts of matter and antimatter. This mystery could possibly be explained if there were undiscovered sources of charge-parity symmetry (CP) violation in the universes [1]. Many extensions to the Standard Model, such as supersymmetry, seek to account for the matter-antimatter asymmetry (baryon asymmetry) by asserting the existence of new CP-violating particles and interactions.

High energy experiments, such as those at the Large Hadron Collider (LHC), directly search for these predicted particles at TeV energy scales by smashing beams of protons together [2]. A powerful way to probe for new particles on even higher energy scales is to look for their low energy signature effects on more "common" particles, like the electron. Specifically, SM extensions nearly always predict that exotic particles will produce a T- and P-violating electron electric dipole moment (EDM, d_e) that is many much larger than the EDM predicted by the Standard Model. Assuming CPT invariance, T violation is equivalent to CP violation. EDM measurements can therefore be used to search for new sources of CP violation and directly test the predictions of proposed modifications to the Standard Model [3].

This thesis describes a new measurement that limits the electron EDM to

$$d_e < 8.7 \times 10^{-29}\, e\,\mathrm{cm} \tag{1.1}$$

with 90% confidence, the most precise electron EDM measurement to date by more than an order of magnitude [4, 5]. This result places strict constraints on new T-violating physics at energy scales ranging from 1 to 20 TeV, depending on the specific SM extension [6, 7, 8]. The unprecedented precision of this measurement was achieved using the high effective electric field within thorium monoxide (ThO) to make a measurable EDM signal from a tiny EDM [9, 10, 11]. Other features of ThO, such as a near-zero magnetic moment and high electric polarizability, allowed potential systematic errors to be drastically suppressed [12].

The work presented in this thesis was conducted as part of the ACME collaboration, a joint effort between the Gabrielse and Doyle groups at Harvard University and the DeMille group at Yale University. The remainder of this chapter discusses the motivation for the EDM measurement in more detail and reviews the limitations of previous experiments. Chapter 2 describes how certain features of ThO allow us to overcome these limitations, and Chapter 3 outlines the procedure used to measure the EDM with ThO molecules. Chapter 7.2.2 summarizes the work done to develop this experimental procedure and to study the unique quantum properties of ThO.

Chapters 7.2.3 and 6 describes the EDM experiment apparatus and data analysis routine. Finally, Chapter 7 describes the many checks we performed to ensure that the EDM measurement was not compromised by systematic offsets.

1.1 Beyond the Standard Model

The Stardard Model has been wonderfully successful in describing fundamental particles with incredible precision. Measurements of the electron electric dipole moment, the most precisely measured property of a fundamental particle, agree with Standard Model predictions to an astonishing one part per trillion. However, the Standard Model provides no explanation for how the matter universe we see today survived annihilation with antimatter after the the Big Bang. To understand how a matter-animatter asymmetry might have come about, it is helpful to consider three fundamental symmetries of nature: parity inversion, time reversal, and charge conjugation. Parity inversion (P) switches the sign of all spatial coordinates (i.e. $x \rightarrow -x$, $y \rightarrow -y$, $z \rightarrow -z$); time reversal (T) inverts the sign of all quantities associated with time ($t \rightarrow -t$) or motion, such as momentum $\vec{p} \rightarrow -\vec{p}$; charge conjugation (C) reverses electric charge ($q \rightarrow q$). All the laws of classical physics are identical under these mathematical operations.

As Andrei Sakharav first noted [1], an asymmetry between matter and antimatter can occur if two fundamental symmetries, C and CP, are broken. Two additional requirements for baryon number asymmetry are thermal non-equilibrium and baryon number violation. Several fundamental symmetries are already known to be broken. P-violation was first observed in 1957 when radioactive Cobalt nuclei were observed to emit more radiation along, instead of against, their spin direction [13]. CP-violation was first observed in the K meson in 1964 [14]. Only CPT is currently believed to be a perfectly unbroken symmetry [15, 16, 17], which implies that T and CP symmetries are equivalent. The Standard Model incorporates all observed symmetry breaking, encoding T-violation (CP-violation) in a complex mixing phase, $\delta_{CKM} = 1.05 \pm 0.24$, in the Cabibbo-Kobayashi-Maskawa (CKM) quark matrix. However, the baryon number asymmetry that can be generated from this complex phase is many orders of magnitude below that observed in the universe [18, 1, 19, 20]. There must still be undiscovered sources of T-violation.

The baryon number asymmetry is certainty not the only physical mystery that the Standard Model cannot explain. The SM also fails to provide a plausible candidate for dark matter, which is currently believed to comprise 83% of the mass of the universe [21, 20, 22]. Similarly, there is no explanation for the dark energy that seems to be causing the universe to expand at an ever-increasing rate [23]. The SM also cannot explain the experimental fact that the CP-violating term in quantum chromodynamics is extremely small, which is commonly referred to as the *strong CP problem* [24]. For these reasons, and others [25], the SM is seems incapable of providing a complete description of nature.

Extensions to the Standard Model seek to resolve some of these problems by positing the existence of new exotic particles not present in the SM. These particles allow addition couplings that can produce new sources of T-violation [8]. The new particles are believed to be very heavy with masses greater than the Higgs boson, so they can also account for dark matter phenomena [20]. Many theories are variations of Supersymmetry, which postulates that every observed boson has a massive partner fermion, and vice versa [26, 27].

1.2 Electron EDMs in Standard Model Extensions

An important consequence of the new particles and interactions proposed by most all extensions to the Standard Model is that they will produce an asymmetric charge distribution, or electric dipole moment (EDM, d_e) in the electron. Nearly all theories that assert the existence of new T-violating particles and interactions also predict electron EDM values within, or just beyond, the sensitivity of previous EDM experiments[6, 28]. EDM searches are therefore powerful tools for testing new physics beyond the Standard Model [29, 30]. To better understand this claim, let us first examine some important properties of EDMs.

1.2.1 EDMs and Fundamental Symmetries

An electron EDM must point along the electron spin direction, $\vec{S}$. One hundred years of atomic spectra indicate that only one vector is needed to describe the electron. A consequence of the Wigner-Eckart theorem is that the expectation value of all vector operators acting on an eigenstate of angular momentum are proportional to one another [31]. Because $\vec{d_e}$ and $\vec{S}$ are both vector operators, this means that $\langle\vec{d_e}\rangle \propto \langle\vec{S}\rangle$.

A non-zero permanent EDM violates both T and P symmetries, as illustrated in Figure 1.1. Spin, an angular momentum, reverses under T but not under P or C. The dipole, only reverses under P. If we begin with $\vec{d_e}$ aligned with $\vec{S}$ and then apply either T or P operations, we end up with $\vec{d_e}$ anti-aligned with $\vec{S}$. This system can be invariant under T or only if either $\vec{d_e}$ or $\vec{S}$ is zero. Since we know that the spin is not zero, then $\vec{d_e}$ must be zero. The alternative is that this system is not invariant under both T and P.

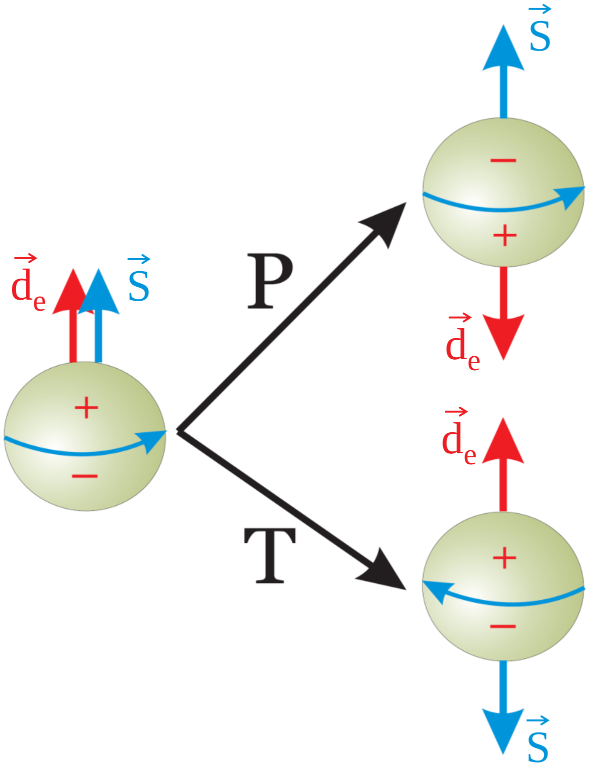

Figure 1.1: The effect of P and T operations on an electron with electric dipole moment. Both operations change the relative alignment of $\vec{d_e}$ and $\vec{S}$.

1.2.2 Predicted EDM Values

Non-zero EDMs are allowed in the Standard Model insofar as P- and T-violation exist in the Standard Model. However, the predicted EDM value, $d_e^{\mathrm{SM}} < 10^{-38}$ e cm, is far below the range of current experimental sensitivity. The SM prediction is so small because the electron is a lepton and the only T-violating term, δ_{CKM}, in the SM is in the quark sector. Feynman diagrams of one, two, and three loops all produce no electron EDM [32]. The contributions of four-loop diagrams are estimated to be no larger than 10^{-38} e cm [33].

If new T-violating particles and interactions exist, as asserted by SM extensions, there is no reason to believe that their contributions to the electron EDM will be suppressed in the same way the contribution from δ_{CKM} is suppressed. For example, large supersymmetric leptons could directly interact with the electron in a one-loop Feynman diagram to produce an EDM [8]. Most SM extensions predict that an EDM will arise from one or two loop interactions [7]. In general, a new particle with mass M_X will interact with the electron in an n-loop diagram to produce an EDM with size

$$d_e \sim \kappa \left(\frac{\alpha_{\mathrm{eff}}}{4\pi}\right)^n \left(\frac{m_e}{M_X^2}\right) \sin(\phi_{\mathrm{T}}) \frac{\hbar e}{c}, \tag{1.2}$$

Here m_e is the electron mass, $\kappa \sim 0.1$-1 is a dimensionless prefactor, ϕ_{T} is a T-violating complex phase, and $\alpha_{\mathrm{eff}} \approx 4/137$ is the weak interaction coupling strength between new particles and electrons [34, 3, 35]. It is generally assumed that the T-violating complex phase ϕ_{T} introduced by new interactions will be of order unity, similar in size to the one T-violating phase in the SM, δ_{CKM}, since there is no compelling reason to expect a much smaller value.

Figure 1.2 show predicted electron EDM values from several SM extensions. The blurred edges reflect the EDM values corresponding to a range of complex phases, prefactors, and particle masses. If experimental limits narrow an EDM range pre-

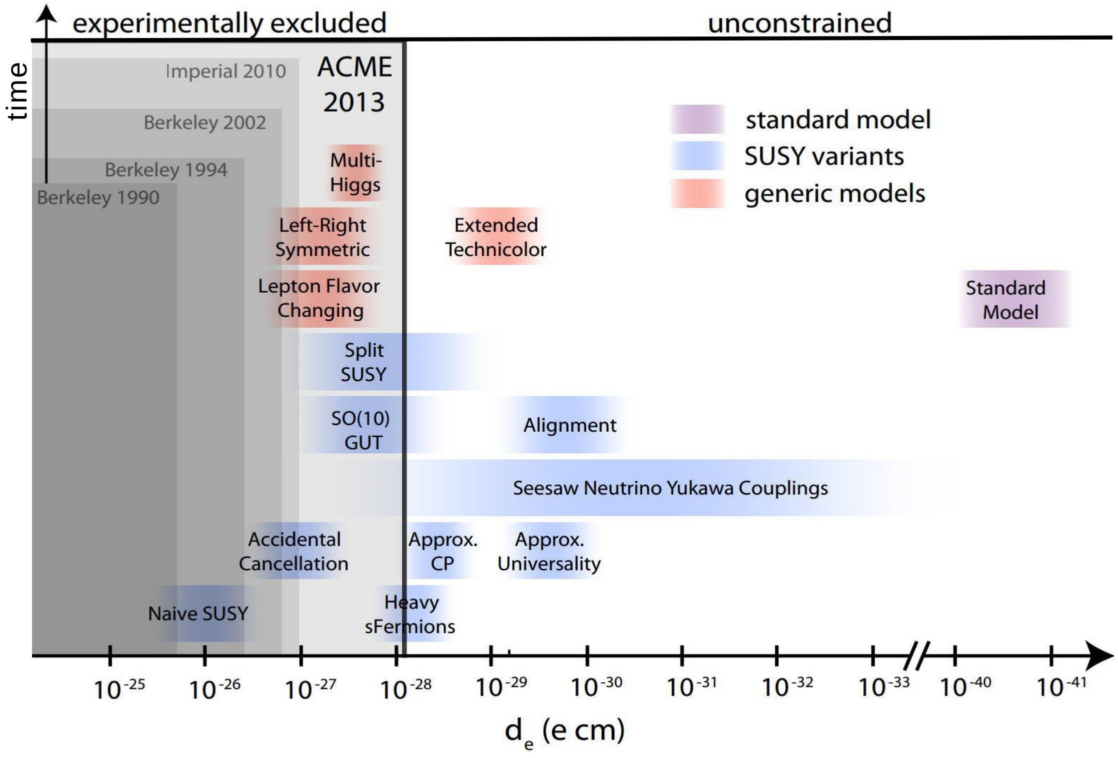

Figure 1.2: Electron EDM Predictions of prominent Standard Model extensions [28]. The latest ACME measurement was precise enough to directly test several variations of Supersymmetry.

dicted by a certain theory, that theory must then resort to special assumptions, or "fine tuning" to a smaller prediction. According to Equation 1.2, an EDM arising from a one-loop interaction with a new particle twice as massive as the Higgs Boson will be larger than 10^{-26} e cm. Clearly this "naive" prediction of supersymmetry was excluded a decade ago by the thallium EDM experiment [36]. ACME is now able to directly test specific theories beyond the standard model. Our first result constrains T-violation at energy scales of $M_X c^2 \sim 1$ TeV or $M_X c^2 \sim 20$ TeV for SM extensions that allow d_e to arise from two or one loop Feynman diagrams, respectively [37, 29, 7, 35]. This energy range is comparable to, and even higher than in some cases, the energy range that can be directly probed by the Large Hadron Collider [2].

Permanent EDM measurements in other particles, such as neutrons and protons, are also important to the search for undiscovered sources of T (CP) violation. The best limit on the neutron EDM, $|d_n| < 2.9 \times 10^{-26}$ e cm, was obtained using ultra-cold neutrons produced at Institut Laue-Langevin [38]. The best limit on the proton EDM, $|d_p| < 7.9 \times 10^{-25}$ e cm, was deduced from the mercury EDM limit, $|d_{\text{Hg}}| < 3.1 \times 10^{-29}$ e cm, obtained at the University of Washington [39]. These experiments are also sensitive to a number of other T-violating quantities, such as T-violating nucleon-nucleon couplings [1] [39]. Whereas electron EDM experiments are sensitive to new sources of T violation arising in the lepton sector of particle physics, neutron and proton EDM experiments are sensitive to T violation in the hadron sector. Like the complex phase δ_{CKM} that encodes T violation arising from weak interactions, strong interactions can also produce a P- and T-violating term δ_{QCD} in quantum

---

[1] Mercury is sensitive to many T-violating quantities, such as T-violating nucleon-nucleon and nucleon-electron couplings, along with the proton, neutron, and electron EDMs [39].

chromodynamics. While δ_{CKM} is of order unity, experimental limits on the neutron EDM have constrained δ_{QCD} to be $\lesssim 10^{-10}$ rad [40]. Providing a natural explanation for this incredibly small value remains a problem for the Standard Model (i.e. the Strong CP Problem) [24]. Because because T (CP) violation in strong interactions is not well understood, and because neutrons and protons are composed of subarticles, it can be difficult to estimate the neutron or proton EDM predicted by the Standard Model or Standard Model extensions [29]. If one assumes that the only contribution to the neutron EDM is from δ_{CKM}, the expected neutron EDM value in the SM is $\sim 10^{-32}$ e cm [2] [40]. Standard Model extensions typically predict neutron EDM values between 10^{-25} and 10^{-28} e cm [41, 29].

1.3 EDMs in Atoms and Molecules

A permanent electron EDM would manifest itself as an energy shift that depends on the electron spin direction relative to an external electric field, $\Delta E_{EDM} = \vec{d_e} \cdot \vec{\mathcal{E}}$. Unfortunately, this energy shift cannot be detected in free electrons: the applied electric field required to induce the energy shift would also exert a force on the electrons and cause them to accelerate out of the experiment. However heavy atoms and molecules that contain electrons with unpaired spins provide a suitable environment for electron EDM measurements [42, 43] [3]. In this case the EDM produces an atomic

---

[2] Estimates of neutron and proton EDMs produced by δ_{CKM} in the SM are generally much larger than the electron EDM predicted by the SM. This is because neutron and proton EDMs can arise in two-loop Feynman diagrams in the SM [40], whereas Feynman diagrams of one, two, and three loops all produce no electron EDM in the SM [32].

[3] Electron pairs have oppositely aligned $\vec{S}$ and therefore oppositely aligned $\vec{d_e}$. To first order the effect of $\vec{d_e}$ in the electron pairs cancel. EDM searches in diamagnetic atoms such as mercury [39] are sensitive to the electron EDM to a lesser degree through higher order couplings.

or molecular energy level shift that depends on the effective electric field that the electron experiences inside the atom or molecule, $\Delta E_{EDM} = \vec{d}_e \cdot \vec{\mathcal{E}}_{\text{eff}}$. As we shall see, $|\vec{\mathcal{E}}_{\text{eff}}|$ is actually many orders of magnitude larger than what can be externally applied in a laboratory [44, 10]. Atoms and molecules can therefore significantly enhance experimental sensitivity to d_e.

At first glance, it seems that the same problem that made it impossible to measure d_e in free electrons would also prevent d_e from being measured in atoms or molecules. An electron in an atomic or molecular orbital cannot experience a net electric field without also experiencing a net acceleration. The fact that orbiting electrons in neutral atoms do not accelerate in an electric field implies that the average internal field they experience is zero, $\langle \vec{\mathcal{E}}_{\text{int}} \rangle = 0$, a consequence first note by Schiff [45]. However, electrons travel at relativistic speeds near heavy nuclei, causing $\vec{d}_e$ to experience Lorentz contraction. The Lorentz contraction causes $\vec{d}_e$ to spatially vary throughout the electron orbit, so $\langle \vec{d}_e \cdot \vec{\mathcal{E}}_{\text{int}} \rangle$ need not be zero even though $\langle \vec{\mathcal{E}}_{\text{int}} \rangle = 0$, a fact first discovered by Sandars [42].

Not only is the overall effective electric field, defined as $d_e \mathcal{E}_{\text{eff}} = \langle \vec{d}_e \cdot \vec{\mathcal{E}}_{\text{int}} \rangle$, not zero in atoms and molecules, it is much larger than what can be achieved in a laboratory [46]. For example, the effective field of ThO molecules used in the ACME experiment was 84 GV/cm [10], a million times larger than the highest possible laboratory field. $\mathcal{E}_{\text{eff}}$ scales with atomic number Z^3 [47], which is why EDM searches profit from using heavy atoms, or molecules with heavy atoms [36, 10, 48, 4, 39]. Only unpaired electrons will produce an EDM energy shift since the contributions of paired electrons with opposite spins will always cancel. Because the required Lorentz contraction only occurs near the nucleus, the atom or molecule used for the EDM measurement must have unpaired electrons with core-penetrating s-shell wavefunctions.

Though we have focused on the electron's interaction with the internal electric field, the externally applied field is crucial to measuring EDMs in atoms and molecules. In the absence of an external field the Hamiltonian of an atom or molecule is rotationally symmetric, with eigenstates of well-defined parity. A parity eigenstate $|\psi\rangle$ does not by itself experience a linear first-order Stark shift from an applied electric field $\vec{\mathcal{E}}$ since the electric dipole operator $\vec{d}$ is a parity odd-quantity,

$$\Delta E^1 = \langle\psi|\, \vec{d}\cdot\vec{\mathcal{E}}\,|\psi\rangle = \langle\psi|\,\vec{d}|\psi\rangle\cdot\vec{\mathcal{E}} = 0. \tag{1.3}$$

The parity eigenstates of dipolar molecules are equal linear combinations of states with opposite internuclear axis orientations, and thus opposite intermolecular electric field orientations. In such states $\vec{d_e}$ is aligned with the intermolecular field as often as it is anti-aligned with the field, so the net EDM energy shift is always zero. However, when the molecule experiences a laboratory electric field, the opposite parity states mix to produce new energy eigenstates [4],

$$|\psi'_\pm\rangle \propto |\psi_\pm\rangle + \frac{-\Delta_0 + \sqrt{\langle\psi_\mp|\,\vec{d}\cdot\vec{\mathcal{E}}\,|\psi_\pm\rangle^2 + \Delta_0^2}}{\langle\psi_\mp|\,\vec{d}\cdot\vec{\mathcal{E}}\,|\psi_\pm\rangle}\,|\psi\mp\rangle\,, \tag{1.4}$$

where $2\Delta_0$ is the energy difference between the two parity states. Polarization P is typically used to quantify the extent to which opposite parity states are mixed,

$$P = \frac{-\Delta_0 + \sqrt{\langle\psi_\mp|\,\vec{d}\cdot\vec{\mathcal{E}}\,|\psi_\pm\rangle^2 + \Delta_0^2}}{\langle\psi_\mp|\,\vec{d}\cdot\vec{\mathcal{E}}\,|\psi_\pm\rangle}. \tag{1.5}$$

---

[4] To simplify the formula, the states shown here are not normalized.

With a sufficient laboratory electric field, such that $\langle\psi_\mp|\,\vec{d}\cdot\vec{\mathcal{E}}\,|\psi_\pm\rangle >> \Delta_0$, a diatomic molecule can be fully polarized, $P \approx 1$, with equal component of the initial parity states,

$$\text{Completely polarized:} \quad |\psi'_\pm\rangle = \frac{|\psi_\pm\rangle + |\psi\mp\rangle}{\sqrt{2}}. \tag{1.6}$$

These completely mixed eigenstates experience a linear Stark shift, $\Delta E^1 = \langle\psi'_\pm|\,\vec{d}\cdot\vec{\mathcal{E}}_{\text{eff}}\,|\psi'_\pm\rangle \neq 0$, which means that the molecular axis now has a preferred orientation in the lab, along $\vec{\mathcal{E}}$. The new eigenstates correspond to the internuclear axis being either aligned or anti-aligned with the laboratory electric field (see Chapter 2 for more details). d_e can then be aligned or anti-aligned with the intermolecular field, resulting in an EDM energy shift $\Delta E_{\text{EDM}} = \vec{d}_e \cdot \vec{E}_{\text{eff}}$.

For most atoms the highest possible laboratory electric field is not strong enough to produce full electric polarization. This is because the detuning Δ_0 between opposite parity states is so large. These atoms will not be as sensitive to the EDM as fully polarized molecules, since the net effective field experienced by an electron scales with P [49, 47]. Assuming dipole matrix elements are comparable in most atoms and molecules, $\langle\psi_\pm|\,\vec{d}|\psi_\mp\rangle \approx ea_0$ where a_0 is the Bohr radius, the extent to which an atom or molecule can be polarized in a given electric field is solely determined by the energy spacing between opposite parity states. In most atoms, electronic states of opposite parity are spaced by at least 100 THz, so a very high laboratory electric field of 100 kV/cm could only produce $P \lesssim 10^{-3}$, using Equation 1.5 and $ea_0 \approx h\times$ 1 MHz/(V/cm). Diatomic molecules, on the other hand, have quantized rotational states of opposite parity that are typically spaced by 10-100 GHz. These states allow for $P \approx 1$ with 100 kV/cm applied fields. The effective fields that can be realistically achieved in molecules is therefore 1000 times what can be achieved in atoms with comparable atomic number Z. As will be discussed in the following chapter, some diatomic molecules exhibit Ω-doublet structure which yields opposite parity states that are spaced by only 0.1-50 MHz. These molecules can be fully polarized with modest electric fields of < 100 V/cm. As we shall see in the next section, the ability to achieve maximum $\mathcal{E}_{\text{eff}}$ in an EDM experiment with relatively small laboratory electric fields has huge advantages for systematic error suppression.

The shot-noise uncertainty limit for an EDM measurement in atoms or molecules can be obtained directly from the uncertainty principle [34], $\delta E \delta t \geq \hbar/2$. Nearly all EDM experiments utilize the method of separated oscillatory fields [50] to extract ΔE_{EDM} by measuring a spin precession phase (see section 2.4 for more detail). Thus δt in the inequality corresponds to the time τ that a coherent state freely precesses without being observed. Assuming $\mathcal{E}_{\text{eff}}$ is constant, the shot-noise uncertainty in the energy shift $\Delta E_{\text{EDM}} = d_e \mathcal{E}_{\text{eff}}$ is directly proportional to the EDM uncertainty,

$$\delta d_e \geq \frac{\hbar}{2\mathcal{E}_{\text{eff}} \tau \sqrt{N}}, \tag{1.7}$$

where N is the number of times the measurement is repeated, or more practically the number of atoms or molecules detected in a measurement. Often the substitution $N \rightarrow \dot{N}T$ is made, with $\dot{N}$ being the rate at which EDM measurements are made, or “counting rate”, and T being the total integration time. For a fixed integration time, EDM measurement precision clearly increases with $\mathcal{E}_{\text{eff}}$, τ, and $\dot{N}$. All EDM experiments are designed so as to maximize these three quantities. In reality other sources of systematic, technical, and background noise add to the EDM uncertainty.

Most experiments, however, have reported EDM uncertainties that are 1.1-1.5 times above the uncertainty limit [39, 5, 36, 4].

1.4 Previous Electron EDM Measurements

Electron EDM measurements have been performed in a number of atoms and molecules over the past 50 years [51, 3], as shown in Figure 1.3. The experimental apparatus used for these measurements includes vapor cells, cold and hot beams, and solid state systems [52]. In this section we discuss the statistical and systematic limitations of three prominent EDM experiments conducted over the past 25 years: the Thallium experiment at U.C. Berkley [36], the YbF experiment at Imperial College [5], and the PbO experiment at Yale University [53]. For over 20 years (1990-2011) the Thallium experiment had the most precise measurement of d_e. Three generations of this experiment were responsible for lowering the d_e limit by two orders of magnitude. Only recently did the YbF experiment at Imperial College, the first EDM experiment conducted with a molecule, surpass this precision. While the PbO experiment at Yale was limited by systematic effects, it effectively demonstrated the advantages of Ω-doublet structure for EDM measurements[48]. In a sense it was a precursor to ACME's ThO experiment.

1.4.1 Thallium

The effective electric field achieved in the Thallium experiment, $\mathcal{E}_{\text{eff,Tl}} \approx 70$ MV/cm, was at the time the highest field ever achieved in an electron EDM experiment. The atoms were only polarized to $P \approx 10^{-3}$, even with applied electric

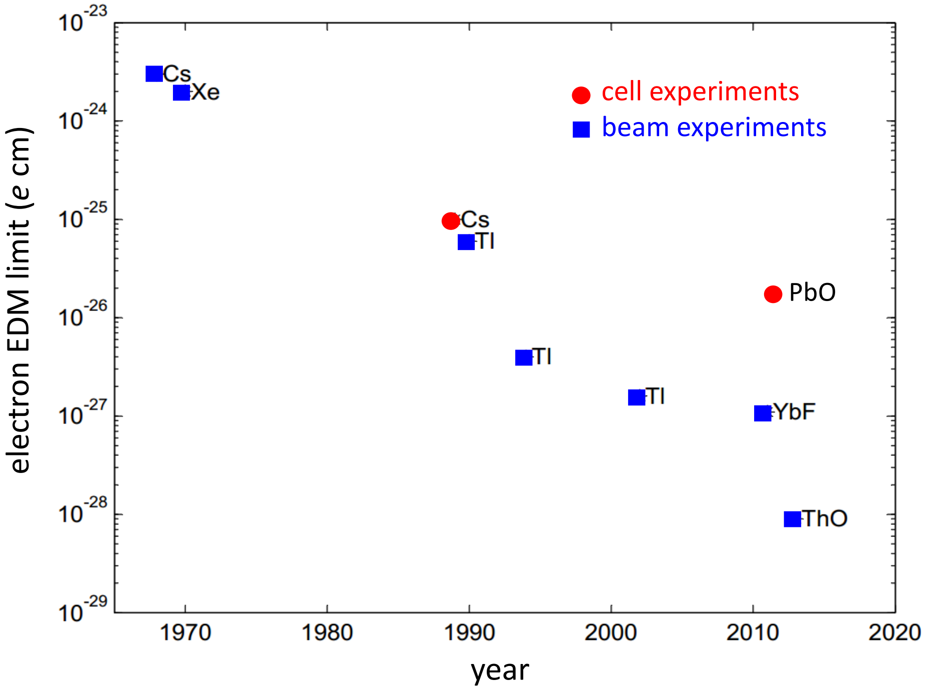

Figure 1.3: Electron EDM measurements of the past 50 years.

fields of $\mathcal{E}_{\mathrm{Tl}} \approx 120$ kV/cm, so this effective field was still only a small fraction of the $\mathcal{E}_{\mathrm{eff}}$ attainable if Tl could be fully polarized. This experiment boasted a thermochemical Tl source which allowed EDM measurements to be performed with $\sim 10^9$ Tl atoms every second. To date this is the highest counting rate, $\dot{N}$, ever achieved in an EDM experiment that used an atomic or molecular beam. The source was hot, however, which gave rise to a fast atomic beam forward velocity of 420 m/s [54]. This limited the spin precession time to $\tau_{\mathrm{Tl}} = 2.4$ ms, since it was difficult to engineer electric field plates longer than 1 m. Ultimately, this experiment was able to achieved a statistical uncertainty of $\delta d_{e,\mathrm{Tl}} = 5.5 \times 10^{-28}$ e cm with $\sim$60 hours of integration time, including auxiliary data to monitor systematic effects [36].

Three systematic effects limited the Thallium experiment: motional magnetic fields, geometric phases, and leakage currents. Motional magnetic fields, arise from atoms moving with velocity v through the high laboratory electric field, $\vec{\mathcal{B}}_{\mathrm{mot}} \sim \vec{v} \times \vec{\mathcal{E}}$. If laboratory electric and magnetic fields are not perfectly aligned, $\vec{\mathcal{B}}_{\mathrm{mot}}$ can induce a spin precession phase correlated with $\vec{\mathcal{E}}$. Likewise, a motional field can couple to magnetic field gradients to produce a geometric phase (Barry's phase) [55]. Leakage currents across the high voltage electric field plates can generate magnetic fields, and therefore spin precession, that depend on the direction of $\vec{\mathcal{E}}$. Just like an EDM, each of these effects produce a phase that reverses with laboratory electric field. These effects were well understood from the first generation of the Tl experiment in 1990. They were greatly suppressed with two separate pairs of counterpropagating Tl beams and monitored with a sodium comagnetometer. However, the effects could not be suppressed beyond $\delta d_{e,\mathrm{Tl}}^{\mathrm{syst}} \approx 5 \times 10^{-28}$ e cm, the systematic uncertainty of the third generation (2002) Tl measurement [36].

1.4.2 Ytterbium Fluoride

The YbF experiment was the first d_e measurement performed with molecules. The 40 GHz rotational line splitting allowed the molecules to be almost fully polarized ($P \approx 0.75$) with applied fields of $\mathcal{E}_{\mathrm{YbF}} \approx 10$ kV/cm. The resulting effective electric field was computed to be 14.5 GV/cm [56]. Though this field was 200 times larger than $\mathcal{E}_{\mathrm{eff,Tl}}$, the pulsed supersonic beam source used for YbF production limited the counting rate to 1.2×10^4 separate measurements per second, five orders of magnitude below the counting rate of the Tl experiment. Furthermore the fast 590 m/s forward velocity of the supersonic beam limited τ_{YbF} to 0.65 ms. The resulting statistical sensitivity of this experiment was five times worse than Tl for a fixed integration time. The YbF molecule, however, was immune to the systematic effects that ultimately limited the Tl experiment, as will soon be discussed. Therefore, with sufficient integration time (280 hours of EDM data, not including auxiliary systematic checks, acquired over three months), the YbF experiment was able to obtain comparable systematic uncertainty to Tl, $\delta d_{e,\mathrm{YbF}} = 5.7 \times 10^{-28}$ e cm. The resulting d_e upper limit was 1.6 times smaller than the Tl limit because of smaller systematic uncertainty and a measured EDM mean closer to zero [5].

All three systematic effects that limited the Tl experiment scaled with applied electric field. These effects were minimized in the YbF experiment since the required laboratory electric field was at least ten times smaller than that of the Tl experiment [56]. The effects were also suppressed by the large Stark splitting of the almost fully polarized YbF molecule. The leading systematic offset of the YbF experiment was rf detunings coupling to non-reversing electric fields. This effect produced an EDM offset of 5×10^{-28} e cm which was continuously monitored and corrected for. Other sources of systematic error were laboratory magnetic fields correlated with $\vec{E}$ and an unexplained correlation between the measured EDM and the field plate voltage offset. The combined systematic uncertainty was $\delta d_{e,\mathrm{YbF}}^{\mathrm{syst}} \approx 1.5 \times 10^{-28}$ e cm [5].

Comparing the YbF and Tl experiment illustrates to the important point that systematic suppression is just as important as high statistical precision in an EDM measurement. The Tl experiment only integrated for a few days, at which point the statistical uncertainty became comparable to the systematic error. It would have been useless to further reduce the statistical sensitivity with more averaging since the final measurement uncertainty was a quadrature sum of both statistical and systematic error contributions. In the YbF experiment systematic effects were suppressed well below the Tl limit statistical sensitivity. Even though Equuation 3.25 shows that the YbF statistical uncertainty for a given integration time was roughly five times larger than that of Tl, the YbF experiment ultimately achieved lower a d_e limit after months of integration time [5].

1.4.3 Lead Oxide

The PbO experiment demonstrated the advantages of Ω-doublet molecular structure to EDM measurements. This structure provided two closely spaced energy levels of opposite parity, allowing PbO to be completely polarized with laboratory fields of $\mathcal{E}_{\mathrm{PbO}} \approx 100V/cm$, which produced $\mathcal{E}_{\mathrm{eff,PbO}} \approx 25$ GV/cm. Unlike proceeding EDM measurements, this experiment used a hot vapor cell to produce PbO molecules. While this led to high molecular densities and counting rates, the spin precession time was limited to 50 μs by molecules sticking to the cell walls. The lifetime of the excited PbO state in which the measurement was conducted also limited this coherence time. As will soon be discussed, spurious effects in this experiment caused much of the collected EDM data to be rendered useless. The resulting statistical uncertainty $\delta d_{e,\mathrm{PbO}} = 9.5 \times 10^{-27}$ e cm was obtained from only four hours of data[53].

While the PbO experiment successfully demonstrated the power of omega doublet structure to minimize and suppress dominant Tl systematic effects [48], it was ultimately limited by other spurious effects arising from electric and magnetic field imperfections. Although the applied electric field was small in this experiment due to the high polarizability of PbO, the field homogeneity was poor. This resulted imperfect alignment of electric and magnetic fields that varied spatially and generated EDM-like signals [57]. Large EDM shifts were observed when stray magnetic fields, magnetic field gradients, and correlated electric and magnetic fields were applied. These parameters were inherently hard to control in this experiment because of the complex design of the vapor cell. It was necessary to apply a number of data cuts to ensure that these effects were not contaminating the EDM measurement. In the end only four hours of EDM data were used in the reported d_e limit [53]. The PbO experiment illustrates the need for a simple, well-controlled EDM apparatus and measurement protocol, in addition to a molecular structure that minimizes systematic effects, to ensure that the EDM measurement will not be jeopardized by spurious effects.

1.4.4 A New electron EDM experiment

As illustrate by the past 30 years of electron EDM experiments, three important requirements must be met to measure the electron EDM with significantly improved precision. First, the measurement must be performed in an atom or molecule that suppresses well-known systematic effects, such as those that limited the Tl experiment. Second, the experiment must allow for precise control of all important experimental parameters, even if it is not immediately apparent that these parameters would affect the measured EDM value. Lastly, the effective electric field, coherence time, and counting rate must be sufficiently high to allow EDM data can be gathered and analyzed within a reasonable integration time.

The ACME EDM experiment described in this thesis meets all three of these requirements. This experiment is conducted in a molecule, thorium monoxide (ThO), which boasts one of the highest effective electric fields, $\mathcal{E}_{\mathrm{eff,ThO}} \approx 84$ GV/cm, ever computed in a molecule. ThO exhibits Ω-doublet structure, with electric polarizability even higher than that of PbO. This structure also allows for spectroscopic reversal of $\mathcal{E}_{\mathrm{eff}}$ independent of applied electric field, a feature the promises to suppress a wide variety of systematic effects [48]. Unlike any previously used atom or molecule, ThO has a near-zero magnetic dipole moment, which further suppresses systematic effects related to any type of magnetic field imperfection (i.e. nearly all previously observed systematic effects). Furthermore, ThO molecules can be produced in large quantities in a buffer gas beam, similar to the YbF and Tl beams except the forward velocity is significantly slower. This slow velocity allows spin precession times comparable to YbF and Tl experiments to be achieved in a smaller apparatus with more uniform electric and magnetic fields. The combination of all of these features resulted in a new d_e limit more than ten times smaller than the previous best limit [4, 5].

Chapter 2

Advantages of the ThO Molecule

When designing a new EDM experiment, it is important to choose an atom or molecule that provides both high statistical sensitivity and systematic error suppression. As described in the previous chapter, effective electric field $\mathcal{E}_{\text{eff}}$, spin precession time τ, and measurement rate $\dot{N}$ must be maximized to achieve high statistical sensitivity. At the same time, the atom or molecule must be immune to the systematic effects that plagued previous experiments. In this chapter we describe the unique features of thorium monoxide (ThO) that allow all of these criteria to be met. ThO boasts one of the highest known effective electric fields, 84 GV/cm [10]. ThO also contains a metastable $^3\Delta_1$ state with many properties advantageous for an EDM measurement [12], including high polarizability, a tiny magnetic dipole moment, and an spectroscopic reversal of the effective electric field independent of the applied lab electric field. Other electronic states in ThO provide a way to populate and manipulate this state with convenient transitions frequencies accessible to diode lasers.

2.1 Ω-doublet stucture

The ThO H state, predominantly a $^3\Delta_1$ state, has many unique properties that are ideal for an EDM measurement. In this state the two ThO valence electrons are primarily in s and d electronic orbitals. The wavefunction of the electron in the s orbital has good overlap with the nucleus, and therefore experiences a high effective electric field [10]. The d orbital electron allows this state to have a near-zero magnetic moment by adding an orbital contribution to the magnetic moment that cancels with the spin contribution (see Figure 2.1). The H state also exhibits Ω-doublet structure, which provides two extremely important features for an EDM measurement: high polarizability and a way to reverse $\vec{\mathcal{E}}_{\text{eff}}$ without reversing the laboratory electric field. This section will describe the Ω-doublet structure in more detail, along with the advantages it provides to our EDM measurement.

In ThO the electron orbital angular momentum and spin are strongly coupled to high electric fields along the internuclear axis, $\hat{n}$, pointing from the oxygen nucleus to the thorium nucleus. Therefore, total electronic angular momentum, J_e, is no longer a good quantum number, although its projection onto $\hat{n}$, $\Omega = \vec{J}_e \cdot \hat{n}$, is still a good quantum number. Because of rotational invariance the eigenvalue J corresponding to total molecular angular momentum, $\vec{J} = \vec{R} + \vec{J}_e$, is also a good quantum number, where $\vec{R}$ is the angular momentum of the nuclei orbiting about their center of mass. In general, the various angular momenta in a molecule can couple together in different ways, depending on the characteristics of the molecule. This gives rise to separate Hund's cases, which each lead to a separate set of well-defined quantum numbers. Most diatomic molecules with two valence electrons can be described as either Hunds case (a) or Hunds case (c). For Hunds case (a) molecules the projection of electron spin, $\Sigma = \vec{S} \cdot \hat{n}$, and orbital angular momentum, $\Lambda = \vec{L} \cdot \hat{n}$, onto the internuclear axis are each considered good quantum numbers in addition to Ω. For Hunds case (c) molecules, $\vec{S}$ and $\vec{L}$ first couple to form $\vec{J_e} = \vec{L} + \vec{S}$, and the projection of this total electronic angular momentum onto the internuclear axis, $\Omega = J_e \cdot \hat{n}$ is the only good quantum number (see 2.1). The ground state of ThO is described well by Hunds case (a) but the excited electronic states of ThO are all Hunds case (c) states.

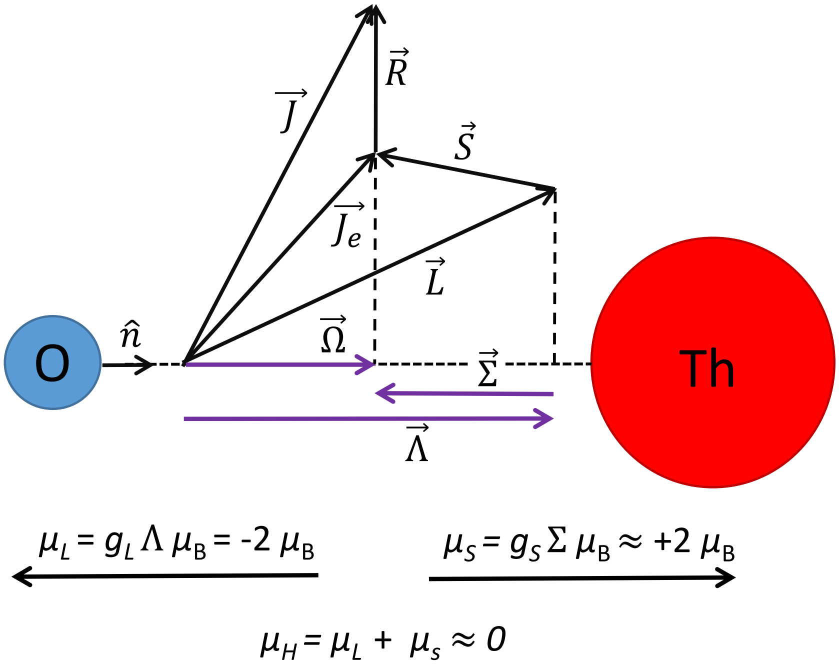

Figure 2.1: The ${}^3\Delta_1$ (H) state of ThO, with all angular momentum quantum numbers shown. Because projections of the orbital and spin angular momenta on the internuclear axis point in opposite directions, their contributions to the total magnetic moment almost perfectly cancel.

Electronic states in a Hunds case (a) molecules are often described in ${}^{(2S+1)}\Lambda_{|\Omega|}$, notation, analogous to ${}^{(2S+1)}L_J$ atomic notation. While this notation does not apply to Hunds case (c) states, these states can still be described as linear combinations of Hunds case (a) states. For example, the H state of ThO is 98.4% $^3\Delta_1$, 1.1%$^3\Pi_1$, and 0.5% $^1\Pi_1$ [58, 59]. We will primarily focus on the $^3\Delta_1$ component of H in this chapter, but it is worth noting that the smaller admixtures allow lasers to drive E1 transitions between H and other ThO electronic states.

With no external electric field, the Hamiltonian of a diatomic molecule does not change if the molecule is reflected about a plane passing through its internuclear axis. Although this reflection does not change molecular energy, it does change the the projection of angular momentum on the internuclear axis. This results in two degenerate states with opposite angular momentum projections, $\Omega = \pm|\Omega|$ (assuming $\Omega \neq 0$). This degeneracy, called Ω-doubling, can also be thought of as the degeneracy between electrons orbiting clockwise and counterclockwise about the internuclear axis. The clockwise/counterclockwise motions will produced opposite angular momentum projections, but in zero field should not yield states with different energies. For the lowest available rotational level, $J = 1$, the Ω-doublet states transform under parity as $P\,|\Omega\rangle = |{-\Omega}\rangle$. Eigenstates of parity $|\pm\rangle$ can therefore be constructed from linear combinations of $|\pm\Omega\rangle$:

$$|\pm\rangle = \frac{|\Omega\rangle \pm |{-\Omega}\rangle}{\sqrt{2}} \tag{2.1}$$

The degeneracy of the two parity states is broken by the coupling of electronic and rotational motion, as describe in [60], [49], and [61]. All ThO electronic states with $\Omega \neq 1$ contain these closely space levels of opposite parity, making them highly polarizable.

2.1.1 High Polarizability

The energy spacing between the ThO H state Ω-doublets is especially small. It was measured by Edvinson *et al* [62] to be only 362 ± 2 kHz for the lowest ($J = 1$) rotational level. Notice that this is 30 times smaller that the zero-field Ω-doublet splitting of state used for the PbO EDM experiment and more than 10,000 times smaller than the rotational splitting of the state used in the YbF EDM experiment. Laboratory fields of only 10 V/cm are more than sufficient to polarize the ThO H state to $P \approx 0.999$ [63]. The ThO EDM experiment can therefore operate with lower applied fields than the Tl and YbF and PbO experiments, minimizing systematic effects related to high $\mathcal{E}$ fields. The ThO experiment can also operate with several different electric fields with essentially no change to $\mathcal{E}_{\text{eff}}$, which allows the the EDM signal to be easily distinguished from spurious laboratory electric field effects. The ACME experiment used electric fields of $|\mathcal{E}| = 36$ and 142 V/cm. To date it is the only EDM experiment to operate with multiple electric fields that differ by more than a factor of two.

2.1.2 Spectroscopic Reversal of $\mathcal{E}_{\text{eff}}$

When ThO is completely polarized, the mixed parity states correspond to the internuclear axis, and effective electric field, either aligned or anti-aligned with the applied electric field. This alignment is denote by the quantum number $\mathcal{N} = \hat{n} \cdot \vec{\mathcal{E}} = \Omega M_J \text{sign}(\tilde{\mathcal{E}} \cdot \text{hatz})$, where M_J is the projection of total angular momentum on the fixed lab frame quantization axis $\hat{z}$, and $\vec{\mathcal{E}}$ is either parallel or anti-parallel to $\hat{z}$. Figure 3.1 show how the six possible Ω-doublet and spin triplet states of $|H, J = 1\rangle$ behave in applied electric fields. In the lower energy ($\mathcal{N} = 1$) states $\mathcal{E}_{\text{eff}}$ points against the laboratory electric field, whereas $\mathcal{E}_{\text{eff}}$ points along the lab field in the higher energy ($\mathcal{N} = -1$) states. Notice that the $M_J = 0$ opposite parity states are not coupled by the electric field [1], so they not mix or experience a second order Stark shift [31]. For the laboratory fields applied in this experiment, upper and lower $\mathcal{N}$ levels are split by > 80 MHz, more than sufficient to spectrally resolve the levels in this experiment with ~1 MHz linewidth lasers. Therefore, $\mathcal{E}_{\text{eff}}$ can be reversed independent of laboratory electric field by switching the N level in which the EDM measurement is performed. This switch corresponds to tuning a laser frequency to either be on resonance with the upper or lower N levels. This spectroscopic reversal of $\mathcal{E}_{\text{eff}}$ can be performed quickly with acousto-optic modulators (AOMs) and results in a 1000-fold suppression of all three systematic effects that limited the Tl experiment. No previous EDM experiment, other than the PbO experiment, has had access to an addition reversal of $\mathcal{E}_{\text{eff}}$ apart from the laboratory electric field.

2.2 High Effective Electric Field

The effective electric field of ThO is computed to be one of the largest in any molecule. The fact that ThO has one valence electron in an s orbital ensures good overlap between the wavefunction of that electron and the heavy Th nucleus. The second d orbital electron experiences a much lower $\mathcal{E}_{\text{eff}}$ and contributes minimally to the EDM energy shift. In general the maximum possible effective field achieved in an atom or molecule scales with atomic number Z^3: the electric field originating

---

[1] The Clebsch-Gordon coefficient $\langle 1, 0, 1, 0 \mid 1, 0\rangle$ is zero.

from a charged nucleus scales with Z, and the overlap of the electron and nucleon wavefunctions scales with Z^2 [47]. With Z = 90 thorium has the highest atomic number of any atom used in an EDM experiment. In the past decade four different theory groups have calculated this field with separate computational techniques [11, 10, 12, 64]. The resulting $\mathcal{E}_{\mathrm{eff,ThO}}$ values range from 75 to 104 GV/cm with uncertainty estimates varying between 3-40%. In this manuscript we use the published value from Anatoly Titov's group in St. Petersburg, $\mathcal{E}_{\mathrm{eff,ThO}} = 84 \pm 13$ GV/cm [10]. This effective field is six and 1000 times larger than that achieved in the YbF and Tl experiments, respectively [2].

2.3 Near-Zero Magnetic Dipole Moment

Nearly all previously observed systematic effects involved correlated or induced magnetic field imperfections that coupled to the atomic or molecular dipole moment via the Zeeman interaction to produced an EDM-like signal. These mechanisms are all suppressed in the ThO H state due to its near-zero magnetic dipole moment, $\mu_H = -0.0088(1)\mu_{\mathrm{B}}$ [66, 63, 12]. Two separate measurements of μ_H are described in detail in the following chapter. The small value of μ_H also minimizes the effects of stray magnetic fields and magnetic field noise, which could wash out the EDM signal if μ_H was large.

The ThO H state magnetic dipole moment is near-zero due to cancellation of spin and orbital magnetic moment contributions from the two valence electrons. Because

---

[2] After we published our result [4], Timo Fleig and his collaborators computed $\mathcal{E}_{\mathrm{eff}} = 76$ GV/cm with an estimated 3% uncertainty. Although two values agree within their estimated uncertainties, the debate over which value is more accurate is ongoing [65].

H is almost entirely comprised of a ${}^3\Delta_1$ state with $\Lambda = 2$ and $\Omega = |\Lambda + \Sigma| = 1$, the electron spin must point against the orbital angular momentum, $\Sigma = -1$, as depicted in Figure 2.1. Plugging in the angular momentum g-factor, $g_L = 1$ and electron spin g-factor, $g_S \approx 2.0023$ [67], we see that the effective H state g-factor is very close to zero, $g_H = g_S\Sigma + g_L\Lambda \approx 0$. The cancelation is not perfect because of the anomalous electron g-factor, the fact the the H state is not perfectly described as a ${}^3\Delta_1$ state, and perturbations from nearby electronic states with large magnetic moments. Because of this unique cancellation in the H state, the ThO EDM experiment is $\sim$100 times less sensitive to all systematics that couple through the magnetic dipole moment, including the effects that ultimately limited the Tl and PbO experiments.

2.4 Convenient Optical Pumping Transitions

All potential advantages of the H state are useless to an EDM measurement unless the state can be efficiently populated and manipulated. In the cold molecular beam source used in this experiment, nearly all ThO molecules initially occupy the lower rotational levels (J=0-4) of the ground state, X. As shown in Figure 2.2, several excited electronic states exist which couple to both X and H states. These states allow for population transfer to H and the creation of a spin superposition by simple optical pumping techniques. The lifetime of the H state must also be long enough to not limit spin coherence time and EDM sensitivity. The only lower energy electronic state for H to decay into is X, a ${}^1\Sigma_1$ state. None of the three leading admixtures of H can directly decay to X via an E1 transition so the leading decay paths involve higher order transitions with longer decay times [58, 59]. The measured lifetime of the H state is $\tau_H = 1.81 \pm 0.03$ ms [60, 68], which allows for H state spin precession times comparable to other atom and molecule beam measurements [54, 5].

Laser-induced E1 transitions are not allowed between states with different electron spin. Admixtures of singlet and triplet spin states are therefore required to transfer populations between the singlet X state and the triplet H state. Thankfully, several excited ThO electronic states have this desired singlet-triplet composition (see Figure 2.2). An additional bonus is that all of transitions relevant to the EDM measurement are accessible with diode lasers. Fiber and/or tapered amplifiers are also available at each transition frequency to provide the power necessary to saturate weaker transitions. The A state, 95.5% $^3\Pi_0$ and 4.7% $^1\Sigma_0$, provides a means to transfer population from X to H. This state couples with moderate strength to X and the $X \rightarrow A$ transition can be sufficiently saturated with ~100 mW/cm^2 of 943 nm laser power. Molecules driven from $|X, J = 1\rangle$ to $|A, J = 0\rangle$ will spontaneously decay both to $|H, J = 1\rangle$ and back to $|X, J = 1\rangle$ (a small fraction will also decay to excited vibrational states of X). Roughly 30% of the molecules excited to A will decay to H, with ~5% reaching a particular $|H, \mathcal{N} = \pm 1, M = \pm 1\rangle$ state. Two states also exist with strong coupling to X and weak coupling to H: C $(76.6\%^1\Pi_0, 19.5\%^3\Pi_1.1.5\%^3\Delta_1, ...)$, and E $(55.3\%^1\Sigma_0, 35.1\%^3\Sigma_0, 9.9\%^3\Phi_0, ...)$ [58, 59]. These provide efficient optical pumping paths to transfer population out of H for spin state preparation and readout. The $H \rightarrow C$ and $H \rightarrow E$ transitions were observed and carefully characterized, as described in the following chapter. Both transitions required powers > 1 W/cm^2 to achieve saturation in the molecule beam. Ultimately, the 1090 nm $H \rightarrow C$ transition was used for the EDM measurement because high power (10W) fiber amplifiers

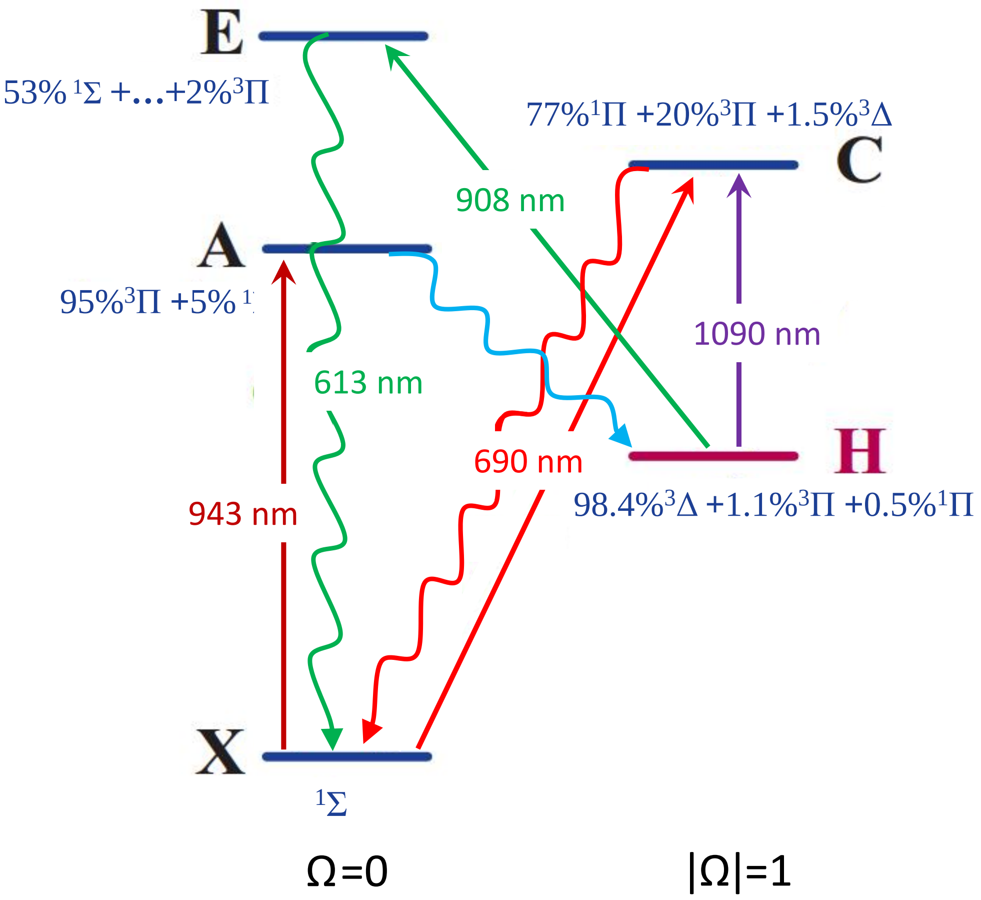

Figure 2.2: ThO electronic states relevant to the EDM measurement. The ${}^3\Delta_1$ H states does not strongly couple to the ${}^1\Sigma_0$ ground state. Excited electronic states that are admixtures of multiple angular momentum states must therefore be used to transfer population into and out of the H state [58, 59].

were available at that wavelength [69]. The (2 W) tapered amplifiers available for the 908 nm $H \rightarrow E$ transition were not sufficient for complete saturation. An additional advantage of the C state is its spectrally resolvable Ω-doublet structure, which helps suppresses a certain class of systematic effects unique to this experiment, as detailed in Chapter 7.

The C state can also be used to enhance the population of a single rotational level of the ground state, a process called "rotational cooling". ThO molecules in the cold beam originally occupy the four lowest rotational levels of X. Only population in $|X, J=1\rangle$, however, can be efficiently transferred to a single rotational level of H. Because C couples strongly to X, most of the population driven to C with a 690 nm laser will decay back down to X, populating all available rotation levels. A 690 nm laser on resonance with a given rotational level of X can therefore optically pump population from that specifical level to other rotation levels. This allows us to enhance the $|X, J=1\rangle$ population by nearly 70% before that population is transferred to the H state. This process is illustrated in 5.3 and described in more detail in Chapter 7.2.3.

The unique features of ThO are almost perfectly suited for an EDM experiment. ThO contains a metastable ${}^3\Delta_1$ H state (lifetime of ∼1.8 ms [60, 68]) in which one of its valence electrons travels near the heavy thorium nucleus and experiences a huge effective electric field of nearly 100 GV/cm [10]. This state also exhibits Ω-doublet structure, which provides very high polarizability and a way to spectroscopically reverse the effective field that the electron experiences without reversing the laboratory electric field. Finally, because of the near perfect cancelation of spin and orbital contributions to the magnetic dipole moment, the ThO H state has a tiny magnetic dipole moment less than on hundredth of a Bohr magneton. These features of the H state both enhance EDM sensitivity and suppress the systematic effects that limited previous EDM measurements [36]. In Chapter 7 we will show that all previously observed systematic effects were in fact suppressed below 10^{-31} e cm, two orders of magnitude below our statistical uncertainty. Other excited electronic states in ThO provide a convenient way to efficiently transfer population into and out of the metastable H state. In the following chapter we will show how these transitions can be used to perform an EDM measurement with ThO.

Chapter 3

A Procedure for Measuring the EDM in ThO

In the previous chapter we described the unique features of ThO that provided both high statistical precision and systematic suppression for the ACME EDM experiment. In addition to the inherent advantages of ThO, it is important to also have a straightforward EDM measurement protocol that provides shot-noise limited sensitivity. In this chapter we will describe in detail how an EDM measurement can be performed in the ThO H state. First we will summarize the effective Hamiltonian of the H state and describe how various terms in that Hamiltonian can be isolated by reversing experimental parameters. We will then describe how the EDM energy splitting can be precisely measured by creating a coherent spin state in H and then reading out that state in a way that normalizes against molecule number fluctuations. Finally we will summarize the complete EDM measurement protocol and estimate the shot-noise limited EDM precision that can be achieved with this experimental procedure.

3.1 Effect of Electric and Magnetic Fields on the ThO H State

The electron EDM can be measured in the H state of ThO by precisely measuring the energy shifts that result from applied electric and magnetic fields. The effects of these laboratory fields on the $|H, J=1\rangle$ manifold, illustrated in Figure 3.1, can be classified by four energy shifts: Stark splitting between opposite $\mathcal{N}$ levels; Zeeman splitting between M_J levels; a small difference in Zeeman splitting between N levels; and the EDM energy shift. The corresponding Hamiltonian of the fully polarized H state is

$$\mathrm{H}_H = -\mathcal{N} d_H |\mathcal{E}| - M_J \mu_H \mathcal{B} - M_J \mathcal{N} \eta \mu_\mathrm{B} |\mathcal{E}| \mathcal{B} - \vec{d_e} \cdot \vec{\mathcal{E}}_\mathrm{eff}, \tag{3.1}$$

where $\mathcal{B} = \vec{B} \cdot \hat{z}$ is the applied magnetic field along the quantization axis, $d_H = h \times 1.03$ MHz/(V/cm) is the induced dipole moment of the H state, and $\eta = 0.79(1)$ nm/V accounts for the $\mathcal{E}$-dependent magnetic moment difference between the $\mathcal{N}$ levels. Direct measurements of the Stark and Zeeman effects in a miniature test apparatus will be described in the following chapter. The Stark and Zeeman shifts are ~100 MHz and ~100 Hz, respectively, with the fields ($\mathcal{E} \approx 100$ V/cm and $\mathcal{B} \approx 20$ mG) typically applied in the ACME experiment. Small perturbations from nearby rotational and electronic states cause the magnetic moment of the two $\mathcal{N}$ levels to be slightly different, as we describe in detail in our upcoming publication [70]. This magnetic moment difference scales with $\mathcal{N}$ level Stark splitting, and therefore $|\mathcal{E}|$, but typically produuces an energy shift of ~ 0.1 Hz in this experiment. The EDM data itself allows for a very precise measurement of η, as described in Chapter 6 and illustrated in Figure 6.8. Non-zero η implies that the suppression of systematic effects related to magnetic fields is not perfect in this experiment. Rather, the systematic suppression factor is $\Delta g/g$, where $g = \mu_H/\mu_{\rm B}$ is the $|H, J = 2\rangle$ g-value, and $\Delta g = \eta|\mathcal{E}|$ is the difference in g-values of the upper and lower $\mathcal{N}$ levels. We experimentally verified this suppression factor by intentionally correlating large magnetic fields with E, as described in Chapter 7 and illustrate in Figure 7.12.

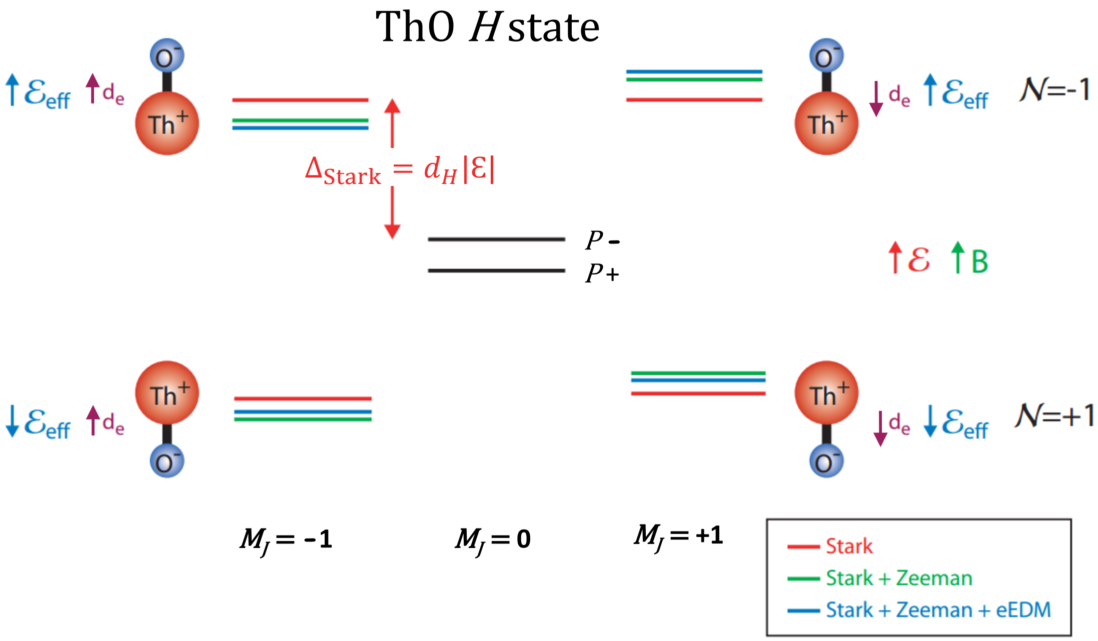

Figure 3.1: The ThO H state in applied electric and magnetic fields. The $\mathcal{N}$ levels experience opposite Stark shifts, and the two M_J levels experience opposite Zeeman shifts. The direction of $\vec{d_e}$ is always along the spin axis with alignment determined by M_J.

The last term in Equation 3.1 corresponds to energy shift produced by an electron EDM. As discussed in the previous chapter, the electron EDM produces energy shift of $\vec{d_e} \cdot \vec{\mathcal{E}}_{\text{eff}}$. $\vec{d_e}$ is always along the electron spin axis determined by the sign of M_J. The direction of $\vec{\mathcal{E}}_{\text{eff}}$, on the other hand, is along the internuclear axis and determined by laboratory electric field and the quantum number $\mathcal{N}$. Therefore, the EDM energy splitting is

$$\Delta E_{\text{EDM}} = -\vec{d_e} \cdot \vec{\mathcal{E}}_{\text{eff}} = -(d_e\vec{S}) \cdot (-\mathcal{E}_{\text{eff}}\hat{n}) = d_e\mathcal{E}_{\text{eff}}\Sigma = -d_e\mathcal{E}_{\text{eff}}\Omega = -M_J\mathcal{N}\text{sign}(\mathcal{E})d_e\mathcal{E}_{\text{eff}}. \tag{3.2}$$

Here we have made us of the fact that $\Sigma = -\Omega$ in the ${}^3\Delta_1$ state, which is apparent from Figure 2.1.

Each term in Equation 3.1 can be isolated by from background energy shifts by reversing the appropriate experimental parameter(s). For example, the magnetic moment can be deduced by measuring the energy shift between M_J sublevels that results from the reversal of magnetic field. Likewise, the EDM can be isolated by measuring the M_J energy shift correlated with reversal of the combined quantity $\mathcal{N}\mathcal{E}$ that determines the orientation of the internuclear axis. If all three $\mathcal{N}$, $\mathcal{E}$, and $\mathcal{B}$ parameters are reversed then eight possible even and odd combinations of energy shifts can be computed, as described in Chapter 6. Each combination corresponds to a unique physical property of ThO and/or the experimental apparatus. Throughout this thesis binary parameter reversals or switches will be denoted with a ˜ accent (e.g. $\tilde{\mathcal{E}} = \pm 1$ denotes the direction of the electric field with respect to the lab quantization axis z). With this notation Equation 3.1 can be written as the overall H state energy splitting

$$\Delta E_H = -\tilde{\mathcal{N}} d_H |\mathcal{E}| - M_J \mu_H \tilde{\mathcal{B}} |\mathcal{B}| - M_J \tilde{\mathcal{N}} \eta \mu_\mathrm{B} |\mathcal{E}| \tilde{\mathcal{B}} |\mathcal{B}| - M_J \tilde{\mathcal{N}} \tilde{\mathcal{E}} d_e \mathcal{E}_\mathrm{eff}. \tag{3.3}$$

Because d_e is the most important quantity to measure, its corresponding switches $\tilde{\mathcal{N}}$ and $\tilde{\mathcal{E}}$ are reversed on the fastest timescale. This minimizes the effects of drifting energy shifts on the EDM measurement. The apparatus is designed to reverse $\tilde{\mathcal{N}}$ and $\tilde{\mathcal{E}}$ on timescales faster than one second (see Chapter 7.2.3).

3.2 A Generic Spin Precession Measurement

The most precise way to determine the EDM energy shift is with a coherent spin precession measurement. In this so-called “Ramsey measurement” (named after its inventor) energy shifts are manifested as spin precession phases [50]. First, a coherent superposition of $M_J = \pm 1$ states is created. The relative phase between the two states then precesses with angular frequency $2\omega = 2\Delta E_M/\hbar$, producing a total precession phase of $2\phi = 2\omega\tau$. Here ΔE_M corresponds to the component of ΔE_H that dependeds on M_J (i.e. the Zeeman and EDM energy shifts). Specifically, let the initial state be prepared along the horizontal lab axis, $\hat{x}$,

$$|\psi_0\rangle = \frac{|M_J = 1\rangle + |M_J = -1\rangle}{\sqrt{2}}. \tag{3.4}$$

Once this state is allowed to precess for time τ in applied electric and magnetic fields, the two M_J components acquire opposite phases,

$$|\psi_f\rangle = \frac{e^{i\phi}\,|M_J = 1\rangle + e^{-i\phi}\,|M_J = -1\rangle}{\sqrt{2}}. \tag{3.5}$$

This phase can be measured by projecting the final state onto a known state. For example, if $|\psi_f\rangle$ is projected back onto the initial state, the resulting population in $|psi_0\rangle$ will be

$$\langle\psi_0 \mid \psi_f\rangle^2 = \cos^2(\phi). \tag{3.6}$$

The final state could just as easily be projected onto another basis state $|\psi'\rangle$ with projected propability

$$\langle\psi_0 \mid \psi'\rangle^2 = \cos^2(\phi - \theta), \tag{3.7}$$

where θ is relative angle in lab x-y plane between the initial state and readout projection state.

This generic spin precession measurement is used in nearly every EDM experiment [36, 5, 3]. In the case of ThO, each precession phase measurement includes all contributions from Equation 3.3 that depend on M_J. The EDM component of the precession phase is isolated by repeating spin precession measurements with all possible combinations of $\tilde{N}$, $\tilde{\mathcal{E}}$, and $\tilde{\mathcal{B}}$. The average of all phases measurements with $\tilde{N}\tilde{E} = -1$ are subtracted from the average $\tilde{N}\tilde{E} = +1$ phase. The phase difference $\phi^{\mathcal{N}\mathcal{E}}$ is directly proportional to the EDM,

$$\phi^{\mathcal{N}\mathcal{E}} = \frac{d_e \mathcal{E}_{\text{eff}} \tau}{\hbar}. \tag{3.8}$$

All other quantities in the H state Hamiltonian can be similarly extracted from combinations of phase measurements (see the data analysis chapter for more detail).

3.3 Preparing a Spin Superposition in the H state

In the ACME experiment, a coherent spin superposition must be created in an initially decoherent H state. The H state is initially populated by spontaneous decay from the A state, which equally populates all $|\mathcal{N} = \pm 1, M_J = \pm 1\rangle$ states, as shown in Figure 3.2 A. A coherent spin superposition can be created by optically pumping out half the population in a given N level with a linearly polarized laser (see Figure 3.2 B). When a 1090 nm laser with linear polarization θ_{prep} in the lab x-y frame couples $|H, M_J = \pm 1\rangle$ and $|C, M_J = 0\rangle$ together, the resulting eigenstates are:

$$|D\rangle = \frac{e^{-i\theta_{\text{prep}}}|H, M_J = +1\rangle + e^{i\theta_{\text{prep}}}|H, M_J = -1\rangle}{\sqrt{2}} \tag{3.9}$$

$$|B_{\pm}\rangle = \frac{-e^{-i\theta_{\text{prep}}}|H, M_J = +1\rangle + e^{i\theta_{\text{prep}}}|H, M_J = -1\rangle}{\sqrt{2}} \pm |C, M_J = 0\rangle \tag{3.10}$$

Here, D and B refer to the "dark" and "bright" dressed states. The C state has a lifetime of $\tau_C \approx 500$ ns [71]. If molecules interacts with 1090 nm laser for time $\tau_{\text{int}} >> \tau_C$ then all bright state population will decay back back to the ThO ground state [1]. Only dark state population, which did not couple to C, will be left in the H state. This dark state is a coherent superposition of spin states with an initial phase in the lab frame that depends on the 1090 nm preparation laser polarization.

3.4 Normalized Readout of Precession Phase

After the dark state has precessed in applied electric and magnetic fields, a second 1090 nm laser is used to project the molecule spin state onto the basis defined by

---

[1] A small fraction of bright state population will be shelved in other long-lived excited states, such as the Q state and excited vibrational states of X.

laser polarization θ_{read}. The state readout process is similar the state preparation process, except that the resulting 690 nm $C \rightarrow X$ fluorescence is monitored with photomultiplier tube (PMT) detectors to deduce spin precession phase (see Figure 3.2 C). The measurement is actually performed on an entire ensemble of thousands of molecules in the pulsed ThO beam. The total fluorescence induced by a linearly polarized readout laser is

$$F(\theta) = \frac{1+|\mathcal{C}|}{2} f N_0 \cos^2(\phi - \theta). \tag{3.11}$$

Here, $\theta = \theta_{\text{read}} - \theta_{\text{prep}} + \pi/2$ is the difference between the readout laser polarization and the initial molecular state, which was orthogonal to the preparation laser polarization. N_0 is the number of molecules in a given $\mathcal{N}$ level and f is the fraction of total fluorescence photons that are detected. Contrast $|\mathcal{C}|$ is a unitless prefactor between 0 and 1 that describes the fraction of total molecules that were prepared in coherent state, and how well that coherent state is aligned with the lab axes. For reasons that will become clear in Chapter 6, C is treated as a signed quantity in this thesis.

Molecule number fluctuations of 50%, which are unavoidable with the ThO buffer gas source, can add significant noise to the precession phase measurement. According to Equation 3.11 molecule number fluctuations cannot be distinguished from phase fluctuations if the readout laser remains at a single fixed polarization. This problem is averted by rapidly switching the readout laser laser between two orthogonally polarizations, $\hat{X} = \theta_{\text{prep}} + \theta$ and $\hat{Y} = \theta_{\text{prep}} + \theta + \pi/2$. The two beam produce fluorescence signals of

$$\begin{aligned} F_X &= \frac{1+|\mathcal{C}|}{2} f N_0 \sin^2(\phi+\theta), && (3.12)\\ F_Y &= \frac{1+|\mathcal{C}|}{2} f N_0 \cos^2(\phi+\theta). && (3.13)\end{aligned}$$

Signal asymmetry $\mathcal{A}$, which is immune to molecule number fluctuations, can then be formed from F_X and F_Y,

$$\mathcal{A} = \frac{F_X - F_Y}{F_X + F_Y} = |\mathcal{C}| \cos(2\phi - 2\theta). \tag{3.14}$$

The magnetic field and readout polarization are chosen so that $\phi - \theta \approx \pi/4$. This corresponds to the linear part of the $\cos^2$ asymmetry fringe where $\mathcal{A}$ is most sensitive to small changes in ϕ. In this case small changes in phase, such as those that would be produced by and EDM, are linearly proportional to small changes in asymmetry,

$$\Delta\phi \approx \frac{\Delta\mathcal{A}}{2\mathcal{C}}. \tag{3.15}$$

Here the absolute value has been removed from $\mathcal{C}$ to account for the fact that the slope of the asymmetry fringe near zero can be positive or negative.

The $|C, J=1\rangle$ state, used to measure H state energy shifts, is an $|\Omega| = 1$ state and therefore exhibits Ω-doubling. It has a much larger Ω doublet splitting (50.4 MHz) in zero electric field. It is important to remember that the readout laser can drive the H state to either of the $|C, M_J = 0\rangle$ Ω-doublet states, denote by $|\mathcal{P}\pm\rangle$. Because these two states have oppositive parity, they couple to different components of the H state spin superposition. This results in different projection probabilities and opposite signal asymmetries between $|+\mathcal{P}\rangle$ and $|-\mathcal{P}\rangle$. To prove this, recall that $|H, \mathcal{N} = \pm1, M_J = \pm1\rangle$ states are mixed parity states,

$$|H, N=+1, M_J=+1\rangle \;=\; (|+\rangle + |-\rangle)/\sqrt{2} \tag{3.16}$$

$$|H, N=+1, M_J=-1\rangle \;=\; -(|+\rangle - |-\rangle)/\sqrt{2} \tag{3.17}$$

$$|H, N=-1, M_J=+1\rangle \;=\; (|+\rangle - |-\rangle)/\sqrt{2} \tag{3.18}$$

$$|H, N=-1, M_J=-1\rangle \;=\; (|+\rangle + |-\rangle)/\sqrt{2}. \tag{3.19}$$

Now suppose that a coherent superposition $|\psi_0\rangle = (|M_J = +1\rangle + |M_J = -1\rangle)/\sqrt{2}$ is created in a given $\mathcal{N}$ level by the preparation laser. After the state precesses to $|\psi_f(\phi)\rangle = e^{i\phi}\,|M_J = +1\rangle + e^{-i\phi}\,|M_J = -1\rangle)/\sqrt{2}$, it is coupled by the readout laser to one of the two to $|C, \mathcal{P}\pm\rangle$ levels. Two selection rules are relevant in determining the component of $|\psi_f(\phi)\rangle$ that can couple to $|C, \mathcal{P}\pm\rangle$. First, the laser polarization, which can be written as $\hat{\epsilon} = (-e^{-i\theta}\hat{\epsilon}_{+1} + e^{i\theta}\hat{\epsilon}_{-1})/\sqrt{2}$, can only drive transitions with $\Delta M_J = \pm 1$. Second, E1 transitions can only occur between opposite parity states. Making use of Equations 2.17-2.20, the fluorescence resulting from the population driven to C is

$$\begin{aligned} F(\mathcal{P}\pm) &\propto (\langle\psi_f|\, e\vec{r}\cdot\hat{\epsilon}\,|C, \mathcal{P}\pm\rangle)^2 && (3.20)\\ &= \left(\langle\psi_f(\phi)|\, e\vec{r}\cdot(-e^{-i\theta}\hat{\epsilon}_{+1} + e^{i\theta}\hat{\epsilon}_{-1})\,|C, \mathcal{P}\pm\rangle\right) && (3.21)\\ &= \left(e^{i(\phi-\theta)}/2 \mp e^{-i(\phi-\theta)}/2\right)^2 && (3.22)\\ &= \sin^2(\phi-\theta) \text{ for } \mathcal{P}+ && (3.23)\\ &= \cos^2(\phi-\theta) \text{ for } \mathcal{P}-\,. && (3.24) \end{aligned}$$

Notice that the effect of switching between $|C, \mathcal{P}\pm\rangle$ readout states is identical to switching between orthogonal $\hat{X}$ and $\hat{Y}$ laser polarizations. Either switch can therefore be used to normalize against molecule number fluctuations [49], as we demonstrated in our previous publication [66]. The polarization switch is generally preferred for normalization because detected fluorescence efficiency f differs by ~30% between the two $|C, \mathcal{P}\pm\rangle$ readout states (see Chapter 7.2.3 for details). Because the readout state switch reverses the sign of $\mathcal{A}$ independent of laser polarization, it was implemented on a longer (~50 second) timescale to suppress systematic effects related to mismatched $\hat{X}$ and $\hat{Y}$ beam properties (see Chapter 7 for details).

3.5 Measurement Protocol and Projected Electron EDM Sensitivity

All the pieces are now in place to now describe the complete ACME EDM measurement protocol, shown in Figure 3.2. Every 20 ms, a 2-3 ms pulse of cold ThO molecules with ~200 m/s forward velocity is produced by an ablation and buffer gas source. The molecules are rotationally cooled with microwaves and 690 nm lasers to enhance the population of the $|X, J = 1\rangle$ level by ~65%. After being spatially collimated to 1 cm transverse width, the molecule packet enters a region where precise electric and magnetic fields are applied. A vertically stretched 943 laser (100 mW, 1 mm × 15 mm) then optically pumps ~20% of the total $|X, J = 1\rangle$ population to $|H, J = 1\rangle$. Spontaneous decay from A populates five of the six available states in the H manifold. A coherent spin superposition is created in one of the $\mathcal{N}$ levels by driving the $|H, \mathcal{N} = \pm 1\rangle \to |C, M_J = 0, \mathcal{P}+\rangle$ transition with a linearly polarized 1090 nm laser (3 W, 5 mm × 20 mm). This optically pumps away half the $|H, N = \pm 1\rangle$ population and leaves behind a coherent dark state. The dark state then precesses for 1.1 ms over distance of 22 cm in electric and magnetic fields ap-

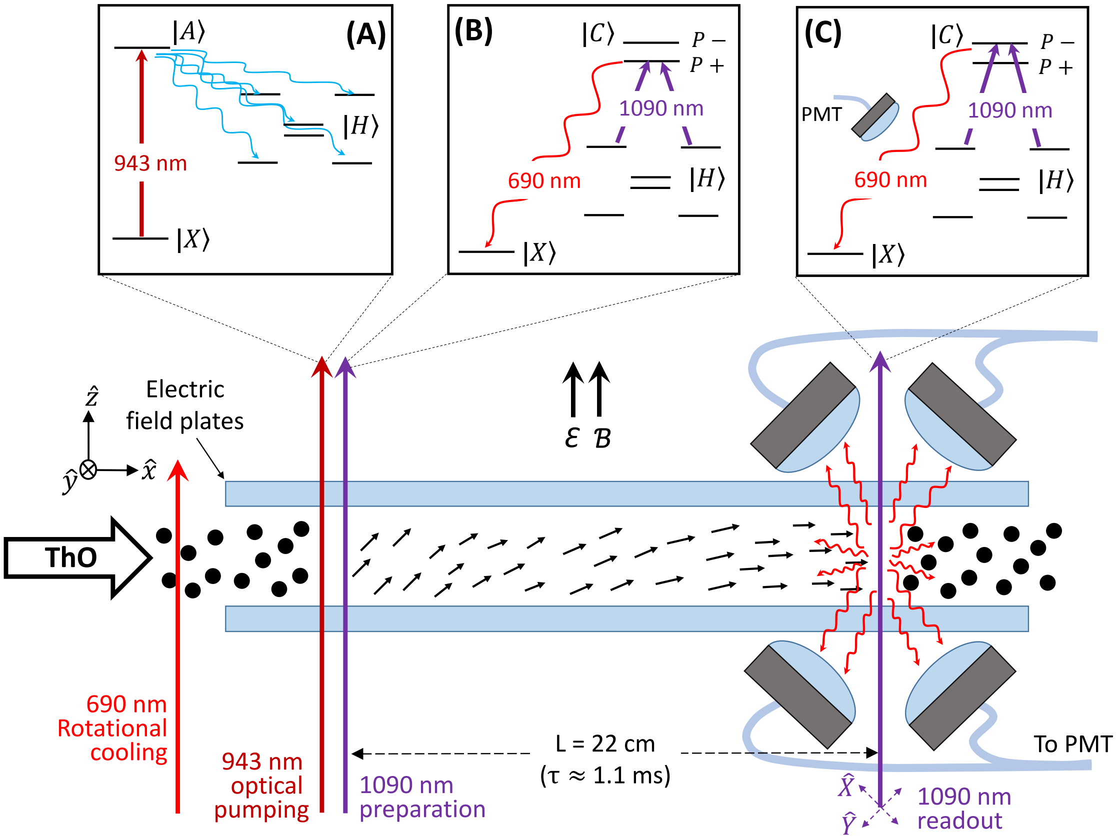

Figure 3.2: The procedure for measuring spin precession the ThO H state. Molecules produced in the buffer gas source are first rotationally cooled into a single rotational level. **(A)** Population is then transferred to the H state by optical pumping through the A state. **(B)** A coherent dark state is formed in either the upper or lower $\mathcal{N}$ level of H by optical pumping through the C state with a linearly polarized 1090 nm laser. **(C)** After the dark state precesses for time τ its phase is read out by again optical pumping through the C state, this time with a laser that rapidly switches between two orthogonal polarizations. A system of lenses, light-pipes, and PMTs detects the resulting 690 nm fluorescence.

plied along $\hat{z}$ and accumulates phase ϕ. The precession phase is read out by exciting $|H, \mathcal{N} = \pm 1\rangle \rightarrow |C, M_J = 0, \mathcal{P}\pm\rangle$ again with a 1090 nm laser (2 W, 5 mm × 30 mm). The linear polarization of this laser rapidly switches between two orthogonal polarizations. Precession phase can be determined by comparing the detected fluorescence corresponding to the two laser polarizations. Roughly 1000 photons are detected for each pulse of ThO molecules. The phase measurement is repeated with different values of $\tilde{N}$, $\tilde{E}$, and $\tilde{B}$, which are reversed every 0.5, 2, and 20 seconds, respectively. Further discussion of the EDM apparatus and measurement procedure will be saved for Chapter 7.2.3.

Plugging the values of $\mathcal{E}_{\text{eff}}$, τ, and time-averaged counting rate $\dot{N} \approx 50,000Hz$ into Equation 3.25, we can predict the statistical uncertainty of the ThO EDM measurement,

$$\delta d_e \approx \frac{\hbar}{2 \times 84\text{GV/cm} \times 1.1\text{ms}\sqrt{4.3 \times 10^9/\text{day}}} \approx 5.5 \times 10^{-29} e \text{ cm}/\sqrt{\text{day}}. \qquad (3.25)$$

This predicted one-day sensitivity is an order of magnitude below any previous electron EDM experiment. In reality, imperfect duty cycle and background noise increase this one-day uncertainty by a factor or ∼2. Even so, a statistical error of 3.7×10^{-29} e cm was ultimately achieved in ThO with only a week of total integration time [4, 72]. The measurement procedure described in this chapter allows individual terms of the H state hamiltonian to be quickly measured with near shot-noise limited uncertainty. Not only are precise EDM measurements performed, but measurements of other energy splitting terms as well. Monitoring these all energy splitting terms allows us thoroughly search for potential systematic effects, as we will describe in detail in

Chapter 7.

Chapter 4

Characterizing ThO

The electron electric dipole measurement described in this thesis relies on unique quantum properties of the ThO molecule to suppress the systematic effects that limited previous EDM experiments. Specifically, the $^3\Delta_1$ H state has very high electric polarizability and a very small magnetic dipole moment, two important properties that minimize the effects of motional magnetic fields, leakage currents, and geometric phases on the EDM measurement. While these advantageous properties were predicted by molecular orbital theory before work on the ACME experiment began [12], they had never been directly measured. To confirm these predictions we measured the magnetic and induced electric dipole moment of the ThO H state in a miniature test apparatus [63] while the main EDM apparatus was being developed. Knowing the precise value of these two moments allowed us to design electric field plates and magnetic field coils for the main apparatus to provide the necessary level of Stark and Zeeman splitting for the EDM measurement.

Using the same miniature ThO apparatus we demonstrated that excited electron states in ThO could be used to efficiently populate and manipulate the metastable H state (lifetime of $sim1.8$ ms), where the EDM measurement is performed. Relevant transition strengths and branching ratios were measured to determine the laser power required for complete transition saturation in the EDM experiment. These states were then used to prepare and read out a coherent spin superposition in the H state. This work played a crucial role in the development of the main EDM apparatus and measurement procedure.

4.1 Miniature ThO Apparatus

The measurements presented in this chapter were carried out in an apparatus that was similar to, but much smaller than, the apparatus eventually developed for the reported EDM measurement [73]. A photograph of the apparatus is shown in Figure 4.1. Helium buffer gas at 4K is used to cool a pulse of ThO molecules produced in a 4K cell by pulsed YAG laser ablation of a ceramic ThO_2 target. A bath of liquid helium cools the cell, and 4K surfaces of coconut charcoal cryopump the buffer gas. Molecules exit the cold cell through a 3 mm diameter aperture and enter a $\sim 10^{-6}$ Torr room temperature vacuum region enclose by a KF-50 aluminum tube. After traveling a distance of 30 cm the molecules are collimated to 3 mm (horizontal) × 7 mm (vertical) by razor blades. Immediately after the collimator, molecules enter a four-port KF-50 cross with anti-reflective (AR) coated windows (650-1100 nm) that provide optical access to the molecules.

Cold molecules leaving the buffer gas cell primarily occupy the lowest four rotational levels of the lowest electronic and vibrational ThO state, $|X, \nu = 0, J = 0 - 3\rangle$.

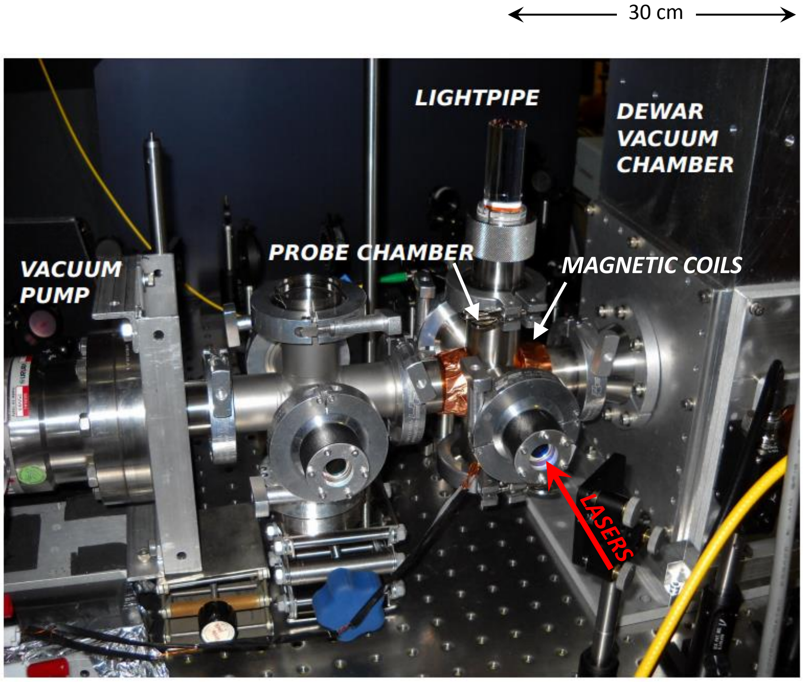

Figure 4.1: A picture of the miniature ThO apparatus. Molecules formed in a 4 K buffer gas source travel along a room temperature KF-50 tube into a region where they interact with lasers and electric or magnetic fields. Laser induced fluorescence is collected with a light pipe. A turbo pump maintains a vacuum pressure of $\sim 10^{-6}$ Torr.

ThO population is transferred between these lower energy states and the metastable H state, used for the EDM measurement, by driving molecules through various optical pumping transitions shown in Figure 2.2. The 690 nm, 908 nm, 943 nm, and 1090 nm diode lasers used to drive these transitions are frequency stabilized to an iodine clock [74] using a scanning Fabry-Perot cavity [49]. All lasers are placed in identical optical assemblies, shown in Figure 5.13, that contain isolators, beam-shapers, and multiple fiber couplers. The amount of 690 nm, 908 nm, 943 nm, and 1090 nm laser power power delivered to the ThO molecules was 5 mW, 100 mW, 100 mW, and 250 mW, respectively. The 690 nm laser is fiber-coupled to the vacuum region but other lasers were free-space coupled so that maximum laser power could be delivered to the ThO molecules. A home-built tapered amplifier was used to obtain the required 1090 nm power [1]. All laser beams were vertically stretched with beam profiles of 2 mm × 10 mm. The 613 nm or 690 nm fluorescence induced by these lasers was channeled through a quartz lightpipe and bandpass interference filter and detected with a photomultiplier tube (PMT).

The configuration of the ThO-laser interaction region depended on the type of measurement being performed. For all measurements the PMT and light-pipe were located on the upper KF-50 port and lasers propagated through the two horizontal KF-50 side ports. For the induced electric dipole measurement, 3 cm × 3 cm × 1 mm glass plates coated with indium tin oxide (ITO) were mounted inside the vacuum region on the bottom of the KF-50 cross to provide a polarizing electric field. For the magnetic dipole measurements these plates were replaced with permanent magnets to

---

[1] The Nufern fiber amplifiers had not yet been purchases and the Keopsys fiber amplifiers were in France for repair during the time of these measurements.

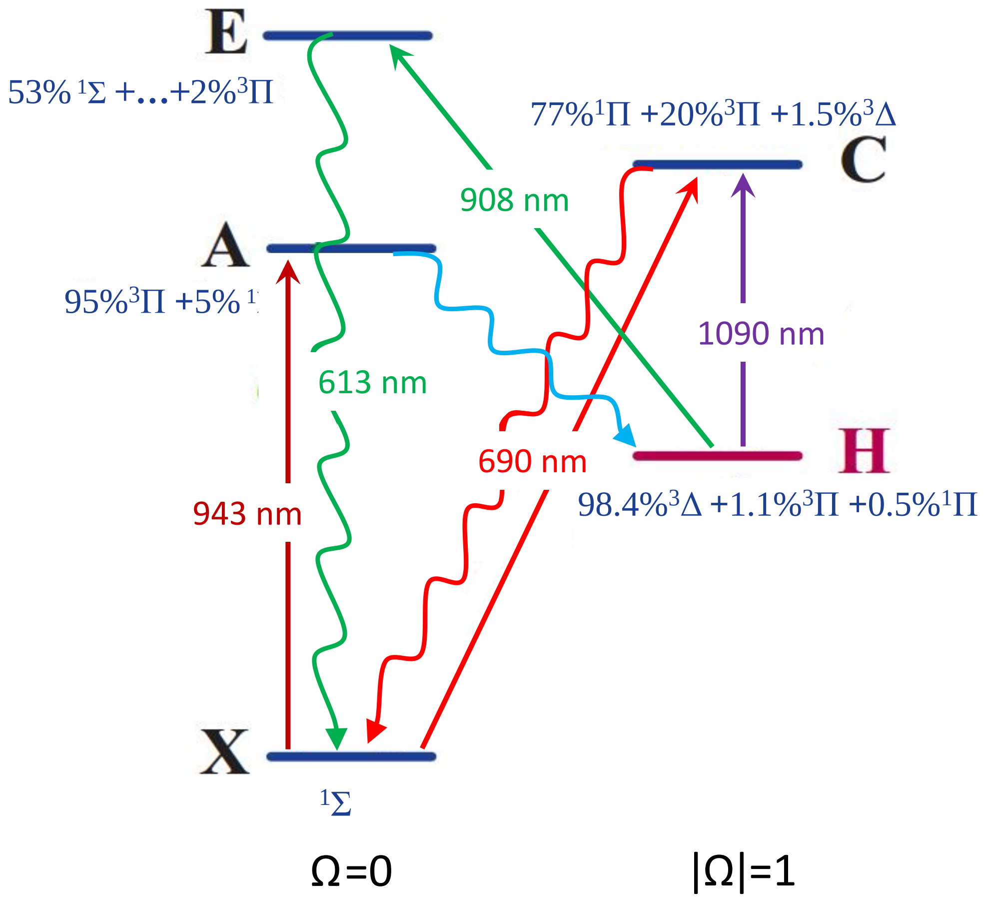

Figure 2.2: ThO electronic states relevant to the EDM measurement. The EDM measurement is performed in the $^3\Delta_1$ H state.

provide large Zeeman splitting. For transition saturation measurements, a confocal mirror was placed on the bottom port to focus additional fluorescence light into the PMT. Hulmholtz coils were later added to this configuration to provide the tunable magnetic field required to demonstrate coherent state precession.

This apparatus, often referred to as “mini-beam II” was constructed by Amar Vutha based on previous designs from the Doyle and DeMille groups [75, 73, 76]. I modified the buffer gas cell and charcoal plate geometry to increase molecule beam yield by an order of magnitude. All preliminary ThO measurements required to developed an EDM measurement procedure were either performed in this apparatus or in an older version, “mini-beam I”, while the main ThO beam sources was being developed.

4.2 Characterizing ThO Transitions

While all the ThO energy levels in Figure 2.2 used in the EDM measurement were previously observed by molecular spectroscopists [77, 78, 79, 80], ThO transition strengths had not been well measured. For example, it was not known what fraction of ThO population excited to the A state would decay to H, where the EDM measurement would be performed, instead of decaying back to X. Similarly, the laser intensity required to excite significant H state population to C or E was not well measured, since these states weakly couple to H. Indeed, the $H \to C$ and $H \to E$ transitions had never been directly observed until we excited them in the mini-beam I apparatus [49]. It was therefore necessary to characterize these transitions to determine how efficiently the H state could be populated and how much laser power would be required in the EDM experiment. With the miniature ThO apparatus, I measured the strengths of three transitions, $X \to A$, $H \to A$, and $H \to E$, that could be used for the EDM measurement, along the the $A \to H$ branching ratio. From these measurements I calculated the laser powers that would be required in the EDM apparatus and the expected population transfer efficiency from the ground state to the H state.

4.2.1 Saturating ThO Transitions

To minimize statistical and systematic uncertainties in the EDM measurement, all transitions used to transfer population to and from the H state should be fully saturated. Saturation is achieved by driving all transitions with sufficiently high laser intensity such that the power-broadened linewidth is much larger than all other broadening mechanisms, such as Doppler and lifetime broadening, which are typically $\sim$4 MHz and $\sim$0.3 MHz, respectively, in these measurements. This maximizes EDM statistical sensitivity by ensuring that the highest number of ThO molecules possible participate in the spin precession measurement. It also makes the EDM measurement immune to fluctuations and correlations in laser power and intensity. Chapter 7 describes in detail many mechanisms that can cause laser detuning and intensity correlations. The most dangerous of these are correlated with the experimental parameters that the EDM signal is correlated with, namely the lab electric field $\mathcal{E}$ and the H state $\mathcal{N}$ level. Apart from these correlations, the lasers used for the EDM measurement are typically observed to drift in frequency by $\sim$0.1 MHz/hour and fluctuate in power by 5%/hour. Saturating all ThO transitions ensures that these fluctuations and correlations do not translated into fluctuations and correlations in coherent state preparation efficiency or total fluorescence.

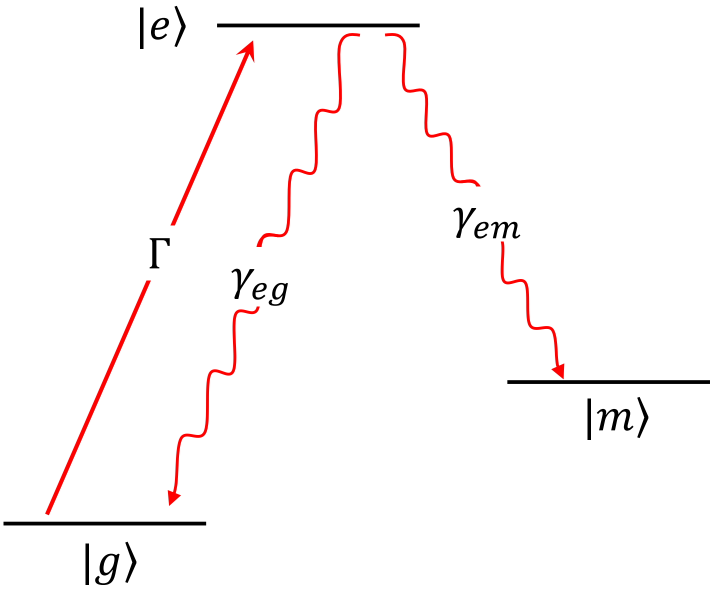

Figure 4.2: The level scheme pertaining to most off-diagonal ThO transitions used for optical pumping, including 943 nm, 908 nm, and 1090 nm transitions. A laser drives population from the initial state $|g\rangle$ to an excited state $|e\rangle$ with excitation rate Γ. Population from the excited state decays weakly back to $|g\rangle$ and strongly to a long-lived state $|m\rangle$ where it is shelved.

The conditions for saturation in this EDM experiment are unique to the ACME apparatus and measurement procedure; the fly-through saturation conditions derived in this section should not be confused with saturation conditions and saturation parameters derived for steady state systems in equilibrium [31]. In particular, the condition for saturation in the ThO beam is that the excitation rate Γ be much larger than the fly-through molecule-laser interaction time T for all molecule velocity classes. To see why this is the case, consider the three-level optical pumping diagram in Figure 4.2, where a laser drives population from a lower level $|g\rangle$ to an excited level

$|e\rangle$ which is then shelved in a third level $|m\rangle$. Nearly all ThO transitions used in the ACME experiment (Figure 2.2) can be described in the context of this diagram, with the long-lived X or H states as either the $|g\rangle$ or $|m\rangle$ [2] and short lived excited states, A, E, and C, as $|e\rangle$. The rate equations for this three level system are:

$$\begin{aligned}
\frac{dN_g}{dt} &= -\Gamma N_g + \gamma_{eg} N_e && (4.1)\\
\frac{dN_e}{dt} &= -(\gamma_{em} + \gamma_{eg} + \Gamma) N_e + \Gamma N_g && (4.2)\\
\frac{dN_m}{dt} &= -\gamma_{em} N_e && (4.3)\\
N_g(0) &= N_0 && (4.4)\\
N_e(0) &= N_m(0) = 0 && (4.5)
\end{aligned}$$

where γ_{em} and γ_{eg} are the excited state decay rates to $|m\rangle$ and $|g\rangle$ respectively, and N_0 is the intial ThO population the $|g\rangle$ state before entering the laser field. When off-diagonal $H \to E$, $H \to C$, or $X \to A$ optical pumping transitions are driven, it is valid to assume that $\gamma_{em} >> \gamma_{eg}$. In that case the solutions to the rate equations are:

$$\begin{aligned}
N_g(t) &= N0 e^{-\Gamma t} && (4.6)\\
N_e(t) &= \frac{\Gamma N_0 (e^{-\Gamma t} - e^{-\Gamma t - \gamma_{em} t})}{\gamma_{em}} && (4.7)\\
N_m(t) &= \frac{\gamma_{em} N_0 (1 - e^{-\Gamma t}) + \Gamma N_0 (e^{-\gamma_{em} t} - 1)}{\gamma_{em} + \Gamma}. && (4.8)
\end{aligned}$$

Once molecules leave the laser field at time T, they quickly decay out of $|e\rangle$. The total detected fluorescence, F, is proportional to the final population in $|m\rangle$ after

---

[2] The H state lifetime is ∼2 ms [60], much longer than the laser-molecule interaction time, so $H \to X$ decay will be neglected in this chapter.

time $T' > T + \gamma_{em}$.

$$N_g(t) = N_0 e^{-\Gamma T} \tag{4.9}$$

$$F(T') = f N_m(T) = f N_0 (1 - e^{-\Gamma T}) \tag{4.10}$$

where f is the fluorescence collection efficiency. Clearly the total fluorescence and $|g\rangle \rightarrow |e\rangle \rightarrow |m\rangle$ population transfer efficiency approach their maximum values for $\Gamma >> T$.

Not only is population transfer efficiency maximized for $\Gamma >> T$, it is also more immune to changes in laser intensity, I, and detuning, Δ. The excitation rate is, of course, a function of both of these quantities.

$$\Gamma = \Gamma_0(I) L(\Delta), \tag{4.11}$$

where $L(\Delta)$ is the transition lineshape and the resonant excitation rate $\Gamma_0(I)$ scales linearly with laser intensity [31],

$$\Gamma_0(I) = \frac{2 I d_{eg}^2}{c \epsilon_0 \gamma \hbar^2}, \tag{4.12}$$

where d_{eg}^2 is the transition dipole matrix element and γ is the natural linewidth of the excited state. The excitation lineshape $L(\Delta)$ is a convolution of a Lorentzian lineshape, $\text{Ł}_L(\Delta) = (\gamma/4)/(\gamma^2/4 - \Delta)$, and a Gaussian lineshape arising from Doppler broadening and laser broadening, $L_G(\Delta) = e^{(-\Delta^2/\sigma^2)}$. Here $\sigma = \sqrt(\sigma^2_{\text{Doppler}} + \sigma^2_{\text{laser}})$ $/2\sqrt(\ln 2)$ is the combination of laser and Doppler widths (γ, σ_{Doppler}, and σ_{Doppler}) are all full widths at half maximum). The convolution of the Lorentzian and Gaussian lineshapes is given by the Voigt profile [81],

$$L(\Delta) = V(\Delta, \gamma, \sigma) = L_L(\Delta) * L_G(\Delta) = \frac{\mathrm{Re}\left[w\left(\frac{\Delta + i\gamma/2}{\sigma}\right)\right]}{\sigma}, \tag{4.13}$$

where,

$$w(z) = e^{-z^2}\left(1 + \frac{2i}{\sqrt{pi}}\int_0^z e^{x^2}\mathrm{d}x\right). \tag{4.14}$$

Equations 4.11–4.14 give us an expression for the $|g\rangle \rightarrow |e\rangle$ excitation rate as a function of laser intensity and detuning [3]. This expression can be combined with Equation 4.10 to see how the $|g\rangle$ and $|m\rangle$ populations and emitted fluorescence depend on I and Δ. Clearly the effects of detuning and intensity fluctuations decrease as the average laser intensity increases, as illustrated by the data in Figure 4.3.

Saturation Criteria

The specific criteria for saturation in the ACME experiment are different for each laser. For the 943 nm ($X \rightarrow A$) laser that populates the H state, and the 1090 nm ($H \rightarrow C$) or 908 nm ($H \rightarrow E$) laser that reads out the coherent spin state in H, the laser intensity needs to be sufficiently high to ensure that fluorescence signals are 95% of their maximum possible value. This value was chosen by the collaboration somewhat arbitrarily but is based in part on previous EDM measurements [5].

The saturation criteria for the 1090 nm or 908 nm laser preparing the coherent spin state in H is more stringent than that of the other lasers. This criteria is based on potential systematic effects caused by known correlations of laser detuning and excitation rate with experimental switches. Specifically, a detuning correlated with

---

[3] Admittedly the Voigt profile is not simple analytic function to work with, and we will need help from Mathematica when fitting to our saturation data.

applied electric field and $\mathcal{N}$ level, $\Delta^{\mathcal{N}\mathcal{E}} \approx 5$ kHz, is known to be caused by a ~5 mV/cm non-reversing electric field in the experimental apparatus. The laser excitation rate is correlated with these same switches, with $|\Gamma_0^{\mathcal{N}\mathcal{E}}/\overline{\Gamma_0}| \approx 1.5\%$, where $\overline{\Gamma_0}$ is the average resonant excitation rate of all configurations of $\mathcal{N}$ and $\mathcal{E}$ (see Chapter 7 for more details on all correlated quantities in the EDM apparatus). These correlations are especially dangerous to the EDM measurement since the EDM signal is also correlated with applied electric field and $\mathcal{N}$ level. To the extent that population optically pumped out of the H state depends on Δ and Γ_0, $\Delta^{\mathcal{N}\mathcal{E}}$ and $\Gamma_0^{\mathcal{N}\mathcal{E}}$ will cause the asymmetry fringe contrast $\mathcal{C}$, described the the previous chapter, to be correlated with electric field and $\mathcal{N}$ level. This can be seen by recalling that the contrast is simply a ratio of the bright and dark state populations in H. The bright state has population $N_0 e^{-\Gamma T}$ after being excited by the preparation laser for time T, while the dark state did not interact with the laser and still has population N_0. The contrast can therefore be written as a function of excitation rate

$$\mathcal{C} = \frac{N_0 - N_0 e^{-\Gamma T}}{N_0 + N_0 e^{-\Gamma T}} \approx 1 - 2e^{-\Gamma T}. \tag{4.15}$$

If a component of the excitation rate, $\Gamma^{\mathcal{N}\mathcal{E}}$, is correlated with the applied electric field and $\mathcal{N}$ level, a component of contrast, $\mathcal{C}^{\mathcal{N}\mathcal{E}}$, will also be correlated with those two switches. If we make the substitution $\Gamma = \overline{\Gamma_0} + \Gamma^{\mathcal{N}\mathcal{E}}$, where $\overline{\Gamma_0}$ is the average resonant excitation rate, and assume $\Gamma^{\mathcal{N}\mathcal{E}} << \overline{\Gamma_0}$, we have,

$$\mathcal{C}^{\mathcal{N}\mathcal{E}} \approx \Gamma^{\mathcal{N}\mathcal{E}} T e^{-\overline{\Gamma_0} T}. \tag{4.16}$$

Because phase ϕ is computed from contrast, $\phi \approx \mathcal{A}/(2\mathcal{C})$, this contrast correlation

$\mathcal{C}^{\mathcal{N}\mathcal{E}}$ can produce a shift in $\phi^{\mathcal{N}\mathcal{E}}$, which would be a systematic EDM offset.

The saturation criteria for the preparation laser is that the uncorrelated resonant excitation rate be sufficiently large such that the potential EDM systematic effect produced by $\mathcal{N}\mathcal{E}$-correlated detuning and excitation rate be less than 10^{-31} e cm. In Chapter 6 we describe a method of "state-averaged" data analysis that has been demonstrated to suppress systematic effects caused by contrast correlations by a factor of ∼100 [4] (see Figure 6.6). The unsuppressed effect must therefore be kept below 10^{-29} e cm by sufficienetly saturating the preparation laser. In units of phase, 10^{-29} e cm corresponds to $\phi^{\mathcal{N}\mathcal{E}} = 1.3$ μrad. From Equation 3.14 it can be shown that for typical asymmetry values of $|\mathcal{A}| < 0.1$, $C^{\mathcal{N}\mathcal{E}} \approx 10^{-5}$ can produce $\phi^{\mathcal{N}\mathcal{E}} \approx 1$ μrad. Plugging in $\Delta^{\mathcal{N}\mathcal{E}} \approx 5kHz$ and $\Gamma_0^{\mathcal{N}\mathcal{E}} \approx 0.015\overline{\Gamma_0}$ into equation 4.11, we see that the effect of $\Gamma_0^{\mathcal{N}\mathcal{E}}$ is actually much larger than the detuning correlation for typical experimental conditions. We can use Equation 6.10 to determine the average resonant excitation rate required to achieve $C^{\mathcal{N}\mathcal{E}} \gtrsim 10^{-5}$:

$$\mathcal{C}^{\mathcal{N}\mathcal{E}} \approx 0.015\overline{\Gamma_0}Te^{-\overline{\Gamma_0}T} \lesssim 10^{-5} \tag{4.17}$$

$$\Rightarrow \overline{\Gamma_0}T \gtrsim 10 \tag{4.18}$$

Therefore the saturation criteria for the preparation laser is that the resonant excitation rate averaged over all configurations of $\mathcal{N}$ and $\mathcal{E}$ be about an order of magnitude higher than the molecule-laser interaction time.

---

[4] In theory the state-averaged data analysis should completely suppress the effects of contrast correlations, but to be cautious we only assume that it suppresses the effects by the demonstrated factor of 100.

Demonstrating Saturation and Extracting Dipole Matrix Elements

The determine how much laser power would be needed to meet the saturation criteria in the EDM measurement, I demonstrated saturation on all relevant ThO transitions in the minature ThO apparatus. The saturation data is shown in Figure 4.3. The plots on the right show laser induced fluorescence for multiple laser detunings and fixed laser intensity. The plots on the left show fluorescence for multiple laser intensities with zero laser detuning. The data is fit to the fluorescence expressions of Equation 4.10 and the broadened excitation lineshape of 4.11. The fact that the diagonal $X \rightarrow C$ transition fits well to the fluorescence expression derived for off-diagonal transitions indicates that perhaps the population from C is being shelved in a dark rotational state of X after very few cycles. From these fits the transition dipole matrix elements d_{eg} can be extracted:

$$d_{HC} = 0.022 \pm 0.009\, ea_0 \tag{4.19}$$

$$d_{HE} = 0.018 \pm 0.011\, ea_0 \tag{4.20}$$

$$d_{XC} = 0.34 \pm 0.13\, ea_0 \tag{4.21}$$

$$d_{HA} = 0.071 \pm 0.038\, ea_0 \tag{4.22}$$

The values used to extract these matrix elements are: $\gamma_{Doppler} = 4 \pm 1$ MHz, $\gamma_{laser} = 1.5 \pm 0.5$ MHz, $\gamma = (0.32 \pm 0.01)$ MHz for the C state [71] and $\gamma = 0.32 \pm 0.1$ MHz for the E and A state [5], and $T = 10 \pm 3$ ms. Fluctuations in the yield of the ThO source while data was gathered add additional uncertainties to the fits, resulting in overall uncertainties of $\gtrsim$50% for each computed dipole matrix element.

---

[5] Unlike the C state, these lifetimes were never directly measured. It is assumed here with some uncertainty that they are comparable to the C state.

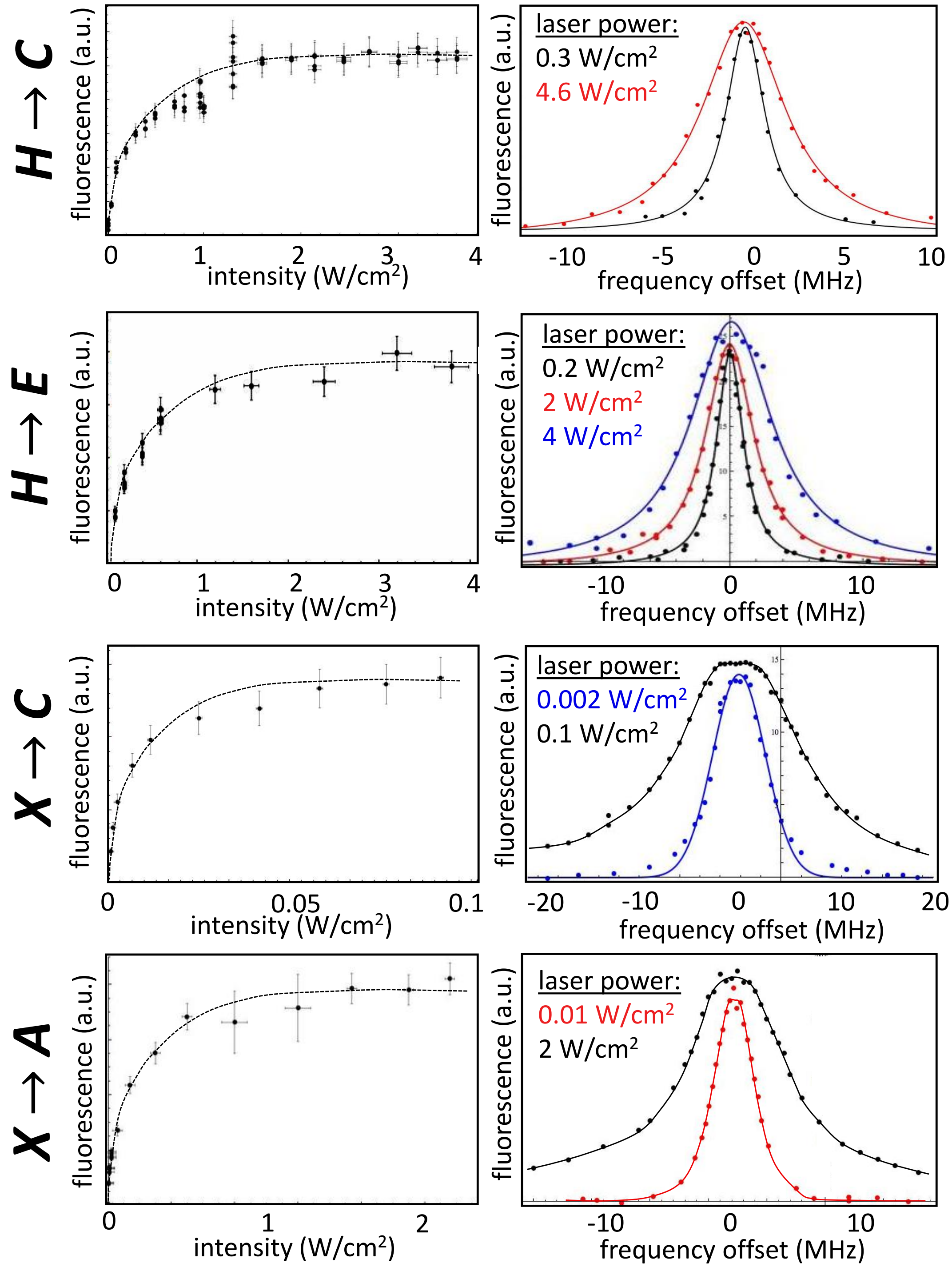

Figure 4.3: Saturation data for all ThO transitions relevant to the EDM experiment. For each transition, laser fluorescence is measured while the intensity is stepped with lasers on resonance (left), and while laser detuning is stepped for several fixed laser intensities (right). The data is fit using Equations 4.11-4.14.

From the computed transition matrix elements, the amount of laser power required for saturation in the EDM apparatus can be estimated. In this apparatus, the lasers are stretched to 20–30 mm × 5 mm, more than five times the ares of those in the miniature apparatus, resulting in longer interaction time $T \approx 25$ ms. The Doppler width, $\sim$2 MHz, is also narrower, and the transitions out of H will be weaker by a factor of 2 due to parity state mixing. I estimated that $\gtrsim 50$ mW of 943 nm light, $\gtrsim 3$ W of 1090 nm or 908 nm preparation light, and $\gtrsim 2$ W of 1090 nm or 908 nm readout light would be required to meet all saturation requirements. Because tapered amplifiers at 908 nm only provided insufficient laser power $\sim$1.5 W, the 1090 nm transition, which could be amplified to 10 W with fiber amplifiers, was chosen instead.

4.3 The $A \rightarrow H$ Branching Ratio

With saturation demonstrated, an accurate measurement of the $A \rightarrow H$ decay branching ratio could be obtained. This branching ratio determines how efficiently ground state population can be transferred to the H state for the EDM measurement. The branching ratio was measured by comparing the ground state population with the population transferred into the H state, as illustrated in Figure 4.4. The ground state population was measured by exciting the 690 nm $X \rightarrow C$ transition and then detecting 740 nm decay to the first vibrationally excited level of X (the off-diagonal fluorescence detection allowed 690 nm scattered light to be blocked with interference filters). The H state population was measured by exciting the 908 nm $H \rightarrow C$ transition and monitoring 613 nm fluorescence form E to the ground state. Notice that this comparison of populations would not be accurate if all transitions were not saturated since an unknown number of molecules would be left in the H and X states. The $A \to H$ branching ratio can be determined by comparing the 613 nm fluorescence, F_{613} with the 740 nm fluorescence, F_{740}, taking into account the Franck-Condon factor for the vibrationally excited state, W_{FC}, the relative detection efficiencies f [6], and available M_J sublevels for each excitation and decay path:

$$\xi_{X\to A} = \frac{F_{613}}{F_{740}}\frac{f_{740}}{f_{613}}\frac{N_{cyc}b}{W_{\mathrm{FC}}}. \tag{4.23}$$

Here $N_{cyc} = 1.6 \pm 0.2$ is the estimated number of $X \leftrightarrow C$ cycles, $b = 6$ accounts for the fact that only one M_J sublevel in X is excited to A, while two are excited to C, and that one third of the population that decayed to H was excited to E. Using $W_{\mathrm{FC}} = 6.5 \pm 0.5$ [77], $f_{740}/f_{613} = 0.6 \pm 0.1$, and $F_{613}/F_{740} = 0.33 \pm 0.05$ yields an $A \to H$ branching ratio of

$$\xi_{X\to A} = 0.29 \pm 0.07. \tag{4.24}$$

This implies that even when all lasers are completely saturated, only one third of the population in a given sublevel of X can be transferred to the H state manifold. Improving the efficiency of this population transfer is an important upgrade planned for the next generation of the ACME experiment [72].

4.4 Magnetic Dipole Measurement

The small magnetic moment of the H state predicted by molecular orbital theory is a great advantage for an EDM measurement. Specifically, the small near-zero

---

[6] This detection efficiency includes PMT quantum efficiency and bandpass filter transmission.

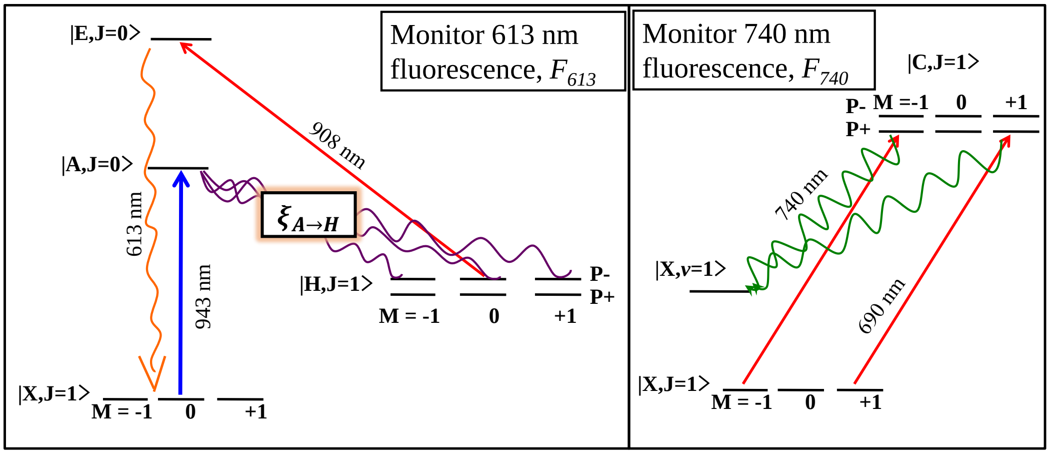

Figure 4.4: The relevant transitions for the measurement of $A \to H$ branching ratio. The 613 nm fluorescence signal is proportional to the population transferred to H via A. This fluorescence can be compared to 740 nm fluorescence proportional to the intial ground sate population to deduce the fraction of molecules in A that decay to H.

magnetic moment ensures that the EDM measurement will be almost completely immune to the correlated magnetic fields that limited previous experiments. The ThO H state is almost entirely comprised of ${}^3\Delta_1$, which has two unites of orbital angular momentum ($\Lambda = 2$) and one unit of spin angular momentum ($\Sigma = -1$) projected onto the internuclear axis. The contributions of these to the magnetic moment cancel out to a large extent, since the orbital g-factor ($g_L = 1$) is very nearly half as large as the spin g-factor ($g_S = 2.002$) [67]. The effective g-factor is therefore $g_H = g_L\Lambda + g_S\Sigma \approx 0$ [82]. The magnetic moment of this state is nonzero only becuase of small effects such as the anomalous electron g-factor [67], and the fact that H has small admixtures of ${}^1\Pi_1$ and ${}^3\Pi_1$ states. The predicted g_H value is typically $\sim$0.01 [59, 83], but the value had never been directly measured.

A measurement of the H state magnetic dipole moment $\mu_H = g_H\mu_{\mathrm{B}}$, where μ_{B} is the bohr magneton, was carried out by directly detecting the Zeeman splitting between $|H, J = 1, M_J = \pm 1\rangle$ sublevels [63]. In order to split these levels by a frequency greater that the molecular beam doppler width ($\sim$10 MHz in this case), it was necessary to apply a large magnetic field $B > 1$ kG. This was accomplished by constructing a compact permanent magnet assembly using NdFeB magnets (see Figure 4.5). The separation and alignment of the magnets was adjusted to obtain a uniform magnetic field over the region probed by the laser. The magnet was oriented parallel to the molecule beam forward velocity, $\vec{\mathcal{B}}||\vec{v}$, in order to avoid spurious effects due to motional electric fields ($\vec{E}_{mot} = \vec{v} \times \vec{\mathcal{B}}$), which could polarize the molecular state (note the difference in magnetic field orientation from the main EDM apparatus).

ThO molecules first encountered a 943 nm laser which transferred population from

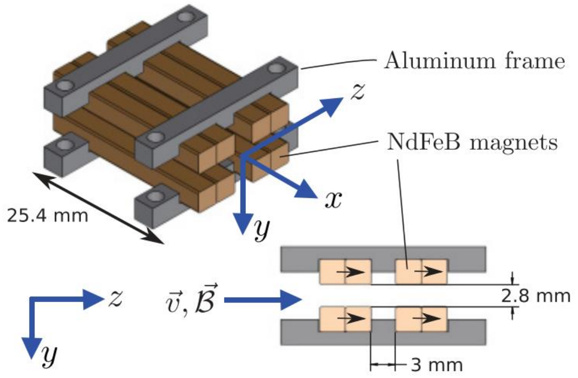

Figure 4.5: The permanent magnets supplying the 1.9 kG magnetic field to measure the H state magnetic dipole moment. The magnetic field $\vec{\mathcal{B}}$ is applied along the molecule beam direction and perpendicular to the laser propagation direction.

the ground state to the metastable H state. The H state was then probed with a 908 nm ($H \rightarrow E$) linearly polarized laser which induced 613 nm fluorescence. Both lasers propagated perpendicular to $\vec{\mathcal{B}}$. To spatially select a well-defined region near the center of the magnet assembly, the readout laser was collimated to < 1 mm. The readout laser polarization $\hat{\epsilon}$ could be adjusted to be perpendicular to $\vec{\mathcal{B}}$ to probe Zeeman shifted $M_J = \pm 1$ levels or parallel to $\vec{\mathcal{B}}$ to probe the unshifted $M_J = 0$ levels.

A plot of the 613 nm laser-induced fluorescence as a function of 908 nm laser detuning is shown in Figure 4.6. Spectra with $\hat{\epsilon}||\vec{B}$ and $\hat{\epsilon} \perp \vec{B}$ were simultaneously fit to a sum of three Gaussian line shapes, with the centers and linewidths constrained to have the same value for both data sets. Three Gaussians were included to account for the fact that the imperfectly polarized 908 nm laser contained $\sim$15% circular polarization, which excited unwanted M_J sublevels. The fit frequency separation

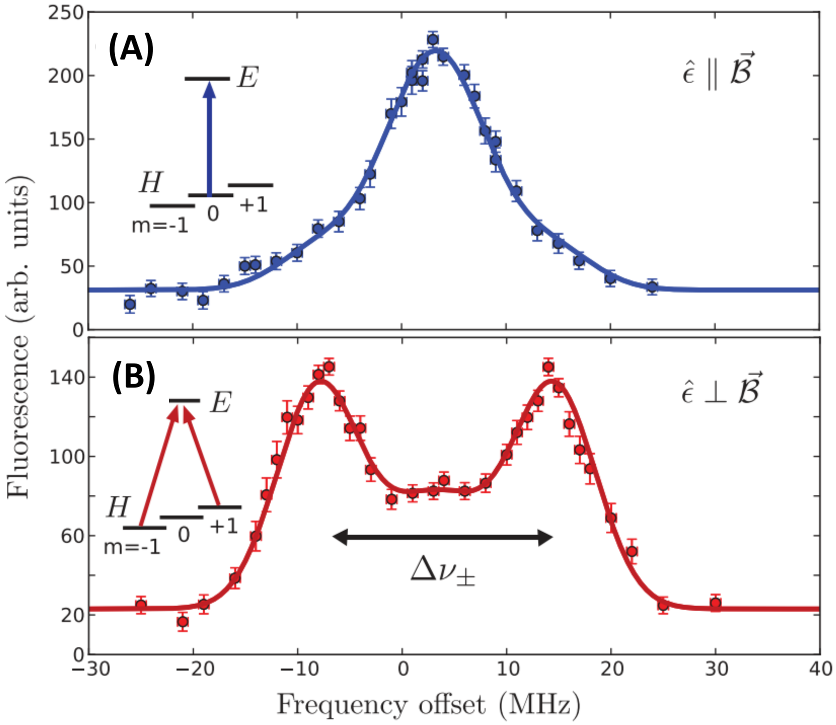

Figure 4.6: The Zeeman spitting produced by the 1.9 kG permanent magnets. **(A)** The readout laser polarization parallel to $\vec{B}$ excites the unshifted $|H, M_J = 0\rangle$ sublevel. **(B)** The readout laser polarization perpendicular to $\vec{B}$ excites the Zeeman $|H, M_J \pm 1\rangle$ sublevels, providing a measurement of μ_H.

between the $M_J = \pm 1$ peaks is $\Delta_{Zeeman} = 22.66 \pm 1.21$ MHz [7]. This yields a magnetic dipole moment

$$\mu_H = \frac{h\Delta_{Zeeman}}{2\mathcal{B}\mu_\mathrm{B}} = (-8.5 \pm 0.6 \times 10^{-3})\mu_\mathrm{B}, \tag{4.25}$$

where $\mathcal{B} = 1.9 \pm 0.1$ kG is the average magnetic field, measured with a Hall probe, in the region where molecules interact with the readout laser.

This measurement of μ_H was one of the first direct measurements of a $^3\Delta_1$ state magnetic moment [60]. The measured value agreed with theory predictions, and confirmed that systematic effects would be suppressed in the EDM experiment. Knowing μ_H with <10% uncertainty allowed us to design the magnetic field coils in the main EDM apparatus with sufficient range induce coherent state precession phase up to $3\pi/4$. This μ_H measurement is in good agreement with a more precise μ_H measurement conducted in the main apparatus, which yielded $\mu_H = (-8.8 \pm 0.1 \times 10^{-3})\mu_\mathrm{B}$ [66].

4.5 Induced Electric Dipole Moment

The presence of Ω-doublets, levels of opposite parity spaced millions of times closer than typical atomic energy levels, leads to extremely high electric polarizability in some diatomic molecules. For the ThO H state, electric polarization $P \approx 1$ was predicted with modest electric fields [12]. Like the small magnetic dipole moment, the high polarizability of the H state promises to enhance EDM measurement sensitivity and suppress of number of systematic effects related to laboratory electric field correlations. The high polarizability, however, had also never been directly observed.

---

[7] The leading uncertainty in $\Delta_\pm$ is the laser frequency calibration.

The $|H, J = 1\rangle$ state Stark splitting was directly observed by applying an electric field with a pair of glass plates, coated with transparent conducting indium tin oxide (ITO). The plates were space 3 ±0.05 mm apart, with molecules passing between them. Because the molecule beam was only collimated to ~7 mm at the time, molecules could also pass on the outside of the field plates. As with the magnetic dipole measurement, the H state is first populate by a 943 nm laser, and then immediately read out by a 908 nm laser . Both lasers propagate perpendicular to the electric field plates.

In the absence of electric field, the sublevels of H are parity eigenstates, $|\pm\rangle$, separated in frequency by $2\Delta_0$. An electric field mixes states of opposite parity, and the effective two-state Hamiltonian is

$$\mathrm{H}_H = \begin{pmatrix} h\Delta_0 & -d_H\mathcal{E} \\ -d_H\mathcal{E} & h\Delta_0 \end{pmatrix} \tag{4.26}$$

where d_H is the electric dipole matrix element connecting $|+\rangle$ and $|-\rangle$ in $|H, J = 1\rangle$ and $\mathcal{E}$ is the applied electric field. The energy spacing between the new eigenstates is

$$2\Delta_{\mathrm{Stark}} = 2\sqrt{\Delta_0^2 + (d_H\mathcal{E}/h)^2}. \tag{4.27}$$

In the limit where $d_H\mathcal{E} >> \Delta_0$ the parity eigenstates are completely mixed and Stark spliiting can be approximated as

$$\Delta_{\mathrm{Stark}} \approx |d_H\mathcal{E}|/h. \tag{4.28}$$

Figure 4.7A shows 613 nm fluorescence as a function of 908 nm frequency for $\mathcal{E}$ = 20 V/cm. The side peaks have clearly been Stark shifted, while the center peak(s) correspond to molecules outside the electric field plates. A fit to the two side peaks yields $\Delta_{\text{Stark}} = 22.6 \pm 1.7$ MHz, where the uncertainty is dominated by the calibration of the laser frequency with the locking cavity. The measurement is repeated with multiple electric fields and the Stark splitting shows clear linear dependence on the magnitude of electric field, as shown in Figure 4.7B, which implies that ThO has been fully polarized. From the linear fits in Figure 4.7B the induced dipole moment can be obtained,

$$d_H = |\partial\Delta_{\text{Stark}}/\partial\mathcal{E}| = h \times 1.07 \pm 0.05\text{MHz}/(\text{V/cm}). \tag{4.29}$$

As Equations 4.27 and 4.28 imply, the sign of d_H cannot be deduced from Stark splitting data alone. In keeping with convention [63] it is presented here as a positive value.

In the EDM experiment it is advantageous to have the $|H, J = 1\rangle$ states Stark shifted by $>$ 100 MHz, so that off-resonant sublevels of the C state, separate by 50 MHz, do not interfere with with the measurement. This measurement of the induced electric dipole moment allowed us to design the electric field plates, and corresponding voltage supplies, of the main EDM apparatus to produce Stark shifts up to 150 MHz, far detuned from off-resonant sublelvels. This measurement of d_h agrees with the more precise determination of d_h later achieved in the main EDM apparatus: $d_h = h \times 1.03 \pm 0.01$ MHz/(V/cm).

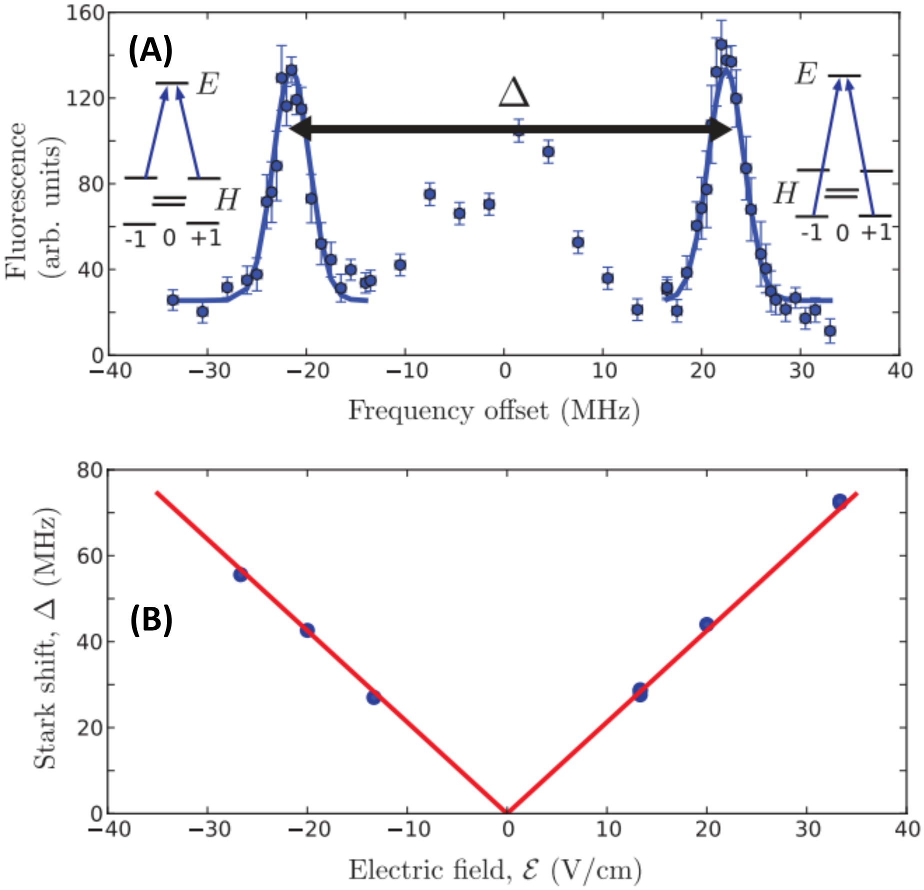

Figure 4.7: **(A)** The Stark Splitting between N levels of the H state with $\mathcal{E} = 20$ V/cm. The fluorescence near resonance is produced by unshifted molecules outside the electric field plates. **(B)** Measured Stark splitting as function of electric field. The fact that all points fit very well to a linear slope indicates that the ThO molecules are fully polarized.

4.6 Demonstration of EDM State Preparation and Spin Precession Readout

In addition to measuring important ThO dipole moments and transition strengths, the first demonstration of coherent spin state preparation was performed in the miniature ThO apparatus. For this demonstration 943 nm, 1090 nm, and 908 nm laser beams, spaced ∼7 mm apart from each other, propagated perpendicular to the molecular beam at a distance 30 cm from the source. Following the method described in Chapter 3, ThO molecules were first transferred into the H state by the 943 nm optical pumping laser. A coherent dark state was formed by a ∼200 mW beam of linearly polarized 1090 nm light driving $|H, M_J = \pm 1\rangle \rightarrow |C, M_J = 0\rangle$. A linearly polarized 908 nm laser beam was used to read out the coherent state. Unlike the main EDM experiment, the preparation and readout lasers were in close proximity in the miniature ThO apparatus. It was therefore necessary to use two different transitions for state preparation and readout so that the induced fluorescence produced by the preparation and readout lasers could be distinguished with bandpass filters. Evidence of coherent spin state preparation is shown in Figure 4.8A, where readout fluorescence is plotted vs readout laser polarization. When the readout laser polarization is parallel to the the preparation laser polarization, fluorescence is minimized since the readout state is driving the superposition of $|H, M_J\rangle$ levels that was already transferred out of the H state. Fluorescence is maximized when the readout laser polarization is perpendicular to the preparation laser polarization, causing it to excite the spin superposition that was dark to the preparation laser.

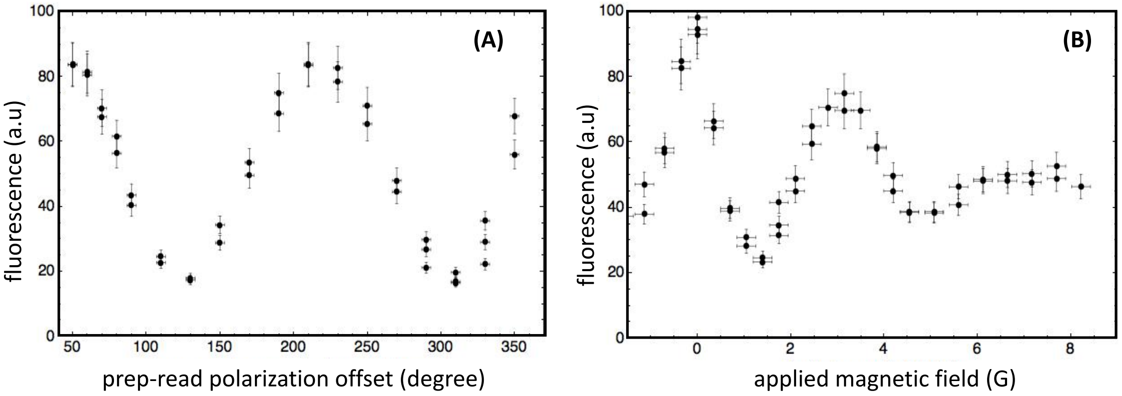

Figure 4.8: The first demonstration of a coherent spin state in H. **(A)** Fluorescence clearly depends sinusoidally on the relative polarization between preparation and redout lasers, indicating that a dark state has been formed.**(B)** A magnetic field causes the coherent state to precess with the fluorescence depending sinusoidally on the total precession phase.

Once the coherent spin state was created in H, two 50-loop Helmholtz coils wrapped around the KF-50 vacuum cross were used to produce a magnetic field that induced coherent spin precession. These coils were attached to a 3A current supply to produce magnetic fields up to 10G along the laser propagation direction. Figure 4.8B shows readout fluorescence vs applied magnetic field, for fixed laser polarization. The sinusoidal dependence shows that the coherent state clearly precesses in the applied magnetic field. The decoherence at larger magnetic fields is due to molecule forward velocity dispersion and the fact that significant precession occurs within the preparation and readout laser fields.

With the demonstration of coherent spin state preparation and magnetic field induced precession, all important characterization of ThO necessary for the EDM measurement was complete. The demonstration of saturated population transfer, H-state Stark splitting, and coherent spin state preparation were all crucial pieces of the EDM measurement procedure developed in the miniature ThO apparatus. Measurements of H state magnetic and induced electric dipole moments confirmed advantageous properties of ThO and informed our design of the electric and magnetic field sources in the main apparatus. Similarly, ThO transition strength measurements helped to determine the laser powers required for the EDM measurement. With the completion of this work, we focused our efforts on constructing and testing the main EDM apparatus described in the following chapter

Chapter 5

Experimental Apparatus

The EDM apparatus was designed to maximize sensitivity to the electron EDM while minimizing systematic error. At the heart of the apparatus is the “interaction region” where ThO molecules spin precess in precisely controlled electric and magnetic fields. To achieve high statistical sensitivity a buffer gas beam source and rotational cooling region are optimized to provide high ThO flux to the interaction region. Light collection optics are optimized to capture a significant fraction of molecule fluorescence. Systematic error is minimized in part using an apparatus designed to provide precise control, broad tuning, and careful monitoring of many important experimental parameters, such as electric and magnetic fields and properties of laser light.

This chapter provides an overview of the five main components of the EDM apparatus: molecule beam source, rotational cooling region, interaction region, lasers and optics, and data acquisition system. These components were designed, assembled, and tested in parallel over a four year period (2007-2011). A schematic of the molecule beam source, rotational cooling region, and interaction region is shown in Figure 5.1. Nearly every member of the ACME collaboration contributed to development of the apparatus. In this chapter I will describe the each component of the apparatus, providing extra detail on the parts to which I significantly contributed: lasers and optics, electric field plates, vacuum chamber, and the fluorescence collection system.

5.1 Buffer Gas Beam Source

Cold ThO molecules used for this EDM measurement are produced by laser ablation and buffer gas cooling, a technology developed in Professor John Doyle's group over the past decade [73, 75]. The molecule source consists of a cold (~15 K) cylindrical copper cell (7.5 cm long, 1.3 cm diameter) inside a 0.5 m cubic vacuum chamber, cryopumped by 4 K surfaces to $\sim 1 \times 10^{-7}$ Torr. A pulse tube refrigerator cools the cell and cryopumping surfaces. Neon buffer gas flows into the cell at 30-40 SCCM (cm^3/minute) and out through a circular 0.5 cm exit aperture. A high power pulsed YAG laser (50 Hz repetition rate, 30-40 mJ per pulse) ablates a flat ceramic ThO_2 target (~1 cm diameter) inside the cell, producing hot ThO molecules. Repeated cell-neon and neon-ThO collisions bring hot ThO molecules into thermal equilibrium with the cold cell. Cold molecules are then caught up in the buffer gas flow and exit the cell, forming a molecular beam with measured ~0.3 sr transverse spread. Transverse velocity spread is narrowed with ~1 cm collimators placed near the cell (2 cm from aperture), in the rotational cooing region (0.5 m from aperture), and in the interaction region (1.3 m from aperture). With each ablation pulse $\sim 10^{11}$ ThO molecules in the $|X, J = 1\rangle$ state exit the cell within a 2-3 ms window. Because of

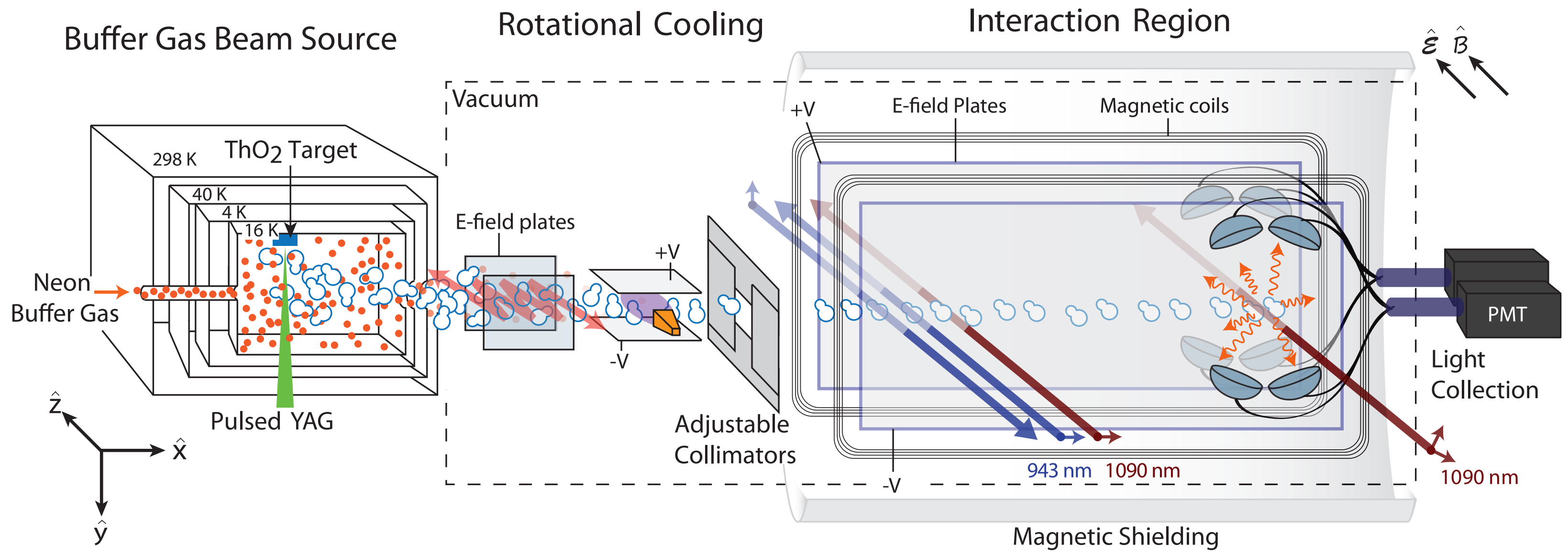

Figure 5.1: A cold pulsed beam of ThO molecules is created via laser ablation and buffer gas cooling. Molecules travel through a rotational cooling region and enter a magnetically shielded region. An aligned spin state, prepared via optical pumping, precesses in parallel electric and magnetic fields. The final spin alignment is read out by a laser with rapidly alternating linear polarizations, $\hat{X}, \hat{Y}$, with the resulting fluorescence collected and detected with photomultiplier tubes (figure not to scale).

solid angle loss, only $\sim 10^6$ of those molecules clear the final collimator and enter the interaction region.

This buffer gas beam has several key advantages over molecule/atom sources used in previous EDM measurements [5, 36, 73]. Due to its low rotational temperature, a significant fraction of ThO molecules populate quantum states useful for this EDM measurement [84]. Also, the yields of the buffer gas beam are 10-100 times larger that of supersonic beams with comparable rotational temperature [5]. This is mostly due to high ThO ablation yields and efficient cell extraction, but is also due to the higher duty cycle available in buffer gas beams. While supersonic beams typically cannot operated above $\sim$25 Hz repetition rates due to high backing pressures, the ThO pulse rate is limited only by the heat load of the YAG laser and could potentially be > 100 Hz if sufficient cooling power were available. The EDM experiment also benefits from the buffer gas beam's relatively slow forward velocity, half that of supersonic beams. This allows us to achieve coherence time $\tau \approx 1.1$ ms, comparable to the lifetime of the H state, within a relatively short (22 cm) interaction region length. Nick Hutzler led the effort to develop and characterize the ThO beam apparatus. Elizabeth Petrik produced the ceramic ThO_2 targets in house. Max Parsons and Jacob Baron have also supported these efforts.

5.1.1 Molecule Velocity and Yield Fluctuations

The ThO beam properties are thoroughly documented in our journal article [84] and Nick Hutzler's thesis [61]. Here I will highlight certain properties that have heavily influenced our measurement and data analysis routines.

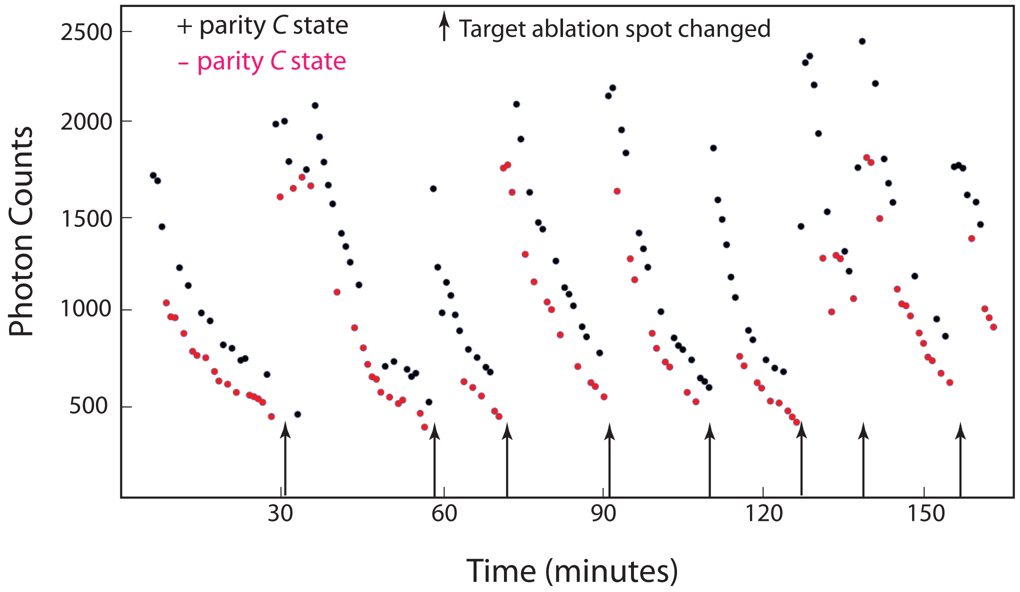

Figure 5.2: Detected molecule fluorescence over a three-hour period. Molecule beam yield quickly increases when the ablation laser pointing is adjusted and then steadily decays. Photons emitted from the positive parity readout state (black) are detected with ∼30% higher efficiency than those emitted from the negative parity state (red) due to the geometry of the fluorescence collection optics [66].

Molecule yield fluctuates by as much as 50% from pulse to pulse. On a slower timescale the average molecule yield decays fairly linearly for a fixed ablation spot on the target (see Figure 5.2). The yield recovers once the ablation laser pointing is moved. The decay timescale can vary from a minute to an hour depending on the properties of the ablated target region. Molecule yield also fluctuates throughout the 2-3 ms pulse on 0.1 ms timescales. The distribution of molecules as a function of arrival time also varies significantly, depending on the ablation laser pointing and focus. To obtain shot-noise limited phase measurements throughout the molecule pulse, we must normalize against these fluctuations [66]. To accomplish this we have implemented 100 kHz fast polarization switching of the readout laser and a corresponding data analysis routine that extracts precession phase by comparing the fluorescence produced by each laser polarization.

Molecule forward velocity also fluctuates from pulse to pulse and typically decreases by ~1% per minute for a fixed ablation spot. This produces fluctuations in coherence time and accumulated precession phase (see Figure 6.5). The EDM measurement relies on comparing molecular precession phase under different experimental conditions. Therefore, important parameter switches must be performed on timescales much faster than the phase drift. For this reason internal molecule alignment and laboratory electric field are reversed on the fastest timescales, 0.5 s and 2 s respectively. They are also switched in an ABBA sequence and/or a random sequence to cancel out the effects of linear phase drift. As discussed in the following chapter, the analysis routine also accounts for long-term velocity drift by extracting a separate measurement of τ from each block of data and then computing angular frequency,

$\omega = \phi/\tau$.

When the ablation spot on the target is moved by adjusting the YAG laser pointing, the molecule forward velocity rapidly increases by ∼10% in less than one second. This causes similarly fast changes to the molecule precession phase, which cannot be accounted for with fast parameter switching [1]. For this reason the experiment operating policy is to only adjust the the ablation laser pointing between data blocks, when no data is being acquired. As an additional precaution we separately record [2] the ablation laser pointing and, in the data analysis, throw away any block of data in which the ablation pointing was changed.

The beam forward velocity can drift so much that the overall precession phase significantly deviates from $\pi/4$, where the experiment is most sensitive to the EDM. It is well known that forward velocity scales with buffer gas flow rate [84, 73]. Therefore, when it was not convenient to adjust the magnitude of the magnetic field, we used the buffer gas flow to manually feed back on molecule velocity on a ∼ 30 minute timescale and ensure that $\phi \approx \pi/4$. The flow was always within 30-50 SCCM.

We also observed that flow rate affected molecule beam yield in a nonlinear manner, consistent with our previously reported observations [84]. For some ablation spots the yield increased with flow until leveling off at 50 SCCM. For other spots the yield decreased with flows above 30 SCCM. This behavior also changed with ablation laser power and focus. Because EDM sensitivity scales linearly with τ, we generally sought to operate with the lowest flow rate, and thus the slowest forward velocity,

---

[1] Not counting the 100 kHz polarization switching, the fastest parameter switching timescale is ∼1 s (for $\tilde{\mathcal{E}}$ and $\tilde{\mathcal{N}}$).

[2] The ablation laser pointing is automated through motorized mirrors, and the mirror angle is recorded with each fluorescence trace.

that still produced sufficiently high molecule yield.

5.2 Rotational Cooling Region

The rotational cooling region, also referred to as the stem region, consists of of three KF-50 aluminum vacuum modules between the beam source and the interaction region. Rotational cooling takes place in the module (10 cm × 10 cm × 16 cm) closest to the beam source, which contains 2 cm × 4 cm flat copper electrodes and allows for horizontal optical and microwave access. The middle module contains collimating razor blades on translatable mounts. Typically the razors are set to form a 1 cm square collimating aperture, but they can be moved to clip all or part of the molecule beam from all four directions (up, down, left, right) in the y-z plane. The final module is nearly identical to the first, except that it also has optical access from above and contains no electrodes. This region was not used during the EDM measurement but has been used to study the buffer gas beam. High speed turbo pumps are attached directly below the first and last vacuum modules. These keep the stem region pressure, monitored by an ion gauge on the middle module, between 1-10 $\times 10^{-6}$ Torr, depending on the buffer gas flow rate. KF-50 bellows and gate values connect the stem region on both ends to the beam source and interaction region. The bellows serve to mechanically decouple all three regions, and the gate valves allows maintenance to be performed on one region without breaking vacuum in the other two regions. Elizabeth Petrik designed the three stem region modules and variable collimators.

When molecules leave the beam source, their population is spread throughout

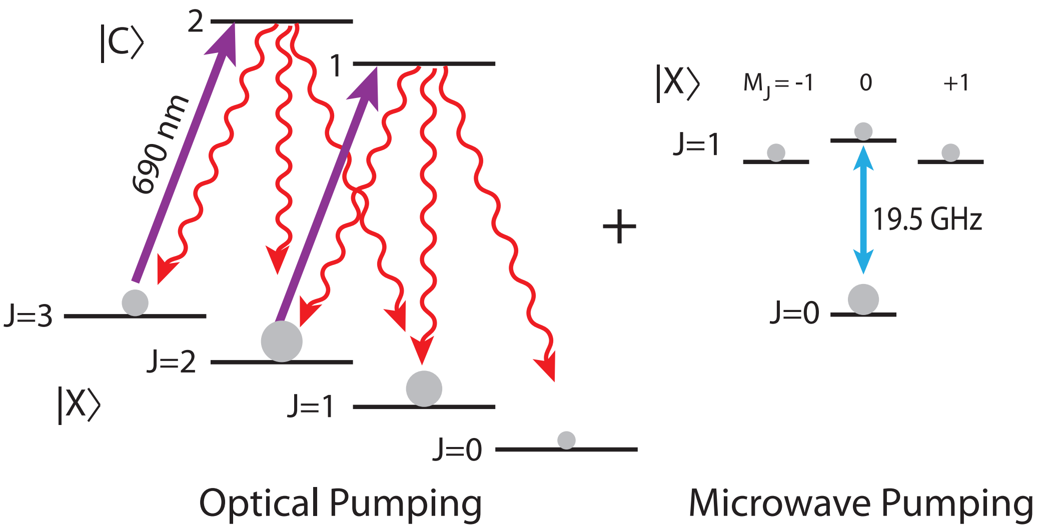

Figure 5.3: Rotational cooling scheme. Molecules first encounter two 690 nm lasers which optically pump ThO population from the $J = 2$ and $J = 3$ rotational levels to the $J = 0$ and $J = 1$ rotational levels. Next, 19.5 GHz microwaves drive population from $J = 0$ to $J = 1$.

several lower rotational levels according to a Maxwell-Boltzmann distribution. About ~25% of molecules occupy the $|X, J = 1\rangle$ rotational level [84], which will later be used to populate the EDM state in the interaction region. Lasers (690 nm, ~10 mW power, and 1 mm × 10 mm beam profile) and microwaves (19.514 GHz, 10-15 dBm) in the first stem region module transfer additional population to this state from nearby rotational states. This process, referred to as rotational cooling, is illustrated in Figure 5.3.

In more detail, a 43 V/cm electric field in the vertical direction is applied through copper electrodes (see Figure 5.1). This field Stark shifts all $|X, M_J \neq 0\rangle$ and $|C, M_J \neq 0\rangle$ levels, partially mixing the parity of $|C, M_J \neq 0\rangle$ states. Microwaves can resolve X state Stark splitting but the power-broadened 690 nm lasers cannot resolved the splitting in either the X or C states. Molecules first encounter lasers tuned to

$|X, J = 3\rangle \rightarrow |C, J = 2\rangle$ and $|X, J = 2\rangle \rightarrow |C, J = 1\rangle$ transitions. These linearly polarized lasers are retro-reflected at least five times through the molecule beam, rotating polarization by 90 degrees with each reflection. This effectively transfers population from $|X, J = 2, 3\rangle$ to $|X, J = 0, 1\rangle$.

Microwaves then mix the populations of $|X, J = 0, M_J = 0\rangle$ and $|X, J = 1, M_J = 0\rangle$ but do not interact with Stark shifted $|X, J = 1, M_J = \pm 1\rangle$ levels. Because the population of $|X, J = 0, M_J = 0\rangle$ is greater than the population of $|X, J = 1, M_J = 0\rangle$, the microwaves provide a net increase to $|X, J = 1\rangle$ population. All M_J sublevels of $|X, J = 1\rangle$ are remixed by earth's magnetic field before molecules enter the interaction region. This process typically increases fluorescence signals in the interaction region by 60-70% ($\sim$25% from microwaves, $\sim$25% from the $|X, J = 2\rangle \rightarrow |C, J = 1\rangle$ laser, and $\sim$15% from the $|X, J = 3\rangle \rightarrow |C, J = 2\rangle$ laser). This exactly enhancement factor depends on the rotational temperature of the beam source. The efficiency of this process is limited due to C state decay to other electronic and vibrational states (primarily Q and $|X, v = 1\rangle$). Emil Kirilov took the lead in developing and implementing this rotational cooling technique. The upgrades planned for the next generation of the ACME experiment should increase the rotational cooling population enhancement by a factor of $\sim$5.

5.3 Interaction Region

At the heart of the experiment is the interaction region where the EDM measurement is performed. In this evacuated region ThO population is transferred to the metastable H level and a coherent superposition of $|H, J = 1, M_J = \pm 1\rangle$ states is formed. The coherent state then precesses in applied electric and magnetic fields and the accumulated phase is read out via laser-induced fluorescence. Lenses, fiber bundles, and light pipes collect fluorescence light and transfer it to photomultiplier tubes (PMTs) outside the vacuum chamber. Five layers of mu-metal shielding surround the entire region to ensure that external magnetic fields do not affect the EDM measurement. The photograph in Figure 5.4 shows the important components of the interaction region.

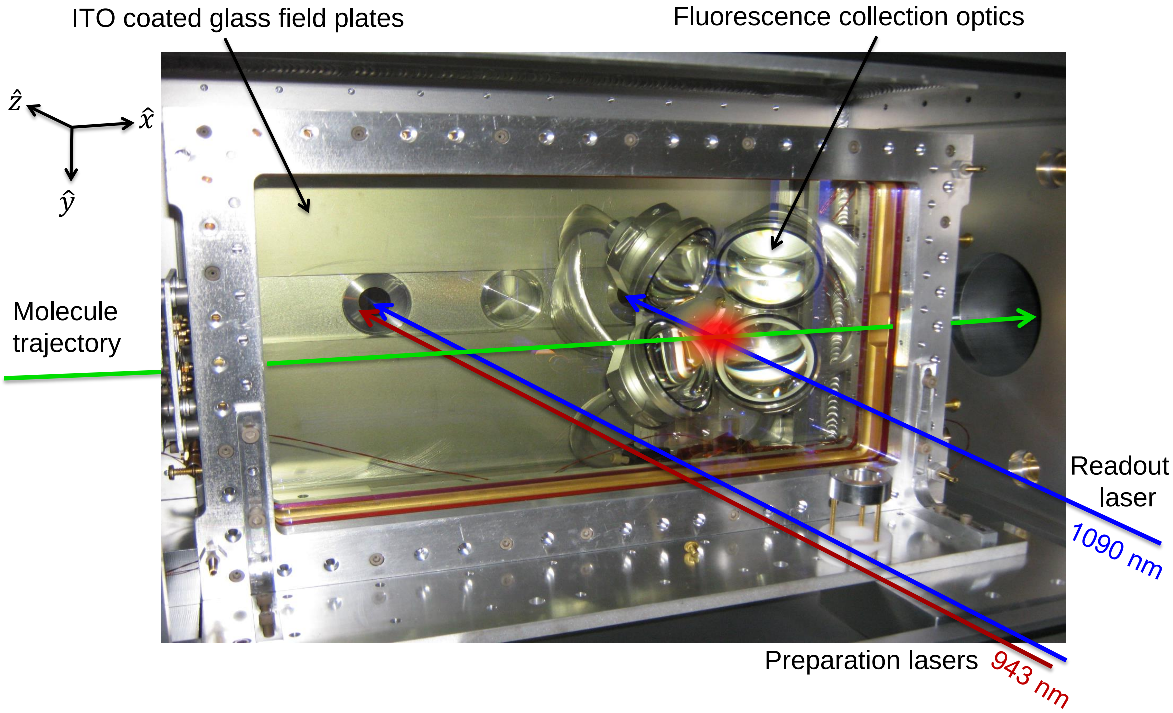

Figure 5.4: Photograph of electric field plates and collection optics inside of interaction region vacuum chamber. Colored arrows denote laser and molecule beam trajectories.

5.3.1 Vacuum Chamber

The interaction region vacuum chamber (40 cm × 40 cm × 60 cm) connects to the rotational cooling region through a cylindrical trunk (10 cm diameter × 50 cm long) that extends through the end of the magnetic shield layers. An identical trunk connects the other end of the chamber to a high speed turbo pump that sits outside the shielded region. An aluminum 80/20 structure, bolted to the ground, rigidly supports the vacuum chamber. Two 2.5 cm diameter anti-reflective (AR) coated windows, spaced 22 cm apart, on each side of the vacuum chamber allow 943 nm and 1090 nm state preparation and readout lasers to propagate perpendicular to the molecule beam and field plate surfaces. The vacuum chamber was originally designed and assembled by Amar Vutha [60] and later modified by Emil Kirilov, Nick Hutzler, and myself.

It generally requires 1-3 weeks to pump the vacuum chamber down below 1×10^{-7} Torr, depending on how long the interaction region vacuum chamber has been exposed to atmosphere. When the empty chamber was first assembled, a residual gas analyzer (RGA), located between the turbo pump and the chamber, indicated the presence of many heavier molecules ($>$ 200 amu). After 30 hours of pumping the total pressured was 2×10^{-6} Torr, with water being the dominant peak on the RGA. After baking out the chamber at ∼150 C for three days and then letting it cool, the pressure dropped to 5×10^{-8} Torr. No peaks heavier than acetone (58 amu, 3×10^{-10} Torr partial pressure) were observed on the RGA. For reference, the neon partial pressure measured by the RGA is 2×10^{-7} Torr with 35 SCCM flow rate.

Though baking shortens the pump out time, it was avoided when electric field plates were in the vacuum chamber to avoid possible migration of heavier molecules from the heated chamber surfaces to the cooler electric field plates. Such migration might cause unwanted patch potentials on the plate surfaces. When the field plates were installed in December, 2012, two weeks of pump out time were required for the total pressure to fall below 1×10^{-7}. ThO fluorescence could still be detected with background pressures as high as 8×10^{-7} Torr. It was not clear whether the background gas attenuated ThO beam fluxes. The chamber was not opened again until September, 2013, after all EDM data was gathered and the magnetic field had to be mapped out.

Ground loops as large as 10 mA were originally observed in the vacuum chamber, 80/20 structure, and magnetic shields. The currents produced stray magnetic fields measured to be as large as 1 mG inside the vacuum chamber. If aligned with the electric field axis, these fields could produce uncontrolled phase precession of 0.05 rad. The ground loops were caused by electrical connections through vacuum components between the interaction region, stem region, and beam source. Each region contained multiple components (e.g. turbo pumps, vacuum gauges, and pulse tube coolers) plugged into different wall outlets. Vacuum parts were also electrically connected to the 80/20 supporting structure, which in turn was connected to PMTs, power strips, and voltage supplies. Electrical connections to the beam source caused the largest ground loops, possibly because the pulse tube cooler was connected to a custom three-phase power outlet in a different room. Ground loops were removed by electrically isolating the interaction region from the beam source and ensuring that all vacuum pumps, gauges, and automatic gate valves were plugged into the same power outlet.

PMTs, voltage supplies, and power strips were isolated from the 80/20 structure. The result was that no ground loop currents larger than 10 μA could be observed.

5.3.2 Electric Field plates

The two electric field plates are 1.25 cm thick float glass with a 200 nm thick indium tin oxide (ITO) coating on their inner surface and an 800-1200 nm AR coating on their outer surface. The inner surfaces are spaced 2.5 cm from each other and aligned to be as parallel as possible. Gold coated guard rings cover the inner edges of the glass plates. These served to minimize fringing fields and to hold the the glass plates to an aluminum frame (see Figure 5.4). The field plates, guard rings, and aluminum frame are electrically isolated from each other by thin pieces of kapton. Separate electrical leads, connected to separate voltage supplies, are clamped to each guard ring and field plate. One aluminum frame is fixed and the other serves as a kinematic mount with adjustable precision screws at three corners. These screws determine the spacing and relative angle of the two field plate surfaces. The frame is fixed to a baseplate mounted to the bottom of the vacuum chamber. A 1 cm square collimator made of four titanium razor blades is attached to the end of the aluminum frame closest to the beam source. The field plate assembly was designed by Amar Vutha [60] and assembled by Emil Kirilov, with Elizabeth Petrik building the collimator.

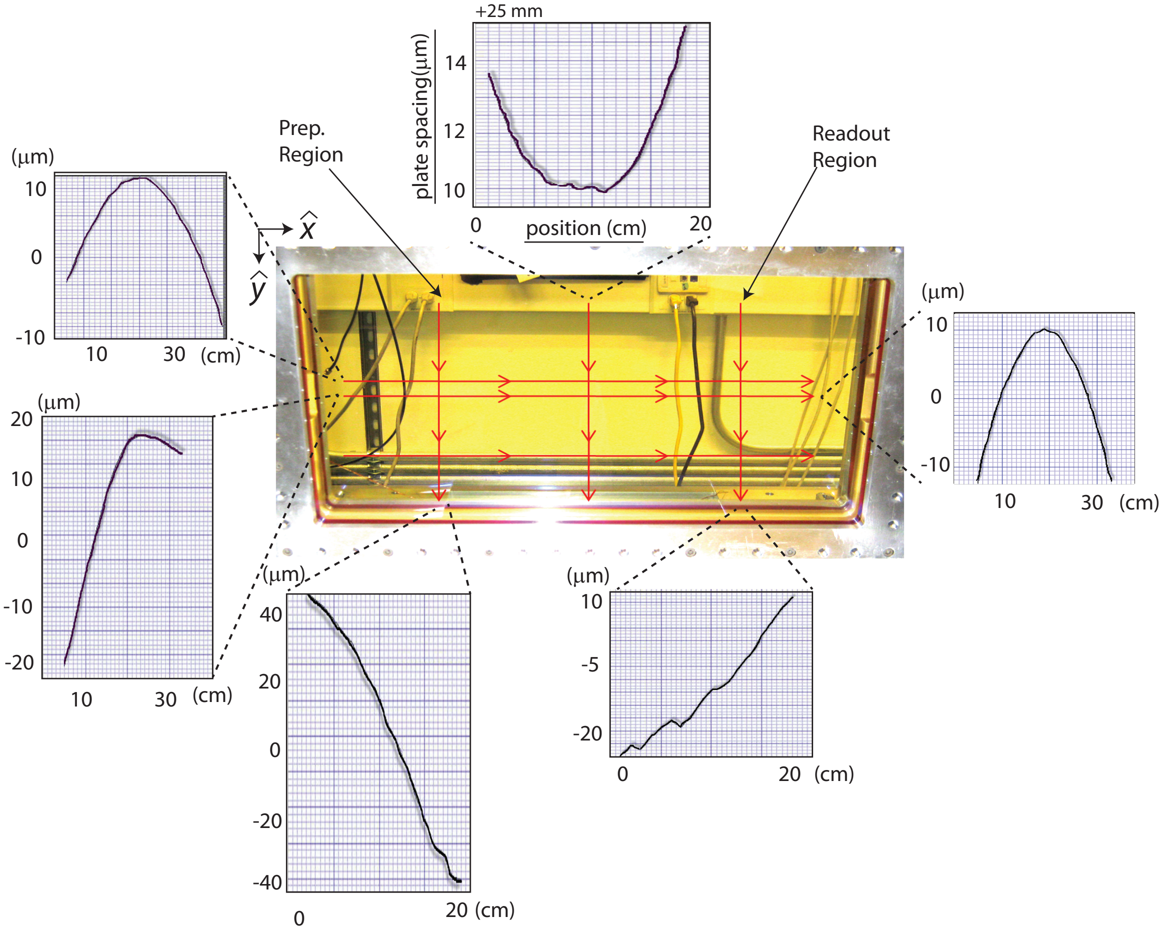

Figure 5.5: Electric field plate spacing, after plate alignment was optimized, measured with a scanning Michelson interferometer along several field plate cross-sections. Multiple scans indicate a saddle-like contortion along the diagonal axis. The plates are positioned to minimize the gradient along the molecule beam line (far right).

Electric Field Gradients

Using a scanning Michelson Interferometer, based on [85] and built by Ivan Kozyryev at Yale, I performed the final alignment of the electric field plates after installing them in the vacuum chamber. The interferometer revealed $\sim$50 μm warping in either one or both of the plates, as illustrated in Figure 5.5. The data indicated saddle-like contortion along the diagonal axis of the plates: the upper left and lower right corners were spaced farthest apart and the upper right and lower left corners were closest together. Neither the shape nor magnitude of the contortion changed when the clamps holding the plates were loosened and tightened in a number of different combinations. This implied that the contortion was inherent to the plates, although the manufacturer specified plate flatness to within 1 μm. I aligned the plates to equalize the averaged spacing in the upper and lower halves. I then equalized the spacing of the regions where the state preparation and readout lases would intersect the plates. Along the molecule beam line between the two laser regions, the plates bowed by $\sim$15 μm (see Figure 5.5). The plate bow was confirmed by microwave spectroscopy measurements of $\mathcal{N}$ level Stark splitting as a function of molecule position along $\hat{x}$, shown in figure Figure 5.6.

Non-Reversing Electric Fields

Voltage, V, is supplied to the electric field plates with a precision voltage supply (built in-house by Jim MacArthur, designed to provide 2 mV voltage stability). The leads connecting the supply to the plates are switched by a series of automated mercury-wetted relays near the interaction region. Lead switching cancels the effects

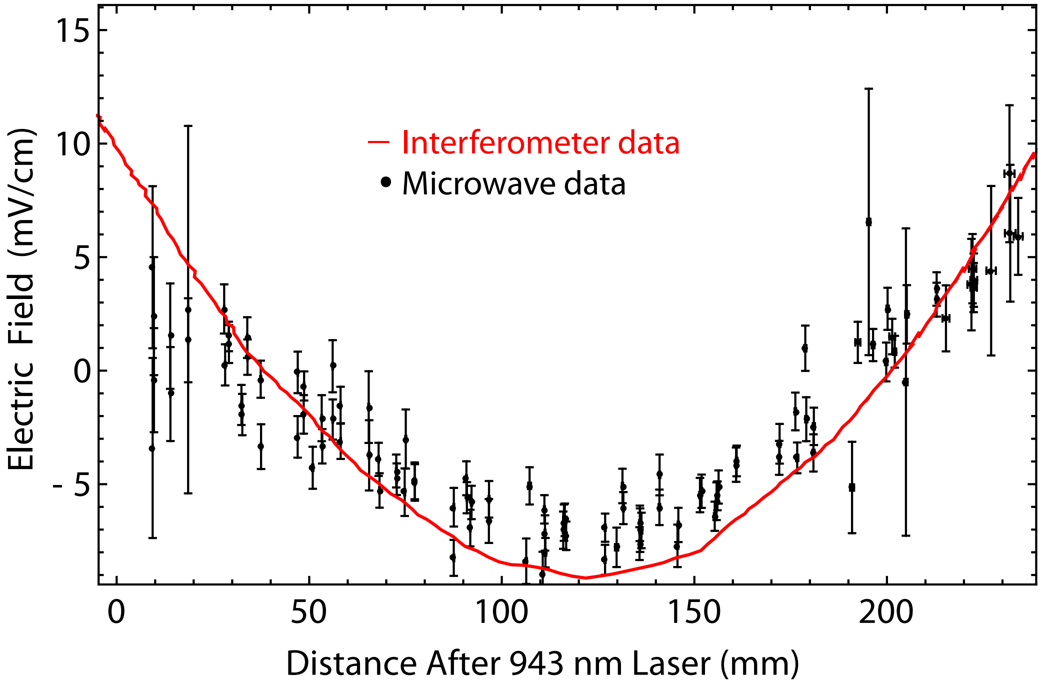

Figure 5.6: Measured electric field between the preparation and readout regions, along the molecule beam centerline. $\mathcal{N}$ level Stark splitting (black) measured by driving the $|H, J = 1\rangle \rightarrow |H, J = 2\rangle$ transition with microwaves agrees well with the electric field gradient predicted by Michelson interferometer plate spacing measurements (red)

of imperfect voltage reversal caused by offsets in the voltage source. Such voltage offsets are typically tuned out to the level of 5 mV, limited by the resolution of the supply, producing a non-reversing electric field, $\mathcal{E}_{\rm nr} \approx 2$ mV/cm, that reverses with the lead switch (see Figure 7.14A).

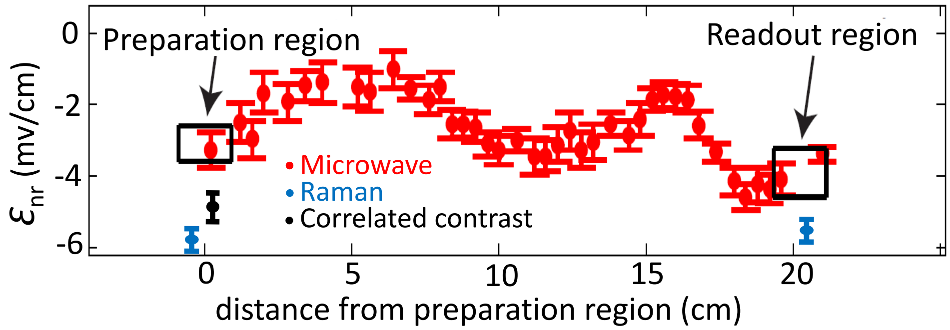

Figure 5.7: The non-reversing electric field internal to the interaction region. We used three different methods to measure the non-reversing field: microwave spectroscopy (red), Raman spectroscopy (blue), and a correlated component of the contrack (black). Only the microwave measurement allowed $\mathcal{E}_{\rm nr}$ to be measured in regions with no optical access.

A slightly larger non-reversing electric field is produced by patch potentials on the field plates themselves. This internal $\mathcal{E}_{\rm nr}$ cannot be suppressed by lead switching. The stray field was measured in several different ways using ThO molecules. With microwave spectroscopy, Brendon O'Leary and Adam West measured $\mathcal{E}_{\rm nr}$ at all locations between the preparation and readout regions [4]. The measured field was 4 ± 0.5 mV/cm averaged between the two laser regions and fluctuated by ~3 mV/cm between the two regions [4], as shown in Figure 5.7. Paul Hess used Raman spectroscopy to measure $\mathcal{E}_{\rm nr} 6.0 \pm 0.3$ mV/cm averaged between the two laser regions [71]. As described in Chapter 7, I used the component of contrast correlated with two parameter switches to measure $\mathcal{E}_{\rm nr} \approx 5 \pm 0.5$ mV/cm in the state preparation region throughout the published EDM data sets (see Figure 7.14). Similarly, I used a component of fluorescence signal correlated with the same two switches to limit $\mathcal{E}_{\rm nr} < 10$ mV/cm in the readout region. Each method of determining $\mathcal{E}_{\rm nr}$ has its own advantages. Microwave spectroscopy is the only method that allows $\mathcal{E}_{\rm nr}$ to be determined in the center region of the field plates where there is no optical access. Measurements from Raman spectroscopy generally had the least statistical uncertainty. Only correlated contrast measurements allowed us to obtain *in situ* measurements of $\mathcal{E}_{\rm nr}$ while we gather EDM data. While these measurements roughly agree with each other, as shown in Figure 5.7 it should be noted that they were all performed at different times, sometimes months apart. Microwave measurements gathered in June and August of 2013 suggest that $\mathcal{E}_{\rm nr}$ might drift over time on the level of 2 mV/cm. If this is is the case, it would explain the slight disagreement between the various $\mathcal{E}_{\rm nr}$ measurement methods.

Leakage Currents

It is important for the electric field plates to be well isolated from the aluminum stand and vacuum chamber. Otherwise leakage currents can create magnetic fields correlated with the direction of eclectic field, a potential EDM systematic effect [36, 39]. By unplugging the cables and voltage source from the field plates and monitoring the $\mathcal{N}$ level Stark splitting, $\Delta_{\rm Stark} = (d_h\mathcal{E})/h$, I determined how much the electric field, and thus the plate voltage, was changing with time (see Figure 3.1 for an illustration of H state Stark splitting). Here $d_H = 1.03$ $h\times$ MHz/(V/cm) is the induced electric dipole of the H state (Chapter 7.2.2 describes a measurement of d_H). The plate capacitance, C, can then be used to relate the leakage current, I_{leak}, to the change in electric field,

$$I_{\text{leak}} = \mathrm{C}\frac{\partial V}{\partial t} = \left(\epsilon_0 \frac{A}{D}\right)\left(D\frac{\partial \mathcal{E}}{\partial t}\right) = \frac{\hbar A \epsilon_0}{d_H}\frac{\partial \Delta_{\text{Stark}}}{\partial t}, \tag{5.1}$$

where D is the spacing between the two field plates, t is time, and A is the area of the field plates. The capacitance of the thin wires connecting the field plates to the vacuum feed-through is neglected since it is assumed to be much smaller than the capacitance of the large plates. Figure 5.8 shows Δ_{Stark} drifting over time, corresponding to $I_{\text{leak}} = 1.2 \pm 0.05$ pA according to Equation 5.1. Though it is possible that the current leaks across the voltage lead vacuum feed-through, far away from the molecules, we make the worst case assumption that all current flows directly between the two plates. If we also conservatively assume that the magnetic field resulting from this current flow creates a magnetic field along the electric field direction, $\hat{z}$, then component of $\mathcal{B}_z$ correlated with $\mathcal{E}$ due to leakage current is $< 10^{-13}$ G. Accounting for the 1000-fold suppression provided by the $\mathcal{N}$ level switch, this small leakage current corresponds to a negligible systematic offset $\lesssim 10^{-37}$ e cm, much less than the $\sim 10^{29}$ e cm predicted EDM sensitivity of the ACME experiment.

5.3.3 Magnetic Coils and Shields

Three sets of magnetic coils allow magnetic fields to be applied along all three lab axes, $\hat{x}$, $\hat{y}$, and $\hat{z}$. They also allow all possible first order magnetic field gradients to be applied. All coils are located outside the vacuum chamber and inside the

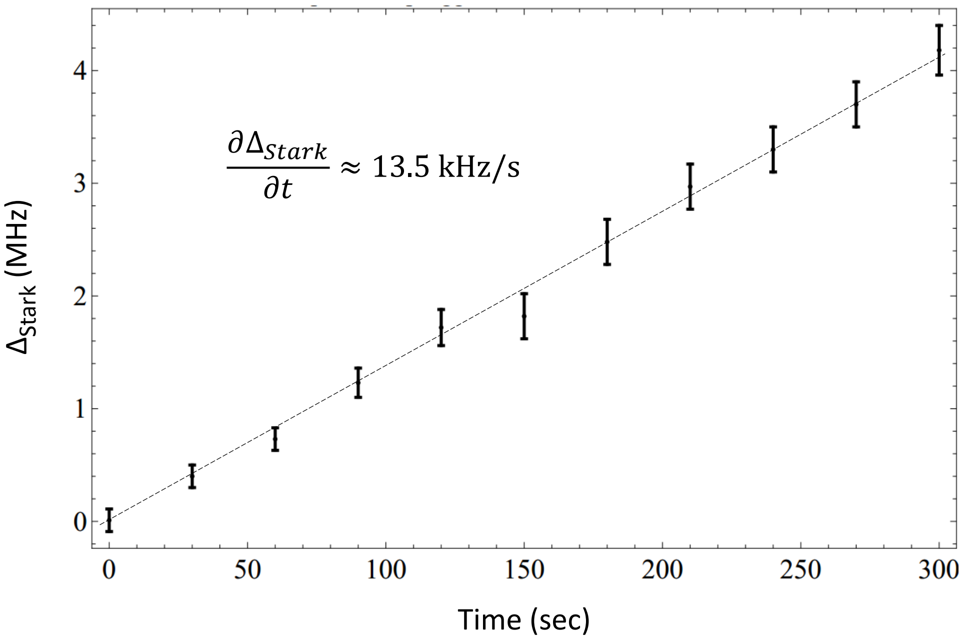

Figure 5.8: Stark splitting between $\mathcal{N}$ levels as a function of time after the electric field plates are disconnected from their voltage source. The linear drift corresponds to a maximum leakage current of 1.2 pA across the field plates.

magnetic shields. Cosine theta coils [86] on both sides of the vacuum chamber apply the primary magnetic field along $\hat{z}$. Additional coils near the end of the vacuum chamber apply a compensating field along $\hat{z}$ which minimizes $\partial\mathcal{B}_z/\partial x$ during normal operating conditions (see Figure 5.10). A pair of Helmhotz coils allow $\mathcal{B}_x$ to be applied as a systematic check. Similarly, four separate pairs of Helmholtz coils located above and below the vacuum chamber provide B_y, and three separate gradients of B_y, as a systematic check. The magnetic coil assembly was designed and constructed by Emil Kirilov.

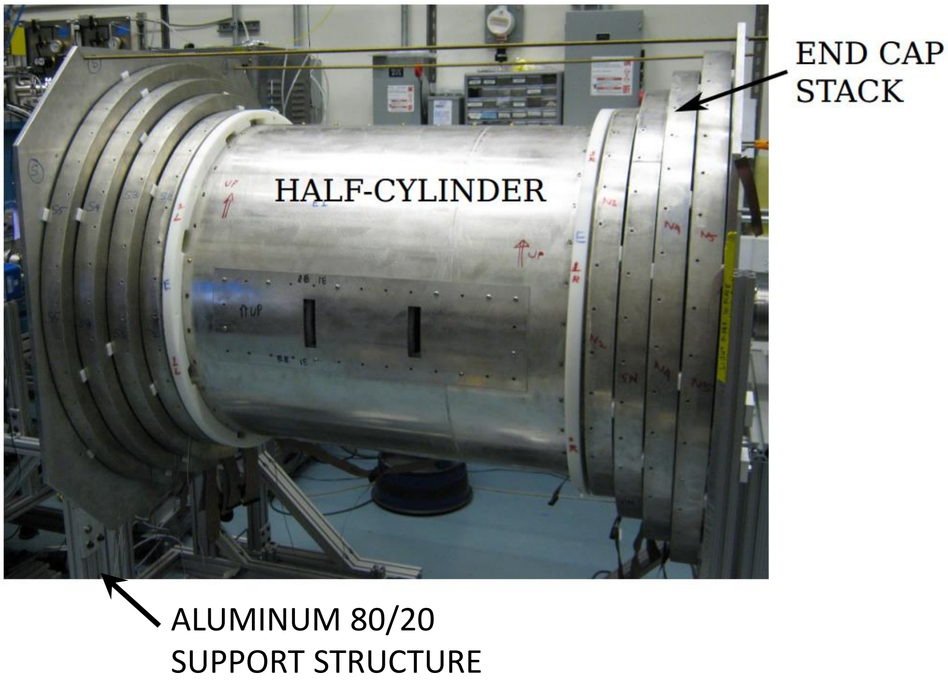

Figure 5.9: Photograph of magnetic shields. The smallest of five cylindrical shields is shown, along with five pairs of end caps mounted to an aluminum 80/20 structure mechanically decoupled from the vacuum chamber.

Five nested cylinders of mu-metal magnetic shielding surround the interaction

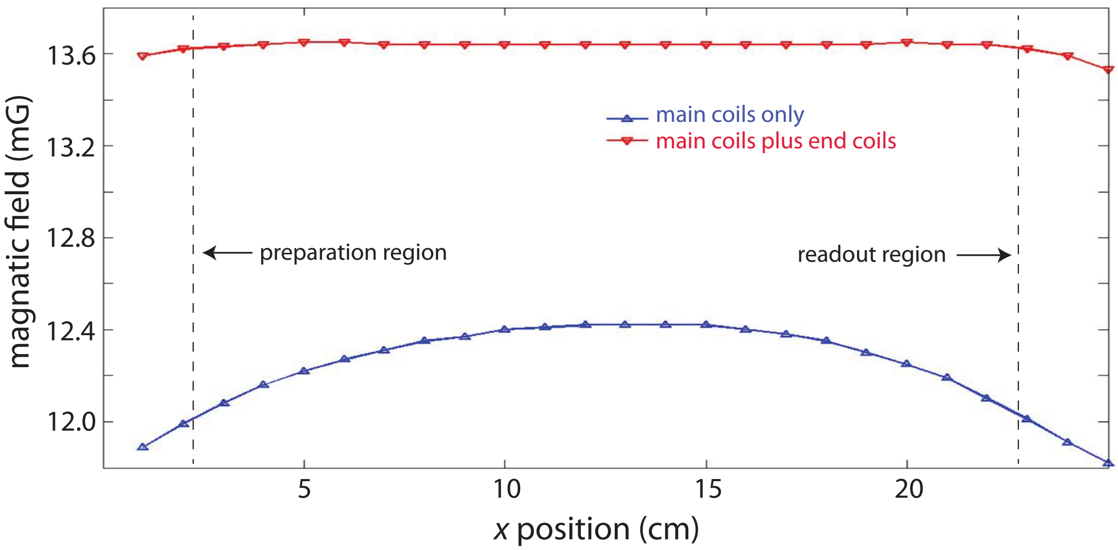

Figure 5.10: Magnetic field in the $\hat{z}$ direction between the preparation and readout regions, as measured with a fluxgate magnetometer. The field gradient along the molecule beam line is much smaller with the addition of the end coils.

region to minimize stray magnetic fields. Each layer consists of two circular end caps and two half cylinders, as shown in Figure 5.9. The four pieces are connected with small non-magnetic brass screws. The shields are supported by an aluminum 80/20 stand mechanically decoupled from the vacuum chamber. Degauss coils (40 turns) loop around the bottom of each shield layer. Estimates typically predict that each mu-metal layer should suppress an external field by a factor of 10, for a total suppression factor of 10^5. External fields in the laboratory are no higher that 1 G, so stray fields in the interaction region should be less than 10 mG.

Once sufficient EDM data had been gathered, the magnetic field along all three laboratory axes was measured. Magnetic field data was gathered with a small three-axis magnetometer carefully inserted between the electric field plates and then moved along the molecule beam line. An unexpected $\sim$600 mG field along $\hat{y}$ was observed. This field were caused by frozen-in magnetization in the magnetic shields that was not taken out by the degaussing procedure because of insufficient degaussing current. The field was removed by increasing the degauss current by a factor of three. As we discuss in Chapter 7, we used intentional parameter exaggeration to show that this stray field did not affect the EDM measurement above the level of 10^{-30} e cm. Elizabeth Petrik and Brendon O'Leary built, automated, and aligned the translation stage used to hold the magnetometer.

5.3.4 Fluorescence Collection Optics

Molecule fluorescence is collected in the readout region by eight identical pairs of high numerical aperture lenses, each focusing light onto 1 cm fiber bundles (Figure

5.4). The eight fiber bundles are then combined into two separate 1.5 cm fiber bundles which couple to two 1.5 cm light pipes. The light pipes then pass through the vacuum chamber and connect to PMTs (Hamamatsu 8900U-40). To filter out laser and background light, 690 nm bandpass filters (Semrock FF01-689/23-25-D) are placed between the end of the light pipes and the PMTs. High-vacuum compatible optical coupling gel (Dow Corning Q2-3067) is used to maximize the coupling efficiency between fiber bundles and light pipes. Four lenses are held on either side of the electric field plates by an aluminum mount fixed to the same baseplate as field plates. The fluorescence collection system was designed and built by Nick Hutzler.

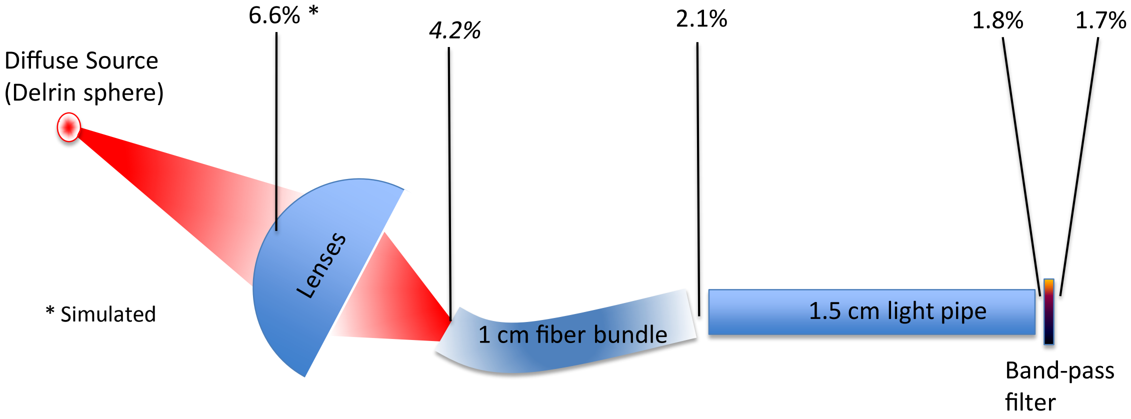

Figure 5.11: Measured fraction of total emitted fluorescence at different points in the fluorescence collection system. Only one of the eight identical optics assemblies is shown.

I assembled, tested, and optimized the fluorescence collection system before installing it in the vacuum chamber. For the test setup I mounted uncoated 1.25 cm glass plates, similar to the actual field plates, on a baseplate identical to that used in the vacuum chamber. To simulate diffuse molecule fluorescence, an optical fiber was inserted into a 1 cm diameter Delrin ball, which was then positioned between the glass plates. The 690 nm light coupled into the fiber was modulate at 50 Hz by a chopper wheel. The total diffuse output light was measured with a large area photodiode (Hamamatsu S3584). The lens assembly was then positioned on the base plate so as to maximize the light after the second lens, measured by the same photodiode. The position of each fiber bundle behind the second lens was optimized to maximize fiber bundle output light. Figure 5.11 indicates the typical fraction of total light measured after each segment of the collection optic assembly. The largest losses are from the solid angle of the large lenses and the packing ratio (65%) of the fiber bundles.

The collection efficiency is ∼30% higher when exciting through the positive parity (lower energy) C state, rather than the negative parity (higher energy) state, as illustrated in Figure 5.2. This is due to the fact that the only detectable decay from the positive parity state is to $|X, J = 1, M_J = \pm 1\rangle$. The resulting $M_J = \pm 1$ fluorescence is preferentially distributed along the lab $\hat{z}$ axis [66, 87], where the collection optics are most densely packed. On the other hand, the negative parity state decays to $|X, J = 1, M_J = 0, \pm 1\rangle$ and $|X, J = 0, M_J = 0\rangle$. The combined decay is preferentially distributed in the plane of the field plates, where there are no collection optics.

5.4 Lasers and Optics

The EDM measurement requires lasers at several different wavelengths to manipulate the quantum state of ThO molecules. Conveniently, all required ThO transitions (690 nm, 943 nm, and 1090 nm) can be accessed with commercially available laser diodes. External cavity diode lasers used for the spin precession measurement are housed and frequency stabilized in Professor Gerald Gabrielse's "Laser Lab" in Jefferson 162. Laser light is then transported through 100 m polarization-maintaining (PM) fibers to the main experiment in LISE G14. There laser light is amplified, frequency shifted with a series of acousto-optic modulators (AOMs), and directed into the interaction region through an assembly of optics that precisely controls the laser beam shape, pointing, and polarization. Figure 5.12 provides an overview of the laser and optics apparatus.

The requirements for each laser are based on ThO branching ratios and properties of the molecule beam. The lasers must be frequency stabilized below the molecule beam Doppler width (1.5 MHz). The laser beam must be stretched to at least 2 cm vertically so that all molecules experience roughly equal laser intensity. Similarly, the horizontal laser beam width must be at least 2 mm so that the molecule-laser interaction time is much longer than the ThO excited state decay time. As discussed in the previous chapter, the laser power required to saturate and power-broaden the ThO transition depends on the branching ratios between different electronic transitions. For the stronger 690 nm transition, $\sim$10 mW laser power is sufficient. However, $\sim$3 W is required to saturate the 1090 nm transition, and $\sim$100 mW is required for the 943 nm transition.

5.4.1 Frequency Stabilized Diode Lasers

The 1090 nm and 943 nm lasers used in the interaction region were purchased from Toptica (SYST DL Pro 940 and 1090-custom), while the 690 nm lasers used for rotational cooling were built in-house in Littrow configuration (Thorlabs diode

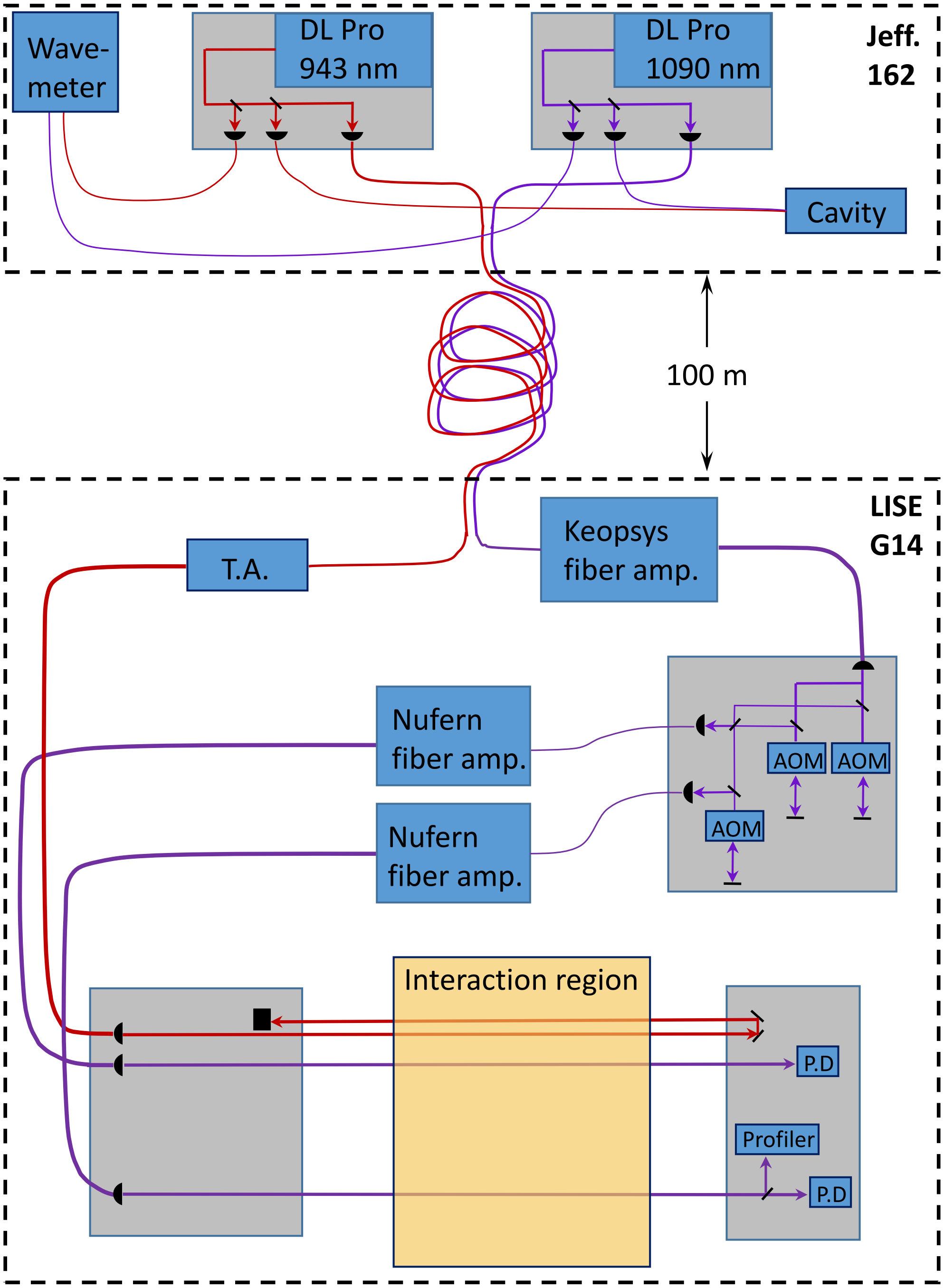

Figure 5.12: Overview of laser and optics apparatus. Light from 943 nm and 1090 nm commercial lasers in Jefferson 162 is transmitted to LISE G14 through long fibers. Light is then amplified, and in some cases frequency shifted, before entering the interaction region. Line thickness indicates laser power.

HL6750MG). A complete set of homemade lasers built by Yulia Gurevich (690 nm, 908 nm, 943nm, and 1090 nm) served in development experiments and then as backup lasers [49]. The 943 nm DL Pro was originally purchased with an AR coated diode with 905-950 nm tuning range. This diode did not provide sufficient power to seed the 943 nm tapered amplifier, so I replaced it with a higher power non-AR coated diode (Roithner Lasertechnik RL T940-300GS) that provided ∼100 mW output power. I also installed Toptica DigiLock modules in the laser controllers to allow for remote control of the laser current, temperature, and piezo voltage. The rotational cooling lasers were located in LISE G14 and the interaction region lasers were located in Jefferson 162.

All lasers were surrounded by identical arrangements of optics on 1 × 2 ft breadboards. This allowed for easy rearrangement and/or stacking of lasers. The optics assembly, shown in Figure 5.13, consists of a pair of beam shaping anamorphic prisms, an isolator, 5% pick-off windows, and three fiber couple ports. A multi-mode fiber sends 5% of light a HighFinesse wavemeter (WSU-30) in Jefferson 162, and a single-mode mode fiber sends light to a frequency locking cavity. A polarization-maintaining single-mode fiber sends the remaining laser light to an amplifier in LISE G14 or, in the case of the 690 nm lasers, directly to the experiment.

To stabilize the laser frequency to ∼1 MHz, light from each laser is coupled into a 750 MHz free spectral range confocal Fabry-Perot cavity made of Invar [49, 88]. The cavity mirrors (Layertec 102965) have high reflectivity (> 99.8%) over the 630-1100 nm wavelength range. A ring piezo (Noliac CMAR03) attached to one cavity mirror allows for scanning of cavity length. The cavity is housed in an evacuated

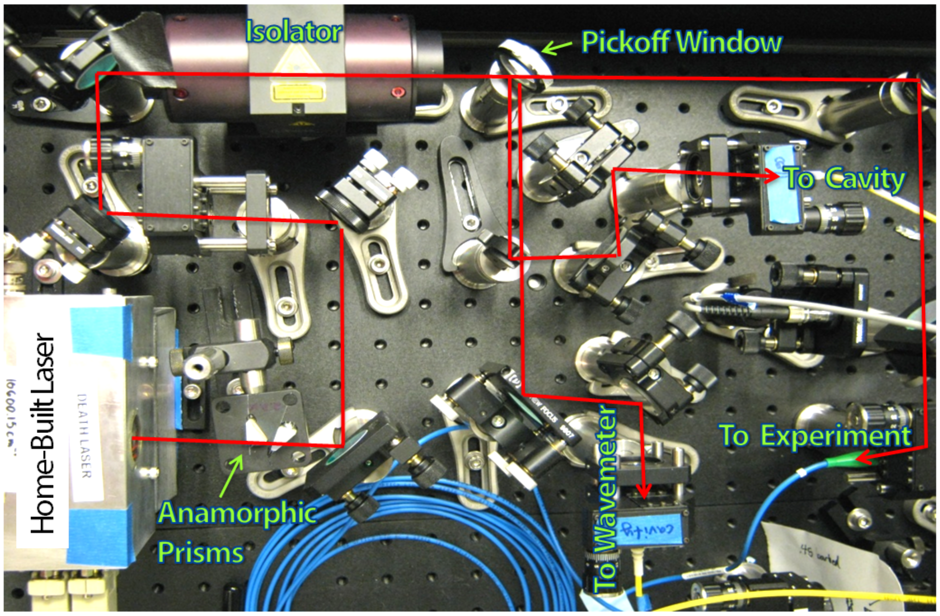

Figure 5.13: Typical optical layout surrounding each diode laser. Light from the laser is sent to the experiment, a Fabry-Perot cavity, and a wavementer. Here a home-built external-cavity diode laser is shown.

KF-50 vacuum tube to minimize vibration and thermal drift. Before entering the cavity, multiple laser beams are combined with a series of dichroic beam splitters and polarizing beam splitters. An identical arrangement of beam splitters separates each laser beam after the cavity, directing each beam in to a different photodiode (Thorlabs PDA36A). A Labview servo program monitors the time during the cavity scanning cycle when each laser comes into resonance with the cavity. If the peak position in time drifts the program adjusts the laser grating piezo voltage to correct the laser frequency. The cavity length is itself locked to an iodine clock, with ∼10 kHz frequency stability, inherited from the Gabrielse precision helium spectroscopy experiment [74]. Separate cavities in LISE G14 and Jefferson 162 lock the rotational cooling and interaction region lasers, respectively. Typically lasers in Jefferson 162 remain locked for 2-3 days while lasers in LISE G14 remain locked for ∼12 hours. The cavity, optical setup, an Labview servo programs were developed and built by Yulia Gurevich [49].

5.4.2 Fiber Pathway

Many 100 m long fiber optic patch cables allow laser light to be transported between the Jefferson and LISE laboratories. In total, we installed 12 multi-mode fibers (L-com SP57692), six single-mode PM fibers (OZ Optics PMJ-3A3A-λ-4/125-3-100, where λ = 633 nm, 780 nm, 850 nm, and 1060 nm), and three single mode non-PM fibers (OZ Optics SMJ-3A3A-λ-4/125-3-100, where λ = 633 nm, 850 nm, and 1064 nm). Multi-mode fibers allow the HighFinesse wavemeter to monitor lasers housed in LISE. They are also used to connect computers between labs with fiber-optic ethernet ports. Single-mode fibers transport laser light to be directly used in the EDM measurement. All 21 fiber-optic cables are laid within a 1.5 inch diameter flexible conduit.

Because the single-mode fibers were so long, OZ Optics did not specify a transmission efficiently or polarization extinction ratio (ER)[3]. In general, we required the long fibers to have transmission efficiency greater than 60% and ER greater than 100, with less than 1% added intensity noise. These requirements were based on the seed requirements of the laser amplifiers located in LISE G14. With < 10 mW input light, I measured the fiber transmission efficiency to be 60% for 690 nm, 75% for 943 nm, and $> 80\%$ for 1090nm. Additional 20% losses were observed at fiber-fiber connections at either end of the 100 m path cables, if optical coupling gel was not used. For 1090 nm light, I measured ER > 700, which is not significantly worse than the specified ER of 10 m patch cables. With < 10 mW input light the amplitude noise through the 100 m fibers, measured as the ratio of AC power fluctuations to DC power level, was $< 10^{-4}$. With vigorous shaking of the fiber this noise increased to $\sim 10^{-3}$. I observed increased noise and decreased transmission efficiency at higher input power levels, due to stimulated Brillouin scattering. With 120 mW input light the transmission efficiency decreased to $\sim 40\%$ with $> 10\%$ power fluctuations that degraded the performance of the laser amplifiers seeded by the long fiber output light.

---

[3] The extinction ratio is typically defined as the intensity of light polarized along the fiber PM axis divided by the intensity of light with off-axis polarization.

5.4.3 Tapered and Fiber Amplifiers

Because transmission through the 100 m fiber pathway is limited by stimulated Brillouin scattering to < 100 mW, laser light must be amplified in LISE G14. A commercial tapered amplifier (Toptica SYS-BoosTA-L-940) is used to amplify 943 nm light, producing ∼400 mW output power with 30 mW seed power. Only 75% of this light survives the output isolator due to the inherently low extinction ratio and non-Gaussian beam profile of tapered amplifiers [89]. At best, 50% of the output light can be coupled into the single-mode fiber that transfers light to the interaction region. Typically, 120 mW of 943 light, more than enough to power broaden the $H \rightarrow A$ transition to 4 MHz, reaches the interaction region.

The 1090 nm light is amplified twice in LISE G14 by ytterbium doped fiber amplifiers before entering the interaction region. First, a Keopsys (KPS-BT2-YFA-1083-SLM-PM-05-FA) amplifier, seeded with > 5 mW from the 100 m fiber, outputs 250 mW of light onto the "High-$\mathcal{E}$" AOM assembly. Five percent of the output light is split off to seed an identical fiber amplifier which outputs light onto the "Low-$\mathcal{E}$" AOM assembly. The AOM assemblies output 1.5-2.5 mW for the readout beam, and 5 mW for the state preparation beam. State preparation and readout beams are separately amplified by identical Nufer fiber amplifiers (PSFA-1084-01-10W-1-3) that use double-clad fiber technology. The readout and preparation Nufern amplifiers output 3 W and 4 W, respectively. Both amplifiers are capable of producing laser powers up to 10 W, but we run with lower power to minimize laser-induced thermal heating of the field plates, as discussed in Chapter 7. Nufern output power drift of ∼5% is typical on one hour timescales. These amplifiers servo their internal pump laser power so that their output power is fairly independent of seed power. A 500% change in seed power causes an output power shift of only 5%. I measured the time constant of this servo to be $\sim$30 μs. I built a $\sim$2 W 1090 fiber amplifier, also based on ytterbium-doped double-clad fiber, which was initially used as the readout laser before the Nufern amplifiers were purchased. This amplifier was later used in Paul Hess's Raman spectroscopy measurements of the non-reversing electric field [71].

5.4.4 AOM Breadboard for Frequency Switching

A series of AOMs, controlled with automated RF sources (Nova-Tech 409-B) switch the laser frequency between four possible $|H, \mathcal{N} \pm 1\rangle \rightarrow |C, \mathcal{P} \pm 1\rangle$ transitions [71]. Separate assemblies, "High-$\mathcal{E}$" and "Low-$\mathcal{E}$", are required for to match the $\mathcal{N}$ level Stark splitting of the two different electric fields, $\mathcal{E} = 141.5$ mV/cm and $\mathcal{E} = 36$ mV/cm, used in when gathering EDM data. Each assembly contains two double-passed AOMs that shift the laser frequency up/down to match the $\mathcal{N}$ level Stark splitting. These are followed by one double-passed AOM that provides an additional frequency shift to drive to one of the two C parity states. State preparation light is fiber-coupled before the final AOM, since the preparation beam always drives to the lower parity state of C. Readout light is fiber coupled after the final AOM. Emil Kirilov assembled the first High-$\mathcal{E}$ frequency-switching AOM assembly. It was later rebuilt and modified by myself and then Brendon O'Leary to improve overall transmission efficiency. Brendon al who also built the Low-$\mathcal{E}$ AOM assembly.

Four separate laser frequencies are produced by the AOM assembly to drive the four possible $|H, N = \pm 1\rangle \rightarrow |C, \mathcal{P}\pm\rangle$ transitions used for the EDM measurement.

Each possible laser frequency corresponds to a separate beam path in the AOM assembly. These beam paths are well-aligned with each other so that the readout light seeding the Nufern amplifier is between 1.5 mW and 2.5 mW for all possible frequencies. Similarly the two preparation beam paths are aligned so that 5-7 mW is transmitted to the Nufern amplifier. When the power or fiber couple incidence angle is significantly mismatched we observed the pointing and/or power of the readout beam propagating through the interaction region to vary between the four possible laser frequencies (see Chapter 7 for more detail).

5.4.5 Coupling Lasers into Interaction Region

After the amplifiers, 943 and 1090 nm laser beams pass through a number of optical components before entering the interaction region (Figure 5.14). These optics serve to precisely control the polarization, pointing, and shape of the laser beams. A majority of the optics sit on a rigid 2 × 3 ft honeycomb breadboard, supported by an aluminum 80/20 frame on casters. The entire frame can be moved from one side of the interaction region to the other, as is necessary to reverse laser propagation direction, $\hat{k}$, for systematic error suppression (see Chapters 6 and 7). Other optics sit on a smaller 1 × 2 ft honeycomb breadboard that sits on the opposite side of the interaction region.

Readout Laser

Output light from the readout laser amplifier is coupled directly onto the 2 × 3 ft breadboard. The collimated beam passes through a 30 dB isolator before entering an AOM (A1) that provides power modulation. The RF powering this AOM is off during normal operation, but can be correlated with parameter switches to study systematic effects, as described in Chapter 7. Next the beam enters a series of two identical AOMs, A2 and A3 (IntraAction ATM-80/A2), connected to an 80 MHz RF source (PTS 160). A gate and delay generator (SRS DG645) and two RF switches (DigiKey ZWSW-2-50DR) rapidly switch the RF on and off so that A2 and A3 are never both on at the same time. Diffracted light from A2, also called the $\hat{Y}$ beam, is picked off by a half-mirror and directed through a half-waveplate which rotates the polarization by 90 degrees. Light that is not diffracted by A2 passes through to A3. Diffracted light from A3, the $\hat{X}$ beam, passes through a 1 mm iris to a high ER polarizing beam splitter (Thorlabs GL15-C) where it is combined with the $\hat{Y}$ beam, as shown in Figure 5.14. Light that is not diffracted by either A2 or A3 is blocked by the 1 mm iris. The RF switch is timed such that first the $\hat{X}$ beam is on for 3.8 μs. This is followed by a 1.2 μs period where both beams are off. Then only $\hat{X}$ is on for 3.8 μs, which is again followed by a 1.2 μs period with both beams off. The entire polarization cycle repeats every 10 μs.

After $\hat{X}$ and $\hat{Y}$ beams are combined on a polarizing beam splitter, a half-waveplate (CVI QWPO-1090-05-2-R10) on an automated rotation stage (Newport URS50BCC) adds an identical polarization offset to both readout beams. This rotation stage and waveplate provide the polarization rotation required to measure fringe contrast, as described in Chapter 6. After the waveplate are two pairs of cylindrical lenses which expand the laser beam by 4x in the horizantal direction and 30x in the vertical direction. The final stretched Gaussian beam width is 4.5mm × 30 mm (13.5% full

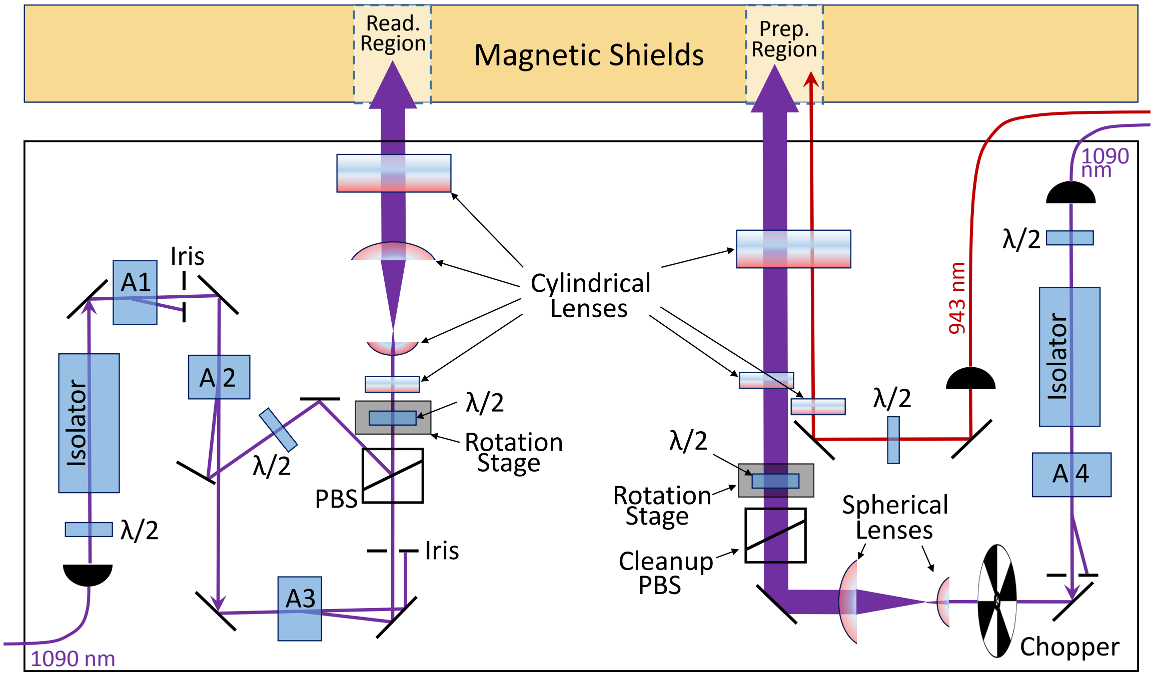

Figure 5.14: Layout of optics that launch 943 nm and 1090 nm preparation and readout lasers into interaction region. The optical assembly allows laser polarization, pointing, and beam shape to be precisely controlled.

width). After the final lens the readout beam passes through holes in the magnetic shields and enters the vacuum chamber. On the opposite side of the interaction region the power and position of the readout beams are monitored with a beam profiler (Thorlabs BC106-VIS) and photodiode (Thorlabs PDA10A).

Roughly 3 W of 1090 nm light exits the Nufern amplifier, which is set to 45% power through the Nufern control program. About 1.9 W enters the interaction region after isolator and AOM transmission losses. Each electric field plate transmits ∼90% of 1090 nm light, and the vertical tails of the Gaussian beam are clipped by the vacuum windows. I typically measure readout laser powers of 1.2 W on the opposite side of the interaction region.

Preparation Laser

The preparation laser optical setup is similar to that of the readout laser, except that no polarization switching AOMs are required. Also, the beam expansion lenses consist of a pair of spherical lenses (magnification of 5x) followed by a pair of cylindrical lenses (vertical magnification 4x). The first spherical lens is angled by ∼15 degrees to induce significant spherical aberration on the expanded laser beam, shown in Figure 7.6C. The flat surface of the first lens faces the incident laser beam, a configuration that maximizes spherical aberration. The spherical aberration produces a sharp cutoff on side of the laser beam that the molecules encounter last. This sharp cutoff helps to minimize systematic EDM effects caused by ac Stark shifts, as discussed in Chapter 7 (see Figure 7.5). The polarization of the preparation laser, determined by a half waveplate in an automate rotation state, is also chosen to minimize ac Stark shift effects, as shown in Figure 7.5.

An AOM (A4) allows for correlated power modulation for systematic studies. The Nufern amplifier, set to 60% through the control program, produces 4 W of preparation light. Preparation laser power is also monitored with a photodiode on the opposite side of the interaction region.

943 nm Laser

No polarization control is needed for the 943 nm laser before it passes through the interaction region. However, on the opposite side of the interaction region the 943 nm laser polarization is rotated by 90 degrees and retro-reflected back through the interaction region. This doubles the numbers of molecules transferred to the ThO H state by allowing the laser to drive two of three M_J sublevels of $|X, J = 1\rangle$ to $|A, M_J = 0\rangle$. The 943 nm lasers are vertically, but not horizontally, stretched (vertical expansion 15x) by a pair of cylindrical lenses, one of which is shared with the 1090 preparation laser setup (see Figure 5.14). The 943 nm beam entering the interaction region is 2 mm wide. The retro-reflected beam is spaced 3 mm downstream from this beam. The the 1090 nm preparation beam is spaced 5 mm downstream from the retro-reflected beam. The spacing between the three laser beams is set to allow ThO population to completely decay from the excited optical pumping state before encountering the next laser. Roughly 110 mW of 943 nm light enter the interaction region, and 80 mW are retro-reflected after attenuation from field plates.

Alignment Procedure

Ideally the laser propagation direction would be along the molecule quantization axis, $\hat{z}$, perpendicular to the electric field plates. I utilized the 5-10% back reflection from the ITO field plate surface to align the lasers. When I directed red laser light into the interaction region, four reflected beams, one from each vacuum window and ITO surface, were clearly visible. The ITO reflections can be identified by their close proximity to one another. The beam pointing is adjusted so that the reflected and incident beams overlap, ensuring the that beam is perpendicular to the ITO surface. The beam, which is launched from a two-axis translation stage, is also centered on the interaction region windows. Once the beam is fully aligned, reference markings are made on both sides of the the magnetic shields to indicate the laser position before and after the vacuum chamber. The expanded 1090 nm and 943 nm beams are then aligned using these reference markings. I used the same alignment procedure for preparation and readout laser regions. Using this procedure the lasers were aligned perpendicular to the field plates to within 1 mrad.

To align the $\hat{X}$ and $\hat{Y}$ readout beams to each other, I used a beam profiler to measure the horizontal and vertical position of each beam to within 10 μm before and after the interaction region. Typically the $\hat{X}$ beam is first aligned to $\hat{z}$ using the reference markings on shields. The PBS and $\hat{Y}$ pick-off mirror provide the necessary degrees of freedom to align the $\hat{Y}$ beam to the $\hat{X}$ beam. The pointing of the $\hat{X}$ and $\hat{Y}$ beams were typically aligned to within 0.1 mrad while EDM data was being taken.

5.5 Data Acquisition System

An network of five computers, two in Jefferson 162 and three in LISE G14, control and monitor many experimental parameters and collect PMT fluorescence data. All parameter switches implemented during the EDM data set (Figure 6.4) were automated by the data acquisition system except for electric field magnitude a laser propagation direction. For each fluorescence trace the the electric field, magnetic field, and laser polarization, power, and frequency are recorded. We record both the measured value and the set value of each parameter. These values are later used in the data analysis to form switch parity components of measured precession phase. Some parameter are monitored in multiple ways. For example, in addition to measuring the current flowing through the magnetic field coils with precision resistors, we use magnetometers to directly measure the magnetic field at four different locations just outside the vacuum chamber. Additionally, we record the values of a number of experimental parameters that are not directly controlled, such as vacuum pressure, room temperature, and buffer gas cell temperature. A majority of this data acquisition system was set up by Paul Hess and is documented in his thesis [71].

Currents produced by the PMTs are converted to voltage and amplified (SRS partnumber) before being digitized (National Instruments PXI-5922). Digitized signals are then downloaded to a computer, where PMT and axillary data is stored. The precision of the digitizer is at least 20 bits and the timing resolution of the digitizer is set to 5 MHz, slightly larger that the homemade 2 MHz LC low-pass filters placed within the voltage amplifier. Because of this high resolution, running the EDM experiment for a single day yields dozens of gigabytes of data. In the following chapter we describe how terabyte of data collected over several weeks is analyzed to extract the EDM value.

The robust experimental apparatus described in this chapter provided precise control of many important experimental parameters over a broad tuning range. This allowed us to thoroughly search for a number of systematic effects, described in Chapter 7. The high molecule yields and ThO population transfer and state readout efficiencies provided by this apparatus also ensured high statistical sensitivity for the EDM measurement. Apart from replacing ThO_2 ceramic targets every two months and making slight adjustments to the optics assemblies, this EDM apparatus did not need to be altered or repaired during the two years in which we took EDM data and studied systematic effects.

Chapter 6

Data Analysis

Here we discuss in detail how to deduce the EDM value and other important quantities from the terabytes of PMT fluorescence data collected for our EDM measurement. The raw fluorescence data is made up nearly a million 9 ms long traces with 0.2 μs resolution, corresponding to 45,000 data points per trace. A trace consisting of data from twenty-five ablation pulses averaged together is collected every 0.5 s. The read-out laser polarization is rapidly switched throughout each trace, allowing us to form "signal asymmetry" measurements by comparing the fluorescence corresponding to each lase polarization. Quantities such as fringe contrast and precession phase are then calculated from this signal asymmetry. Finally, multiple phase measurements, taken under different experimental conditions, are combined to extract the EDM value and important quantities. We also describe the data cuts used to ensure that only data gathered in appropriate experimental conditions was for the EDM measurement.

6.1 Signal Asymmetry

6.1.1 Rapid Switching of Laser Polarization

The molecular spin precession phase is read out by exciting the $H \rightarrow C$ transition with linearly polarized light and monitoring the resulting fluorescence. The readout laser is rapidly switched between orthogonal polarizations, $\hat{X}$ and $\hat{Y}$, to produce maximum fluorescence and to normalize against molecular flux variations. As described in our previous journal article [66], shot-noise limited phase measurements can be achieved in our apparatus by switching the laser polarization faster that the maximum rate of ThO flux variation, ∼5 kHz. We chose to operate with 100 kHz polarization switching rate, well above the rate of signal fluctuations. This switching rate, which corresponds to 5 μs of $\hat{X}$ polarized light followed by 5 μs of $\hat{Y}$ polarized light, allows molecules to experience both laser polarizations during the ∼20 μs fly-through interaction time with the readout laser. This produces twice the total fluorescence than that produced when the molecules only experience one laser polarization.

The rapid switching of the laser polarization results in a modulated PMT fluorescence signal, F, as shown in Figure 6.1A. Immediately after the laser polarization is switched, the fluorescence signal increases linearly proportional to Γ, where Γ is the $H \rightarrow C$ excitation rate and γ is the rate of C-state decay, $\gamma \approx 2$ MHz [71], predominantly to the ThO ground state. The signal then decays with rate $\gamma/2$ to a stead state, due to additional molecules entering the laser region. Lastly, the signal decays with rate γ after the laser is turned off for a period of 1.2 μs to minimize the amount of overlapping residual fluorescence (see Chapter 7.2.2 for complete rate equations). The modulated signal is also affected by a 2 MHz low pass filter, intentionally matched to the C state lifetime, in the voltage amplifier connected to the PMT.

In addition to the ThO fluorescence signal, the raw PMT signal, S, contains a background signal, B, produced by scattered laser light, room light, and PMT dark counts. This background must be subtracted to accurately determine the fluorescence produced by each polarization state, $F = S - B$. For this reason, 9 ms of data are collected for each molecule pulse, even though the molecule pulse only lasts for $\sim$3 ms. The first millisecond of data, which contains no fluorescence signal, is used for background subtraction. Figure 6.1B shows a typical background signal with modulation caused by the readout laser.

As shown in Equation 3.14 signal asymmetry, $\mathcal{A}$, is computed by comparing the fluorescence produced by $\hat{X}$ polarization, F_X, to that of $\hat{Y}$ polarization, F_Y. For each laser polarization cycle, we sum over a specific time window, or "polarization bin", to determine F_X and F_Y. A typical polarization bin in illustrated in Figure 6.1A-B by the red and blue coloring. The background data, B_X and B_Y, is also summed over the same polarization bin. As we discuss later, nearly all deduced quantities, including the EDM, were independent of the chosen polarization bin.

6.1.2 Background Subtraction

Several mechanisms in the readout region can produce a different background levels from the $\hat{X}$ and $\hat{Y}$ polarizations. First, birefringence effects in the electric field

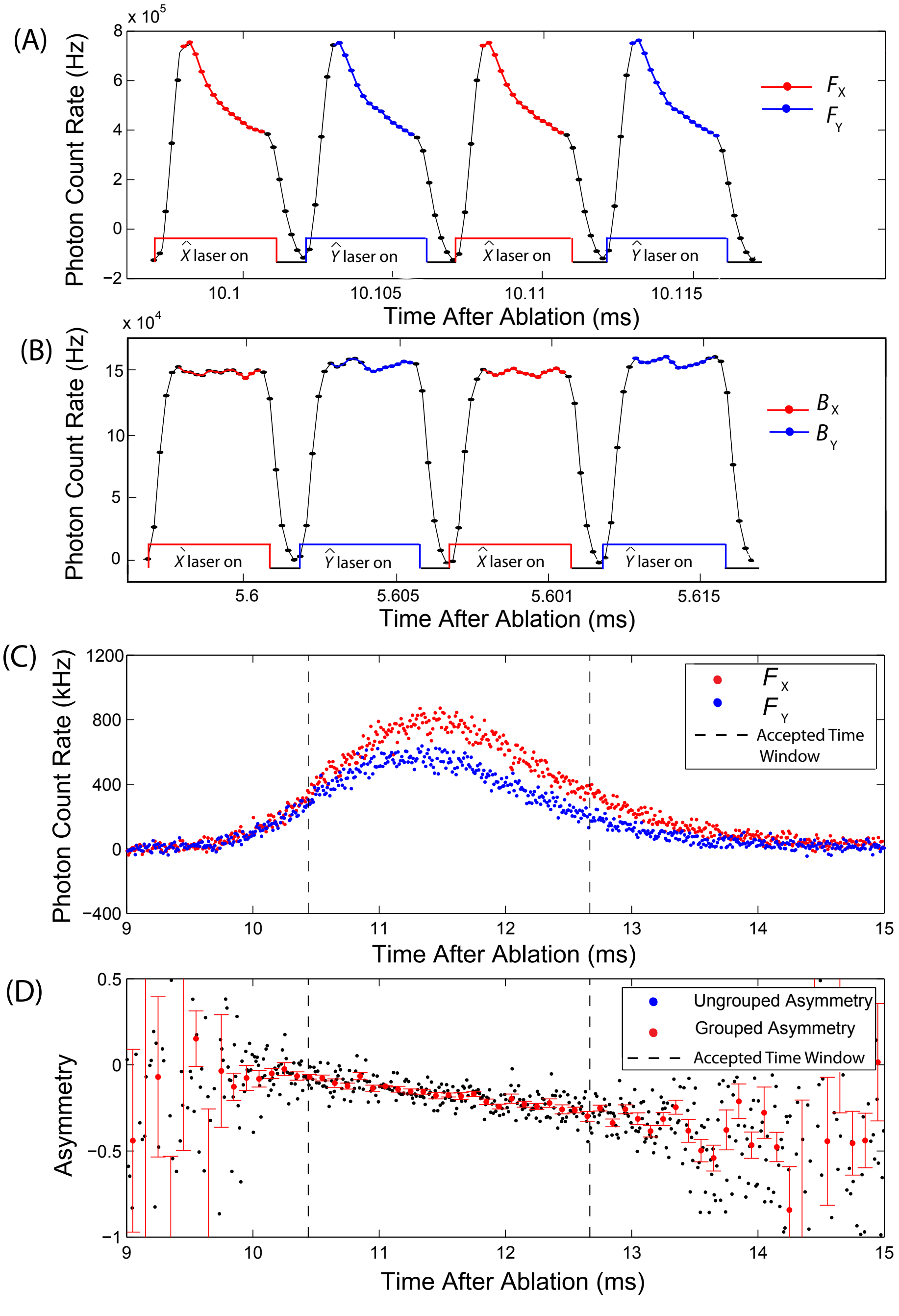

Figure 6.1: Asymmetry computed from raw fluorescence data. **(A)** Fluorescence signal from molecules for $\hat{X}$ and $\hat{Y}$ readout laser polarization. **(B)** Background fluorescence signal before the arrival of molecules in the readout region. **(C)** Fluorescence summed over each $\hat{X}$ and $\hat{Y}$ polarization bin, after background subtraction, throughout the molecule pulse. The dashed lines indicate where the mean count rate is above a fluorescence threshold. **(D)** Computed asymmetry throughout the molecule pulse. In this example, 10 asymmetry points are grouped together to compute mean and uncertainty.

plates or fluorescence collection lenses can cause more laser light from one polarization to scatter into, or be accepted by, the collection optics. As previously described, the two readout laser polarizations correspond to two separate laser beams that have been coupled through separate AOMs and then recombined. Though the properties of the two beams have been well matched, we typically measure few percent differences in the the power and profile of $\hat{X}$ and $\hat{Y}$ beams. This difference can also cause the background scatter to slightly differ between the two beams. Both mechanisms have been observed to produce an asymmetric background level. Typically the background count rate of the two read-out beams differs by a few kHz, a small fraction of the total background count rate (∼300 KHz). We tried two different background subtraction methods in our analysis. In Method 1, we subtract the $\hat{X}(\hat{Y})$ background $\bar{B}_X(\bar{B}_Y)$, time-averaged over the first millisecond of the trace, from $S_X(S_Y)$ to account for small background difference:

$$\text{Method 1}: \ \mathcal{A} = \frac{(S_X - \bar{B}_X) - (S_Y - \bar{B}_Y)}{(S_X - \bar{B}_X) + (S_Y - \bar{B}_Y)}. \tag{6.1}$$

In Method 2, we simply subtract a one time-averaged background $\bar{B} = (\bar{B}_X + \bar{B}_Y)$ from all fluorescence data:

$$\text{Method 2}: \ \mathcal{A} = \frac{(S_X - \bar{B}) - (S_Y - \bar{B})}{(S_X - \bar{B}) + (S_Y - \bar{B})} = \frac{S_X - S_Y}{S_X + S_Y - 2\bar{B}}. \tag{6.2}$$

While Method 1 might seem more thorough, we found that it caused the uncertainty of the background asymmetry to inflate the uncertainty of $\mathcal{A}$. This increased the uncertainty $\mathcal{A}$ and all quantities, including the EDM, computed from measurements of $\mathcal{A}$. The reason for this uncertainty inflation can be seen by comparing the asymmetry uncertainty, $\delta\mathcal{A}$, for both background subtraction methods,

$$\text{Method 1: } \delta\mathcal{A} \approx \sqrt{\frac{2(\delta S)^2 + 2(\delta\bar{B})^2}{(S_X + S_Y - 2\bar{B})^2} + \frac{2\mathcal{A}^2[(\delta S)^2 + (\delta\bar{B})^2]}{(S_X + S_Y - 2\bar{B})^2}}, \tag{6.3}$$

$$\text{Method 2: } \delta\mathcal{A} \approx \sqrt{\frac{2(\delta S)^2}{(S_X + S_Y - 2\bar{B})^2} + \frac{2\mathcal{A}^2[(\delta S)^2 + (\delta\bar{B})]^2}{(S_X + S_Y - 2\bar{B})^2}}. \tag{6.4}$$

Here we have made the reasonable assumption that the uncertainty of two fluorescence signals and two background signals are approximately the same, so that the combined signal uncertainty is $\delta S \approx \sqrt{2}\delta S_X \approx \sqrt{2}\delta S_Y$ and the combined background uncertainty is $\delta\bar{B} \approx \delta\bar{B}_X \approx \delta\bar{B}_Y$. The second term of Equations 6.3 and 6.4 is identical. The first term, however, is larger for Method 1, with an extra contribution in the numerator from the uncertainty in the background. Moreover, the first term is the main contributor to $\delta\mathcal{A}$ since we operate with near-zero asymmetry, $\mathcal{A} \approx 0$, which makes the second term negligible. For this reason $\delta\mathcal{A}$, and all quantities computed from $\mathcal{A}$ is always ~1.5 times larger when Method 1 is used instead of Method 2. We confirmed that the mean value of most quantities, including the EDM, did not significantly differ between the two background subtraction methods. We therefore chose to use Method 2 when analyzing our EDM data set.

6.1.3 Combining Many Asymmetry Measurements

Figure 6.1C shows F_X and F_Y as a function of time, and figure 6.1D shows the asymmetry computed from this data. The asymmetry depends linearly on time because slower molecules accumulate a larger precession phase that faster molecules in the magnetic field. A separate asymmetry measurement, $\mathcal{A}_i$, is computed every 10 μs polarization switching cycle,

$$\mathcal{A}_i = \frac{S_{x,i} - S_{y,i}}{S_{x,i} + S_{y,i}} \tag{6.5}$$

As illustrated by the window of accepted signal in 6.1C-D, $S_{X,i}$ and $S_{Y,i}$ must have an average fluorescence rate greater than 300,000 kHz for the resulting asymmetry point to be included in the analysis routine. This signal threshold, approximately the size of the background count rate, was chosen to include the maximum number of asymmetry points in our measurement, while also cutting out low signal asymmetry measurements that would add to the overall EDM uncertainty.

To determine the statistical uncertainty of the asymmetry, a number, n, of adjacent asymmetry points are grouped together. For each group we calculate the standard mean and error, depicted as red points in Figure 6.1D,

$$\overline{\mathcal{A}}_j = \frac{1}{n}\sum_{i=1}^{n} \mathcal{A}_i, \tag{6.6}$$

$$\delta\mathcal{A}_j = \sqrt{\frac{1}{n}\sum_{i=1}^{n}\left(\mathcal{A}_i - \overline{\mathcal{A}}_j\right)^2}, \tag{6.7}$$

where j denotes the position in time of the asymmetry group. This calculated uncertainty will be propagated to all quantities deduced from asymmetry. Typically, $n \approx 20$ in our analysis, and we checked that all deduced quantities did not significantly change if n were varied between 10 and 30.

6.2 Computing Contrast and Phase

According to Equation 3.14, we must not only measure the asymmetry, but also the fringe contrast, $\mathcal{C}$, and laser polarization, θ, in order to extract the precession phase, ϕ. As previously discussed, the laser polarization is measured by external polarimetry measurements [71]. Contrast is determined by the asymmetry fringe slope and can be computed by dithering the precession phase or the laser polarization, $\mathcal{C} = \partial\mathcal{A}/(2\partial\phi) = \partial\mathcal{A}/(2\partial\theta)$. We chose to dither the laser polarization because it can be dithered on a fast timescale with minimal dead time (< 1 s). Figure 6.2 shows asymmetry as a function θ. We operate the experiment at the steepest part of the asymmetry fringe and measure contrast for each asymmetry group, $\mathcal{A}_j$, by switching θ between two angles, $\theta_0 \pm \Delta\theta$:

$$C_j = \frac{\mathcal{A}_j(+\Delta\theta) - \mathcal{A}_j(-\Delta\theta)}{\Delta\theta}. \tag{6.8}$$

Because contrast is fairly constant over the duration of the molecule pulse (Figure 6.3A), we perform a weighted averaged over all $\mathcal{C}_j$ measurements within the cut region to obtain the value of $\mathcal{C}$ used to compute ϕ. We typically achieve $|\mathcal{C}| \approx 95\%$. This value is constant over a 2 MHz laser detuning range (Figure 6.3B) because the state preparation laser power broadens the $H \to C$ transition. Contrast can be positive or negative depending on the sign of the asymmetry fringe slope (Figure 6.2). Assuming that we operate near zero asymmetry, where the fringe slope is steepest, we can Taylor expand equation 3.14, to compute phase,

$$\phi_j = \frac{\mathcal{A}_j}{2C} + q\frac{\pi}{4}. \tag{6.9}$$

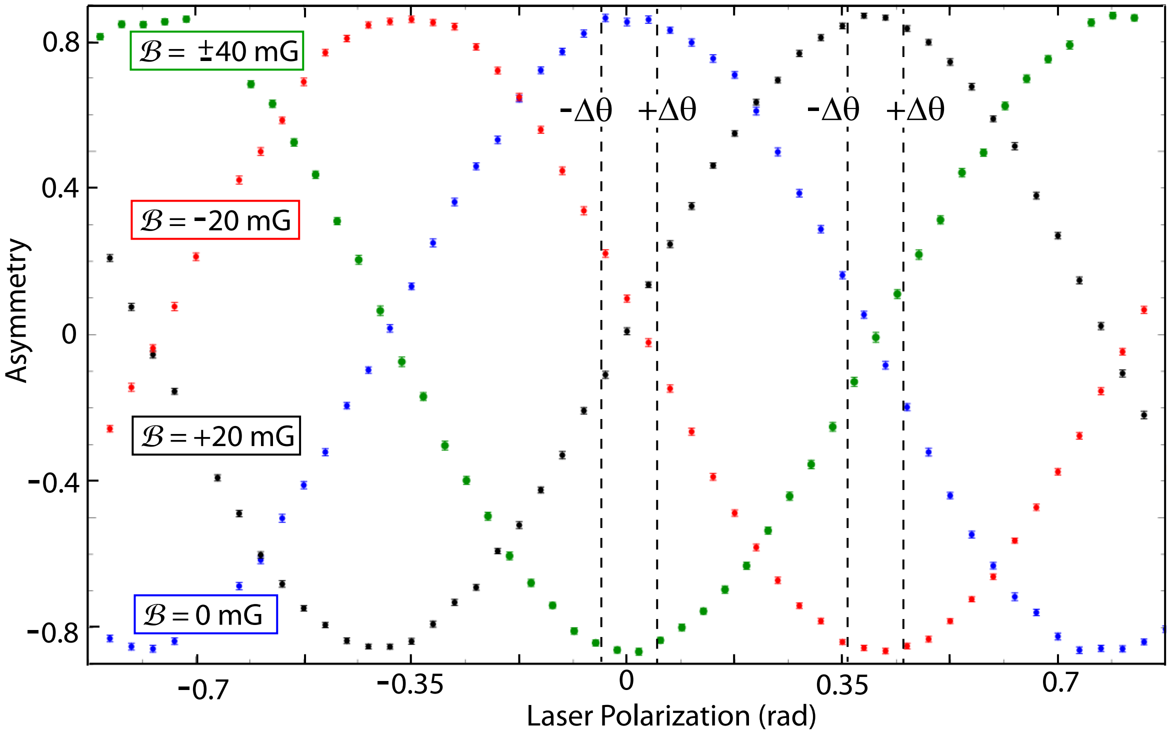

Figure 6.2: Asymmetry vs. readout laser polarization angle, θ, for several magnetic field values. The polarization is dithered by $\pm\Delta\theta$ to measure fringe contrast. To stay on othe steepest part of the fringe, we choose $\theta_0 = 0$ rad for $\mathcal{B} = \pm 20$ mG and $\theta_0 = \pi/4$ rad for $\mathcal{B} = 0$ or ± 40 mG. For this data the contrast is less the 90% due to low preparation laser power (i.e. the high power Nufern fiber amplifiers had not yet been implemented)

Here, $q = 0, 1$ or 2, corresponding to applied magnetic fields of 1, 20, and 40 mG. Figure 6.2 illustrates how different values of θ_0 must be used for different magnetic fields in order to always stay on the steepest part of the asymmetry fringe.

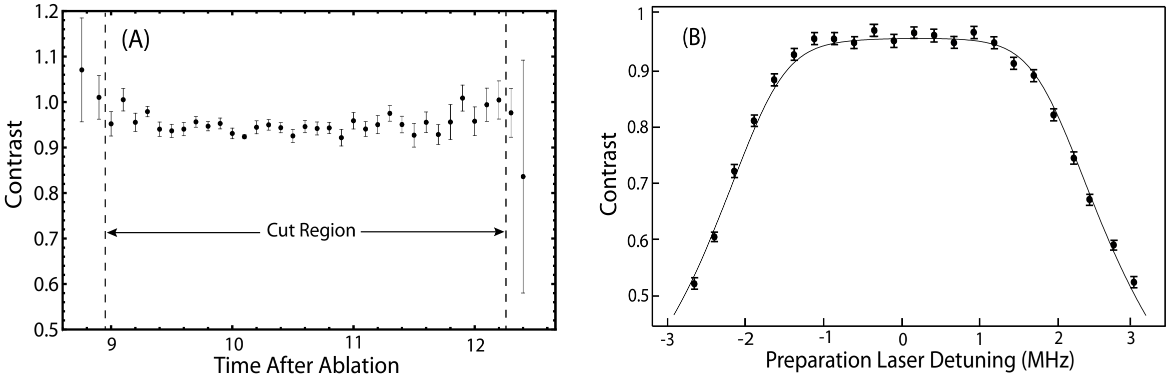

Figure 6.3: Contrast vs time after ablation **(A)**, averaged over 64 traces, and detuning **(B)**, with each point corresponding to 64 averaged traces.

6.3 Extracting the EDM and Correlated Phases

6.3.1 Parameter Switches

To measure the EDM we repeatedly measured spin precession phase with different experimental conditions. Specifically, we performed four experimental binary switches on different timescales: internal molecule alignment, $\tilde{\mathcal{N}}$ (0.5 s), applied electric field direction, $\tilde{\mathcal{E}}$ (2 s), laser polarization dither state, $\tilde{\theta}$ (10 s), and applied magnetic field direction, $\tilde{\mathcal{B}}$ (20 s). Figure 6.4A shows the timescales of these switches. $\tilde{\mathcal{N}}$ and $\tilde{\mathcal{E}}$ allow the EDM energy shift to be distinguished from background frequencies, $\tilde{\theta}$ is required to measure contrast, and $\tilde{\mathcal{B}}$ is required to measure precession time, τ, as we shall see in section 2.3.3. The data taken under all 16 experimental states derived from these binary switches constitutes a “block” of data and is sufficient to extract the EDM value.

The timescale of these four switches was chosen based on the time required to perform the switch, and on the importance of the switch to the EDM measurement. Significant dead time is required for both $\tilde{\mathcal{B}}$ and $\tilde{\theta}$, so these are chosen as slower switches. Because the EDM signal is correlated with both $\tilde{\mathcal{N}}$ and $\tilde{\mathcal{E}}$, it is important to switch these parameters on a sufficiently fast timescale to minimize the effect of molecule velocity drift on The EDM signal. Molecule beam forward velocity drift, common to ablation and buffer gas sources, is typically 1%/minute, or 2(m/s)/minute, in our apparatus. The rate of velocity change can be much larger if the ablation laser pointing is altered, so the pointing is only adjusted in between blocks of data. The velocity drift causes a corresponding drift of coherence time, τ, and precession phase. Figure 6.5 shows the typical phase drift from several hours of EDM data. Because the shot-noise uncertainty from one minute of data is always less than 1% of the total precession phase, this drift would add significant noise, and possibly a systematic offset, to the EDM measurement if $\tilde{\mathcal{N}}$ and $\tilde{\mathcal{E}}$ were not switched on timescales much faster than the velocity drift. Also, these parameters are also switched in a random order or a ABBA order to cancel out the effects of linear phaser drift.

Many other experimental parameters are also switched between different blocks of data to suppress and monitor certain systematic effects (6.4B). These include: excited-state parity addressed by state readout lasers, $\tilde{\mathcal{P}}$ (1 block, random); reversal of the leads connecting the electric field plates to their voltage supply, $\tilde{\mathcal{L}}$ (4 blocks); a rotation of the readout polarization basis by $\theta \to \theta + \pi/2$, $\tilde{\mathcal{R}}$ (8 blocks); a global

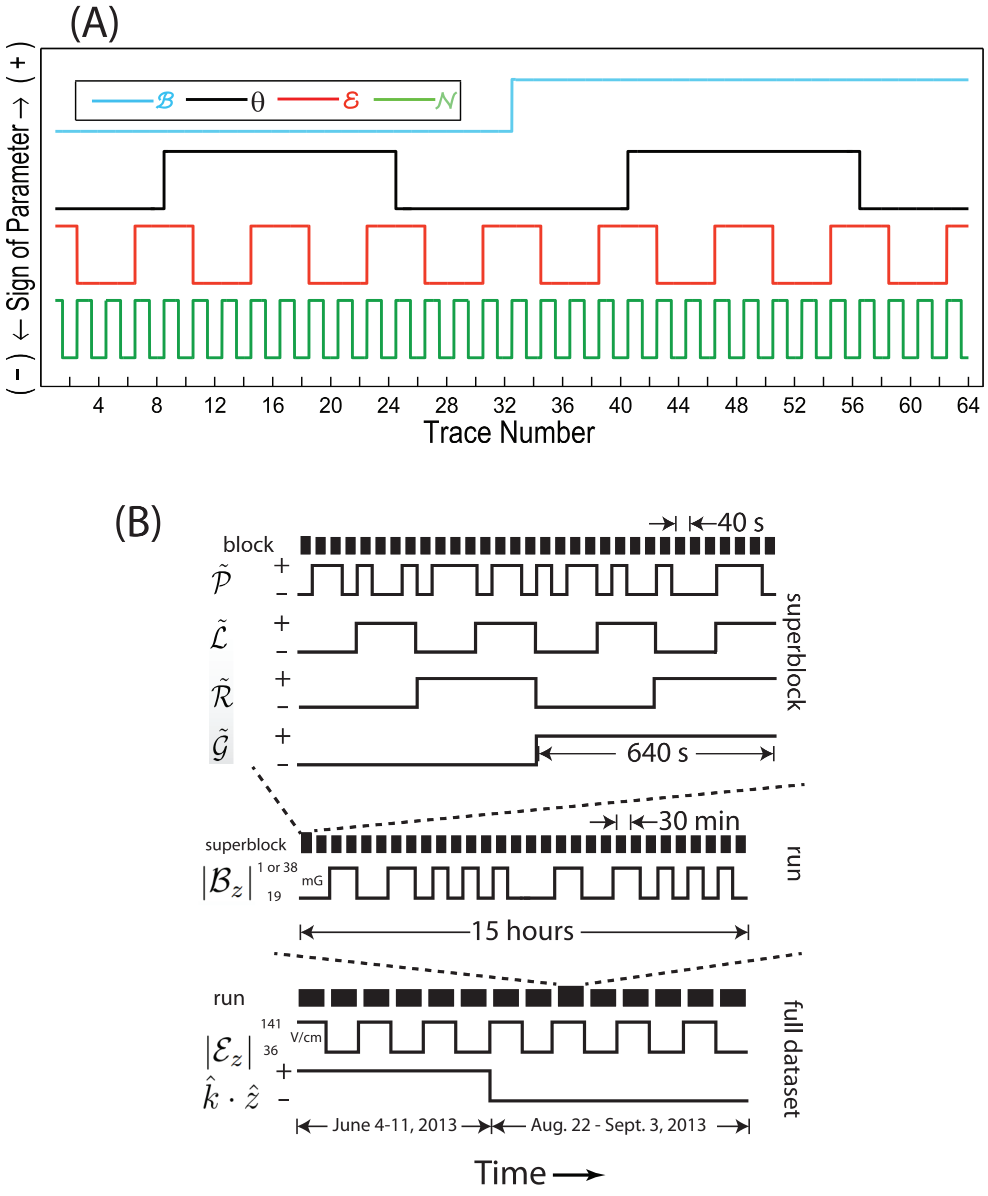

Figure 6.4: **(A)** Order of experimental switches performed within a block of data. A trace is collected every 0.5 s. **(B)** Order of longer timescale experimental switches performed between blocks of data.

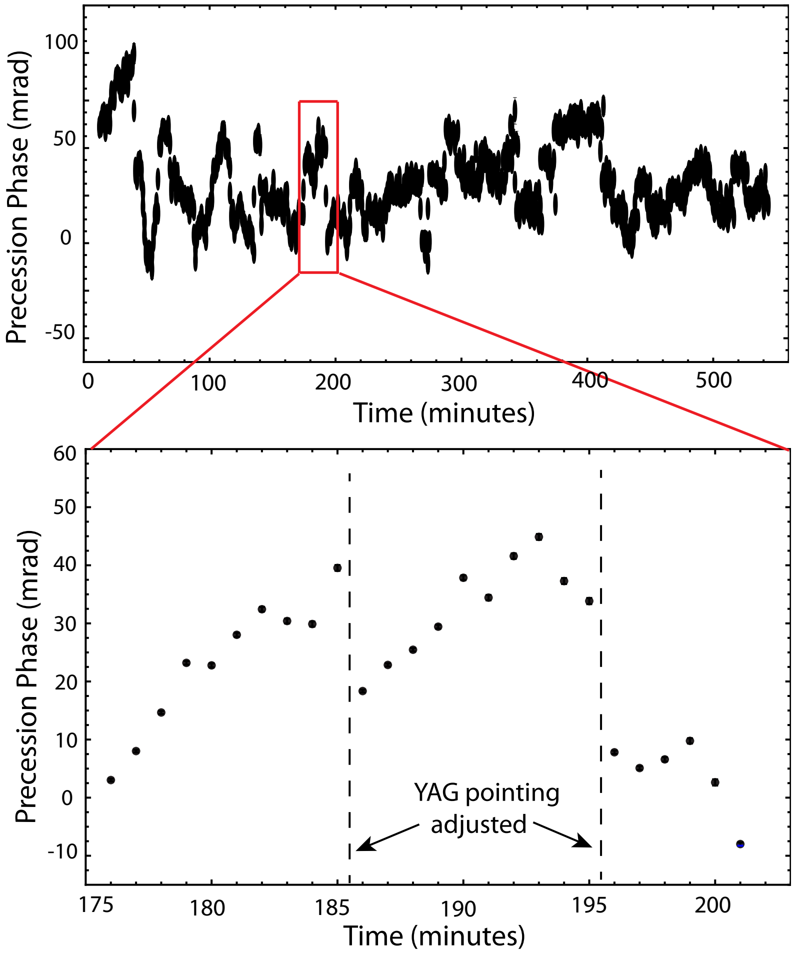

Figure 6.5: Measured phase fluctuations over time caused by molecule beam velocity fluctuations. Generally, the beam velocity slows down linearly over time for fixed ablation laser pointing. When the pointing changes, the beam velocity can change very quickly.

polarization rotation of both state preparation and readout lasers, $\tilde{\mathcal{G}}$ (16 blocks); the magnitude of magnetic field,$|\mathcal{B}_z|$ (64-128 blocks), electric field magnitude, $|\mathcal{E}_z|$ (1 day), and laser prorogation direction, $\tilde{k}$ (1 week). The motivation for each of these parameter switches is discussed in the following chapter.

6.3.2 Accounting for Correlated Contrast

It is possible for fringe contrast to differ for different experimental states. For example, if state preparation laser detuning or background fluorescence are correlated with any of the three block switches, $\tilde{\mathcal{N}}$, $\tilde{\mathcal{E}}$, or $\tilde{\mathcal{B}}$, then contrast will also be correlated with those switches. Under certain conditions, we have observed both $\tilde{\mathcal{N}}$- and $\tilde{\mathcal{N}}\tilde{\mathcal{E}}$-correlated contrast. In the next chapter we will discuss the specific mechanisms that produce these contrast correlations. If we use a value for contrast averaged over all states in a block ("block-averaged" contrast) to compute phase, these contrast correlations will produce false phase correlations. The potential $\tilde{\mathcal{N}}\tilde{\mathcal{E}}$-correlated contrast is particularly troubling since it can lead to a systematic offset in the measured EDM if not properly accounted for. We account for contrast correlations by calculating contrast separately for each combination of $\tilde{\mathcal{N}}$, $\tilde{\mathcal{E}}$, and $\tilde{\mathcal{B}}$ experimental states ("state-averaged" contrast [1]),

$$\mathcal{C}(\tilde{\mathcal{N}},\tilde{\mathcal{E}},\tilde{\mathcal{B}}) = \frac{\mathcal{A}(+\Delta\theta,\tilde{\mathcal{N}},\tilde{\mathcal{E}},\tilde{\mathcal{B}}) - \mathcal{A}(-\Delta\theta,\tilde{\mathcal{N}},\tilde{\mathcal{E}},\tilde{\mathcal{B}})}{\Delta\theta}. \tag{6.10}$$

Notice that we have dropped the j subscript; from now on it is implied that independent measurements of asymmetry, contrast, and phase are computed from many

---

[1] Since there are 8 different $\tilde{N}$, $\tilde{E}$, and $\tilde{B}$ states in each 64-trace block, $64/8 = 8$ traces are averaged together to determine the contrast for each experimental state.

separate groups of data across the ∼3 ms molecule pulse. Precession phase can be calculated from each state-specific asymmetry and contrast measurement,

$$\phi(\tilde{\mathcal{N}}, \tilde{\mathcal{E}}, \tilde{\mathcal{B}}) = \frac{\mathcal{A}(\tilde{\mathcal{N}}, \tilde{\mathcal{E}}, \tilde{\mathcal{B}})}{2\mathcal{C}(\tilde{\mathcal{N}}, \tilde{\mathcal{E}}, \tilde{\mathcal{B}})} + q\frac{\pi}{4}, \tag{6.11}$$

where $\mathcal{A}(\tilde{\mathcal{N}}, \tilde{\mathcal{E}}, \tilde{\mathcal{B}})$ is the average asymmetry over both $\tilde{\theta}$ states,

$$\mathcal{A}(\tilde{\mathcal{N}}, \tilde{\mathcal{E}}, \tilde{\mathcal{B}}) = \frac{\mathcal{A}(+\Delta\theta, \tilde{\mathcal{N}}, \tilde{\mathcal{E}}, \tilde{\mathcal{B}}) + \mathcal{A}(-\Delta\theta, \tilde{\mathcal{N}}, \tilde{\mathcal{E}}, \tilde{\mathcal{B}})}{2}. \tag{6.12}$$

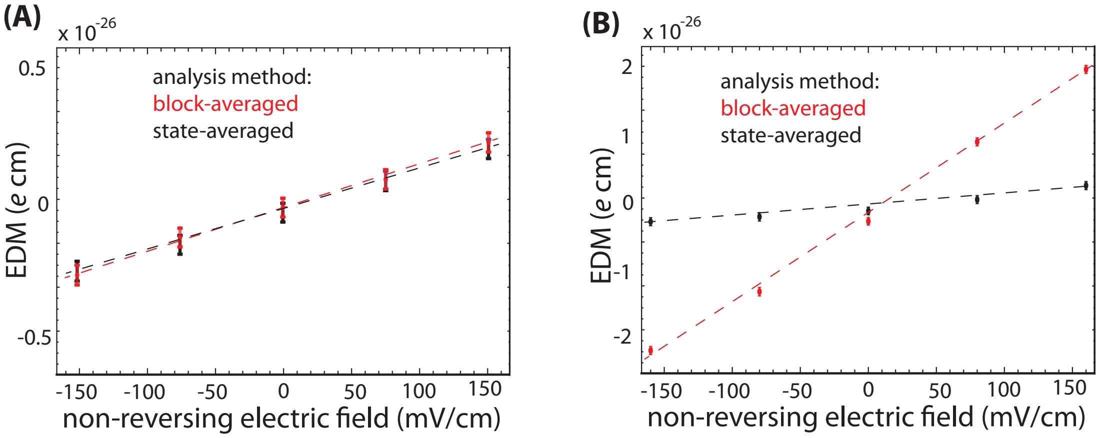

Figure 6.6: **(A)** Measured EDM vs non-reversing electric field, $\mathcal{E}_{NR}$, with no correlated contrast. The block- and state-averaged contrast analyses agree for all $\mathcal{E}_{NR}$ values. The small EDM dependence on $\mathcal{E}_{NR}$ is caused by a separate systematic effect discussed in detail in the next chapter. **(B)** Here there is a significant $\tilde{\mathcal{N}}\tilde{\mathcal{E}}$-correlated contrast that scales with $\mathcal{E}_{NR}$. For the block-averaged contrast analysis, this produces a significant EDM systematic shift that also scales with $\mathcal{E}_{NR}$. However when the EDM is computed with state-averaged contrast, there is no systematic shift from the correlated contrast.

Quantities computed from state-averaged contrast are by definition immune to contrast correlations, as illustrated in Figure 6.6. In Figure 6.6B there is a nonzero

$\tilde{\mathcal{N}}\tilde{\mathcal{E}}$-correlated contrast that scales with non-reversing electric field, $\mathcal{E}_{NR}$. This produces significant EDM dependence on $\mathcal{E}_{NR}$ when the block-averaged contrast analysis is used. This dependence is removed by the state-average contrast analysis. The residual EDM vs $\mathcal{E}_{NR}$ slope is caused by a separate light shift systematic effect. In Figure 6.6B there is no $\tilde{\mathcal{N}}\tilde{\mathcal{E}}$-correlated contrast and the state- and block-averaged contrast analyses agree for multiple values of $\mathcal{E}_{NR}$.

While phase computed from state-averaged contrast (Equation 6.11) is immune to contrast correlations, its uncertainty can be larger than phase computed from block-averaged contrast. To show this we consider the simplified measurement scheme with only one parameter switch, $\tilde{\mathcal{E}}$, in addition to $\tilde{\theta}$. The $\tilde{\mathcal{E}}$-correlated phase, $\phi^{\mathcal{E}}$ phase computed from block-averaged and state-averaged contrast are,

$$\text{State-averaged:}\quad \phi^{\mathcal{E}} = \frac{\mathcal{A}(\tilde{\mathcal{E}}+)}{2\mathcal{C}(\tilde{\mathcal{E}}+)} - \frac{\mathcal{A}(\tilde{\mathcal{E}}-)}{2\mathcal{C}(\tilde{\mathcal{E}}-)}$$

$$= \frac{\mathcal{A}(\tilde{\mathcal{E}}+,+\Delta\theta) + \mathcal{A}(\tilde{\mathcal{E}}+,-\Delta\theta)}{2\left[\mathcal{A}(\tilde{\mathcal{E}}+,+\Delta\theta) - \mathcal{A}(\tilde{\mathcal{E}}+,-\Delta\theta)\right]/\Delta\theta} - \frac{\mathcal{A}(\tilde{\mathcal{E}}-,+\Delta\theta) + \mathcal{A}(\tilde{\mathcal{E}}-,-\Delta\theta)}{2\left[\mathcal{A}(\tilde{\mathcal{E}}-,+\Delta\theta) - \mathcal{A}(\tilde{\mathcal{E}}-,-\Delta\theta)\right]/\Delta\theta}, \tag{6.13}$$

$$\text{Block-averaged:}\quad \phi^{\mathcal{E}} = \frac{\mathcal{A}(\tilde{\mathcal{E}}+) - \mathcal{A}(\tilde{\mathcal{E}}-)}{2\mathcal{C}(\tilde{\mathcal{E}}+) + 2\mathcal{C}(\tilde{\mathcal{E}}-)}$$

$$= \frac{\left[A(\tilde{\mathcal{E}}+,+\Delta\theta) + \mathcal{A}(\tilde{\mathcal{E}}+,-\Delta\theta)\right] - \left[A(\tilde{\mathcal{E}}-,+\Delta\theta) + \mathcal{A}(\tilde{\mathcal{E}}-,-\Delta\theta)\right]}{2\left[\mathcal{A}(\tilde{\mathcal{E}}-,+\Delta\theta) - \mathcal{A}(\tilde{\mathcal{E}}-,-\Delta\theta)\right]/\Delta\theta}, \tag{6.14}$$

where $\tilde{\mathcal{E}}\pm$ indicates the direction of the electric field. In normal operating conditions the electric field switch does not significantly change the asymmetry, $\mathcal{A}(\tilde{\mathcal{E}}+) \approx \mathcal{A}(\tilde{\mathcal{E}}-)$, within a single block and the correlated contrast is proportionally small, $\mathcal{C}(\tilde{\mathcal{E}}+) \approx \mathcal{C}(\tilde{\mathcal{E}}-) \approx \mathcal{C}$. We also assume the shot-noise uncertainty of each signal asymmetry measurement is comparable, $\delta\mathcal{A}(\tilde{\mathcal{E}}\pm, \pm\Delta\theta) \approx \delta\mathcal{A}$. Therefore the resulting $\phi^{\mathcal{E}}$ uncertainty is

$$\text{State-averaged: } \delta\phi^{\mathcal{E}} \approx \frac{1}{2}\left(\frac{\delta\mathcal{A}}{2\mathcal{C}}\right)\sqrt{1+\left(\frac{\mathcal{A}(\tilde{\mathcal{E}}\pm)}{\Delta\theta\mathcal{C}}\right)^2}, \tag{6.15}$$

$$\text{Block-averaged: } \delta\phi^{\mathcal{E}} \approx \frac{1}{2}\left(\frac{\delta\mathcal{A}}{2\mathcal{C}}\right)\sqrt{1+\left(\frac{\mathcal{A}(\tilde{\mathcal{E}}+)-\mathcal{A}(\tilde{\mathcal{E}}-)}{2\Delta\theta\mathcal{C}}\right)^2}. \tag{6.16}$$

Because block switches produce little or no change in asymmetry, the quantity $\mathcal{A}(\tilde{E}+) - \mathcal{A}(\tilde{E}-)$ is near zero and varies only within the shot-noise uncertainty of each data block, ~0.003. However, the average value of $\mathcal{A}(\tilde{\mathcal{E}}\pm)$ will range between ±0.1 for typical data. Therefore, the state-averaged phase uncertainty will be significantly larger than the block-averaged phase uncertainty unless $\mathcal{A}(\tilde{\mathcal{E}}\pm)/(\Delta\theta C) << 1$. To determine the optimal value for $\Delta\theta$, we simulated EDM data with varying values of $\Delta\theta$ and average $\mathcal{A}$ (Figure 6.7). These simulations show that if $|\mathcal{A}| \leq 0.1$, then $\Delta\theta \geq 6$ degrees is sufficient to make state-averaged phase uncertainty nearly shot-noise limited.

6.3.3 Computing Phase and Angular Frequency Correlations

In Chapter 3 we showed that the total energy splitting between $M_J = \pm 1$ sublevels in H can be written as

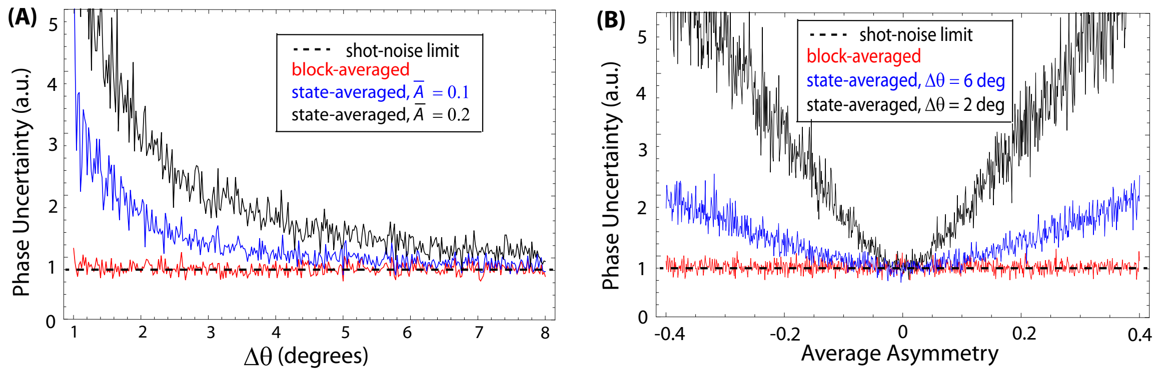

Figure 6.7: Simulated phase uncertainty for analysis versions using block- and stat-averaged contrast. Uncertainty is plotted as a function of polarization step angle, $\Delta\theta$, **(A)** and average asymmetry,$\bar{\mathcal{A}}$ **(B)**. Typically $|\mathcal{A}| \leq 0.1$ for our data set.

$$\Delta E_M = -M_J\mu_H\tilde{\mathcal{B}}|\mathcal{B}| - M_J\tilde{\mathcal{N}}\eta\mu_{rmB}|\mathcal{E}||\mathcal{B}|\tilde{\mathcal{B}} - M_J\tilde{\mathcal{N}}\tilde{E}d_e\mathcal{E}_{\text{eff}}, \tag{6.17}$$

To isolate terms various terms contributing to this energy splitting, we add together even and odd combinations of the eight different $\phi(\tilde{\mathcal{N}},\tilde{\mathcal{E}},\tilde{\mathcal{B}})$ measurements performed in a single block. Specifically, we calculate the component of phase that is odd with respect to $\tilde{\mathcal{N}}\tilde{\mathcal{E}}$, $\phi^{\tilde{\mathcal{N}}\tilde{\mathcal{E}}}$ to extract the EDM value,

$$\phi^{\mathcal{N}\mathcal{E}} = \frac{1}{8}\sum_{\tilde{\mathcal{N}},\tilde{\mathcal{E}},\tilde{\mathcal{B}}} \tilde{\mathcal{N}}\tilde{\mathcal{E}}\phi\mathcal{N},\tilde{\mathcal{E}},\tilde{\mathcal{B}}) = d_e\mathcal{E}_{\text{eff}}\tau. \tag{6.18}$$

We use unweighted averaging when summing $\phi(\tilde{\mathcal{N}},\tilde{\mathcal{E}},\tilde{\mathcal{B}})$ over different experimental configurations. Eight separate "switch parity components" of the phase can be similarly calculated, each with different physical interpretations, including

$$\phi^{\mathcal{B}} = \frac{1}{8}\sum_{\tilde{\mathcal{N}},\tilde{\mathcal{E}},\tilde{\mathcal{B}}} \tilde{\mathcal{B}}\phi(\tilde{\mathcal{N}},\tilde{\mathcal{E}},\tilde{\mathcal{B}}) = \mu_{\text{B}}g|\vec{\mathcal{B}}|\tau, \tag{6.19}$$

$$\phi^{\mathcal{N}\mathcal{B}} = \frac{1}{8} \sum_{\tilde{\mathcal{N}},\tilde{\mathcal{E}},\tilde{\mathcal{B}}} \tilde{\mathcal{N}}\tilde{\mathcal{E}}\phi(\tilde{\mathcal{N}},\tilde{\mathcal{E}},\tilde{\mathcal{B}}) = \mu_{\mathrm{B}}\Delta g|\vec{\mathcal{B}}|\tau, \tag{6.20}$$

where Δg is the difference in g-values between the upper and lower $\mathcal{N}$ levels of the $|H, J = 1\rangle$ state. Throughout this text the switch parity components of the phase will also be referred to as "phase channels" or correlated phases.

We observe that molecule beam forward velocity, and thus τ, can fluctuate by up to 10% over a 10 minute time period (Figure 6.5). It is therefore important to measure τ for each block of data. Because $|\mathcal{B}|$ and $\mu_{\mathrm{B}}g$ are precisely known from auxiliary measurements, we can extra coherence time for each block from $\phi^{\mathcal{B}}$. The forward velocity dispersion of the molecule beam causes τ to linearly drift across the molecule pulse. We therefore perform a three-polynomial fit to $\phi^{\mathcal{B}}$ to calculate τ as function of time after ablation.

With precise measurements of τ calculated directly from our data, we can convert phase parity components into angular frequency. Specifically, for the component correlated with $\tilde{\mathcal{N}}\tilde{\mathcal{E}}$,

$$\omega^{\mathcal{N}\mathcal{E}} = \frac{\phi^{\mathcal{N}\mathcal{E}}}{\tau} = d_e\mathcal{E}_{\mathrm{eff}}. \tag{6.21}$$

Figure 6.10A shows multiple measurements of $\omega^{\mathcal{N}\mathcal{E}}$ throughout the molecule pulse for a single block of data.

Other $\mathcal{N}$, $\mathcal{E}$, and $\mathcal{B}$ switch parity components can be used to monitor important systematic effects, discussed in detail in the next chapter. We can also measure important properties of ThO through phase components, as is the case with $\omega^{\mathcal{N}\mathcal{B}}$. This component allows us to measure Δg, the magnetic moment difference between upper and lower $\mathcal{N}$-levels arising from perturbations from other electronic states [57].

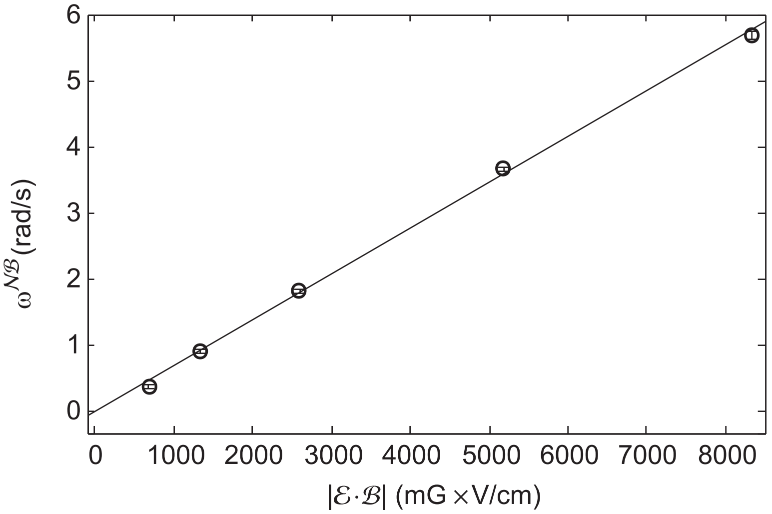

Figure 6.8: The difference between magnetic moments of the two omega doublet levels as measured by $\omega^{\mathcal{NB}}$. As expected, this phase component scales linearly with $\mathcal{E}$ and $\mathcal{B}$.

Because this difference limits the extent to which the $\mathcal{N}$ reversal can suppress certain systematic effects [68], it is important to understand both in our experiment and in other experiments measuring EDMs in molecules with Ω-doublet or Λ-doublet structure [90]. We observed that Δg scaled linearly with applied electric field (Figure 6.8), $\Delta g = \eta|\mathcal{E}|$, as was predicted [57]. Since $\mathcal{E}$ and $\mathcal{B}$ are precisely known from axillary measurements, the constant η cen be directly calculated from our angular frequency measurements,

$$\eta = \frac{\hbar\omega^{\mathcal{NB}}}{\mu_{\mathrm{B}}|\mathcal{EB}|}. \tag{6.22}$$

However, our measurement of η (Figure 6.8) was nearly a factor of two smaller than what was predicted by the theory treatment of [57]. The discrepancy was caused by second and third order perturbations from higher rotational levels and electronic states, as documented in [70]. The $\omega^{\mathcal{NB}}$ channel illustrates the importance of monitoring the understanding other phase correlations besides the one that corresponds to the EDM.

6.4 Data Cuts

Three data cuts, fluorescence rate threshold, polarization bin, and contrast threshold, were applied as part of the analysis. These cuts remove background noise from the data and ensure that the EDM value is only deduced from data taken collected under appropriate experimental conditions. We thoroughly investigated how each these cuts affected the calculated EDM mean and uncertainty. In each case, we significantly varied the cut, and in some cases removed it entirely. As illustrated in Figure 6.9, the EDM mean was very robust against significant variation of each of these cuts.

As previously mentioned, a fluorescence threshold cut, $F_{cut} = 300{,}000$ photons/sec, is applied to each trace to ensure that the fluorescence rate would always be larger than the background count rate. Also, an entire block of data was removed from the analysis if all 64 of its traces did not have at least 0.5 ms of fluorescence data above S_{cut}. Because asymmetry is a ratio of two Gaussian distributions ($F_x - F_y$ and $F_x + F_y$), its distribution is not inherently Gaussian. Rather, it approaches a Gaussian distribution as the denominator, $F_x + F_y$, increases. The same follows for all quantities computed from asymmetry, including the EDM. The fluorescence threshold cut therefore ensures that the distribution if EDM measurements is Gaussian. We computed the EDM mean and uncertainty for a number of different F_{cut} values (6.9A). The uncertainty increases if F_{cut} is increased to cut out a significant faction of data. The mean does not significantly change with F_{cut}.

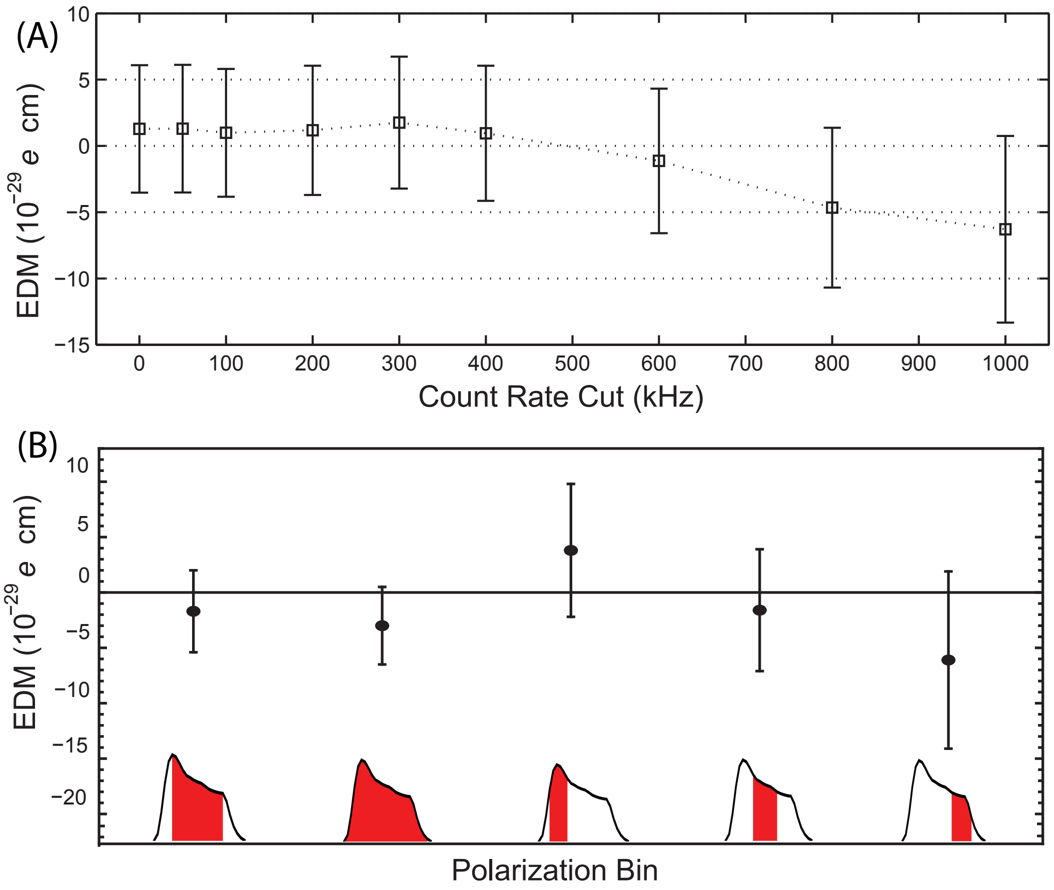

Figure 6.9: Measured EDM mean and uncertainty as a function of signal threshold (A) and polarization bin (B).

The individual data points used to compute asymmetry were between $i = 5$ and $i = 20$ (Figure 6.1A), where $i = 0$ corresponds to the laser turning on. This polarization bin was chosen to cut out background counts and overlapping fluorescence between polarization states while retaining as many fluorescence counts as possible. As shown in Figure 6.9B, we used a number of different polarization bins to compute the EDM. The EDM uncertainty increases, as expected, for polarization bins that cut out data with significant fluorescence, but the mean values are all consistent with each other within their respective uncertainties.

In order for a block of data to be used in our measurement, all of its 64 traces must have a measured fringe contrast above 80%. The primary causes of blocks flailing to meet this requirement is the state preparation laser frequency becoming unlocked. This cut results in less than 1 % of blocks being thrown away. If the contrast cut is lowered, or not applied at all, the EDM mean and uncertainty change by less than $10^{-30}e$ cm. Similar to the signal threshold, if this cut is increased above 90%, close to the average value of contrast, then a large fraction of data will be neglected and the EDM uncertainty will increase.

6.5 EDM Mean and Statistical Uncertainty

The final data set consists of $\sim 10^4$ blocks of data taken over the course of ~ 2 weeks ((Figure 6.10B)). Each block contains ~ 20 separate EDM measurements over the duration of the molecule pulse (Figure 6.10A). All $\sim 2 \times 10^5$ measurements are combined with standard Gaussian error propagation to obtain the reported mean and uncertainty. Figure 6.10C shows a histogram of all measurements, normalized to

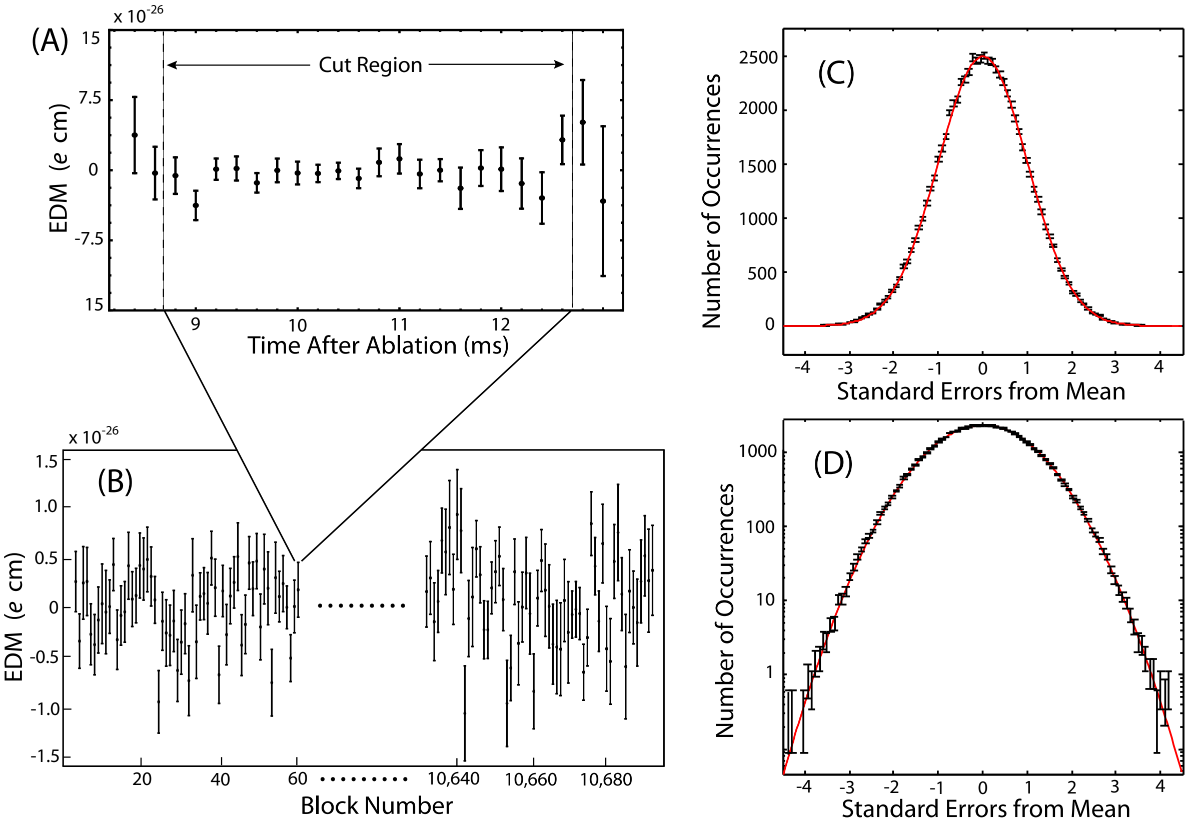

Figure 6.10: EDM statistics for published data set. **(A)** For each block of data, about 20 EDM measurements are obtained from different parts of the molecule pulse. **(B)** Over 10,000 blocks of data were taken over a combined period of about two weeks. **(C)-(D)** The distribution ∼200,000 separate EDM measurements (black) agrees matches very well with a Gaussian fit (red). In these histograms the mean of each individual measurement was normalized to its corresponding error bar.

their individual uncertainties. The measurement distribution agrees very well with a Gaussian fit, even in the far edges of the distribution (Figure 6.10D). The resulting uncertainty is 1.15 times the calculated photon shot-noise limit, taking into account the photon count rate from molecule fluorescence, background light, and PMT dark noise. When the EDM measurements are fit to a constant value, the reduced χ^2 is 0.996 ± 0.006.

EDM measurements taken with identical experimental conditions are always combined with standard weighted averaging to obtain overall mean and uncertainty. Due to molecule number fluctuations, each block of data will have a different uncertainty. The overall uncertainty will thus be unnecessarily inflated if data is combined with unweighted averaging. When combining measurements taken with different experimental conditions, determined by the long timescale parameter switches, we used weighted averaging in some cases and unweighted averaging in other cases. Weighted averaging can produce an inaccurate EDM mean if the EDM values change for different experimental conditions. This would be the case if a longer timescale switch were directly suppressing an EDM systematic effect. In reality, none of the longer timescale switches significantly changed the measured EDM value. Therefore it is justifiable to use weighted averaging across different experimental states. It is clearly advantageous to combine measurements with different values of $|\mathcal{B}|$, $|\mathcal{E}|$, and $\tilde{k}$ with weighted averaging, since unequal amounts of data were collected for each value of these parameters. For example, 40% of data was gathered with preparation and readout lasers pointing east, $\tilde{k} = 1$, and 60% of data was gather with lasers pointing west, $\tilde{k} = 1$. Roughly equal amounts of data were gathered for different values of the readout parity state $\tilde{\mathcal{P}}$, field plate lead configuration $\tilde{\mathcal{L}}$, readout laser polarization $\tilde{\mathcal{R}}$, and global polarization of preparation and readout lasers $\tilde{\mathcal{G}}$. The overall uncertainty is therefore comparable (within 10%) when the data is combined with weighted or unweighted averaging. The EDM mean also changes by less than 10% between the two averaging methods. For the reported value, I used weighted averaging for all switches except $\tilde{\mathcal{P}}$ and $\tilde{\mathcal{R}}$, while Nick and Brendon used unweighted averaging for those switches as well as $\tilde{\mathcal{L}}$ and $\tilde{\mathcal{G}}$.

The final EDM mean and statistical uncertainty, averaged between the independent analyses of Nick, Brendon, and myself, was $d_e = -2.1 \pm 3.7 \times 10^{-29} e$ cm [2]. The current theory value of $\mathcal{E}_{\text{eff}} = 84$ GV/cm [10] was used to compute these values from $\omega^{\mathcal{N}\mathcal{E}}$. To prevent experimental bias, we performed a blind analysis by adding an unknown offset to the mean of the EDM channel, $\omega^{\mathcal{N}\mathcal{E}}$. The offset was randomly generated in software from a $\sigma = 10^{-27} e$ cm Gaussian distribution and added as part of our analysis algorithm. The mean, statistical error, systematic shift, and procedure for calculating the systematic error were all determined before revealing the blind offset.

---

[2] The EDM uncertainties for all three independent analysis versions were nearly identical, and the computed EDM means agreed to within 2×10^{-29} e cm

Chapter 7

Systematic Uncertainty

In precision measurement experiments, it is crucial to accurately determine the systematic uncertainty. If unrecognized, a systematic offset will jeopardize the accuracy of the measurement by shifting the value of the measured quantity by an unknown amount. A systematic that produces a phase correlated with reversals of molecule alignment and laboratory electric field, $\tilde{\mathcal{N}}\tilde{\mathcal{E}}$ would mimic and EDM signal. However, this effect would not arise from P- and T-violation, but rather from imperfections in the experimental apparatus or measurement scheme.

In previous EDM experiments, dominant systematic offsets have arisen from leakage currents, geometric phases, and motional magnetic fields ($\vec{v} \times \vec{\mathcal{E}}$). Each of these effects scale with laboratory electric field, $\mathcal{E}$, and produces a precession phase that is correlated with $\tilde{\mathcal{E}}$. Past EDM experiments could not reverse $\mathcal{E}_{\text{eff}}$ independent of $\mathcal{E}$, as allowed by ThO's Ω-doublet structure, so such effects produced systematic EDM offsets. As described in Chapter 2, each of these effects should be drastically suppressed in our experiment because of ThO's high electric polarizability, small magnetic dipole moment, and Ω-doublet structure. Indeed, our preliminary calculations predicted that systematic offsets in our measurement would be well below 10^{-32} e cm [60, 68], three orders of magnitude smaller than our statistical precision. However, there are several important differences between our experiment and past EDM experiments. For example, our experiment is the first to use a buffer gas molecular source, and to shine lasers directly through transparent electric field plates. We cannot only rely on predictions based on previous EDM experiments to determine the extent of systematic offsets to our measurement. Instead, we must directly search for systematic offsets that could potentially change our result.

7.1 Determining Systematic Uncertainty

A true EDM should produce an $\tilde{\mathcal{N}}\tilde{\mathcal{E}}$-correlated phase that does not scale with any experimental parameter except coherence time. The easiest way to discriminate between a systematic offset and a true EDM is to vary a wide range of experimental parameters other than $\tilde{\mathcal{N}}$ and $\tilde{\mathcal{E}}$, or experimental imperfections, while closely monitoring the behavior of the EDM phase channel. If the measured EDM value changes with an experimental parameter, then there is likely to be a systematic effect related to that parameter.

For this reason we designed our apparatus to allow us to vary and exaggerate a wide range of experimental imperfections, including stray electric and magnetic fields, all possible magnetic field gradients, molecule beam pointing, and laser profile, pointing, detuning, and polarization, just to name a few. We broadened our systematic search by not only monitoring the $\tilde{\mathcal{N}}\tilde{\mathcal{E}}$-correlated phase while varying these parameters, but all combinations of $\tilde{\mathcal{N}}$, $\tilde{\mathcal{E}}$, and $\tilde{\mathcal{B}}$ phase correlations as well. We also monitored a number of naturally fluctuating parameters, such as molecule beam velocity, vacuum pressure, and room temperature [71], to determine whether the EDM value was correlated with any of these parameters.

To search for possible systematic offsets, we varied more than 40 separate parameters (see Tables 7.1 and 7.2). For each parameter, P, we calculated the mean slope, $S = \partial\omega^{\mathcal{N}\mathcal{E}}/\partial P$, and the slope uncertainty δS. Keeping with tradition [36, 39, 5], we assume a linear $\omega^{\mathcal{N}\mathcal{E}}$ dependence on P to compute the systematic shift, $\omega^{\mathcal{N}\mathcal{E}}_{\text{syst}} = S\bar{P}$, and the systematic uncertainty,

$$\delta\omega^{\mathcal{N}\mathcal{E}} = [\bar{P}^2(\delta S)^2 + (\delta P)^2 S^2 + (\delta S)^2(\delta P)^2]^{1/2}. \tag{7.1}$$

Here, $\bar{P}$ and δP are the mean and uncertainty of parameter P under normal operating conditions. They are calculated from auxiliary measurements or other phase correlations. For parameters, such as a non-reversing electric field, that produced significant EDM offsets, S was monitored throughout the EDM data set. If S was not monitored throughout the EDM data set, as was the case with most parameters that produced no significant EDM offset, we chose not to apply a apply a systematic correction for that parameter and instead included an upper limit of $[(SP)^2 + (\delta\omega^{\mathcal{N}\mathcal{E}})^2]^{1/2}$ in our systematic error budget. An example of the systematic uncertainty computed from a stray magnetic field is shown in Figure 7.1.

Although Equation 7.1 assumes only linear $\omega^{\mathcal{N}\mathcal{E}}$ dependence on P, we sought to be as general as possible in computing our systematic uncertainty. In addition to fitting parameter variation data to a linear slope, we also fit quadratic and other higher-order polynomial functions to this data. In all cases the linear fit resulted it the largest

Table 7.1: **Category I Parameters:**Parameters that were varied far from their values under normal conditions of the experiment. For each of these parameters direct measurements or limits were placed on possible systematic errors.

Category I Parameters
Magnetic Fields - Non-Reversing $\mathcal{B}$-Field: $\mathcal{B}_z^{\mathrm{nr}}$ - Transverse $\mathcal{B}$-Fields: $\mathcal{B}_x, \mathcal{B}_y$ (even and odd under $\tilde{\mathcal{B}}$) - Magnetic $\mathcal{B}$-Field Gradients: $\frac{\partial \mathcal{B}_x}{\partial x}, \frac{\partial \mathcal{B}_y}{\partial x}, \frac{\partial \mathcal{B}_y}{\partial y}, \frac{\partial \mathcal{B}_y}{\partial z}, \frac{\partial \mathcal{B}_z}{\partial x}, \frac{\partial \mathcal{B}_z}{\partial z}$ (even and odd under $\tilde{\mathcal{B}}$) - $\tilde{\mathcal{E}}$ correlated $\mathcal{B}$-field: $\mathcal{B}^{\mathcal{E}}$ (to simulate $\vec{v} \times \vec{\mathcal{E}}$/geometric phase/leakage current)
Electric Fields - Non-Reversing $\mathcal{E}$-Field: $\mathcal{E}^{\mathrm{nr}}$ - $\mathcal{E}$-Field Ground Offset
Laser Detunings - Prep/Read Laser Detuning: Δ_{prep}, Δ_{read} - $\tilde{\mathcal{P}}$ correlated Detuning: $\Delta^{\mathcal{P}}$ - $\tilde{\mathcal{N}}$ correlated Detunings: $\Delta^{\mathcal{N}}$, $\Delta_0\Delta^{\mathcal{N}}$
Laser Pointings along $\hat{x}$ - Change in Pointing of Prep/Read Lasers - Readout laser $\hat{X}/\hat{Y}$ dependent pointing - $\tilde{\mathcal{N}}$ correlated laser pointing - $\tilde{\mathcal{N}}$ and $\hat{X}/\hat{Y}$ dependent laser pointing
Laser Powers - Power of Prep/Read Lasers - $\tilde{\mathcal{N}}\tilde{\mathcal{E}}$ correlated power to simulate $\Omega_r^{\mathcal{N}\mathcal{E}}$ - $\tilde{\mathcal{N}}$ correlated power, $P^{\mathcal{N}}$ - $\hat{X}/\hat{Y}$ dependent Readout laser power
Laser Polarization - Preparation Laser Ellipticity
Molecular Beam Clipping - Molecule Beam Clipping along the $\hat{y}$ and $\hat{z}$ (changes $\langle v_y \rangle$,$\langle v_z \rangle$,$\langle y \rangle$,$\langle z \rangle$ of molecule beam)

Table 7.2: **Category II Parameters:** Parameters for which there is no single ideal value. Although direct limits on systematic errors cannot be derived, these served as checks for the presence of unanticipated systematic errors.

Category II Parameters
Experiment Timing - $\hat{X}/\hat{Y}$ Polarization Switching Rate - Number of Molecule Pulse Averages contributing to an Experiment State
Analysis - Signal size cuts, Asymmetry magnitude cuts, Contrast cuts - Difference between two PMT detectors (changes fluorescence region dependence) - Variation with time within molecule pulse (serves to check v_x dependence) - Variation with time within polarization switching cycle - Variation with time throughout the full dataset (autocorrelation) - Search for correlations between all switch parity components of phase, contrast and fluorescence signal - Correlations with auxiliary measurements of $\mathcal{B}$-fields, laser powers, and vacuum pressure - 3 individuals performed independent analyses of the data

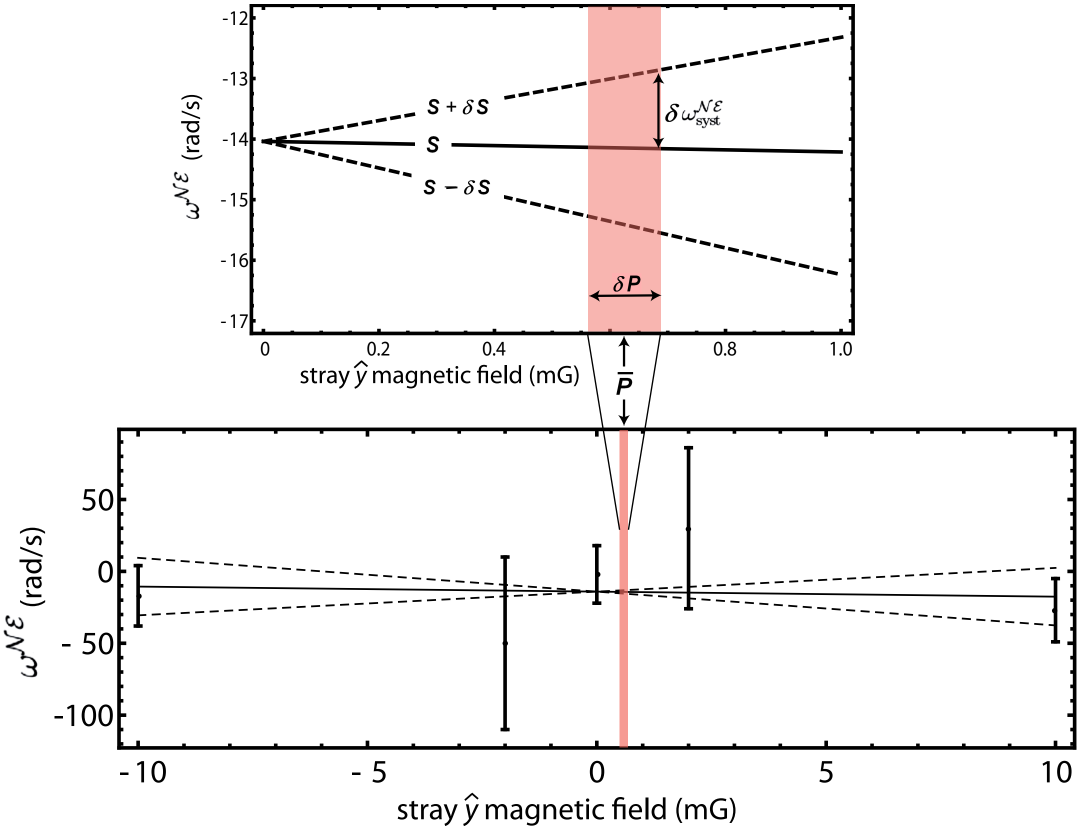

Figure 7.1: Example of how systematic uncertainty is deduced from EDM measurements with intentionally exaggerated parameter imperfections. In this case a stray magnetic field in the vertical direction is exaggerated to at least 10 times its typical value, $\bar{P}$, during normal operating conditions.

Table 7.3: Systematic shifts and uncertainties for $\omega^{\mathcal{N}\mathcal{E}}$, in units of mrad/s. All systematic and statistical errors are added in quadrature to obtain the total EDM uncertainty. In EDM units, 1.3 mrad/s $\approx 10^{-29}$ e cm. Values listed here are averaged over all three versions (Hutzler, O'Leary, and Spaun) of the data analysis.

Parameter	Shift	Uncertainty
$\mathcal{E}^{\mathrm{nr}}$ correction	−0.81	0.66
$\Omega_{\mathrm{r}}^{\mathcal{N}\mathcal{E}}$ correction	−0.03	1.58
$\phi^{\mathcal{E}}$ correlated effects	−0.01	0.01
$\phi^{\mathcal{N}}$ correlation		1.25
Non-Reversing $\mathcal{B}$-field ($\mathcal{B}_z^{\mathrm{nr}}$)		0.86
Transverse $\mathcal{B}$-fields $\left(\mathcal{B}_x^{\mathrm{nr}}, \mathcal{B}_y^{\mathrm{nr}}\right)$		0.85
$\mathcal{B}$-Field Gradients		1.24
Prep./Read Laser Detunings		1.31
$\tilde{\mathcal{N}}$ Correlated Detuning		0.90
$\mathcal{E}$-field Ground Offset		0.16
Total Systematic	−0.85	3.24
Statistical		4.80
Total Uncertainty		5.79

estimate of EDM systematic uncertainty [1] and was therefore used to determine the systematic error budget shown in Table 7.3. We did not observe significantly nonlinear EDM dependence on any of the parameters we adjusted.

Table 7.3 contains a complete list of all contributions to our systematic error. Each of these contributions will be discussed in detail throughout this chapter, along

---

[1] One can always argue that $\omega^{\mathcal{N}\mathcal{E}}$ dependence on P might, hypothetically, resemble a dispersion curve, where the slope is steep for values of P near zero but flat for larger values. In this case the method of linear fitting would underestimate the true systematic uncertainty. We looked for this type of nonlinear dependence by conducting most systematic searches with multiple values of P, as illustrated in Figure 7.1. Such nonlinear behavior was never observed in the EDM channel.

with the effects of other other parameters not included in Table 7.3. In general, we include in our error budget the systematic uncertainty from a certain parameter if *any* of the following three criteria are met.

A) The parameter caused a direct change in the EDM value. We identified two imperfections that produced such a change by coupling to ac Stark shifts.

B) The parameter caused unexplained behavior in one of the following non-EDM channels: $\omega^{\mathcal{N}}, \omega^{\mathcal{E}}, \omega^{\mathcal{NB}}, \omega^{\mathcal{EB}}$, or $\omega^{\mathcal{NEB}}$[2]. One parameter related to $\tilde{\mathcal{N}}$-correlated laser pointing met this criterion.

C) The parameter is physically analogous to another parameter that caused an *unexplained* EDM shift in a previous electron EDM experiment. Several parameters in our experiment fall into this category, including stray magnetic fields and magnetic field gradients [53], laser detunings, and a field plate voltage offset [5].

Each of the contributions listed in Table 7.3 will be discussed in detail throughout this chapter, along with the results of other systematic searches performed with parameters that did not meet any of these criteria. As with the EDM mean and uncertainty, all reported systematic shifts and uncertainties are averaged between the three versions of data analysis carried out by Nick Hutzler, Brendon O'Leary, and myself. The EDM shifts and uncertainties for all parameters agree to within 10^{-29} e cm between the three analysis versions.

---

[2] These channels were chosen because they are computed with switches performed on the fastest timescales, within a single block, and therefore are not affected by drifts in spin precession time caused by molecule velocity fluctuations. Each of these channels is well characterized and can be measured with the same precision as the EDM channel. The $\omega^{\mathcal{B}}$ and ω channels are not included since velocity drift causes them to significantly fluctuate from block to block.

7.2 Light Shift Systematic Effects

We discovered that laser-induced ac Stark shifts (light shifts), produced by imperfections in laser polarization, could couple to other experimental imperfections to significantly shift our EDM measurement. This systematic was first discovered by observing clear EDM dependence on a deliberately introduce non-reversing electric field, $\mathcal{E}_{\text{nr}}$. By observing how this EDM dependence changed with various laser parameters, we were able to develop a model that explained how light shifts coupled to $\mathcal{E}_{\text{nr}}$ to shift the EDM value. We later discovered other imperfections besides $\mathcal{E}_{\text{nr}}$ that could couple to light shifts to produce an EDM offset. We will describe how all systematic offsets and uncertainties arising from light shifts were suppressed well below the statistical uncertainty of our EDM measurement.

7.2.1 EDM dependence on Non-Reversing Electric Field

One of the first experimental imperfections we intentionally exaggerated was a non-reversing electric field. A non-reversing electric field is a permanent component of the electric field along the $\hat{z}$ axis (i.e. the electric field axis and laser prorogation direction) which does not reverse the with the parameter switch $\tilde{\mathcal{E}}$,

$$\mathcal{E}_z = \mathcal{E}_0 \tilde{\mathcal{E}} + \mathcal{E}_{\text{nr}}. \tag{7.2}$$

Clearly a non-reversing electric field causes ThO molecules to experience a larger electric field magnitude for one direction of the applied field compared to the other direction, $|\mathcal{E}(\tilde{\mathcal{E}}+)| \neq |\mathcal{E}(\tilde{\mathcal{E}}-)|$. Here, $\tilde{\mathcal{E}}+$ and $\tilde{\mathcal{E}}-$ correspond to electric fields parallel and antiparallel to $\hat{z}$. With three separate methods, Raman Spectroscopy [71], microwave spectroscopy [4, 72], and $\tilde{\mathcal{N}}\tilde{\mathcal{E}}$-correlated contrast, we have measured the residual $\mathcal{E}_{\text{nr}}$ in our apparatus to be about -5 mV/cm in both the preparation and readout regions. We intentionally exaggerate this value by increasing/decreasing the magnitude of voltage applied across the electric field plates in correlation with $\tilde{\mathcal{E}}$ (i.e. when the electric field pointed east, the voltage across the plates was set to be larger than when the electric field pointed west).

As shown in Figure 7.2, the measured EDM value originally scaled linearly with $\mathcal{E}_{\text{nr}}$. The slope $\omega^{\mathcal{N}\mathcal{E}}/\mathcal{E}_{\text{nr}}$ was very significant, 6.7 ± 0.4 (rad/s)/(V/cm). When combined with the -5 mV measured $\mathcal{E}_{\text{nr}}$ value, this slope yields an systematic shift of -2.5×10^{-28} e cm. While the magnitude of this shift was ∼4 times smaller that the previous best electron EDM limit, it was at least 5 times larger than our final statistical uncertainty. Clearly, we had encountered a systematic effect that needed to be understood and suppressed.

7.2.2 Detuning Correlations

We can show that one consequence of a non-reversing electric field is an $\mathcal{N}$ level Stark splitting, Δ_{Stark}, that depends on the direction of the laboratory electric field, as illustrated by Figure 7.3. The polarizability of ThO is completely saturated in the electric field of typical operation, $|\mathcal{E}_z| =$ 36-142 mV/cm, so Δ_{Stark} scales linearly with $|\mathcal{E}_z|$, as we showed in Chapter (see Equations 4.27 and 4.28). Combining Equations 4.28 and 7.2, we see that $\mathcal{E}_{\text{nr}} \neq 0$ implies that Δ_{Stark}, depends on the electric field direction, $\tilde{\mathcal{E}}$,

$$\Delta_{\text{Stark}} = -\frac{d_H}{h}\left(|\mathcal{E}_0| + \mathcal{E}_{\text{nr}}\tilde{\mathcal{E}}\right)\tilde{\mathcal{N}}. \tag{7.3}$$

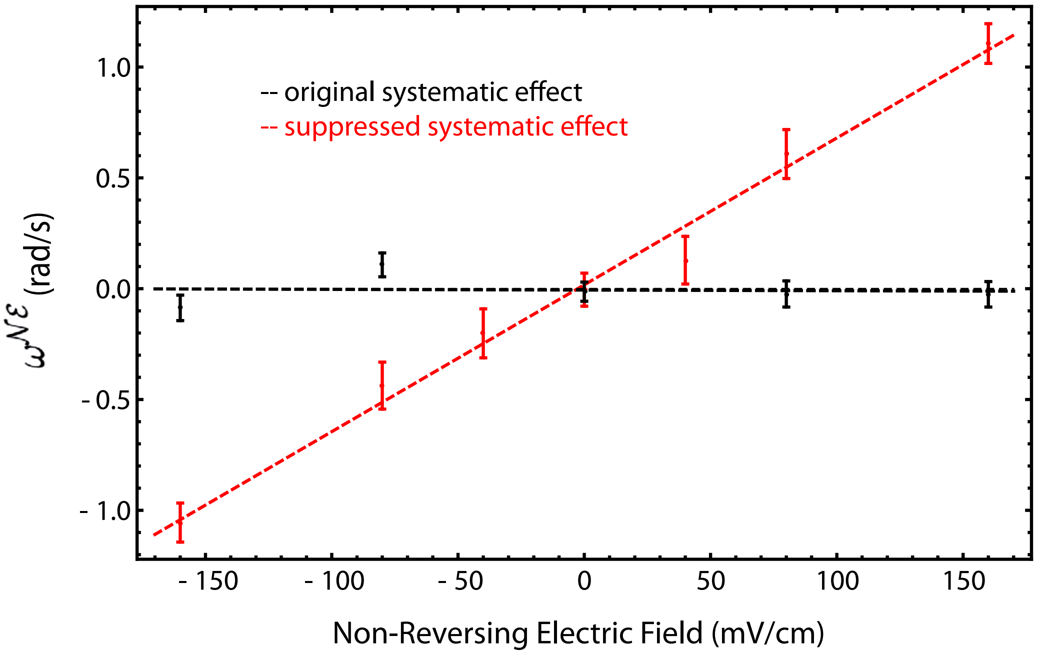

Figure 7.2: Systematic offset of EDM channel caused by non-reversing electric field. The original systematic effect was very significant (red). We suppressed the effect (black) by optimizing the preparation laser shape, power and polarization.

The laser frequency, of course, does not depend on $\tilde{\mathcal{E}}$. Rather, it remains constant throughout a data block, apart from shifting by $2\nu^{\mathcal{N}}$ to switch resonance between the $\mathcal{N}$ levels. Because the laboratory electric field Stark shifts the two $\mathcal{N}$ levels in opposite directions, a nonzero $\mathcal{E}_{\mathrm{nr}}$ causes the laser detuning from resonance, Δ, to be correlated with $\tilde{\mathcal{N}}\tilde{\mathcal{E}}$:

$$\begin{aligned}
\Delta &= \Delta_0 - \nu^{\mathcal{N}}\tilde{\mathcal{N}} - \Delta_{\mathrm{Stark}} && (7.4)\\
&= \Delta_0 + \left(\frac{d_H|\mathcal{E}_0|}{h} - \nu^{\mathcal{N}}\right)\tilde{\mathcal{N}} + \frac{d_H\mathcal{E}_{\mathrm{nr}}}{h}\tilde{\mathcal{N}}\tilde{\mathcal{E}} && (7.5)\\
&= \Delta_0 + \Delta^{\mathcal{N}}\tilde{\mathcal{N}} + \Delta^{\mathcal{N}\mathcal{E}}\tilde{\mathcal{N}}\tilde{\mathcal{E}}. && (7.6)
\end{aligned}$$

For simplicity the various detuning contributions have been grouped according to the parameter switch with which they are correlated, with Δ_0 being the component of laser detuning common to all experimental configurations. We see that $\tilde{\mathcal{N}}$-correlated detuning arises if $\nu^{\mathcal{N}}$ is not matched to the average $\mathcal{N}$ level Stark splitting, and $\tilde{\mathcal{N}}\tilde{\mathcal{E}}$-correlated detuning results from $\mathcal{E}_{\mathrm{nr}}$.

The first breakthrough in understanding the dependence of $\omega^{\mathcal{N}\mathcal{E}}$ on $\mathcal{E}_{\mathrm{nr}}$ was showing that $\omega^{\mathcal{N}\mathcal{E}}$ did not depend on $\mathcal{E}_{\mathrm{nr}}$ itself but instead on the $\tilde{\mathcal{N}}\tilde{\mathcal{E}}$-correlated detuning, $\Delta^{\mathcal{N}\mathcal{E}}$, produced by $\mathcal{E}_{\mathrm{nr}}$. We demonstrated this in two different ways. First, we intentionally exaggerated $\mathcal{E}_{\mathrm{nr}}$ while also applying an equivalent $\tilde{\mathcal{N}}\tilde{\mathcal{E}}$-correlated laser frequency, $\nu^{\mathcal{N}\mathcal{E}} = d_H\mathcal{E}_{\mathrm{nr}}/h$, to keep $\Delta^{\mathcal{N}\mathcal{E}} = d_H\mathcal{E}_{\mathrm{nr}}/h - \nu^{\mathcal{N}\mathcal{E}} = 0$. The resulting $\omega^{\mathcal{N}\mathcal{E}}$ vs $\mathcal{E}_{\mathrm{nr}}$ slope was consistent with zero (see Figure 7.4A). Next, we applied no additional $\mathcal{E}_{\mathrm{nr}}$, but applied the same $\nu^{\mathcal{N}\mathcal{E}}$, which resulted in nonzero $\Delta^{\mathcal{N}\mathcal{E}}$. This again produced a systematic EDM shift (see Figure 7.4B), comparable to that of $\mathcal{E}_{\mathrm{nr}}$.

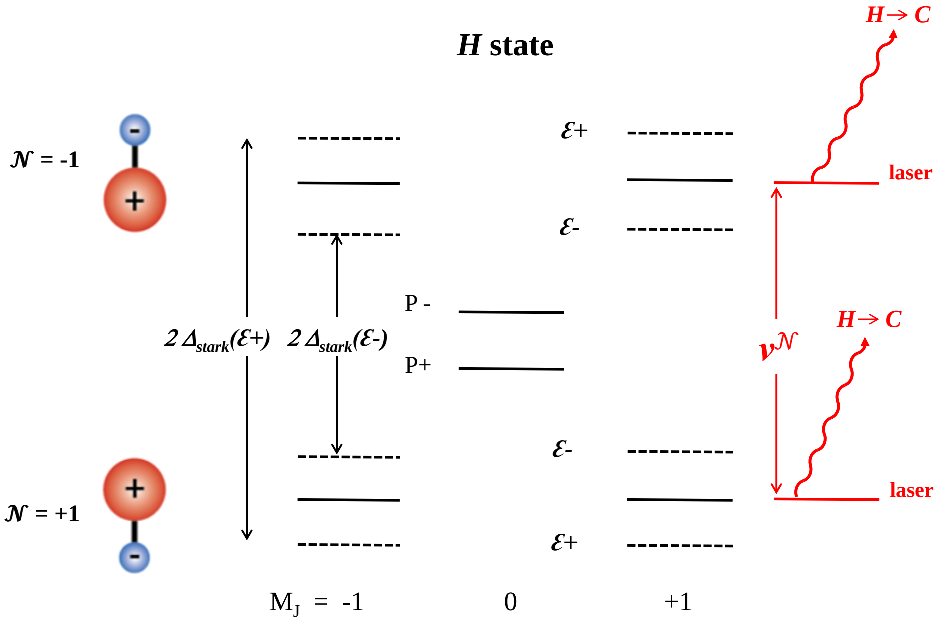

Figure 7.3: H state level diagram with non-reversing electric field. When a non-reversing electric field is present, the stark splitting, Δ_{Stark} between the two $\mathcal{N}$ levels depends on the direction of the electric field. This causes the detuning, Δ of the laser exciting the $H \rightarrow C$ transition to be correlated with $\tilde{\mathcal{N}}\tilde{\mathcal{E}}$. Energy level spacings are not to scale.

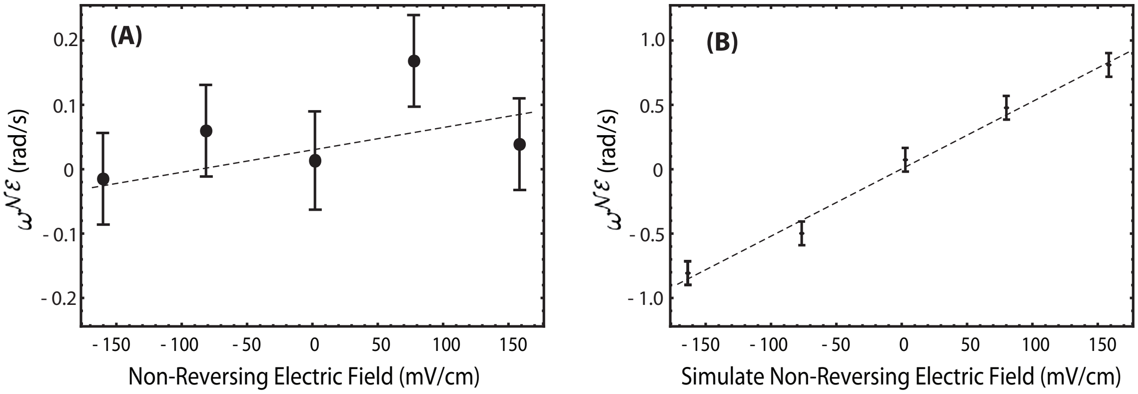

Figure 7.4: **(A)** EDM dependence on non-reversing electric field when $\tilde{\mathcal{N}}\tilde{\mathcal{E}}$-correlated laser frequency is applied to always keep lasers on resonance in all experimental states. **(B)** The effect of a simulated non-reversing electric field produced by intentionally applying $\tilde{\mathcal{N}}\tilde{\mathcal{E}}$-correlated laser frequency with electric field held constant.

7.2.3 Controlling the Detuning-Dependent Phase

Having established that $\tilde{\mathcal{N}}\tilde{\mathcal{E}}$-correlated phase is produced by $\tilde{\mathcal{N}}\tilde{\mathcal{E}}$-correlated detuning, we proceeded to directly verify that the measured phase depended on detuning, as would be expected:

$$\phi^{\mathcal{N}\mathcal{E}} \propto \Delta^{\mathcal{N}\mathcal{E}} \Rightarrow \phi \propto \Delta. \tag{7.7}$$

To measure this dependence, we used an AOM to rapidly step the laser detuning, Δ_0, through 10-15 different values spanning ± 2 MHz. The AOM switched to a different frequency every 0.5 s. To insure that molecule beam velocity fluctuations did not add noise to these measurements, Δ_0 was rapidly stepped on the 0.5 s timescale. For this data θ was switched between two values on a 10 s timescale monitor the contrast. The $\tilde{\mathcal{B}}$ switch was implemented on the 20 s timescale for some of this data, and for other data $\mathcal{B}$ was zero. The $\tilde{E}$ and $\tilde{\mathcal{N}}$ switches were performed on longer timescale switches to verify that the phase vs detuning slope did not depended on either switch. This data revealed a clear detuning-dependent phase, with slope $\partial\phi/\partial\Delta_0 = 0.1$ rad/MHz (see Figure 7.5A) consistent with the previously observed $\omega^{\mathcal{NE}}$ dependence on $\Delta^{\mathcal{NE}}$.

Since laser detuning is strictly a property of the preparation and readout lasers, we sought to better understand this detuning-dependent phase by varying different properties of the laser. The first laser parameter which clearly affected the value of $\partial\phi/\partial\Delta_0$ was the preparation laser polarization, θ_{prep}. Figure 7.5B shows measured phase as a function of detuning for multiple values of θ_{prep}. Only data with $|\Delta_0| < 1$ MHz is used for the linear fit since $\partial\phi/\partial\Delta_0$ tapers off for $|\Delta_0| > 1$ MHz. Figure 7.5C shows that $\partial\phi/\partial\Delta_0$ follows a clear sinusoidal dependence on θ_{prep}. This means that for properly chosen values of θ_{prep}, the detuning dependence of the phase, and thus the EDM systematic shift, can be zeroed out.

We also found that $\partial\phi/\partial\Delta_0$ changed with preparation laser beam shape and time-averaged power (see Figure 7.5C). Typically all laser profiles are Gaussian, stretched in the vertical direction, a shown in Figure 7.6A. When we clipped the downstream side of the preparation laser beam with a razor blade (Figure 7.6B) or used spherical aberration to produce a sharp cutoff on the downstream side of the beam (Figure 7.6C), then $|\partial\phi/\partial\Delta_0|$ decreased for all polarization angles. We saw no such change when the upstream side of the laser beam was clipped. The spherical abberation beam shaping method, described in Chapter .4, was eventually adopted because it produced a steeper intensity cutoff and smaller diffraction pattern than the razor clipping method. A similar decrease in $|\partial\phi/\partial\Delta_0|$ was observed when the time-averaged preparation laser power was decreased by a factor of two by adding a chopper wheel

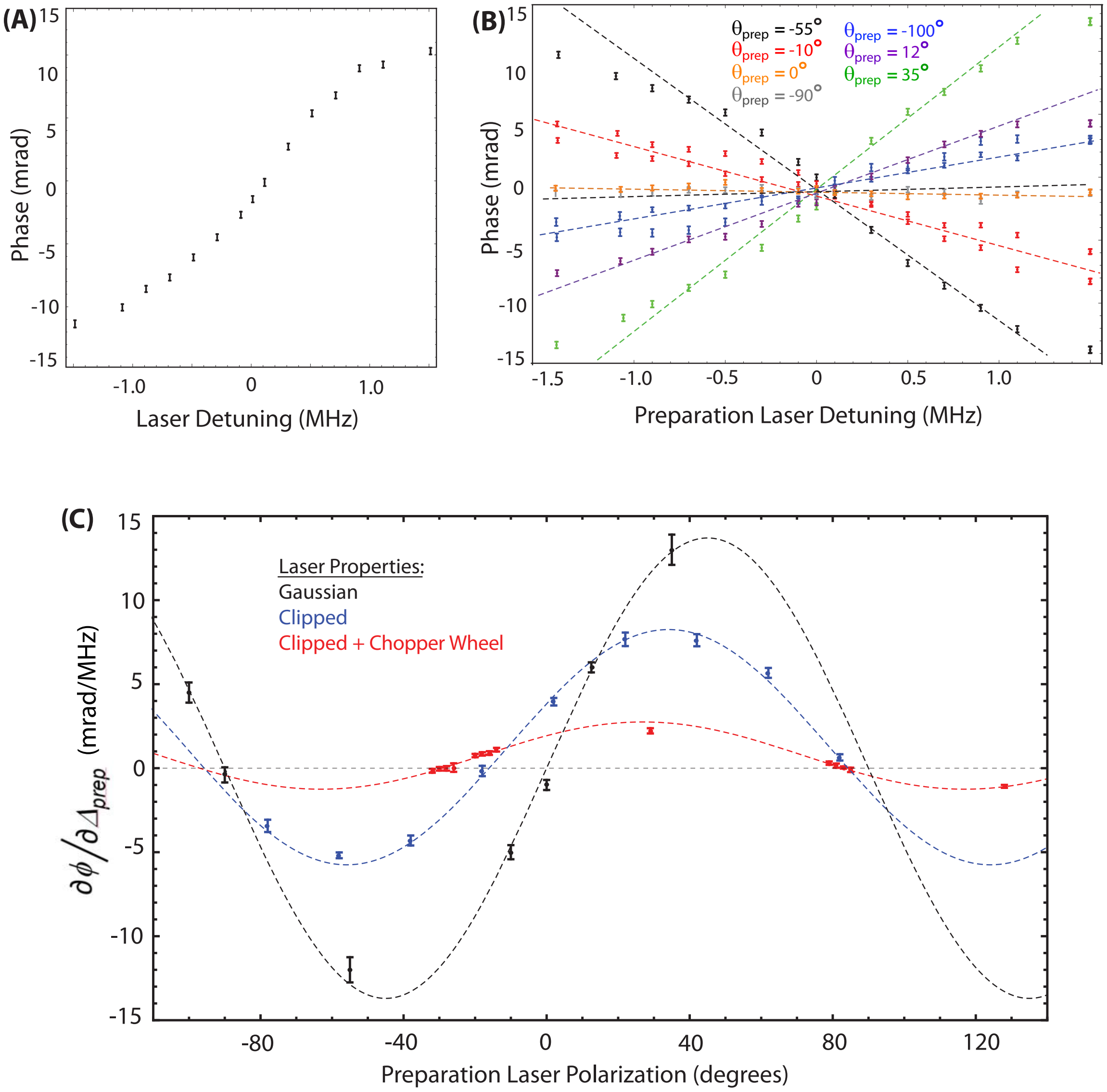

Figure 7.5: **(A)** Molecule phase as a function of preparation laser detuning. The slope agrees with originally observed $\phi^{\mathcal{NE}}$ dependence on $\Delta^{\mathcal{NE}}$. **(B)** Phase dependence on detuning for multiple preparation laser polarization angles. **(C)** $\partial\phi/\partial\Delta_0$ shows clear sinusoidal dependence on preparation laser polarization. The magnitude of $\partial\phi/\partial\Delta_0$ decreases for all polarization angles when the Gaussian beam tails are clipped (blue) and the laser power is reduced (red).

which blocked the preparation laser beam when molecules were not present in the interaction region (i.e. between ablation laser pulses). With the chopper wheel the preparation laser light was on for 10 ms and then blocked for 10 ms.

By independently stepping the preparation laser detuning, Δ_{prep}, and the readout laser detuning, Δ_{read}, we found the phase contribution arising from Δ_{prep} was much larger than that of Δ_{read} (see Figure 7.7). This is consistent with the sinusoidal θ-dependence of $\partial\phi/\partial\Delta_0$ (Figure 7.5) and the fact that the readout laser is rapidly switched between two orthogonal polarizations. The orthogonal $\hat{X}$ and $\hat{Y}$ components of the readout laser correspond to roughly equal and opposite phase vs detuning slopes, and therefore acquire opposite phase shifts, ϕ_{shift}. The resulting fluorescence signals $\hat{X}$ and $\hat{Y}$ are

$$F_X = N_0\left[\frac{1-\mathcal{C}}{2} + \mathcal{C}\cos^2(\phi+\theta+\phi_{\text{shift}})\right], \tag{7.8}$$

$$F_Y = N_0\left[\frac{1-\mathcal{C}}{2} + \mathcal{C}\sin^2(\phi-\theta+\phi_{\text{shift}})\right]. \tag{7.9}$$

Where ϕ is the molecule precession phase, θ is the polarization of the $\hat{X}$ beam, and ϕ_{shift} is the systematic phase shift. When these fluorescence signals are combined to form asymmetry, the phase shifts are suppressed:

$$\mathcal{A} = \frac{F_X - F_Y}{F_X + F_Y} \approx \mathcal{C}\cos(2\phi+2\theta) + \mathcal{C}^2\sin(4\phi+4\theta)\phi_{\text{shift}}. \tag{7.10}$$

Here it is assumed that $\phi_{\text{shift}} << \phi+\theta$. Since we operate on the side of the asymmetry fringe with $\phi+\theta \approx \pi/4$, the contribution of ϕ_{shift} is largely suppressed. Indeed, all data indicated that $\partial\phi/\partial\Delta_{\text{read}}$ was completely independent of the readout laser polarization, and instead depended on θ_{prep}. Figure 7.7 shows $\partial\phi/\partial\Delta_{\text{read}}$ as a function

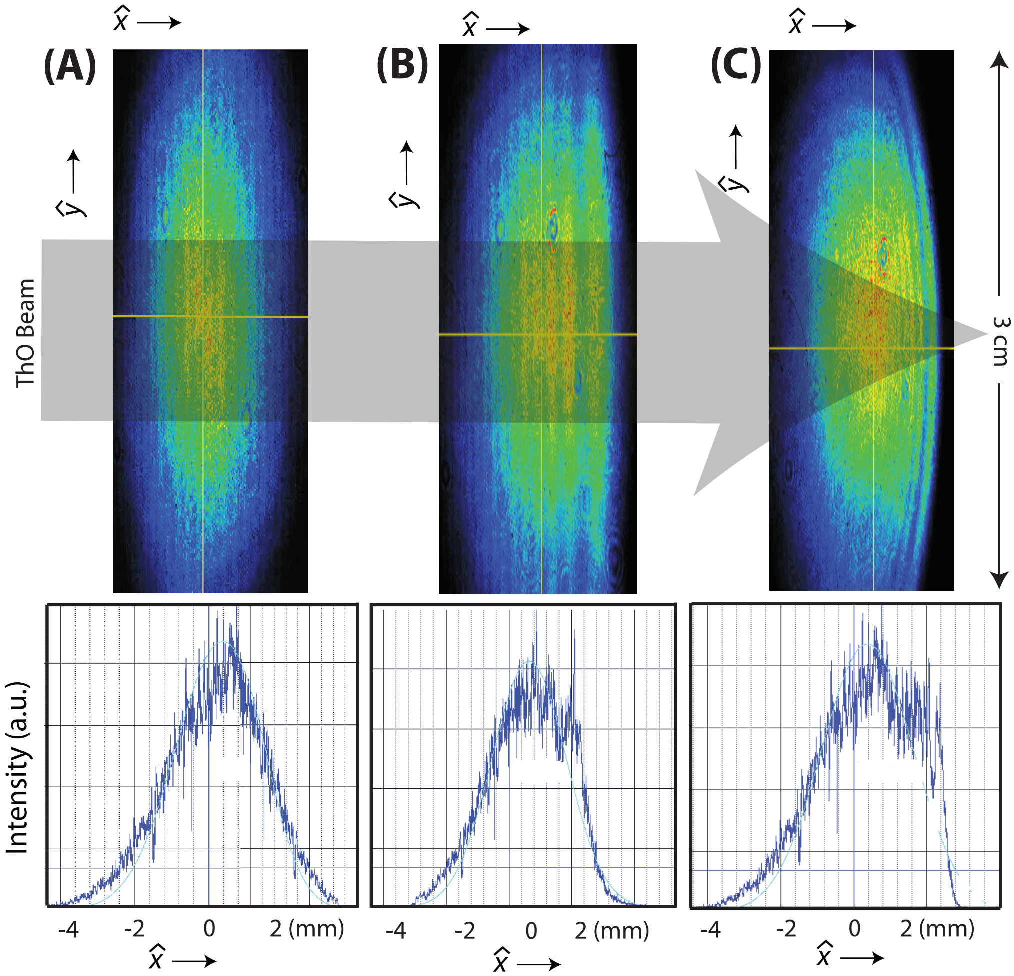

Figure 7.6: **(A)** Vertically stretched Gaussian laser beam profile.**(B)** Laser beam clipped by razor blades, imaged at distance equivalent to center of interaction region. Diffraction limits the steepness of the intensity cutoff. **(C)** A steep intensity cutoff can be achieved by utilizing spherical aberration from beam expansion lenses. In all cases laser beams are vertically stretched to ~3 times the vertical distribution of the molecule beam.

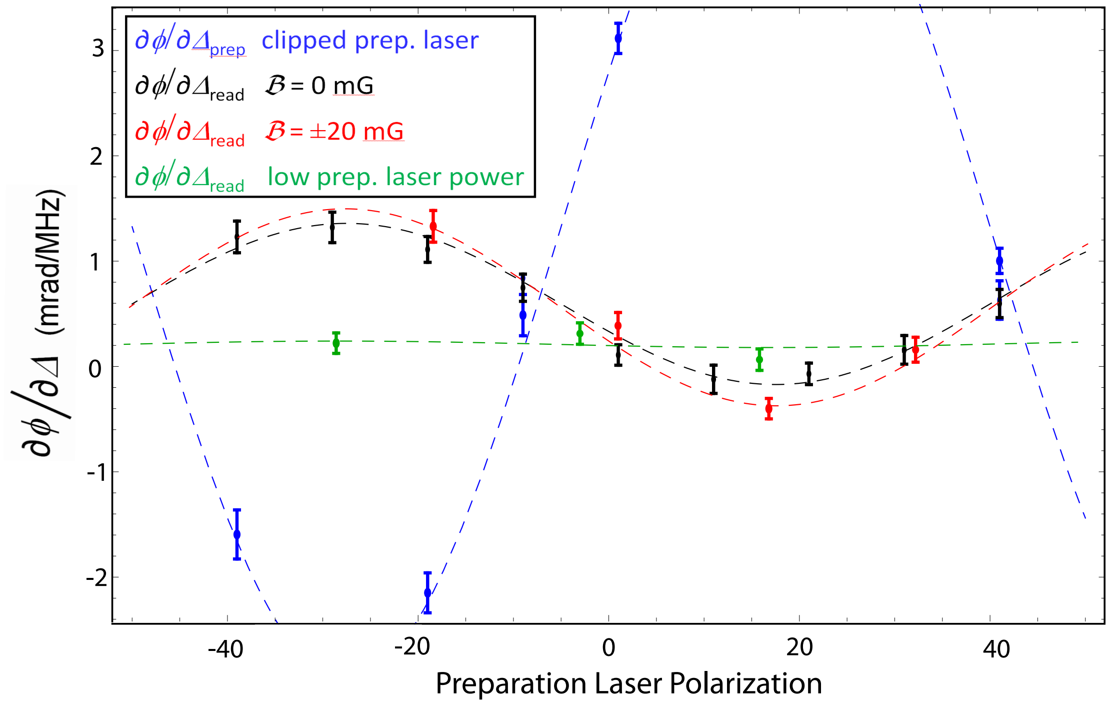

Figure 7.7: Comparison of phase dependence of preparation laser detuning vs readout laser detuning. Data reveals that $\partial\phi/\partial\Delta_{\mathrm{read}}$ (black) is much smaller than $\partial\phi/\partial\Delta_{\mathrm{prep}}$ (blue) and opposite in sign. Moreover, when a 20 mG magnetic field is applied and θ_{read} is shifted by $\pi/4$ (red), there is no change in $\partial\phi/\partial\Delta_{\mathrm{read}}$. This implies that $\partial\phi/\partial\Delta_{\mathrm{read}}$ is primarily caused by the polarization gradient in the preparation laser, not the readout laser. This is confirmed by the fact that $\partial\phi/\partial\Delta_{\mathrm{read}}$ significantly decreases when the preparation laser power is reduced (green).

of θ_{prep} for $\mathcal{B} = 0$ data and $|\mathcal{B}| = 20$ mG data. As discussed in the previous chapter and illustrate in Figure 6.2, the averaged readout laser polarization for $|\mathcal{B}| = 20$ mG data is $\pi/4$ rad offset from that of $\mathcal{B} = 0$ data. The fact that the sinusoidal dependence of $\partial\phi/\partial\Delta_{\text{read}}$ on θ_{prep} in Figure 7.7 is similar for both $\mathcal{B} = 0$ and $|\mathcal{B}| = 20$ mG, instead of being out of phase by $\pi/4$ rad, implies that $\partial\phi/\partial\Delta_{\text{read}}$ depends largely on θ_{prep}. Similarly, we observed that $\partial\phi/\partial\Delta_{\text{read}}$ changed with with preparation laser beam profile and time-averaged power, but not with readout laser beam profile and time-averaged power.

The observed behavior of $\partial\phi/\partial\Delta_{\text{read}}$ can be explained by considering that, because of Doppler shifts, Δ_{read} chooses which of the molecule beam transverse velocity components contribute to the fluorescence signals by which the phase is measured,

$$\bar{v}_z = a\Delta_{\text{read}}\lambda, \tag{7.11}$$

where λ is the laser wavelength, $\bar{v}_z$ is the average transverse velocity of molecules excited by the readout laser, and a is a proportionality constant between 0 and 1 that accounts for effects of nonzero laser linewidth, power broadening, and finite molecule molecule Doppler width. Because of Doppler shifts, laser detuning varies across the molecule beam transverse velocity distribution. Therefore if $\partial\phi/\partial\Delta_{\text{prep}} \neq 0$, then the phase will also vary across the molecule beam. According to Equation 7.12, this will lead to nonzero $\partial\phi/\partial\Delta_{\text{read}}$:

$$\frac{\partial\phi}{\partial\Delta_{\text{prep}}} = -\frac{\partial\phi}{\partial\Delta_{\text{Doppler}}} = -\lambda\frac{\partial\phi}{\partial\bar{v}_z} = -a\frac{\partial\phi}{\partial\Delta_{\text{read}}}. \tag{7.12}$$

Notice that the phase dependence on the Δ_{read} is opposite that of Δ_{prep}, in agreement with the plot in Figure 7.7. The proportionality constant, $a \approx 0.2$, determined by comparing Δ_{read} to Δ_{prep} in Figure 7.7, is also consistent with typical readout laser power broadening. This Doppler shift model is consistent with all observed behavior of $\partial\phi/\partial\Delta_{\text{read}}$. In the future this model can be further tested by adjusting readout laser intensity and/or linewidth, which should both change the value a.

7.2.4 Polarization Gradients

Although we had discovered three laser parameters (polarization, shape, and power) that changed the detuning-dependence of molecule phase, we did not fully understand the mechanism that produced this dependence until we precisely measured the laser properties. An important imperfection the the preparation and readout laser beams was discovered when we precisely measured the polarization with a polarimetry device similar to the one described in [91]. Before the lasers entered the interaction region, lasers passed through high extinction ratio (ER) polarizing beam splitters (Thorlabs GL15-C). Their measured polarization was very linear and uniform throughout all parts of the expanded beams for a wide range of laser powers (0.5-4 W). However, upon exiting the vacuum chamber, the laser ellipticity, θ_{e}, varied across the $\hat{x}$ direction of the laser beams [71], as shown in Figure 7.8. Furthermore, this polarization gradient, $\partial\theta_{\text{e}}/\partial x$ showed sinusoidal dependence on the laser polarization, similar to the dependence of $\partial\phi/\partial\Delta_0$. Like the detuning dependence of the phase, the polarization gradient also scaled with time-averaged laser power. The gradient decreased when the output laser power of the Nufern fiber amplifiers was decreased, and when the previously described chopper wheel was installed.

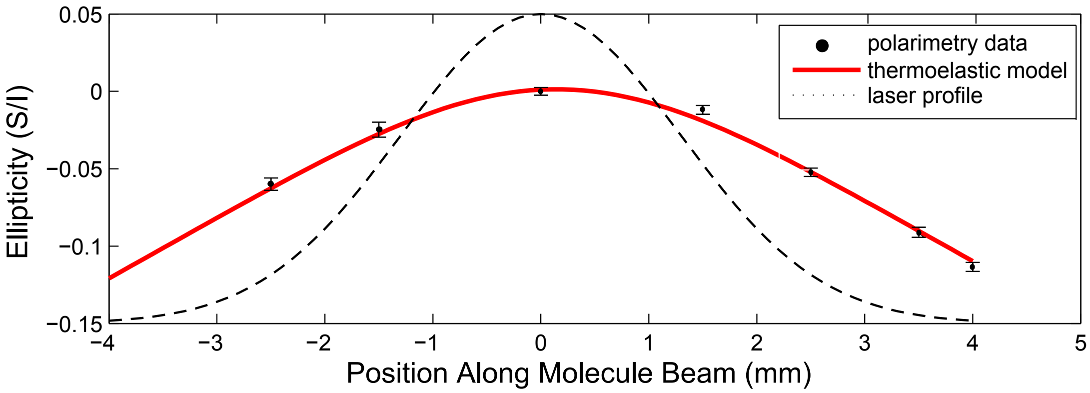

Figure 7.8: Measurements of ellipticity (quantified by Stokes parameters S and I) across the preparation and readout laser beams show a clear circular polarization gradient [71]. This data agrees with a thermoelectic model of the effects of laser-induced heating of the field plates [61]. Polarimetry measurements were performed by Paul Hess and the thermoelastic analysis was performed by Nick Hutzler.

Each laser beam propagates through four glass components (two electric field plates and two vacuum windows) when traveling from one side of the interaction region to the other. Clearly, one or more of these components was exhibiting birefringence. The fact that birefringence changed with laser power indicated that thermal stress, caused by the multi-watt lasers themselves, was the source of the birefringence. This was supported by the fact that the birefringence axes, which corresponds to the zero-crossing of the sinusoidal $\partial\theta_{\mathrm{e}}/\partial x$ and $\partial\phi/\partial\Delta_0$ curves, matched up with the long and short axes of the stretched laser beam profile. We suspected that the birefringent elements were the electric field plates instead of the vacuum windows because they were thicker (0.5 in vs of 0.12 in), made of less uniform glass (float glass vs borosilicate), and were more absorptive of 1090 nm light because of their ITO coating. One check of this comes from an analysis of the thermoelastic effects of laser-induced heating of the electric field plates, as described in our upcoming paper [72] and Nick Hutzler's thesis [61]. The results of this analysis were consistent with our experimental observations, with the predicted birefringence falling within the range of the measured birefringence mean and uncertainty (see Figure 7.8).

7.2.5 Light Shift Model

The behavior of laser ellipticity gradient closely followed the behavior of detuning dependence of the phase, $\partial\phi/\partial\Delta_0$; both clearly scale with time-averaged laser power and in terms of laser polarization as $\sin(\theta)$. This led us to numerically simulate the effect of the gradient on molecule phase by integrating the Schrödinger equation. The results of the this analysis qualitatively agreed with our experimental observations. It allowed us to explain from first principles the mechanism producing the detuning-dependent phase and resulting EDM systematic effect. Here we summarize the results and important components of this model, which is described elsewhere in full detail [72, 61].

To illustrate the basic idea of the light shift model we approximate the Gaussian laser beam as a more intense circular area surrounded by a less intense ring area [3]. In the center bright region the laser intensity is sufficiently high to drive the ThO population from the H state to the C state within the ThO fly-though interaction time with the laser. Specifically, $\Omega_{\mathrm{r}} \gtrsim 1/\tau_{\mathrm{f.t.}}$, where Ω_{r} is the $H \rightarrow C$ Rabi frequency and $\tau_{\mathrm{f.t.}} \approx 10\mu\mathrm{s}$ is the molecule-laser interaction time. In this laser region the coherent dark state is either either prepared, by the state-preparation laser, or read out, by

---

[3] Because the laser beams are vertically stretched with an aspect ratio > 5, we will treat the laser as a 1-D Gaussian beam and only consider the dimension of molecule forward trajectory.

the readout laser. However, in the dim regions of the laser beam the laser intensity is not high enough to transfer ThO population. Instead, the less intense laser light ac Stark shifts (light shifts) the molecular states. The dim regions that affect our measurement are between the bright regions of the preparation and readout lasers, (i.e. the downstream tail of the preparation beam and the upstream tail of the readout beam). Light shifts that occur in other dim regions do not influence our data, either because the coherent state has not yet been created, or because the molecule phase has already been read out.

Once the dark state is created by the bright portion of the preparation laser, the dim laser region will only interact with the dark state if it has different polarization than the bright laser region (i.e. a polarization gradient), or if the state has precessed between laser regions, as would be the case with an applied magnetic field. Otherwise, the prepared state will remain dark to all regions of the laser beam and no ac Stark shifts will be induced. If the preparation laser polarization or molecule state has changed between bright and dim regions, then the dim light will induce an additional light shift phase, ϕ_{ls}. This phase will depend on laser detuning, laser intensity, the time the molecules spend in the dim laser region, and the extent of the polarization gradient or state precession across the laser beam [72, 61],

$$\phi_{\mathrm{ls}} \approx \alpha_{\mathrm{e}}\Delta + \alpha_{\mathrm{l}}\Omega_{\mathrm{r}} + \tilde{\mathcal{B}}|\mathcal{B}|\left(\beta_1\Omega_{\mathrm{r}} + \beta_2\Delta^2\right). \tag{7.13}$$

Here α_{e} and α_{l} depend on the laser elliptical and linear polarization gradient, respectively, and β_1 and β_2 arise from the state precession produced by a magnetic field. All coefficients also depend on the shape of the laser beam, since this shape determines how much time the molecules spend in the dim laser region. For example, if the downstream portion of the otherwise Gaussian preparation laser beam is clipped, then the induced light shift phase will decrease, as we originally observed (Figure 7.5C). It should be noted that while α_{e} and α_{l} will be zero if there is no laser polarization gradient, β_1 and β_2 are always nonzero; there is no way to avoid molecule state precession across the laser beam in a magnetic field.

While Equation 7.13 corresponds to the light shift phase induced by the preparation laser, the effect of the readout laser will be similar, though more complex. This effect is complicated by the fact that the readout laser is switched between four different laser polarizations, $\hat{X} \pm \Delta\theta$ and $\hat{Y} \pm \Delta\theta$, in a data block. As previously discussed, the $\hat{X}$-$\hat{Y}$ polarization switching leads to suppression of light shift phases induced by the readout laser polarization gradient.

Equation 7.13 shows that if an elliptical polarization gradient is present across the preparation laser, the laser will induce a light shift phase in the molecules that scales linearly with detuning. If the detuning is correlated with $\tilde{\mathcal{N}}\tilde{\mathcal{E}}$, as is the case with a non-reversing electric field, then ϕ_{ls} will also be correlated with $\tilde{\mathcal{N}}\tilde{\mathcal{E}}$, producing an EDM systematic offset,

$$d_{e,\mathrm{syst}} = \frac{\hbar\omega^{\mathcal{N}\mathcal{E}}_{\mathrm{syst}}}{\mathcal{E}_{\mathrm{eff}}} = \frac{\alpha_{\mathrm{e}}\hbar\Delta^{\mathcal{N}\mathcal{E}}}{\mathcal{E}_{\mathrm{eff}}\tau} = \frac{\alpha_{\mathrm{e}} d_H \mathcal{E}_{\mathrm{nr}}}{\mathcal{E}_{\mathrm{eff}}\tau}. \tag{7.14}$$

Our explanation of why $\mathcal{E}_{\mathrm{nr}}$ systematically shifted the measured EDM value is complete. We will now describe the effects that the α_{l}, β_1, and β_2 light shift terms have on our data.

7.2.6 Correlated Rabi Frequency

Two terms in Equation 7.13 scale linearly with Ω_{r}, with one of the terms also depending on the sign and magnitude of magnetic field. Similar to the $\tilde{\mathcal{N}}\tilde{\mathcal{E}}$-correlated detuning produced by $\mathcal{E}_{\mathrm{nr}}$, an $\tilde{\mathcal{N}}\tilde{\mathcal{E}}$-correlated Rabi frequency, $\Omega_{\mathrm{r}}^{\mathcal{N}\mathcal{E}}$ will lead to a systematic EDM offset, if $\alpha_l \neq 0$, and $\omega^{\mathcal{N}\mathcal{E}\mathcal{B}} \neq 0$ because of the β_1 term. We carefully monitor our preparation and readout lasers to ensure the laser power and intensity do not vary with any experimental parameter switches. However, it is possible for nonzero $\Omega_{\mathrm{r}}^{\mathcal{N}\mathcal{E}}$ to arise from interference between the $H \rightarrow C$ E1 and M1 transitions driven by the preparation and readout lasers. Although E1 and M1 transitions have different selection rules, both transitions are allowed because H and C are both compositions of electronic spin states, $H \Rightarrow [98.4\%{}^3\Delta_1, 1.1\%{}^3\Pi_1, 0.5\%{}^1\Pi_0]$, and $C \Rightarrow [76.6\%{}^1\Pi_0, 19.5\%{}^3\Pi_1, 1.5\%{}^3\Delta_1, ...]$, and because $|H, \mathcal{N} \pm 1, M_J = \pm 1\rangle$ levels have mixed parity in an electric field. For E1-M1 interference to produce a nonzero $\Omega_{\mathrm{r}}^{\mathcal{N}\mathcal{E}}$, there must be a complex phase between the E1 and M1 amplitudes, as detailed in [72] and [61]. While the presence of this complex phase has not yet been confirmed by theory, we observe strong evidence of nonzero $\Omega_{\mathrm{r}}^{\mathcal{N}\mathcal{E}}$ in our apparatus. We therefore include in our systematic uncertainty a contribution from a light shift phase coupling to $\Omega_{\mathrm{r}}^{\mathcal{N}\mathcal{E}}$.

Measurements of nonzero $\tilde{\mathcal{N}}\tilde{\mathcal{E}}$-correlated fluorescence signal, $F^{\mathcal{N}\mathcal{E}}$, and $\tilde{\mathcal{N}}\tilde{\mathcal{E}}\tilde{\mathcal{B}}$-correlated phase, $\omega^{\mathcal{N}\mathcal{E}\mathcal{B}}$, provided the first evidence that $\Omega_{\mathrm{r}}^{\mathcal{N}\mathcal{E}}$ existed in our system. Only after extensive integration (June 4-11, 2014), was it obvious that $\omega^{\mathcal{N}\mathcal{E}\mathcal{B}}$ scaled linearly with $|\mathcal{B}|$, as predicted by Equation 7.13. One consequence of E1-M1 interference is that the sign of $\Omega_{\mathrm{r}}^{\mathcal{N}\mathcal{E}}$ should depend on the laser propagation direction, $\hat{k}$.

This is because $\hat{k}$ determines the sign of the relative phase between the oscillating electric and magnetic fields of the laser in the lab frame. When we reversed $\hat{k}$ for our preparation and readout lasers, $\omega^{\mathcal{N}\mathcal{E}\mathcal{B}}$ and $F^{\mathcal{N}\mathcal{E}}$ also reversed, consistent with the prediction of E1-M1 interference.

Furthermore, both $\omega^{\mathcal{N}\mathcal{E}\mathcal{B}}$ and $F^{\mathcal{N}\mathcal{E}}$ showed clear linear dependence on an artificial $\Omega_{\mathrm{r}}^{\mathcal{N}\mathcal{E}}$ that we applied by correlating a component of the laser power with $\tilde{\mathcal{N}}\tilde{\mathcal{E}}$ using AOMs placed after the preparation and readout laser fiber amplifiers. When the ratio of $\tilde{\mathcal{N}}\tilde{\mathcal{E}}$-correlated laser power to average laser power, $\mathrm{P}^{\mathcal{N}\mathcal{E}}/\mathrm{P}_0$, was +1.8% (–1.6%) with lasers propagating parallel (antiparallel) to $\hat{z}$, there was no offset in $\omega^{\mathcal{N}\mathcal{E}\mathcal{B}}$ (see Figure 7.9). Under those conditions the applied artificial component of $\Omega_{\mathrm{r}}^{\mathcal{N}\mathcal{E}}$ is equal and opposite to the component of $\Omega_{\mathrm{r}}^{\mathcal{N}\mathcal{E}}$ caused by E1-M1 interference. Assuming the $\mathcal{N}\mathcal{E}$-correlated component of Rabi frequency is small compared to the average Rabi frequency, $\mathrm{P}^{\mathcal{N}\mathcal{E}}/\mathrm{P}_0$ can be converted to $\Omega_{\mathrm{r}}^{\mathcal{N}\mathcal{E}}/\Omega_{\mathrm{r}}$ using the conventional relationship between laser power and Rabi frequency,

$$\begin{aligned}
\mathrm{P}_0 + \mathrm{P}^{\mathcal{N}\mathcal{E}} &= \frac{A\hbar^2}{d_{H\to C}^2}\left(\Omega_{rmr} + \Omega_{rmr}^{\mathcal{N}\mathcal{E}}\right)^2, && (7.15)\\
\mathrm{P}_0\left(1 + \frac{\mathrm{P}^{\mathcal{N}\mathcal{E}}}{\mathrm{P}_0}\right) &\approx \left(\frac{A\hbar^2\Omega_{\mathrm{r}}}{d_{H\to C}^2}\right)\left(1 + \frac{2\Omega_{\mathrm{r}}^{\mathcal{N}\mathcal{E}}}{\Omega_{\mathrm{r}}}\right), && (7.16)\\
\mathrm{P}_0\left(1 + \frac{\mathrm{P}^{\mathcal{N}\mathcal{E}}}{\mathrm{P}_0}\right) &\approx \mathrm{P}_0\left(1 + \frac{2\Omega_{\mathrm{r}}^{\mathcal{N}\mathcal{E}}}{\Omega_{\mathrm{r}}}\right), && (7.17)\\
\frac{\mathrm{P}^{\mathcal{N}\mathcal{E}}}{\mathrm{P}_0} &= \frac{2\Omega_{\mathrm{r}}^{\mathcal{N}\mathcal{E}}}{\Omega_{\mathrm{r}}}, && (7.18)
\end{aligned}$$

where A is the area of the laser profile and $d_{H\to C}$ is the transition dipole between the H and C states. Thus the data shown in Figure 7.9 indicates that the $\tilde{\mathcal{N}}\tilde{\mathcal{E}}$-correlated Rabi frequency resulting from E1-M1 interference is $\Omega_{\mathrm{r}}^{\mathcal{N}\mathcal{E}}/\Omega_{\mathrm{r}} = (-8.3\pm.8)\times10^{-3}(\hat{k}\cdot\hat{z})$.

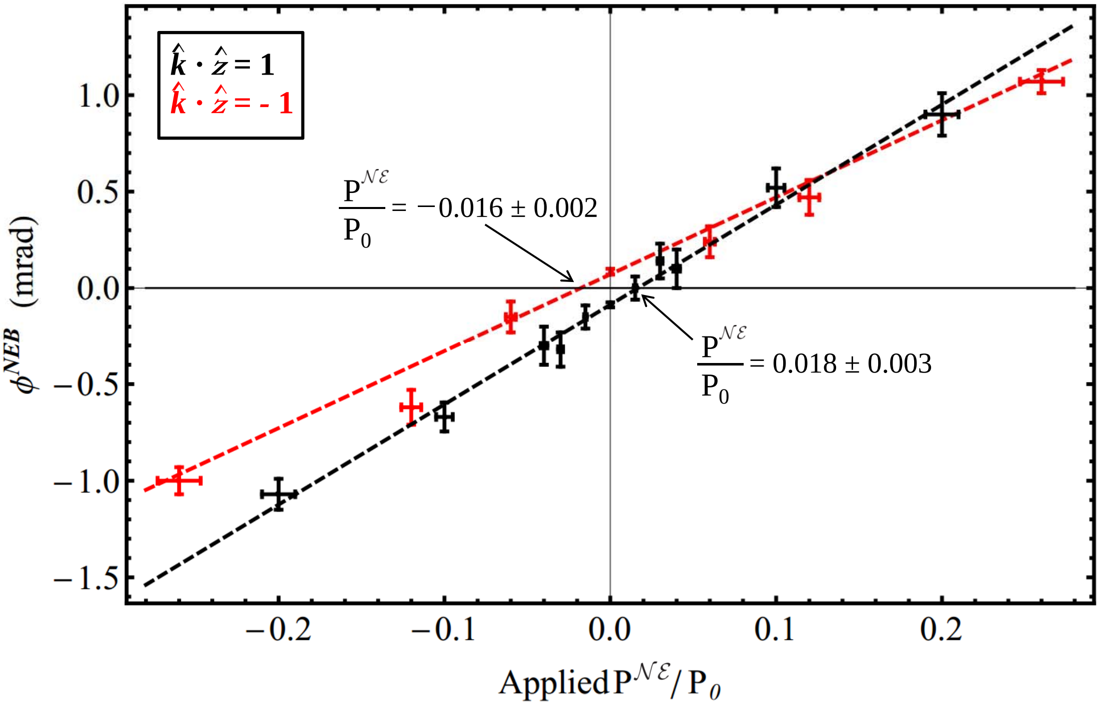

Figure 7.9: $\tilde{\mathcal{N}}\tilde{\mathcal{E}}\tilde{\mathcal{B}}$-correlated phase as a function of applied $\tilde{\mathcal{N}}\tilde{\mathcal{E}}$-correlated laser power, $\mathrm{P}^{\mathcal{N}\mathcal{E}}$, with preparation and readout lasers propagating east (black) and west (red). The artificial $\tilde{\mathcal{N}}\tilde{\mathcal{E}}$-correlated Rabi frequency resulting from $\mathrm{P}^{\mathcal{N}\mathcal{E}}$ systematically shifts $\omega^{\mathcal{N}\mathcal{E}\mathcal{B}}$ in accordance with Equation 7.13. $\omega^{\mathcal{N}\mathcal{E}\mathcal{B}}$ is zero when the the applied $\mathrm{P}^{\mathcal{N}\mathcal{E}}$ cancels out the component of $\Omega_{\mathrm{r}}^{\mathcal{N}\mathcal{E}}$ caused by E1-M1 interference, so that there is no net $\tilde{\mathcal{N}}\tilde{\mathcal{E}}$-correlated Rabi frequency.

Unlike the light shift phase resulting from a laser ellipticity gradient that we could independently measure and control, it was not clear that the lasers had a linear polarization gradient. The polarimetry device used to measure the laser ellipticity gradient was not sufficiently sensitive to detect an significant linear polarization gradient [71]. We measured α_{l} and β_1 by rapidly stepping the preparation and readout laser intensity, in the same way that we had previously rapidly stepped the laser frequency. While β_1 was clearly nonzero, as expected from the observed offset of of $\omega^{\mathcal{NEB}}$, α_{l} was only nonzero when we failed to place a cleanup polarizer after the AOMs stepping the laser power. This indicates that the AOM might have produced a small linear polarization gradient, too small to measure with the polarimeter but large enough to cause significant phase dependence on Ω_{r}.

7.2.7 Nonlinear Detuning-Dependent Phase

The last term in Equation 7.13 corresponds to a quadratic detuning-dependence of the light shift phase. This dependence scales with $\mathcal{B}$ since it arises from magnetically induced precession through the laser beam. We observed this quadratic dependence in $\phi^{\mathcal{B}}$ when rapidly stepping laser detuning (see Figure 7.10), which allowed us to extract $\beta_2 \approx 5$ mrad/MHz^2. Unlike light shifts from ellipticity gradients this effect was comparable for both preparation and readout lasers. To the extent that the magnetic field perfectly reverses, this effect will not produce a systematic EDM offset, but rather an offset in $\omega^{\mathcal{NEB}}$, in the presence of a non-reversing electric field. Because this effect depends quadratically on detuning, $\omega^{\mathcal{NEB}}$ will only shift if there is an overall laser detuning in addition $\mathcal{E}_{\mathrm{nr}}$. In the limit of small detuning,

$$\omega_{\text{syst}}^{\mathcal{NEB}} \approx \frac{2\beta_2 \Delta_0 d_H \mathcal{E}_{\text{nr}}}{\hbar \tau}. \tag{7.19}$$

Because this phase effect reverses with $\tilde{\mathcal{B}}$ and quadratically depends on detuning, it will only shift the EDM value if the lasers are off resonant $\Delta_0 \neq 0$ throughout the data set, and if there is a component of magnetic field, $\mathcal{B}_{rmnr}$, that doesn't perfectly reverse with $\tilde{\mathcal{B}}$. The measured average values of these experimental parameters during normal operating conditions, $\Delta_0 < 0.01$ MHz and $\mathcal{B}_{rmnr} < 50$ μG, would produce a systematic EDM shift at least three orders of magnitude below the statistical precision of the EDM measurement.

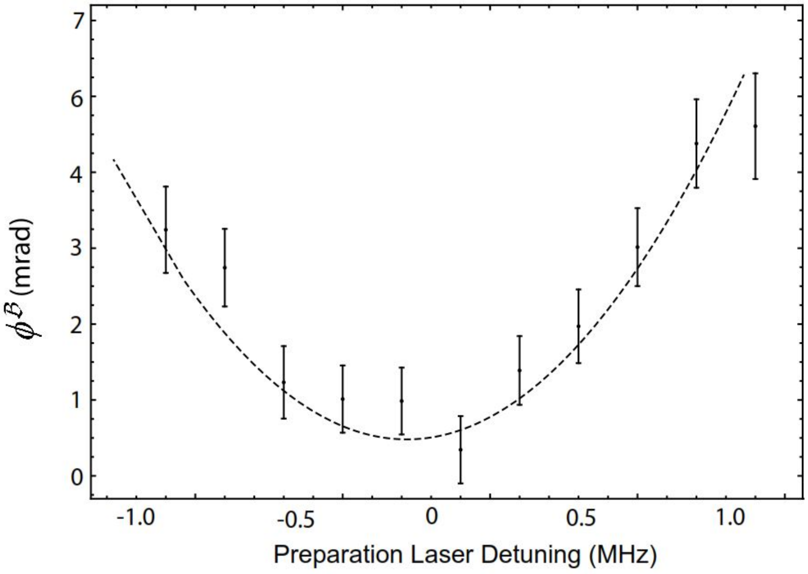

Figure 7.10: The quadratic detuning-dependence of phase, resulting from light shifts, which scales and reverses with magnetic field.

7.2.8 Suppressing and Monitoring Light Shift Effects

As Table 7.3 indicates, all systematic shifts and uncertainty resulting from light shifts were suppressed well below the EDM statistical uncertainty. We suppressed the

Table 7.4: Measured systematic $\omega^{\mathcal{N}\mathcal{E}}$ shifts and uncertainties for light shift effects coupling to $\mathcal{E}_{\mathrm{nr}}$ and $\Omega_{\mathrm{r}}^{\mathcal{N}\mathcal{E}}$. Values are based on intentional parameter exaggeration data acquired throughout EDM data set. Separate corrections were applied for different laser propagation directions and different magnetic fields. In EDM units, 1.3 mrad/s $\approx 10^{-29}$ e cm. Values listed here are from my analysis only and may differ slightly from those reported in [4, 72]

$\hat{k}\cdot\hat{z}$	1	1	-1	-1
$\lvert\mathcal{B}\rvert$	1 or 38 mG	19 mG	1 or 38 mG	19 mG
$\mathcal{E}_{\mathrm{nr}}$ [mV/cm]	-4 ± 1	-4 ± 1	-5 ± 1	-5 ± 1
$\partial\omega^{\mathcal{N}\mathcal{E}}/\partial\mathcal{E}_{\mathrm{nr}}$ [mrad/(mV/cm)]	0.13 ± 0.57	0.13 ± 0.13	-0.51 ± 0.13	-0.26 ± 0.13
$\mathcal{E}_{\mathrm{nr}}$ Systematic shift [mrad]	-0.5	-0.5	2.3	1.3
$\mathcal{E}_{\mathrm{nr}}$ Systematic uncertainty [mrad]	2.3	0.5	0.8	0.7
$\Omega_{\mathrm{r}}^{\mathcal{N}\mathcal{E}}/\Omega_{\mathrm{r}}\times 10^{-3}$	-8.3 ± 0.8	-8.3 ± 0.8	-8.3 ± 0.8	-8.3 ± 0.8
$\partial\omega^{\mathcal{N}\mathcal{E}}/\partial(\Omega_{\mathrm{r}}^{\mathcal{N}\mathcal{E}}/\Omega_{\mathrm{r}})\mathcal{E}_{\mathrm{nr}}$ [mrad/Ω_{r}]	0 ± 730	0 ± 610	-270 ± 230	-300 ± 210
$\Omega_{\mathrm{r}}^{\mathcal{N}\mathcal{E}}$ Systematic shift [mrad]	0	0	-2.2	-2.5
$\Omega_{\mathrm{r}}^{\mathcal{N}\mathcal{E}}$ Systematic uncertainty [mrad]	6.0	5.0	1.9	1.7

effect coupling to $\mathcal{E}_{\mathrm{nr}}$ by installing a chopper wheel (10 ms on, 10 ms off) in the path of the preparation laser, and shaping the laser beam to cut off the downstream portion of the Gaussian tail. Preparation laser polarization was then set to one of the two angles corresponding to zero detuning-dependent phase in Figure 7.5C. The polarization was switched between the two zero-crossing angles every 16 data blocks. $\mathcal{E}_{\mathrm{nr}}$ itself was minimized by switching the leads supplying voltage to the field plates every 4 blocks. This suppressed the component of $\mathcal{E}_{\mathrm{nr}}$ resulting from offsets in the voltage supply, but not the component originating from inside the vacuum chamber (e.g. patch potentials). The listed values of $\mathcal{E}_{\mathrm{nr}}$ are from microwave spectroscopy measurements of the $|H, J=1, \mathcal{N}=\pm 1, M=\pm 1\rangle \rightarrow |H, J=2, M=0\rangle$ transition taken soon after the EDM data set. They are consistent with *in situ* $\mathcal{E}_{\mathrm{nr}}$ measurements computed from contrast correlations (see Figure 7.14). We continuously monitored $\omega^{\mathcal{NE}}/\mathcal{E}_{\text{nr}}$ every 3-4 hours throughout our published EDM data set. This slope was separately monitored for each combination of preparation and readout laser polarization. Table 7.4 shows the systematic shifts and uncertainty computed from this data. If $\omega^{\mathcal{NE}}/\mathcal{E}_{\text{nr}}$ was clearly nonzero after sufficient averaging, then we adjusted the value of θ_{prep} accordingly. Only one such adjustment, made in the middle of the August-September data set, was necessary.

Similarly, we suppressed the light shift effect coupling to $\Omega_{rmr}^{\mathcal{NE}}$ by reversing the propagation direction of all preparation and readout lasers midway through the EDM data set. We also monitored $\omega^{\mathcal{NE}}/\Omega_{\text{r}}^{\mathcal{NE}}$ throughout most of the data set. As with the $\mathcal{E}_{\text{nr}}$ systematic, the slope was monitored separately for all laser polarizations (see Table 7.4). Because we were not aware at the time that $\Omega_{\text{r}}^{\mathcal{NE}}$ could be nonzero, we did not monitor this slope for data taken in June, 2014. The slope was measured the following month. Because $\omega^{\mathcal{NE}}/\Omega_{\text{r}}^{\mathcal{NE}}$ was not monitored *in situ* we did not apply a corresponding systematic correction to the mean EDM computed from June, 2014 data. Instead, we added a systematic uncertainty equal to the quadrature sum of the systematic shift and uncertainty measured later in the summer.

7.3 Signal Asymmetry Correlations

Although signal asymmetry is immune to molecule number fluctuations, it can still vary with laser detuning and Rabi frequency if the properties of $\hat{X}$ and $\hat{Y}$ readout laser beams are not identical. Specifically, a pointing mismatch between the two beams leads to linear asymmetry dependence on detuning, and intensity mismatch leads to quadratic asymmetry dependence on detuning. A combination of these two imperfections causes asymmetry to depend on Ω_{r}. Similar to the light shift phase, these effects couple to $\mathcal{E}_{\mathrm{nr}}$ and $\Omega^{\mathcal{N}\mathcal{E}}$ to produce $\tilde{\mathcal{N}}\tilde{\mathcal{E}}$-correlated asymmetry, $\mathcal{A}^{\mathcal{N}\mathcal{E}}$. Because phase is directly computed from asymmetry, as in Equation 6.9, a shift in $\mathcal{A}^{\mathcal{N}\mathcal{E}}$ can cause a shift in $\phi^{\mathcal{N}\mathcal{E}}$ and the EDM value. We completely suppress such potential systematic effects by continuously reversing the sign of $\mathcal{C}$ in Equation 6.9, thereby reversing the dependence of ϕ on $\mathcal{A}$, throughout our EDM data set. That is accomplished through several parameter switches performed within and between blocks of data.

7.3.1 Mismatched Readout Laser Beams

As described in our apparatus chapter, rapid switching between orthogonally polarized $\hat{X}$ and $\hat{Y}$ readout laser beams is accomplished by coupling the beams through separate AOMs and then recombining them on a polarizing beam splitter. In this type of setup, the two beams can not only have different alignment ($\hat{k}_X \neq \hat{k}_Y$), but different power due to unequal AOM efficiencies [4]. The AOMs can also produce different beam profiles. The pointing of the two beams is realigned daily with a high resolution beam profiler placed before and after the interaction region. The relative pointing of the two beams typically drifts by ~100 μrad throughout the day. The intensity of the center portion of the laser beams is also balanced daily and typically fluctuates by 5%. The small horizantal pointing difference, k_{XY}, of the laser beams couples to Doppler shift from the molecular forward velocity, v, to produce a detuning

---

[4] The previously described birefringence effect can also result in $\hat{X}$ and $\hat{Y}$ beams having non-orthogonal polarizations. This can contribute to imperfect contrast, $|\mathcal{C}| < 1$, but does not shift the EDM value to first order (see Figure 7.7).

difference, Δ_{XY}:

$$\Delta_{XY} = \frac{\Delta_X - \Delta_Y}{2} = \frac{\vec{v}\hat{k}_X}{2\lambda} - \frac{\vec{v}\hat{k}_Y}{2\lambda} \approx \frac{v k_{XY}}{\lambda}, \tag{7.20}$$

where $\vec{v}$ is the velocity of the molecule beam, $\Delta_{X(Y)}$ is the detuning of the $\hat{X}(\hat{Y})$ laser beam from resonance. Similarly, the intensity difference, I_{XY}, causes the laser beams to have power broadened linewidths, Γ, that differ by Γ_{XY}. We typically operate in the regime where average readout laser intensity, I_0, is high enough to power-broaden, but not deeply saturate, the $H \to C$ transition beyond the ~2 MHz Doppler broadened width. This linewidth difference can therefore be approximated as

$$\Gamma_{XY} \approx \Gamma_0 \sqrt{\frac{I_{XY}}{I}}, \tag{7.21}$$

where Γ_0 is the average linewidth.

With incomplete laser saturation, the fluorescence corresponding to the $\hat{X}$ and $\hat{Y}$ beams, F_X and F_Y respectively, depends not only on phase, as Equation 3.13 implies, but also on laser detuning and power-broadened linewidth:

$$F_X(\phi, \Delta_0, \Gamma_0) = N_0 \left[\frac{1-\mathcal{C}}{2} + \mathcal{C}\cos^2(\phi + \theta)\right] F_X(\Delta_0, \Gamma_0), \tag{7.22}$$

$$F_Y(\phi, \Delta_0, \Gamma_0) = N_0 \left[\frac{1-\mathcal{C}}{2} + \mathcal{C}\sin^2(\phi + \theta)\right] F_Y(\Delta_0, \Gamma_0) \tag{7.23}$$

where,

$$F_X(\Delta_0, \Gamma_0) = \frac{1/4(\Gamma_0 + \Gamma_{XY})^2}{(\Delta_0 + \Delta_{XY})^2 + 1/4(\Gamma_0 + \Gamma_{XY})^2}, \tag{7.24}$$

$$F_Y(\Delta_0, \Gamma_0) = \frac{1/4(\Gamma_0 - \Gamma_{XY})^2}{(\Delta_0 - \Delta_{XY})^2 + 1/4(\Gamma_0 - \Gamma_{XY})^2} \tag{7.25}$$

If we operate with $\phi+\theta \approx \pi/4$ with lasers near resonance ($\Delta_0 << \Gamma_0$) and small imperfections ($\Gamma_{XY}, \Delta_{XY} << \Gamma_0$), the signal asymmetry computed for the two fluorescence components can be approximated as a component which depends on precession phase and a component which depends on detuning and linewidth, $\mathcal{A} \approx \mathcal{A}(\phi) + \mathcal{A}(\Delta_0, \Gamma_0)$. The first term was previously given by Equation 3.14, and the second term is

$$\mathcal{A}(\Delta_0, \Gamma_0) = \frac{F_X(\Delta_0, \Gamma_0) - F_Y(\Delta_0, \Gamma_0)}{F_X(\Delta_0, \Gamma_0) + F_Y(\Delta_0, \Gamma_0)} \approx \frac{8\Gamma_{XY}\Delta_{XY}^2}{\Gamma_0^3} + \frac{8\Delta_0\Delta_{XY}}{\Gamma_0^2} + \frac{8\Gamma_{XY}\Delta_0^2}{\Gamma_0^3}. \quad (7.26)$$

Notice that $\mathcal{A}(\Delta_0, \Gamma_0)$ vanishes if Δ_{XY} or Γ_{XY} are zero; the detuning and linewidth dependence of signal asymmetry only arises from mismatched properties of the readout laser beams.

7.3.2 Measuring and Suppressing Asymmetry Effects

By measuring asymmetry while stepping Δ_0 and Γ_0 we confirmed the laser detuning and power dependence of asymmetry predicted by each of the terms in Equation 7.26. Laser detuning and power were controlled with AOMs as described in the section on light shifts. To isolate the asymmetry dependence on detuning and power from the corresponding phase dependence, we turned off the preparation laser. This ensured that no coherent dark state would be formed and no phase precession could occur. The results of this data are shown in Figure 7.11. Figure 7.11A shows the linear asymmetry dependence on detuning, predicted by the second term of Equation 7.26, when Δ_{XY} is exaggerated by misaligning the $\hat{X}$ and $\hat{Y}$ beams. It also shows the quadratic dependence (third term of Equation 7.26) that occurs when the laser beams have unequal intensity, and therefore unequal linewidth. The effects of exaggerating both Δ_{XY} and Γ_{XY} at once (first term of Equation 7.26) were not carefully explored. Later, as part of a separate systematic study of the effects of $\Omega_\mathrm{r}^{\mathcal{N}\mathcal{E}}$, we noticed significant asymmetry dependence on laser power even though $\Delta_0 = 0$ (see Figure 7.11B). The laser properties were not well balanced at the time so we attributed this to the dependence predicted by the first term of Equation 7.26.

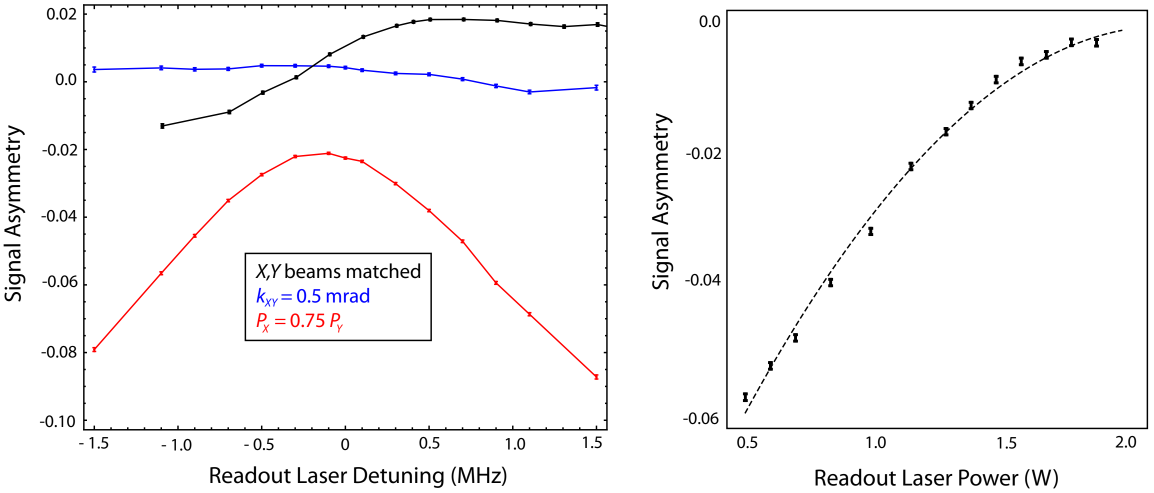

Figure 7.11: Shifts in signal asymmetry resulting from imperfectly matched $\hat{X}$ and $\hat{Y}$ readout beam properties. **(A)** Linear and quadratic detuning-dependence of signal asymmetry resulting from imbalanced probe beam pointing and power, respectively. **(B)** Asymmetry dependence on laser power that occurs when the two probe beams are misaligned and have unequal power.

There are several ways for other experimental imperfections to couple to $\mathcal{A}(\Delta_0, \Gamma_0)$ to produce an $\tilde{\mathcal{N}}\tilde{\mathcal{E}}$-correlated asymmetry. As shown by the first term of Equation 7.26, if both Δ_{XY} and Γ_{XY} or nonzero, $\mathcal{A}^{\mathcal{N}\mathcal{E}}$ will arise from $\Omega_\mathrm{r}^{\mathcal{N}\mathcal{E}}$-induced $\tilde{\mathcal{N}}\tilde{\mathcal{E}}$-correlated linewidth, $\Gamma^{\mathcal{N}\mathcal{E}} = \Gamma_0\sqrt{\Omega_\mathrm{r}^{\mathcal{N}\mathcal{E}}/\Omega_\mathrm{r}}$. If Δ_{XY} is nonzero, $\mathcal{E}_\mathrm{nr}$ will shift $\mathcal{A}^{\mathcal{N}\mathcal{E}}$ by coupling to the detuning-dependence of the second term. Lastly, both $\mathcal{E}_\mathrm{nr}$ and $\Omega_\mathrm{r}^{\mathcal{N}\mathcal{E}}$ will couple to the third term if Γ_{XY} is nonzero and the lasers have drifted off resonance. Given the typical drift in k_{XY} and I_{XY}, these asymmetry effects could produce systematic EDM shifts at least as large as the light shift of the light shift phase effects previously described. It is therefore crucial to prevent asymmetry correlations from becoming phase correlations.

The relationship between phase and signal asymmetry is completely determined by contrast, which can be either positive or negative. If we make two EDM measurements that are identical except that they had equal and opposive values of contrast, then the combined phase from these measurements is immune to asymmetry correlations, such as $\mathcal{A}^{\mathcal{N}\mathcal{E}}$. Thankfully, there are seveal different ways to reverse the sign of contrast without negatively affecting the measurement in any way. First, the magnetic field switch, $\tilde{\mathcal{B}}$, can be used to reverse contrast within a data block. As shown in Figure 6.2, the asymmetry fringe slope changes sign with $\tilde{\mathcal{B}}$ when $|\mathcal{B}| \approx 20$ mG. This results in $\mathcal{A}^{\mathcal{N}\mathcal{E}}$ being translated into $\phi^{\mathcal{N}\mathcal{E}\mathcal{B}}$ instead of the EDM channel. This is beneficial, but not sufficient since we want to also gather data with $|\mathcal{B}| \approx 0$ mG and $|\mathcal{B}| \approx 40$ mG, where contrast does not reverse with $\tilde{\mathcal{B}}$. Another parameter switch, $\tilde{\mathcal{R}}$, also suppresses a correlated asymmetry by rotation the readout laser polarization by $\pi/2$ with respect to preparation laser polarization. This essentially interchanges the polarization $\hat{X}$ and $\hat{Y}$ beams and thereby reverses the sign of beam imperfections Δ_{XY} and Γ_{XY}. Finally, we can reverse contrast by switching the Ω-doublet sublevel of the electronic state, C, used to read out the H state precession phase. This reversal, $\tilde{\mathcal{P}}$, switches the parity of the basis state that the coherent dark state is projected onto by the readout laser. As described in the data analysis chapter, $\tilde{\mathcal{P}}$ and $\tilde{\mathcal{R}}$ are performed on every 1-10 minutes in between blocks of data. Each of these parameter reversals has been demonstrated to suppress asymmetry correlations by a factor of > 100, making the predicted systematic EDM uncertainty from such correlations $< 10^{-31}$ e cm. We do not included a separate systematic uncertainty contribution from asymmetry correlations since their potential effect is already accounted for by monitoring $\partial\omega^{\mathcal{NE}}/\partial\mathcal{E}_{\mathrm{nr}}$ and $\partial\omega^{\mathcal{NE}}/\partial\Omega_{\mathrm{r}}^{\mathcal{NE}}$.

7.4 $\tilde{\mathcal{E}}$-Correlated Phase

Previous electron EDM measurements have often been limited by a variety of systematic effects that produce $\tilde{\mathcal{E}}$-correlated phase, $\omega^{\mathcal{E}}$ [36]. These include $\tilde{\mathcal{E}}$-correlated leakage currents, geometric phases, and motional magnetic fields, which are all described in the first chapter of this thesis. Because past experiments did not have independent control of the internal effective electric field, as we do through reversal of $\mathcal{N}$, these effects could not be distinguished from the phase that would result from a nonzero EDM. Each of these effects scales with the magnitude of applied electric field, which is orders of magnitude smaller in our experiment than any past EDM experiment because of the high polarizability of ThO [36]. Furthermore, shifts from leakage currents and motional magnetic fields couple through the magnetic dipole moment, which is near-zero in the ThO H state. Therefore, we do not expect any significant $\omega^{\mathcal{E}}$ offset in our experiment. Even if these effects did significantly shift our measurement of $\omega^{\mathcal{E}}$, their effect on the EDM value would be largely suppressed since each effect is identical for the two $\mathcal{N}$ states.

The reversal of $\mathcal{N}$, however, does not perfectly suppress an offset of $\omega^{\mathcal{E}}$. This is because the magnetic moments of the two $\mathcal{N}$ levels have different magnetic moments

[92]. As described in the previous chapter. This difference is proportional to $|\mathcal{E}|$ and is the main contribution to $\omega^{\mathcal{N}\mathcal{B}}$. For the higher (142 mV/cm) and lower (36 mV/cm) values of $|\mathcal{E}|$ with which we take EDM data, the magnetic moments differ by ∼0.25% and ∼0.06%, respectively. Therefore, any effect coupling to the magnetic moment to systematically shift $\omega^{\mathcal{E}}$ will also produce a ∼1000-times smaller shift in $\omega^{\mathcal{N}\mathcal{E}}$. We verified this by intentionally correlating a 1.4 mG component of $\mathcal{B}_z$ with $\tilde{\mathcal{E}}$, resulting in a large offset of $\omega^{\mathcal{E}}$ and a ∼1000-times smaller offset of $\omega^{\mathcal{N}\mathcal{E}}$ (see Figure 7.12).

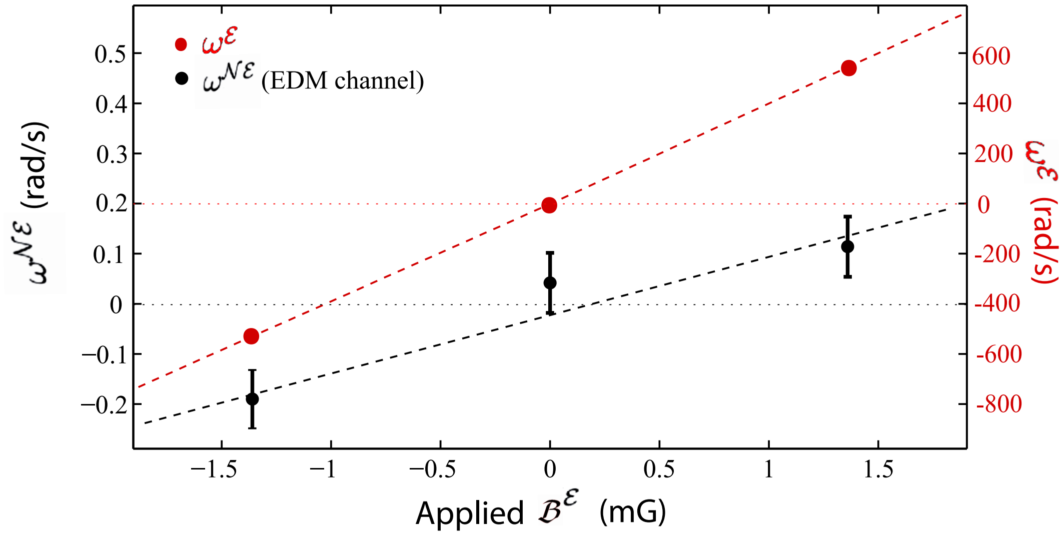

Figure 7.12: Illustration of the ∼1000-fold systematic suppression provided by the $\tilde{N}$ switch. Large shifts of $\omega^{\mathcal{E}}$ occur when a component of $\mathcal{B}_z$ is correlated with $\tilde{\mathcal{E}}$. In previous EDM experiments this would correspond to a systematic shift of the measured EDM value. In our experiment a much smaller shift of $\omega^{\mathcal{N}\mathcal{E}}$ results from the small different in magnetic moments between the two $\mathcal{N}$ levels.

No intentional parameter exaggeration shifted $\omega^{\mathcal{E}}$ other than an $\tilde{\mathcal{E}}$ correlated magnetic field. $\omega^{\mathcal{E}}$ was consistently one of our most robust phase channels. Even large (∼20 mG) magnetic field components along $\hat{x}$ and $\hat{y}$, which exaggerate the effect of motional magnetic fields, did not shift $\omega^{\mathcal{E}}$. $\omega^{\mathcal{E}}$ was also consistent with zero for our reported data set. The mean and uncertainty of $\omega^{\mathcal{E}}$, divided by the measured suppression factor, is included in our $\omega^{\mathcal{NE}}$ systematic error budget.

7.5 $\tilde{\mathcal{N}}$-Correlated Laser Pointing

For a subset of our data, the $\tilde{\mathcal{N}}$-correlated phase $\omega^{\mathcal{N}}$ was nonzero and drifted with time (Figure 7.13A). This behavior was related to an $\tilde{\mathcal{N}}$-correlated laser pointing $k^{\mathcal{N}} \approx 5$ μrad created by the AOMs used for polarization chopping. We minimized $k^{\mathcal{N}}$ and eliminated the drift in $\omega^{\mathcal{N}}$ with improved optical alignment. To study the effect we also exaggerated $k^{\mathcal{N}}$ with mirrors mounted to piezoelectric adjusters and observed that $\partial\omega^{\mathcal{N}}/\partial k^{\mathcal{N}}$ fluctuated significantly (Figure 7.13B). Because we could not identify the mechanism coupling $k^{\mathcal{N}}$ to $\omega^{\mathcal{N}}$, we chose to include in our systematic error budget any effect that might cause fluctuations in $\omega^{\mathcal{N}}$. We looked for correlations between $\omega^{\mathcal{NE}}$ and $\omega^{\mathcal{N}}$, treating the fluctuating $\omega^{\mathcal{N}}$ channel as though it were a tunable parameter. We fit a linear slope to $\partial\omega^{\mathcal{NE}}/\partial\omega^{\mathcal{N}}$, including in this plot all blocks from the published data set and from data sets where we had exaggerated $k^{\mathcal{N}}$. The resulting slope was consistent with zero and allowed us to place a systematic uncertainty limit four times smaller than the EDM statistical uncertainty.

Apart from the fluctuating dependence of $\omega^{\mathcal{N}}$ on $k^{\mathcal{N}}$, the mechanism that produced $k^{\mathcal{N}}$ to begin with was especially peculiar. We observed that laser pointing after the polarization switching AOMs depended on both the Nufern fiber amplifier seed laser power and angle of incidence on the input fiber couple. However, the Nufern output laser beam pointing was always constant. The pointing dependence was only

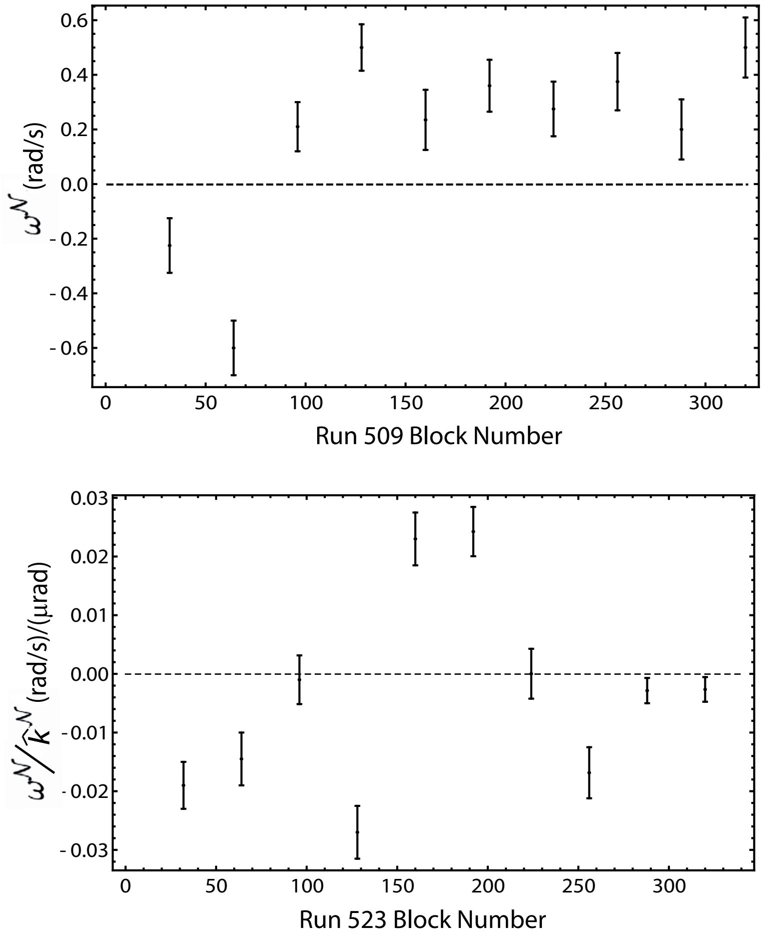

Figure 7.13: **(A)** $\tilde{N}$-correlated phase fluctuating in a portion of the EDM data set. **(B)** The drifting dependence of $\omega^{\mathcal{N}}$ on an intentionally applied $\tilde{\mathcal{N}}$-correlated readout laser pointing.

observed after the polarization switching AOMs. Because the frequency switching AOM breadboard involves four separate beam paths, corresponding to all four combinations of $\tilde{\mathcal{N}}$ and $\tilde{\mathcal{P}}$, it is possible for input power and/or input pointing to be correlated with $\tilde{\mathcal{N}}$, $\tilde{\mathcal{P}}$, or $\tilde{\mathcal{N}}\tilde{\mathcal{P}}$. In reality we observed nonzero $k^{\mathcal{N}}$ and $k^{\mathcal{P}}$ after the polarization switching AOMs. By balancing the properties of the four separate laser beams seeding the fiber amplifier, we were able to minimize $k^{\mathcal{N}}$ in the interaction region to < 1 μrad, which caused the fluctuations of $\omega^{\mathcal{N}}$ to disappear. The mechanism that causes $\tilde{\mathcal{N}}$-correlated seed power and beam pointing to produce nonzero $k^{\mathcal{N}}$ after the polarization switching AOMs, while producing no $k^{\mathcal{N}}$ immediately after the amplifier, is not at all understood at this point.

7.6 Laser Imperfections

A number of laser-related imperfections, some of which have already been mentioned, are possible in our experiment. As part of our search for systematic effects, we intentionally exaggerated all known laser imperfections parameters (Table 7.1) which could be adjusted without dismantling the apparatus. We included a systematic error contribution for certain laser imperfections analogous to the imperfections in other experiments that caused unexplained systematic offsets.

7.6.1 Laser Detuning

A number of detuning imperfections are possible since our experiment requires multiple lasers with frequencies that shift with several parameter switches. First, the overall detuning, Δ_0, common to both preparation and readout lasers typically fluctuates by ~0.1 MHz. It is tuned to resonance every 30-60 minutes by scanning through the readout fluorescence spectrum. This only ensures that the readout laser is kept on resonance. To the extent that the preparation laser pointing is not parallel to the readout laser pointing, the average preparation laser detuning, Δ_{prep}, will be nonzero. We monitor the contrast spectrum several times per week to ensure that $\Delta_{\mathrm{prep}} < 0.2$ MHz. As previously mentioned, relative misalignment between the $\hat{X}$ and $\hat{Y}$ readout laser beams will lead a detuning difference, Δ_{XY}, between the two beams.

Preparation and readout laser detuning can also be correlated with parameter switches. As previously mentioned, a -5 mV/cm non-reversing electric field will lead to $\tilde{\mathcal{N}}\tilde{\mathcal{E}}$-correlated detuning, $\Delta^{\mathcal{N}\mathcal{E}} \approx -5$ kHz. Similarly, if the AOM that switches the laser frequency between between resonance with the two $\mathcal{N}$ levels is not perfectly set to match the $\mathcal{N}$ level Stark splitting, a nonzero $\Delta^{\mathcal{N}}$ will result. A separate AOM provides the $\tilde{\mathcal{P}}$ switch. T0 the extent that the AOM frequency is not matched to energy splitting of the two $\mathcal{C}$-state opposite parity levels, $\Delta^{\mathcal{P}}$ will be nonzero. The AOM frequencies never drift appreciably and $\Delta^{\mathcal{N}}$ and $\Delta^{\mathcal{P}}$ are typically less than 20 kHz and 50 kHz, respectively. Though we can measure $\Delta^{\mathcal{N}}$ with 1 kHz precision, the bow of the field plate surface and fluctuations in the Stark splitting, likely caused by thermal fluctuations of field plate spacing, limit our ability to zero out this correlated detuning.

Accounting for all known sources of laser detuning, the detuning of a specific laser beam for a specific experimental state is,

$$\text{Preparation Laser: } \Delta = \Delta_0 + \Delta_{\mathrm{prep}} + \Delta^{\mathcal{N}}\tilde{\mathcal{N}} - \Delta^{\mathcal{N}\mathcal{E}}\tilde{\mathcal{N}}\tilde{\mathcal{E}}, \tag{7.27}$$

$$\text{Readout Laser: } \Delta = \Delta_0 \pm \Delta_{\mathrm{XY}} + \Delta^{\mathcal{N}}\tilde{\mathcal{N}} - \Delta^{\mathcal{N}\mathcal{E}}\tilde{\mathcal{N}}\tilde{\mathcal{E}} + \Delta^{\mathcal{P}}\tilde{\mathcal{P}}. \tag{7.28}$$

Each detuning imperfection was separately exaggerated, and in some cases simultaneously exaggerated. Most of the detuning terms in equations 7.27 and 7.28 were exaggerated to ± 1-2 MHz. No detuning or detuning correlation produced a significant shift in the measured EDM value. In some cases shifts in other phase channels were induced, but all shifts were consistent with well understood light shift and asymmetry effects. For example the combination of nonzero Δ_0 and $\Delta^{\mathcal{N}}$ coupled to the $\mathcal{B}$-dependent component of ϕ_{ls} (Figure 7.10) to significantly shift $\omega^{\mathcal{N}\mathcal{B}}$. Asymmetry correlations also resulted from these detuning correlations, but these were only manifested as $\tilde{\mathcal{P}}\tilde{\mathcal{R}}$ correlated phases. Because the YbF EDM experiment observed unexplained dependence of the measured EDM value on state preparation microwave detuning, we included a systematic error contribution from all detuning imperfections

7.6.2 Laser Pointing and Intensity

Similar to detuning imperfections, the preparation and readout lasers can have imperfect pointing and correlated intensity. Ideally the laser propagation direction, $\hat{k}$, would be parallel the laboratory electric field. This diminishes the amount of $\hat{z}$ polarized light experienced by the lasers, which can drive unwanted off-resonant transitions, and prevents stray retroflection from the ITO field plate surface. Using this ITO retroflection as a guide we can align $\hat{k}$ perpendicular the field plate surface, and therefore parallel to $\hat{\mathcal{E}}$, to within $\sim$ 3 mrad. Both preparation and readout pointing misalignments were exaggerated in the horizontal direction to ±10 mrad, as was the relative pointing of the $\hat{X}$ and $\hat{Y}$ readout beams. The vacuum windows and

∼1.5 inch wide holes in the magnetic shields prevented us from further misaligning the beams. To decouple pointing imperfections from detuning imperfections, the preparation and readout laser frequency was tuned to resonance after each pointing adjustment. No EDM shift was observed and no systematic error contribution from pointing imperfections was included. Pointing imperfections were only observed to affect the signal asymmetry, as previously discussed. Exaggerating the 943 nm laser pointing imperfection also caused no significant shift of any phase channel.

Unlike laser pointing and detuning, there is no "ideal" value for laser intensity. The preparation and readout laser intensities were chosen to sufficiently power-broaden the $H \to C$ transition without producing unnecessarily thermal stress on the field plates. Still, we decreased each laser intensity by a factor of four to check that the EDM did not depend on intensity. One intensity related imperfection is $\tilde{\mathcal{N}}$-correlated intensity, which is typically present on the 1% level due to $\tilde{\mathcal{N}}$-correlated seed power into the Nufern fiber amplifiers. We exaggerated this imperfection by a factor of 20. Only $\omega^{\mathcal{N}\mathcal{B}}$ was shifted, consistent with our understanding of the $\mathcal{B}$-correlated light shift phase. This intensity imperfection was not included in the systematic error budget.

7.7 Imperfections in Applied Fields and Molecule Beam

7.7.1 Magnetic Field

Due to the high polarizability and small magnetic dipole of ThO, the laboratory electric field completely determines the molecular quantization axis. Ideally the magnetic field would be perfectly aligned to the electric field, $\hat{B} = \hat{E}$, so that $\mathcal{B}_z = \mathcal{B}$ and $\mathcal{B}_x = \mathcal{B}_y = 0$. Since the electric and magnetic fields arise from completely separate parts of the apparatus they will have slightly different alignment and $\mathcal{B}_x$ and $\mathcal{B}_y$ will be nonzero. Given the careful design of the apparatus, we estimate the misalignment between $\hat{\mathcal{B}}$ and $\hat{\mathcal{E}}$ to be $\lesssim 2$ mrad but have no direct measurement of this. Besides this misalignment, unshielded external magnetic fields from earth or other sources can produce nonzero $\mathcal{B}_x$ and $\mathcal{B}_y$. Magnetic field gradients, $\partial B_i/\partial j$ (where i and j can be x , y, or, z) can also arise either from external sources or the magnetic coils. To some degree perpendicular components of the magnetic field can couple the H state $M = \pm 1$ sublevels two each other through the $M = 0$ level [60], and thus induce phase shifts, but such an effect is drastically suppressed by the large Stark splitting and small Zeeman splitting of our experiment [68]. Despite this, our experiment was designed to allow a wide variety of magnetic field tilts and gradients to be applied and we directly looked for systematic effects resulting from magnetic field imperfections.

The two halves of the main cosine coils, the side uniformity coils, the axillary Helmholz x-coils, and the axillary y-coils allowed us to apply $\mathcal{B}_x$, $\mathcal{B}_Y$, $\mathcal{B}_{z,\mathrm{nr}}$, and six magnetic field gradients,$\partial B_z/\partial z$, $\partial B_z/\partial x$, $\partial B_x/\partial x$, $\partial B_y/\partial x$, $\partial B_y/\partial y$, and $\partial B_y/\partial z$.

Both $\mathcal{B}$-correlated and uncorrelated imperfections were applied. We did not precisely measure the residual values of each of these parameters along the molecule beam line until we had studied all systematic effects and collected our published data set. Based on the projected $\sim 10^5$ magnetic shielding factor, we expected all stray magnetic fields and gradients to be on the order of 10 μG and 1 μG/cm, respectively. For this reason we only exaggerated these imperfections to $\sim$2 mG and $\sim$0.5 mG/cm. When we mapped out the magnetic field with a magnetometer inserted between the electric field plates, we discovered that several imperfections were much larger than we expected (e.g. $\mathcal{B}_y \approx 0.5$ mG). This was caused by poor magnetic shielding due to insufficient shield degaussing. For this reason we revisited gathered additional EDM data with some magnetic field parameters exaggerated by an additional factor of five. The EDM, and nearly all other phase channels were not affected by any of these magnetic field parameters. Only ϕ and $\phi^{\mathcal{B}}$ were influenced, as expected. Because uncorrelated stray magnetic fields and magnetic field gradients caused unexpected EDM offsets in the PbO experiment [53], we included contributions from all uncorrelated magnetic field imperfections in our systematic uncertainty.

7.7.2 Electric Field

Unlike the magnetic field, we do not have shims to control electric field gradients and stay electric fields. The field plates are located at the center of the experiment, inside the vacuum chamber and magnetic shields and coils, with no direct access to them apart from the voltage applied to each plate. To search for systematics related the electric field, equal amounts of EDM data are gathered with two different electric field magnitudes. The EDM values from both field magnitudes were consistent with each other. The YbF experiment observed unexplained EDM dependence on the voltage offset common to both field plates, V. For this reason exaggerated V by a factor of 1000 and, even though it did not shift our EDM measurement, included it in our systematic error budget. As previously mentioned, $\mathcal{E}_{\text{nr}}$ is also exaggerated and included in our systematic error budget.

7.7.3 Molecule Beam

The molecule beam would ideally travel parallel to the electric field plates and be well centered between the plates. This minimizes Doppler shifts, protects the plates from being coated with ThO, and ensures that the molecules experience the most uniform electric field. The entire beam box sits on a two axis (y-z) translation stage. With a theodolite, the exit aperture of the buffer gas cell is centered to within 1 mm to the fixed collimator and electric field plates. The geometric constraints of the electric field plates only allow us to exaggerate the cell misalignment by roughly a factor of three before the molecules begin hitting the sides of the field plates. We also shift the molecule beam velocity distribution by using adjustable collimators in the stem region to block half of the beam from the left, right, up, or down directions. Our measured EDM value did not shift with any molecule beam parameter adjustment. At first there seemed to be significant $\omega^{\mathcal{NB}}$ dependence on left/right molecule clipping. However this dependence was not repeatable with $\mathcal{B} = 20$ mG, disappeared altogether with higher magnetic fields, and depended heavily on the polarization bin chosen in the data analysis. We suspect that this behavior might have been related to the small signal sizes, which produced non-Gaussian distributions of data, that resulted from blocking half of the molecule beam.

7.8 Contrast Correlations

As mentioned earlier and illustrated in Figure 6.3A, contrast depends on preparation laser detuning and power, just as fluorescence depends on readout laser detuning and power. $H \rightarrow C$ transition power broadening from the preparation laser decreases this dependence and produces a saturated "flat top" contrast spectrum. To the extent that the transition is not completely saturated, some dependence on detuning and power remains. The correlated detuning and Rabi frequency imperfections described in this chapter can therefore cause contrast to be correlated with experimental switches. Since phase is computed, in part, from contrast, such contrast correlations could produce phase correlations and systematic offsets. However, the "state-averaged" contrast analysis described in the previous chapter allows computed phase to be immune to such correlations.

Since our phase measurement is immune to contrast correlations, we are free to use the detuning and power dependence of contrast to our advantage. For example, $\Delta^{\mathcal{N}\mathcal{E}}$ resulting from $\mathcal{E}_{\text{nr}}$ can be measured *in situ* from the component of contrast that is correlated with $\tilde{N}\tilde{\mathcal{E}}$, $\mathcal{C}^{\mathcal{N}\mathcal{E}}$,

$$\mathcal{E}_{\text{nr}} = \frac{\hbar\Delta^{\mathcal{N}\mathcal{E}}}{d_H} = \frac{\hbar\mathcal{C}^{\mathcal{N}\mathcal{E}}}{d_H}\frac{\partial\Delta_{\text{prep}}}{\partial\mathcal{C}}. \tag{7.29}$$

To this end, for a fraction (∼5%) of the data set we tune the preparation laser ±2 MHz off resonance to increase the contrast dependence on detuning and Rabi frequency, allowing for more accurate measurements of $\mathcal{E}_{\rm nr}$ and $\Omega_{\rm r}^{\mathcal{NE}}$. Like data with intentionally applied $\mathcal{E}_{\rm nr}$ and $\Omega_{\rm r}^{\mathcal{NE}}$, this data does not contribute to the reported EDM mean or statistical uncertainty. For the power-broadened contrast spectrum $\partial\mathcal{C}/\partial\Delta_{\rm prep}$ reverses sign between $\Delta_{\rm prep} = +2$ MHz and $\Delta_{\rm prep} = -2$ MHz, whereas $\partial\mathcal{C}/\partial\Omega_{\rm r}$ is independent of the sign of $\Delta_{\rm prep}$. Therefor, detuning correlations can be measured separately from Rabi frequency correlations by examining the behavior of the contrast correlation under reversal of $\Delta_{\rm prep}$. From $\mathcal{C}^{\mathcal{NE}}$ we measure $\mathcal{E}_{\rm nr}$ to be 4.8 ± 0.9 mV/cm in the preparation region throughout the published data set (Figure 7.14A).

While this $\mathcal{E}_{\rm nr}$ measurement is not as precise as those obtained through microwave or Raman spectroscopy [71, 61, 72], it is the only measurement that can be acquired *in situ* while gathering EDM data. Other methods of measuring $\mathcal{E}_{\rm nr}$ require days of separate data analysis and apparatus setup, while the contrast correlation method simply requires that the preparation laser be tuned off resonance. This measurement provides the important information that $\mathcal{E}_{\rm nr}$ was not drifting significantly as we gathered EDM data. A measurement of $\Delta{\rm r}^{\mathcal{NE}}$ was obtained from the component of $\mathcal{C}^{\mathcal{NE}}$ that did not reversed with preparation laser detuning, though the uncertainty of this measurement was much larger that that obtained from $\omega^{\mathcal{NEB}}$.

The average Stark splitting between $\mathcal{N}$ levels, $\Delta_{\rm Stark}$, can be similarly obtained from $\mathcal{N}$-correlated contrast:

$$\Delta_{\rm Stark} = \nu^{\mathcal{N}} - \Delta^{\mathcal{N}} = \nu^{\mathcal{N}} - \frac{\mathcal{C}^{\mathcal{N}}}{d_H}\frac{\partial\Delta_{\rm prep}}{\partial\mathcal{C}}, \tag{7.30}$$

where $\nu^{\mathcal{N}}$ is the laser frequency shift we apply to switch resonance between $\mathcal{N}$ lev-

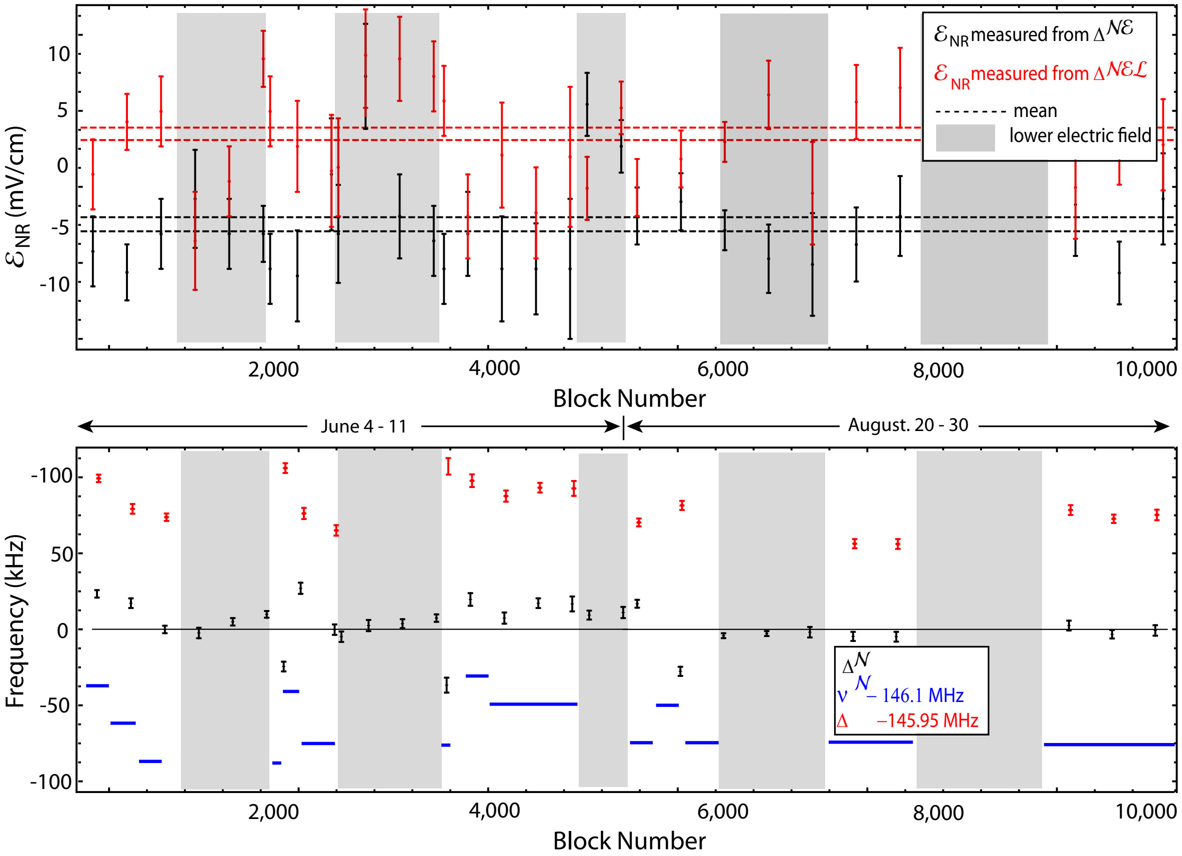

Figure 7.14: **(A)** Measurements of $\mathcal{E}_{\rm nr}$ throughout the EDM data set obtained from $\mathcal{C}^{\mathcal{N}\mathcal{E}}$ (black) when $\Delta_{\rm prep} = \pm 2$ MHz. The component of $\mathcal{E}_{\rm nr}$ originating from the voltage supply and/or other sources outside the interaction region is obtained from $\mathcal{C}^{\mathcal{N}\mathcal{E}\mathcal{L}}$ (red). This component is suppressed by lead switching throughout the data set. **(B)** The fluctuating Stark splitting between the $\mathcal{N}$ levels, present for half of the EDM data set, is measured through $\mathcal{C}^{\mathcal{N}}$.

els. For June 2014 data, Δ_{Stark} drifted significantly on the few hour timescale (see Figure 7.14B). The room temperature and humidity was drifting significantly during that time and we suspect this caused small thermal fluctuations in field plate spacing, would in turn cause Δ_{Stark} to fluctuate. We used $\mathcal{C}^N$ to feedback on the AOM frequency determining $\nu^{\mathcal{N}}$ every 3-4 hours to ensure that $\Delta^{\mathcal{N}}$ is always below 30 kHz.

Throughout the EDM data set we observed significant offsets to $\mathcal{C}^{\mathcal{N}}$ and $\mathcal{C}^{\mathcal{NP}}$ on the 0.1% level that were independent of preparation laser detuning. These offsets both shifted when the laboratory electric field changed. These offsets were caused by correlated background fluorescence from off resonant $|H, M_J = 0\rangle \rightarrow |C, M_J = 1\rangle$ transitions. As can be see from Figure 7.3, the extent to which these transitions are off-resonant depends on the $\tilde{\mathcal{N}}$ and $\tilde{\mathcal{P}}$. The background fluorescence, and resulting reduction of contrast, will have the same dependence on $\tilde{\mathcal{N}}$ and $\tilde{\mathcal{P}}$. The background fluorescence required to produce ~0.1% contrast correlations is consistent with that expected given the 2-3 MHz power-broadened linewidth of the readout transition.

7.9 Searching for Correlations in EDM data set

Until now we have primarily focused on phases correlated with the three field switches, $\mathcal{N}$, $\mathcal{E}$, and $\mathcal{B}$, performed within a data block. As previously mentioned, many other parameters switches are performed from block to block on timescales varying from 1 minute to 1 week (see 6.4). We analyze our data to look for components of phase, contrast, and fluorescence that are correlated with these switches as well. We also look for correlations with other carefully monitored parameters, such as molecule beam velocity, room temperature, and vacuum pressure, that cannot be tuned over a wide range but tend to fluctuate on their own. If each parameter reversal or fluctuation is treated as a binary switch then 2^{N} switch parity components can be computed from N switches. Thus we could potentially compute nearly 100,000 possible phase, contrast, and fluorescence signal correlations from our many parameter switches.

Longer timescale switch parity components are computed in the same manner as block switch components, as in Equation 6.18. Three different magnitudes of magnetic field are chosen, so $|\mathcal{B}|$ cannot technically be considered a binary switch. Because identical laser polarization is used for $|\mathcal{B}| = 1$ mG and $|\mathcal{B}| = 40$ mG data (see Figure 6.2) we group data from those magnetic fields together to compare with $|\mathcal{B}| = 20$ mG data, thereby forming a binary switch of $|\mathcal{B}|$. Besides the switches listed in Figure 6.4, we treat molecule forward velocity dispersion as a binary switch, comparing phase correlations computed from the first and second half of the molecule pulse. In the same way we create a binary polarization bin switch by comparing data from the beginning and end of the $\hat{X}$-$\hat{Y}$ polarization cycle. Since fluoresce was collected by two PMTs, each measuring light collected in lenses on opposing sides of the field plates, we separately analyzed data from each PMT to create a PMT binary switch. To look for correlations between phase channels and fluctuating quantities such as vacuum pressure we simply plotted each phase channel as a function of the drifting quantity and looked for signs of linear dependence.

From the reported EDM data set, we computed about 4000 switch parity components of phase and contrast, shown in Figure 7.15. Each component is represented as a square with shading indicating the extent to which the component is nonzero.

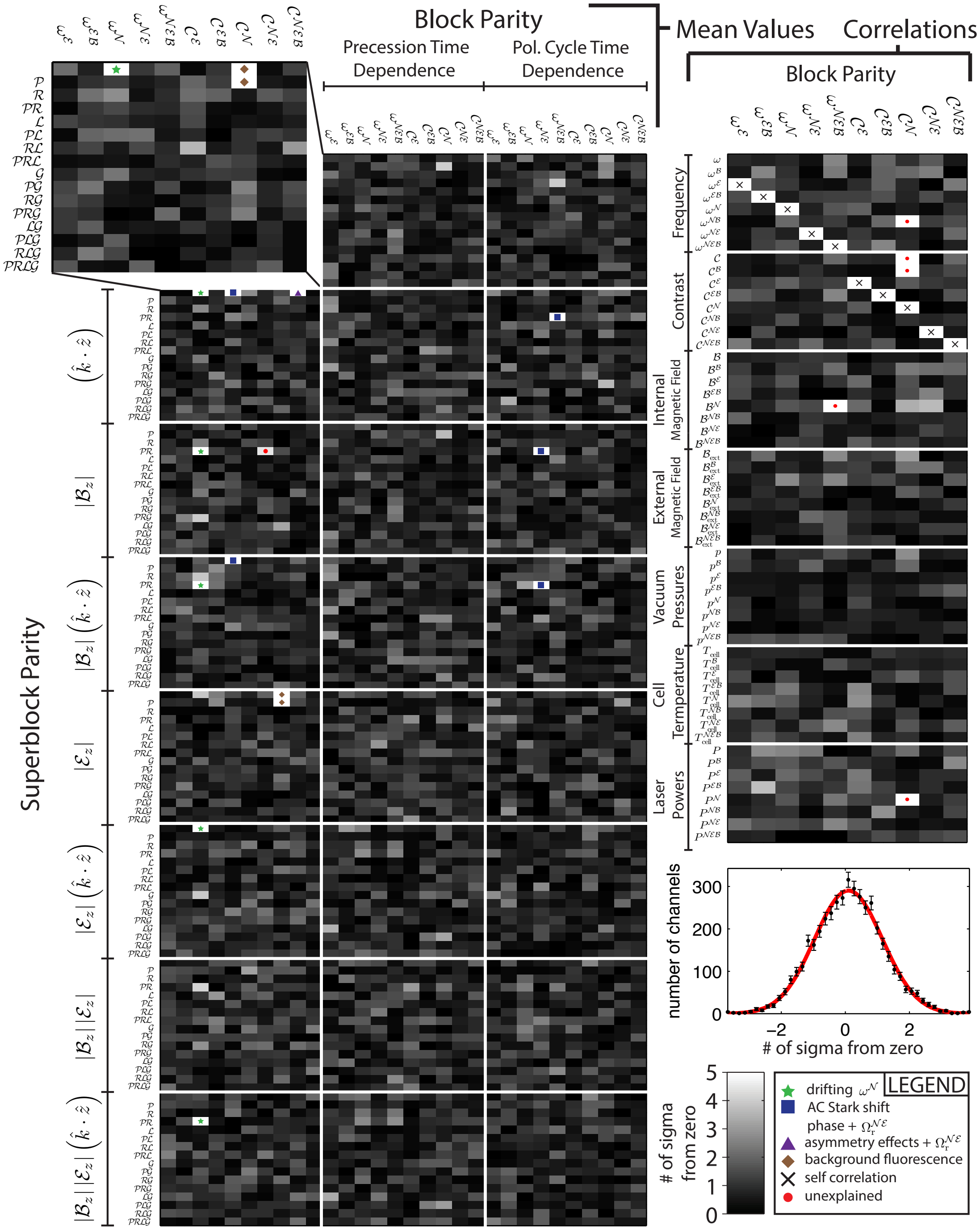

Figure 7.15: Over 4000 switch parity components computed from the EDM data set. The extent to which each channel is nonzero is indicated by the black/white coloring. Nearly all significantly nonzero channels are expected to have offsets based on mechanisms discussed in this chapter, indicated by the colored legends. All other channels have a Gaussian distribution (lower right). We also searched for correlations between phase channels and externally monitored quantities (upper right).

Some phase and contrast correlations have clear offsets from zero (white rectangles). In nearly all cases the offset can be explained by the mechanisms already discussed in this chapter, indicated by the colored legend placed on each white rectangle. As shown in the lower right corner of Figure 7.15, the statistical distribution of these ∼4000 channels is consistent is a Gaussian, with reduced $\chi^2 \approx 1$, once the ∼20 understood nonzero channels are removed. The fact that these thousands of channels behave as expected gives us confidence that the single phase channel which corresponds to the EDM is accurate.

7.10 Total Systematic Uncertainty

Our total systematic uncertainty is $\delta\omega^{\mathcal{N}\mathcal{E}}_{\text{syst}} = 3.25$ mrad/sec, or $\delta d_{\text{e,syst}} = 2.5$ e cm assuming $\mathcal{E}_{\text{eff}} = 84$ V/cm [10]. This includes contributions from sixteen experimental imperfections, three of which were shown to actually shift the measured EDM value (see Table 7.3). These imperfections were included because they met the criteria outlined at the beginning of this chapter. This systematic uncertainty was added in quadrature with the statistical uncertainty to obtain the overall uncertainty of the EDM measurement. This resulted in an overall uncertainty and EDM upper limit ∼20% larger than what it would have been if only statistical uncertainty was considered.

The suppression of known systematic effects was limited only by statistics. To the best of our knowledge to limit of $\partial\omega^{\mathcal{N}\mathcal{E}}/\partial\mathcal{E}_{\text{nr}}$ could have been 10 times smaller if we had collected the data required to tune out that slope with such precision. In addition to this, the following chapter will describe improvements to the electric field plates which should decrease thermal stress-induced birefringence by two orders of magnitude. Therefore, there is no reason to believe that the systematic effects we have discovered in this first generation measurement will limit the next generation of the experiment.

Chapter 8

A New Electron EDM Limit

Precise measurements of electron electric dipole moments provide stringent tests of new physics beyond the Standard Model. This thesis has described a new experiment which uses unique properties of thorium monoxide molecules to enhance EDM sensitivity and suppress systematic offsets that have limited previous measurements. After developing a robust apparatus and measurement procedure, and directly confirming that all systematic effects were sufficiently small, we gathered and analyzed roughly 200 hours of EDM data. The computed statistical and systematic uncertainties were an order of magnitude below that of any previous electron EDM measurement.

The result of this first generation ThO measurement,

$$d_e = -2.1 \pm 3.7_{\mathrm{stat}} \pm 2.5_{\mathrm{syst}} \times 10^{-29}\, e\,\mathrm{cm}, \tag{8.1}$$

is computed from from the measured phase component $\omega^{\mathcal{N}\mathcal{E}} = -d_e \mathcal{E}_{\mathrm{eff}}/\hbar$ corresponding to the EDM using a ThO effective electric field value of $\mathcal{E}_{\mathrm{eff}} = 84$ GV/cm. This $\mathcal{E}_{\mathrm{eff}}$ value was calculated by Anatoly Titov and his collaborators with an estimated

15% uncertainty [10]. Our measurement allows us to place an upper limit of

$$|d_e| < 8.7 \times 10^{-29}\, e\,\mathrm{cm} \tag{8.2}$$

on the electron EDM with 90% confidence, using the Feldman-Cousins approach for computing confidence intervals [93].

Paramagnetic molecules are actually sensitive to more than one time-reversal symmetry (T)-violating effect [94, 95, 96]. The T-violating electron-nucleon coupling, quantified by the dimensionless coupling constant C_S, would manifest itself in ThO in exactly the same way as the EDM. Thus our measurement of $\omega^{\mathcal{N}\mathcal{E}}$ is actually a measurement of the sum of the contributions from both d_e and C_S mechanisms,

$$\hbar\omega^{\mathcal{N}\mathcal{E}} = -d_e\mathcal{E}_{\mathrm{eff}} - C_S W_S, \tag{8.3}$$

where $W_S = h \times 300$ kHz is the C_S enhancement factor for ThO [94, 10]. The likehood of a conspiracy such that d_e and C_S both being significantly non-zero and canceling with each other in our measurement seems extremely unlikely. Keeping with tradition [36, 5] we assume $C_S = 0$ to compute the reported EDM upper limit. Assuming instead that $d_e = 0$ yields the upper limit $|C_S| < 5.9 \times 10^{-9}$ with 90% confidence, nine times smaller than the previous best C_S limit from the mercury EDM experiment [39].

Our new EDM experiment was not only very precise, it was also very robust. The measurement procedure and experimental apparatus provided precise control of many experimental parameters over a broad tuning range. This allowed us to conduct a thorough search for systematic offsets by intentionally exaggerating over 40 experimental imperfections while monitoring the measured EDM value. Unlike any previous experiment, we acquired EDM data while significantly varying the magnitude of laboratory electric and magnetic fields. Nearly 20 such experimental parameters were varied or switched throughout the EDM data set. From these switches over 4000 separate components of measured phase were computed and studied. Because we understand the behavior of these 4000 phase components, we are confident that unknown spurious effects are not contaminating the one phase component from which the EDM is derived.

The ACME collaboration has improved the electron EDM limit by a factor of 12 using the enormous effective electric field and unique quantum properties of the ThO molecule. In the context of Standard Model extensions that allow an EDM to enter in one or two loop level Feynman digarams, this experiment probes new physics on energy scales at or beyond those currently being investigated by the Large Hadron Collider [37, 29, 7, 35, 28, 2].

Upgrades to the EDM apparatus are currently underway to further reduce statistical and systematic uncertainties [72]. These upgrades include electrostatic guiding to decrease solid-angle loss in the molecule beam, a new procedure to more efficiently transfer ThO population from the ground state to the excited coherent spin state, and new electric field plates with improved thermal and optical properties to minimize systematic effects from light shifts. These upgrades promise to reduce the uncertainty of this EDM measurement by at least a factor of 10 over the next five years. This additional precision will either lead to the discovery of the long-predicted electron EDM or force many extensions to the Standard Model into an extremely uncomfortable realm of fine-tuning.

Appendix A

Parity of C State Doublets

Each rotational level of the C state consists two opposite parity states, Ω-doublets, denoted in this thesis by $\mathcal{P}\pm$. In the lowest rotational level of C, these opposite parity states are separated by $\sim$50 MHz. The parity of each level can be deduced by driving $|H\rangle \rightarrow |C, \mathcal{P}\pm\rangle$ in zero electric field and noting which $\mathcal{P}\pm$ transition is forbidden. With two separate tests we confirmed that **the lower energy doublet of $|C, J = 1\rangle$ has positive parity and the higher energy doublet of $|C, J = 1\rangle$ has negative parity**.

On two different occasions I mapped out the allowed $H \rightarrow C$ transitions as a function of electric field. Between April and June of 2012, I measured the allowed $|H, J = 1\rangle \rightarrow |C, J = 1\rangle$ transitions to determine which applied electric field would be optimal for gathering EDM data (see Figure A.1A). The figure reveals that applied electric fields of $\sim$80 V/cm are not desirable since the two of the four $|H, \mathcal{N} = \pm 1, M_J = \pm 1\rangle \rightarrow |C, \mathcal{P}\pm, M_J = 0\rangle$ transitions overlap with unwanted $|H, M_J = \pm 0\rangle \rightarrow |C, M_J = \pm 1\rangle$ transitions. Among other problems, this caused a $\sim$30% contrast correlation with the $\tilde{\mathcal{N}}$-switch. For this data the $|H, J = 1\rangle$ state was populated by exciting $|X, J = 1\rangle \rightarrow |A, J = 0\rangle$ with the 943 nm laser. The parity P of an $\Omega = 0$ state in ThO, such as X or A, goes as $P = (-1)^J$. Therefore $|A, J = 0\rangle$ has positive parity, and only the negative parity Ω-doublet of H will be populated by E1 allowed spontaneous decay. With zero applied electric field, the 1090 nm laser can only drive to the positive parity Ω-doublet of C. Figure A.1A clearly shows that this $|C, J = 1, \mathcal{P}+\rangle$ state is the lower energy state. When an electric field greater than 1 V/cm is applied, the H state oppositive parity levels mix, and transitions to both C state Ω-doublets are allowed, as illustrated by Figure A.1.

In May 2013 I measured the allowed $|H, J = 2\rangle \rightarrow |C, J = 1\rangle$ transitions as a function of applied electric field to determine the induced electric dipole moment of the $|H, J = 2\rangle$ level [1]. The results are shown in Figure A.1B. Here the 943 nm laser excited the $|X, J = 2\rangle \rightarrow |A, J = 1\rangle$ transition. Therefore only the positive parity Ω-doublet of $|H, J = 2\rangle$ was populated by spontaneous E1 decay from $|A, J = 1\rangle$. Similarly, only E1 transitions to the negative parity Ω doublet of C could be induced by the 1090 nm laser. Consistent with the Figure A.1A, the data shown in Figure A.1B reveals that $|C, \mathcal{P}-\rangle$ is the higher energy Ω-doublet of $|C, J = 1\rangle$ state.

---

[1] This was part of a broader study of the $|H, J = 2\rangle$ and $|H, J = 3\rangle$ levels to determine their g-values and Δg values.

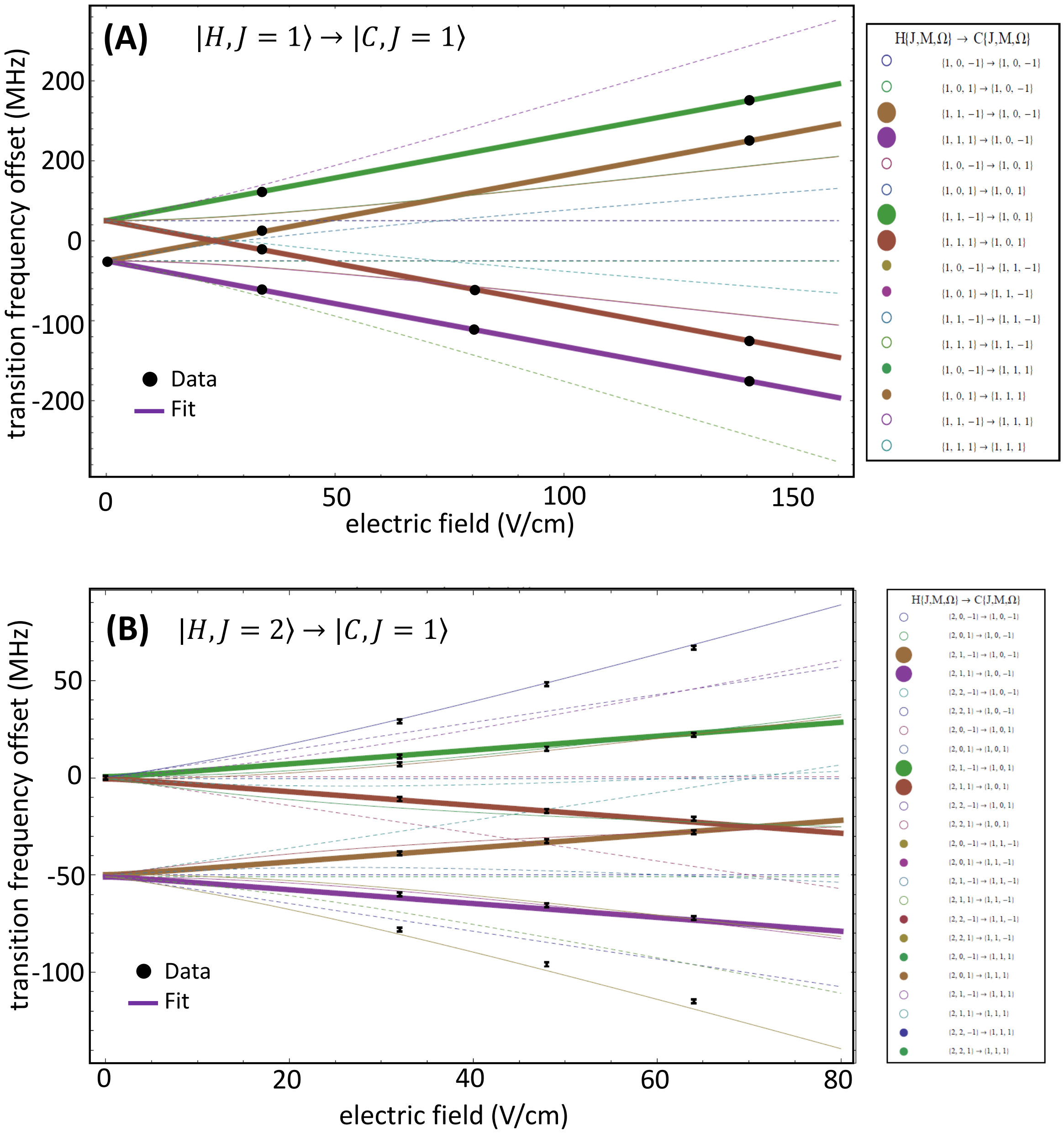

Figure A.1: Stark shifted $H \rightarrow C$ transition frequencies vs applied electric field for **(A)** $|H, J=1\rangle \rightarrow |C, J=1\rangle$ and **(B)** $|H, J=2\rangle \rightarrow |C, J=1\rangle$ transitions. **(A)** With no electric field, only the negative parity Ω-doublet of $|H, J=1\rangle$ is populated from spontaneous decay from the positive parity $|A, J=0\rangle$ state, so only fluorescence from $|C, \mathcal{P}+\rangle$ is observed. **(B)** The positive parity Ω-doublet of $|H, J=2\rangle$ is populated from spontaneous decay from $|A, J=1\rangle$, so only fluorescence from $|C, \mathcal{P}-\rangle$ is observed in zero electric field. (Line fits computed by Paul Hess)

Appendix B

Comparison of Photon Detectors

In this first generation ACME experiment, several photon detection and amplification options were available, each with different advantages and disadvantages. Figure B.1 compares the EDM sensitivity, in units of predicted signal to noise, for several different detector options. **(1)** Photomultiplier tubes (PMTs) offer high internal signal amplification with relatively low dark noise, but their quantum efficiently is only ∼10% at 690 nm. **(2)** Large area silicon photodiodes (Si PD), on the other hand offer near 100% quantum efficiency, but with no internal gain. These detectors must be cooled below 100 K to ensure that their dark noise does not dominate over the fluorescence signal. Furthermore, it is challenging to construct an external amplifier that does not produce voltage noise that dominates over the fluorescence signal [97]. **(3)** Avalanche photodiodes (APDs) provide an intermediate solution with moderate internal amplification and 40-80% quantum efficiency [1]. APDs must also be cooled

---

[1] Most APDs have a specified quantum efficiency near 80%. However, David DeMille first pointed out to us that the noise added in the avalanche amplification process increases the signal/noise by a factor of $\sqrt{2}$. The effective quantum efficiency is therefore ∼40%, at least as far as the EDM sensitivity is concerned.

below freezing to suppress their dark noise [98]. However, the internal amplification makes it feasible to design an external amplifier which does not add significant noise [97].

Figure B.1 compares the EDM sensitivity, in terms of predicted signal to noise, for the three detector options described above. For the $\sim 10^6$ photon/s counting rates per detector achieved in the first generation ACME experiment, PMTs and APDs offered comparable signal/noise. PMTs were chosen because they did not require cooling and could be implemented with a commercial voltage voltage amplifier (SRS SR445A). For the Si PD curves in Figure B.1, it is assumed that an external amplifier similar to a custom design from the DeMille lab [97] will be used to amplify the Si PD signal. The equations for the various types of noise introduced by such an amplifier are shown in figure B.2, along with a model circuit of the Si PD and amplifier [2]. The specific values of the resistors and capacitors that produce minimal voltage noise and Johnson noise depends on the desired detection bandwidth and size (capacitance) of the Si PD. Clearly, over five orders of magnitude in fluorescence counting rate ($\sim 10^{11}$ photon/s) must be achieved before large area Silicon photodiodes could be beneficial to ACME while maintaining the ~100 kHz detection bandwidth required to resolve fast laser polarization switching.

---

[2] Some of these noise equations differ from those of the DeMille paper [97]. David DeMille has confirmed that some of the equations in the paper are incorrect, though the graphs and conclusions of the paper are still accurate.

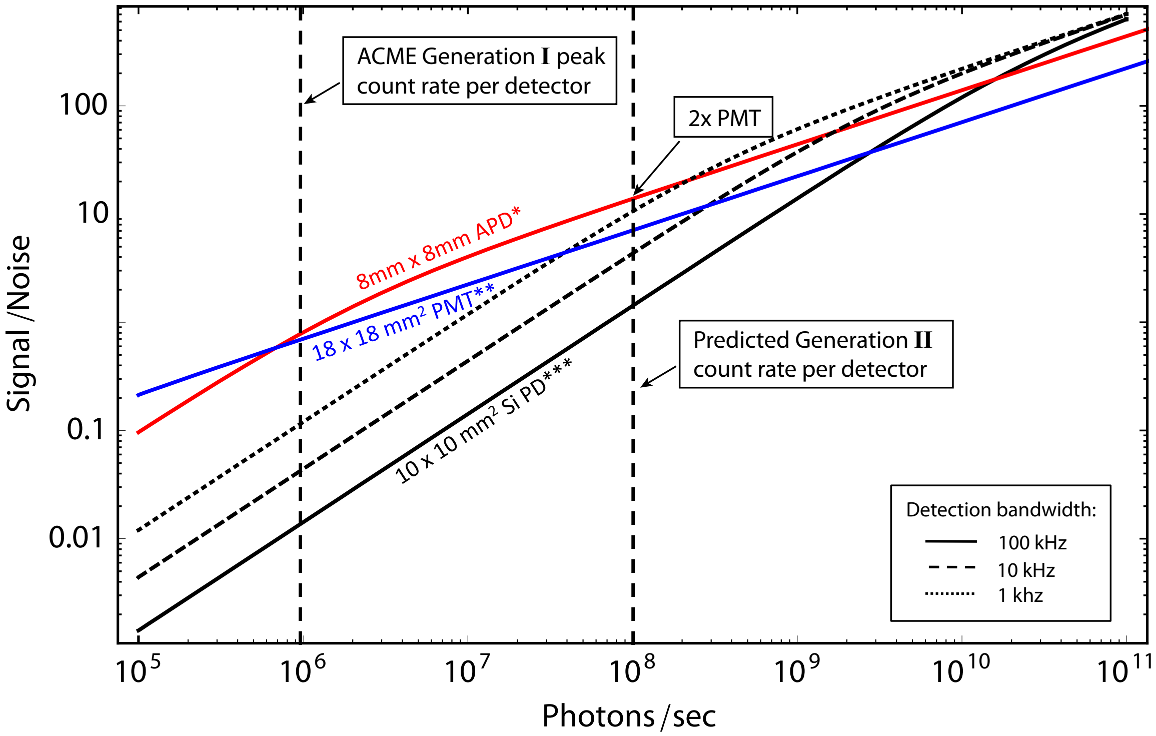

*Fox, et al. 1998
** Hamamatsu R8900
*** Hamamatsu S3950

Figure B.1: Comparison of PMT, APD, and Si PD photon detector options. For each detector, the EDM sensitivity, in terms of signal/noise, is plotted as a function of photon counting rate, $\dot{N}$. Like EDM sensitivity, signal/noise increases as $\sqrt{\dot{N}}$ in the shot-noise limit. Because of their large internal amplification, PMTs (blue) provide shot-noise limited signals with relatively low photon counting rates of $\sim 10^5$ photon/s. Cooled APDs (red) contribute a higher dark count rate, and require more external amplification; a counting rate of $\sim 10^7$ photon/s is required to be shot-noise limited with APDs. The external amplifiers required for cooled Si PDs (black) contribute far too much noise for the these detectors to be useful to ACME in the foreseeable future, assuming that detections bandwidths > 100 kHz are still required to resolve fast laser polarization switching.

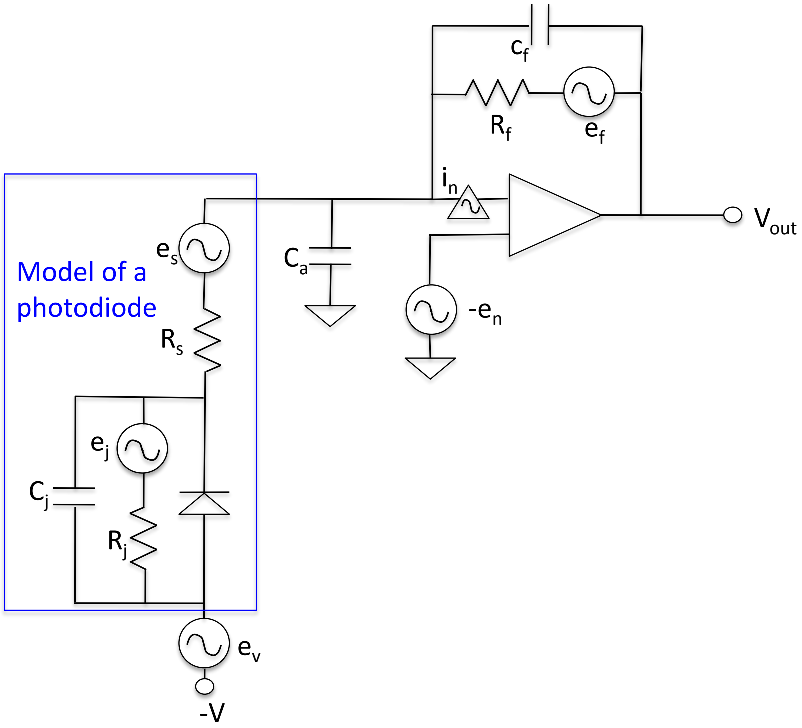

Johnson noise:

$$e_{out,Jj} = \frac{\dfrac{R_f}{1+i\omega R_f C_f}}{R_j + R_s + i\omega R_j R_s C_j} e_{Jj}$$

$$e_{out,Js} = \frac{\dfrac{R_f}{1+i\omega R_f C_f}}{R_s + \dfrac{R_j}{1+i\omega R_i C_j}} e_{Js}$$

$$e_{out,Jf} = \frac{e_{Jf}}{1+i\omega R_f C_f}$$

Voltage noise:

$$e_{out,n} = \left(1 + \frac{\dfrac{R_f}{1+i\omega R_f C_f}}{R_s + \dfrac{R_j}{1+i\omega R_j C_i}}\right) e_n$$

Current noise:

$$e_{out,i} = \frac{R_f i_n}{1+i\omega R_f C_f}$$

Figure B.2: Various noise contributions to an op-amp based photodiode amplifier, similar to the custom amplifier described in [97]. A Model of the photodiode and op-amp is shown on the left. The noise equations are shown on the right. The "voltage noise" source typically dominates for the detection bandwidths used in the ACME experiment. The specific values of the resistors and capacitors that produce minimal voltage noise and Johnson noise depends on the desired detection bandwidth and size (capacitance) of the Si PD.

Bibliography

[1] Sakharov, A. D. Violation of CP Invariance, C Asymmetry, and Baryon Asymmetry of the Universe. *JETP Lett.* 5, 27–30 (1967).

[2] Collaboration, A. Measurements of higgs boson production and couplings in diboson final states with the {ATLAS} detector at the {LHC}. *Physics Letters B* 726, 88 - 119 (2013).

[3] Fortson, N., Sandars, P. & Barr, S. The search for a permanent electric dipole moment. *Physics Today* 56, 33–39 (2003).

[4] Collaboration, T. A., Baron, J., Campbell, W. C., DeMille, D., Doyle, J. M., Gabrielse, G., Gurevich, Y. V., Hess, P. W., Hutzler, N. R., Kirilov, E., Kozyryev, I., OLeary, B. R., Panda, C. D., Parsons, M. F., Petrik, E. S., Spaun, B., Vutha, A. C. & West, A. D. Order of magnitude smaller limit on the electric dipole moment of the electron. *Science* 343, 269-272 (2014).

[5] Hudson, J. J., Kara, D. M., Smallman, I. J., Sauer, B. E., Tarbutt, M. R. & Hinds, E. A. Improved measurement of the shape of the electron. *Nature* 473, 493–6 (2011).

[6] Ilakovac, A., Pilaftsis, A. & Popov, L. Lepton dipole moments in supersymmetric low-scale seesaw models. *Phys. Rev. D* 89, 015001 (2014).

[7] Engel, J., Ramsey-Musolf, M. J. & van Kolck, U. Electric dipole moments of nucleons, nuclei, and atoms: The Standard Model and beyond. *Progress in Particle and Nuclear Physics* 71, 21–74 (2013).

[8] Cirigliano, V., Li, Y., Profumo, S. & Ramsey-Musolf, M. J. MSSM baryogenesis and electric dipole moments: an update on the phenomenology. *Journal of High Energy Physics* 2010, 2 (2010).

[9] Flambaum, V. V. & Khriplovich, I. V. B. On the enhancement of parity nonconserving effects in diatomic molecules. *Physics Letters* 110A, 121–125 (1985).

[10] Skripnikov, L. V., Petrov, A. N. & Titov, A. V. Theoretical study of ThO for the electron electric dipole moment search. *arXiv:1308.0414* (2013).

[11] Fleig, T. & Nayak, M. K. Electron electric dipole moment and hyperfine interaction constants for tho. *Physics Archive* arXiv:1401.2284 (2014).

[12] Meyer, E. R. & Bohn, J. L. Prospects for an electron electric-dipole moment search in metastable ThO and ThF$^+$. *Phys. Rev. A* 78, 10502 (2008).

[13] Wu, C. S. Experimental Test of Parity Conservation in Beta Decay (1957).

[14] Christenson, J. H., Cronin, J. W., Fitch, V. L. & Turlay, R. Evidence for the 2π decay of the K_2^0 meson. *Phys. Rev. Lett.* 13, 138–140 (1964).

[15] Bluhm, R., Kostelecký, V. A., Lane, C. D. & Russell, N. Probing Lorentz and CPT violation with space-based experiments. *Phys. Rev. D* 68, 125008 (2003).

[16] Bluhm, R., Kostelecký, V. A. & Russell, N. CPT and Lorentz tests in Penning traps. *Phys. Rev. D* 57, 3932-3943 (1998).

[17] Fogwell-Hoogerheide, S. *Trapped Positrons for High-Precision Magnetic Moment Measurements.* Ph.D. thesis, Harvard Univ. (2013). (advisor: G. Gabrielse).

[18] Gavela, M., Hernandez, P., Orlo, J. & Pene, P. Standard model cp-violation and baryon asymmetry. *Physics Archive* (1993).

[19] Shaposhnikov, M. Baryon asymmetry of the universe in standard electroweak theory (1987).

[20] Davoudiasl, H., Morrissey, D., Sigurdson, K. & Tulin, S. Unified Origin for Baryonic Visible Matter and Antibaryonic Dark Matter. *Physical Review Letters* 105, 1–4 (2010).

[21] Graham, P. W. & Rajendran, S. Axion dark matter detection with cold molecules. *Phys. Rev. D* (2011).

[22] Bœhm, C. & Ascasibar, Y. More evidence in favor of light dark matter particles? *Phys. Rev. D* 70, 115013 (2004).

[23] Pal, G., Horvth, I. & Lukcs, B. Inflation and compactification from galaxy redshifts? *Astrophysics and Space Science* 191, 107-124 (1992).

[24] Peccei, R. D. & Quinn, H. R. ¡span class="aps-inline-formula"¿¡math¿¡mi¿cp¡/mi¿¡/math¿¡/span¿ conservation in the presence of pseudoparticles. *Phys. Rev. Lett.* 38, 1440–1443 (1977).

[25] Wald, R. M. *General Relativity.* (University of Chicago Press, 1984).

[26] Drees, M. An Introduction to Supersymmetry (1996).

[27] Olive, K., Pospelov, M., Ritz, A. & Santoso, Y. CP-odd phase correlations and electric dipole moments. *Physical Review D* 72, 1–17 (2005).

[28] Nir, Y. Cp violation in and beyond the standard model. *Physics Archive* arXiv:hep-ph/9911321v2 (1993).

[29] Pospelov, M. & Ritz, A. Electric dipole moments as probes of new physics. *Ann. Phys.* 318, 119–169 (2005).

[30] Huber, S., Pospelov, M. & Ritz, A. Electric dipole moment constraints on minimal electroweak baryogenesis. *Physical Review D* 75, 036006 (2007).

[31] Budker, D., Kimball, D. & DeMille, D. *Atomic physics: An exploration through problems and solutions* (Oxford University Press, USA, 2008).

[32] Pospelov, M. E. & Khriplovich, I. B. Electric Dipole Moment of the W boson and the Electron in the Kobayashi-Maskawa Model. *Yad. Fiz.* 53, 1030–1033 (1991).

[33] Archambault, J. P., Czarnecki, A. & Pospelov, M. Electric dipole moments of leptons in the presence of majorana neutrinos. *Phys. Rev. D* 70, 073006 (2004).

[34] Khriplovich, I. B. & Lamoreaux, S. K. *CP Violation Without Strangeness* (Springer, 1997).

[35] Bernreuther, W. & Suzuki, M. The electric dipole moment of the electron. *Reviews of Modern Physics* 63, 313 (1991).

[36] Regan, B., Commins, E., Schmidt, C. & DeMille, D. New Limit on the Electron Electric Dipole Moment. *Physical Review Letters* 88, 18–21 (2002).

[37] Barr, S. A Review of CP Violation in Atoms. *International Journal of Modern Physics A* 08, 209–236 (1993).

[38] Baker, C., Doyle, D. D., Geltenbort, P., Green, K., van der Grinten, M. G. D., Harris, P. G., Iaydjiev, P., Ivanov, S. N., May, D. J. R., Pendlebury, J. M., Richardson, J. D., Shiers, D. & Smith, K. F. Improved Experimental Limit on the Electric Dipole Moment of the Neutron. *Physical Review Letters* 97, 131801 (2006).

[39] Griffith, W., Swallows, M., Loftus, T., Romalis, M., Heckel, B. & Fortson, E. Improved Limit on the Permanent Electric Dipole Moment of ^{199}Hg. *Physical Review Letters* 102, 101601 (2009).

[40] Dar, S. The neutron edm in the sm : A review. *Physics Archive* arXiv:hep-ph/0008248 (2000).

[41] Abel, S., Khalil, S. & Lebedev, O. {EDM} constraints in supersymmetric theories. *Nuclear Physics B* 606, 151 - 182 (2001).

[42] Sandars, P. G. H. The Electric Dipole Moment of an Atom. *Physics Letters* 14, 194 (1965).

[43] Sushkov, O. P., Flarnbaurn, V. V. & Flambaum, V. V. Parity breaking effects in diatomic molecules. *Sov. Phys. JETP* 48, 608–611 (1978).

[44] Porsev, S. G., Safronova, M. S. & Kozlov, M. G. Electric Dipole Moment Enhancement Factor of Thallium. *Physical Review Letters* 108, 173001 (2012).

[45] Schiff, L. I. Measurability of Nuclear Electric Dipole Moments. *Physical Review* 132, 2194 (1963).

[46] Sandars, P. G. H. Measurability of the Proton Electric Dipole Moment. *Physical Review Letters* 19, 1396–1398 (1967).

[47] Commins, E. D., Jackson, J. D. & DeMille, D. P. The electric dipole moment of the electron: An intuitive explanation for the evasion of Schiffs theorem. *American Journal of Physics* 75, 532 (2007).

[48] DeMille, D., Bay, F., Bickman, S., Kawall, D., Krause, D., Maxwell, S. & Hunter, L. Investigation of PbO as a system for measuring the electric dipole moment of the electron. *Physical Review A* 61, 52507 (2000).

[49] Gurevich, Y. V. *Preliminary Measurements for an Electron EDM Experiment in ThO*. Ph.D. thesis, Harvard Univ. (2012). (advisor: G. Gabrielse).

[50] Ramsey, N. F. A Molecular Beam Resonance Method with Separated Oscillating Fields. *Physical Review* 78, 695 (1950).

[51] Sandars, P. G. H. & Lipworth, E. Electric Dipole Moment of the Cesium Atom. *Physical Review Letters* 13, 718 (1964).

[52] Rushchanskii, K. Z., Kamba, S., Goian, V., Vanek, P., Savinov, M., Prokleska, J., Nuzhnyy, D., Knízek, K., Laufek, F., Eckel, S., Lamoreaux, S. K., Sushkov, A. O., Lezaić, M., Spaldin, N. A., Vaněk, P., Prokleška, J., Knížek, K. & Ležaić, M. A multiferroic material to search for the permanent electric dipole moment of the electron. *Nat. Mater.* 9, 649 (2010).

[53] Eckel, S., Hamilton, P., Kirilov, E., Smith, H. W. & DeMille, D. Search for the electron electric dipole moment using Ω-doublet levels in PbO. *Physical Review A* 87, 052130 (2013).

[54] Commins, E., Ross, S., DeMille, D. & Regan, B. Improved experimental limit on the electric dipole moment of the electron. *Physical Review A* 50, 2960–2977 (1994).

[55] Commins, E. D. Berrys geometric phase and motional fields. *American Journal of Physics* 59, 1077 (1991).

[56] Hudson, J., Sauer, B., Tarbutt, M. & Hinds, E. Measurement of the Electron Electric Dipole Moment Using YbF Molecules. *Physical Review Letters* 89, 8–11 (2002).

[57] Hamilton, P. *Preliminary results in the search for the electron electric dipole moment in PbO*. Ph.D. thesis (2010).

[58] Marian, C. M., Wahlgren, U. L. F., Gropen, O. D. D. & Pyykko, P. Bonding and electronic structure in diatomic ThO: quasirelativistic effective core potential calculations. *J. Mol. Struct.* 169, 339 (1987).

[59] Paulovic, J., Nakajima, T., Hirao, K., Lindh, R. & Malmqvist, P. A. Relativistic and correlated calculations on the ground and excited states of ThO. *J. Chem. Phys.* 119, 798–805 (2003).

[60] Vutha, A. C. *A search for the electric dipole moment of the electron using thorium monoxide*. Ph.D. thesis, Yale University (2011).

[61] Hutzler, N. *A New Limit on the Electron Electric Dipole Moment: Beam Production, Data Interpretation, and Systematics*. Ph.D. thesis, Harvard University (2014). (advisor: J. Doyle).

[62] Edvinsson, G. & Lagerqvist, A. Rotational analysis of some violet and green bands in the ThO spectrum. *Journal of Molecular Spectroscopy* 122, 428–439 (1987).

[63] Vutha, A. C., Spaun, B., Gurevich, Y. V., Hutzler, N. R., Kirilov, E., Doyle, J. M., Gabrielse, G. & DeMille, D. Magnetic and electric dipole moments of the $H^3\Delta_1$ state in ThO. *Physical Review A* 84, 034502 (2011).

[64] Porsev, S., Ginges, J. & Flambaum, V. Atomic electric dipole moment induced by the nuclear electric dipole moment: The magnetic moment effect. *Physical Review A* 83 (2011).

[65] Hutzler, N. (2014).

[66] Kirilov, E., Campbell, W. C., Doyle, J. M., Gabrielse, G., Gurevich, Y. V., Hess, P. W., Hutzler, N. R., O'Leary, B. R., Petrik, E., Spaun, B., Vutha, A. C. & DeMille, D. Shot-noise-limited spin measurements in a pulsed molecular beam. *Phys. Rev. A* 88, 013844 (2013).

[67] Hanneke, D., Fogwell, S. & Gabrielse, G. New Measurement of the Electron Magnetic Moment and the Fine Structure Constant. *Physical Review Letters* 100, 120801 (2008).

[68] Vutha, A. C., Campbell, W. C., Gurevich, Y. V., Hutzler, N. R., Parsons, M., Patterson, D., Petrik, E., Spaun, B., Doyle, J. M., Gabrielse, G. & DeMille, D. Search for the electric dipole moment of the electron with thorium monoxide. *Journal of Physics B: Atomic, Molecular and Optical Physics* 43, 74007 (2010).

[69] Zenteno, L. High power double-clad fiber lasers. *Journal of Lightwave Technology* 11 (1993).

[70] Petrov, A., Shripnikov, L., Titov, A., Hutzler, N. R., Hess, P. W., O'Leary, B. R., Spaun, B., Doyle, J. M., DeMille, D. & Gabrielse, G. Zeeman interaction in ThO $H^3\Delta_1$ for the electron EDM search. *To be published in Physical Review A* (2014).

[71] Hess, P. *Improving the Limit on the Electron EDM: Data Acquisition and Systematics Studies*. Ph.D. thesis, Harvard Univ. (2014). (advisor: G. Gabrielse).

[72] Collaboration, T. A., Baron, J., Campbell, W. C., DeMille, D., Doyle, J. M., Gabrielse, G., Gurevich, Y. V., Hess, P. W., Hutzler, N. R., Kirilov, E., Kozyryev, I., OLeary, B. R., Panda, C. D., Parsons, M. F., Petrik, E. S., Spaun, B., Vutha, A. C. & West, A. D. New limit on the electric dipole moment of the electron: Data analysis and systematic uncertainty. *Science* 343, 269-272 (2014).

[73] Hutzler, N. R., Lu, H.-I. & Doyle, J. M. The buffer gas beam: an intense, cold, and slow source for atoms and molecules. *Chemical Reviews* 112, 4803–27 (2012).

[74] Farkas, D. *An Optical Reference and Frequency Comb for Improved Spectroscopy of Helium*. Ph.D. thesis, Harvard University (2006). (advisor: G. Gabrielse).

[75] Maussang, K., Egorov, D., Helton, J. S., Nguyen, S. V. & Doyle, J. M. Zeeman relaxation of CaF in low temperature collisions with helium. *Phys. Rev. Lett.* 94, 123002 (2005).

[76] Shuman, E. S., Barry, J. F. & Demille, D. Laser cooling of a diatomic molecule. *Nature* 467, 820–823 (2010).

[77] Dewberry, C. T., Etchison, K. C., II, G. S. G., Powoski, R. a., Serafin, M. M., Peebles, S. A., Cooke, S. a. & Grubbs Ii, G. S. Oxygen-17 hyperfine structures in the pure rotational spectra of SrO, SnO, BaO, HfO and ThO. *Physical Chemistry Chemical Physics* 9, 5897–5901 (2007).

[78] Wentink, T. & Spindler, R. J. The isoelectronic series ScF through ThO, I notes on the band spectra of TiO, HfO and ThO. *Journal of Quantitative Spectroscopy and Radiative Transfer* 12, 1569–1590 (1972).

[79] Edvinsson, G., Selin, L.-E. & Aslund, N. On the band spectrum of ThO. *Ark. Phys.* 30, 283–319 (1965).

[80] Goncharov, V., Han, J., Kaledin, L. A. & Heaven, M. C. Ionization energy measurements and electronic spectra for ThO. *J. Chem. Phys.* 122, 204311 (2005).

[81] Olivero, J. & Longbothum, R. Empirical fits to the voigt line width: A brief review. *Journal of Quantitative Spectroscopy and Radiative Transfer* 17, 233 - 236 (1977).

[82] Meyer, E. R., Bohn, J. L. & Deskevich, M. P. Candidate molecular ions for an electron electric dipole moment experiment. *Phys. Rev. A* 73, 62108 (2006).

[83] Sauer, S. P. A relation between the rotational g-factor and the electric dipole moment of a diatomic molecule. *Chemical Physics Letters* 297, 475–483 (1998).

[84] Hutzler, N. R., Parsons, M. F., Gurevich, Y. V., Hess, P. W., Petrik, E., Spaun, B., Vutha, A. C., DeMille, D., Gabrielse, G. & Doyle, J. M. A cryogenic beam of refractory, chemically reactive molecules with expansion cooling. *Physical Chemistry Chemical Physics : PCCP* 13, 18976–85 (2011).

[85] Patten, R. Michelson interferometer as a remote gauge. *Applied Optics* 10 (1971).

[86] Gupta, R., Russenschuck, S. & Ramberger, S. Field quality optimization in a common coil magnet design. *Proceedings of the 2001 Particle Accelerator Conference* (1999).

[87] Berestetskii, V., Lifshitz, E. & Pitaevskii, L. *Quantum Electrodynamics, Course of Theoretical Physics*, vol. 4 (Pergamon Press, New York, 1982).

[88] Budker, R. S. M., D. & Yashchuk, V. V. Obtaining frequency markers of variable separation with a spherical mirror fabry-perot interferometer. *Rev. Sci. Instrum.* 71, 29842987 (2000).

[89] Ghafouri-Shiraz, H. Wavelength conversion in tapered-waveguide laser diode amplifiers. *Microwave and Optical Technology Letters* 45, 134–142 (2005).

[90] Loh, H., Cossel, K. C., Grau, M. C., Ni, K.-K., Meyer, E. R., Bohn, J. L., Ye, J. & Cornell, E. A. Precision spectroscopy of polarized molecules in an ion trap. *Science* 342, 1220-1222 (2013).

[91] Berry, H., Gabrielse, G. & Livingson, A. Measurement of the stokes parameters of light. *Applied Optics* 16 (1977).

[92] Bickman, S., Hamilton, P., Jiang, Y. & DeMille, D. Preparation and detection of states with simultaneous spin alignment and selectable molecular orientation in PbO. *Physical Review A* 80, 023418 (2009).

[93] Feldman, G. J. & Cousins, R. D. Unified approach to the classical statistical analysis of small signals. *Physical Review D* 57, 3873–3889 (1998).

[94] Dzuba, V. A., Flambaum, V. V. & Harabati, C. Relations between matrix elements of different weak interactions and interpretation of the parity-nonconserving and electron electric-dipole-moment measurements in atoms and molecules. *Phys. Rev. A* 84, 052108 (2011).

[95] Kozlov, M. G. & Labzowsky, L. N. Parity violation effects in diatomics. *Journal of Physics B: Atomic, Molecular and Optical Physics* 28, 1933–1961 (1995).

[96] Commins, E. D. & DeMille, D. The Electric Dipole Moment of the Electron. In Roberts, B. L. & Marciano, W. J. (eds.) *Lepton Dipole Moments*, chap. 14, 519–581 (World Scientific, 2010).

[97] Bickman, S. & DeMille, D. Large-area, low-noise, high-speed, photodiode-based fluorescence detectors with fast overdrive recovery. *Review of Scientific Instruments* 76, - (2005).

[98] Fox, J. J., Woodward, N. & Lafyatis, G. P. Characterization of cooled large-area silicon avalanche photodiodes. *Review of Scientific Instruments* 70 (1998).